

Document Version

Final published version

Citation (APA)

Wu, Z. (2026). *Investigating membrane voltage in embryonic development: Towards absolutely calibrated lifetime-imaging voltage sensing in developing zebrafish embryos*. [Dissertation (TU Delft), Delft University of Technology]. <https://doi.org/10.4233/uuid:2a1703d5-65ce-4960-93e7-f599c9b163ea>

Important note

To cite this publication, please use the final published version (if applicable).
Please check the document version above.

Copyright

In case the licence states "Dutch Copyright Act (Article 25fa)", this publication was made available Green Open Access via the TU Delft Institutional Repository pursuant to Dutch Copyright Act (Article 25fa, the Taverne amendment). This provision does not affect copyright ownership.
Unless copyright is transferred by contract or statute, it remains with the copyright holder.

Sharing and reuse

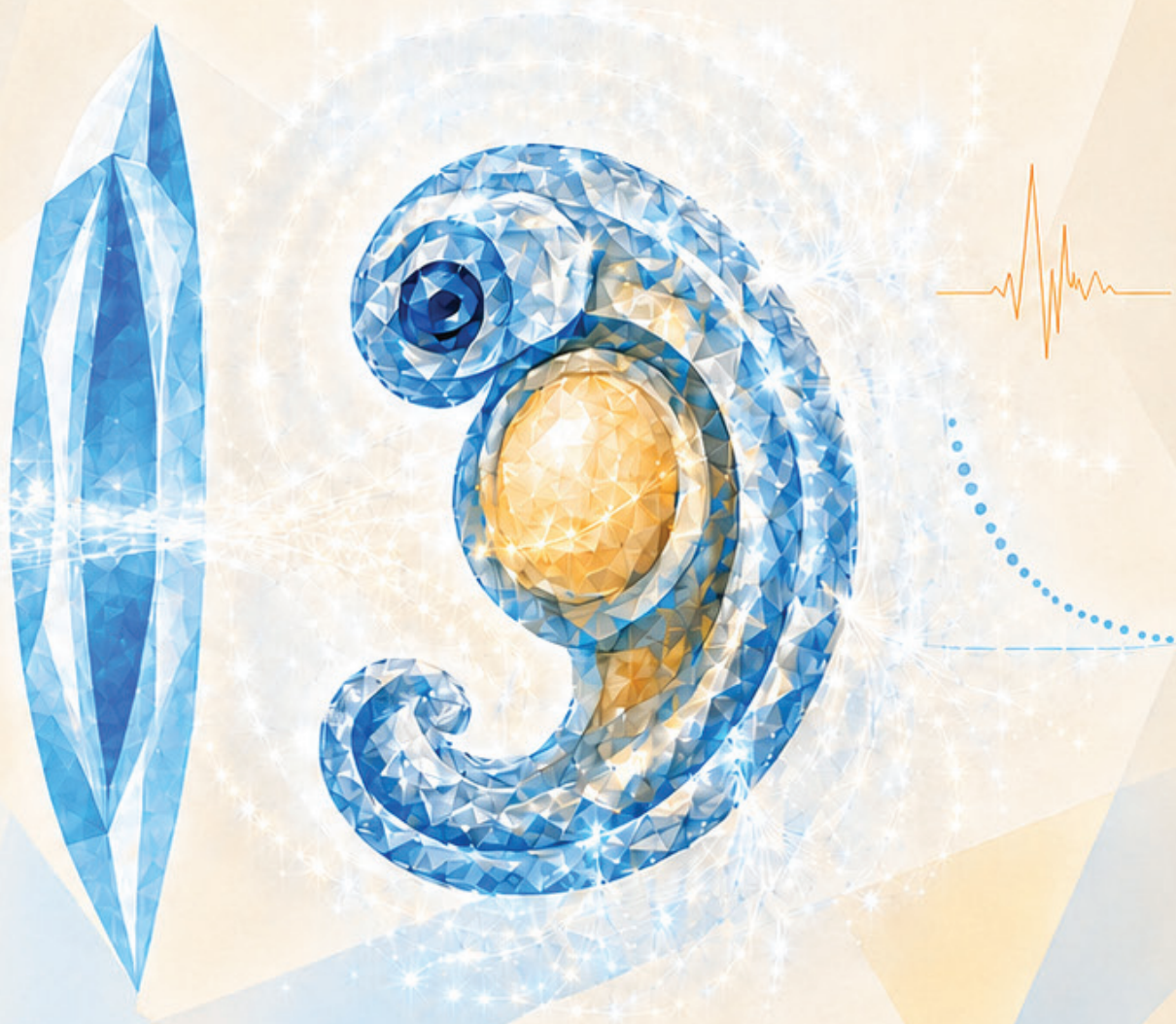
Other than for strictly personal use, it is not permitted to download, forward or distribute the text or part of it, without the consent of the author(s) and/or copyright holder(s), unless the work is under an open content license such as Creative Commons.

Takedown policy

Please contact us and provide details if you believe this document breaches copyrights.
We will remove access to the work immediately and investigate your claim.

INVESTIGATING MEMBRANE VOLTAGE IN EMBRYONIC DEVELOPMENT

Towards Absolutely Calibrated Lifetime-Imaging
Voltage Sensing in Developing Zebrafish Embryos



Zhenzhen Wu 武珍珍

INVESTIGATING MEMBRANE VOLTAGE IN EMBRYONIC DEVELOPMENT

**TOWARDS ABSOLUTELY CALIBRATED
LIFETIME-IMAGING VOLTAGE SENSING IN
DEVELOPING ZEBRAFISH EMBRYOS**

INVESTIGATING MEMBRANE VOLTAGE IN EMBRYONIC DEVELOPMENT

**TOWARDS ABSOLUTELY CALIBRATED
LIFETIME-IMAGING VOLTAGE SENSING IN
DEVELOPING ZEBRAFISH EMBRYOS**

Dissertation

for the purpose of obtaining the degree of doctor

at Delft University of Technology

by the authority of the Rector Magnificus,

Prof.dr.ir. H. Bijl,

chair of the Board for Doctorates

to be defended publicly on

Thursday, 11 June 2026 at 10:00

by

Zhenzhen WU

This dissertation has been approved by the promotor.

Composition of the doctoral committee:

Rector Magnificus,
Prof. dr. ir. J.P. Hoogenboom,
Dr. ir. D. Brinks,

chairperson
Delft University of Technology, promotor
Delft University of Technology, promotor

Independent members:

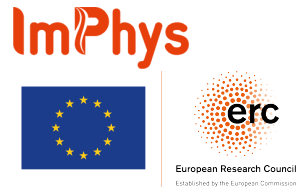
Prof. dr. S.M. Witte,
Prof. dr. M.L. Groot,
Dr. D.H.M. Meijer,
Dr. P. Boukany,
Prof. dr. B. Rieger,

Delft University of Technology
Vrije University Amsterdam
Delft University of Technology
Delft University of Technology
Delft University of Technology, reserve member

Other member:

Dr. L.E. Sanderson,

Erasmus University Medical Center



Key words: FLIM, developmental bioelectricity, membrane potential, eFRET-based GEVIs, absolute calibration, in vivo imaging

Printed by: Ridderprint, the Netherlands

Cover by: Zhenzhen Wu & ChatGPT

Copyright © 2026 by Z. Wu

ISBN: 978-94-6537-599-1

An electronic version of this dissertation is available at

<http://repository.tudelft.nl/>.

CONTENTS

Summary	xi
Samenvatting	xiii
1 Introduction	1
1.1 Developmental bioelectricity in embryogenesis, from fast electrical activity to resting membrane potential	2
1.1.1 Concepts and mechanisms of bioelectricity	2
1.1.2 Spatiotemporal organization and the roles of bioelectric signals in embryonic development.	3
1.1.3 The need to map developmental bioelectric patterns in vivo.	4
1.2 Measuring membrane potential in developing embryos: opportunities and constraints	5
1.2.1 Traditional electrophysiological approaches and their limitations	5
1.2.2 Genetically encoded voltage indicators for in vivo imaging	6
1.3 Fluorescence lifetime imaging and eFRET-based absolutely calibrated voltage sensing.	7
1.3.1 Principles of FLIM and lifetime-based readouts	7
1.3.2 eFRET-based GEVIs and lifetime-voltage transduction.	7
1.3.3 Technical challenges for in vivo FLIM in developing zebrafish	9
1.4 Motivation and outline of this thesis	10
1.4.1 Motivation	10
1.4.2 Outline of this thesis	11
2 A zebrafish Ace2N-mNeon expression library for in vivo voltage imaging of neuronal synchrony and cardiac maturation	21
2.1 Introduction	22

2.2	Results	23
2.2.1	Ace2N-mNeon predominantly localizes to the plasma membrane across diverse cell types during zebrafish (<i>Danio rerio</i>) development	23
2.2.2	Cell-specific promoters drive differential Ace2N-mNeon expression during zebrafish (<i>Danio rerio</i>) development	25
2.2.3	Ace2N-mNeon voltage imaging reveals neurogenesis-specific electrical activity	30
2.2.4	Detection of development-dependent voltage dynamics in the zebrafish heart	32
2.3	Discussion	34
2.4	Methods	36
2.4.1	Zebrafish husbandry	36
2.4.2	Plasmid construction	36
2.4.3	Tol2 transposon system	36
2.4.4	RNA synthesis	37
2.4.5	Microinjection	37
2.4.6	Confocal imaging sample preparation	37
2.4.7	Confocal imaging setup	37
2.4.8	Voltage imaging of neurons	38
2.4.9	Neuronal voltage imaging analysis	38
2.4.10	Voltage imaging of heart dynamics	38
2.4.11	Anesthesia and euthanasia compliance	39
2.5	Supplementary Materials	40
2.5.1	Supplementary tables	40
2.5.2	Supplementary figures	42
2.6	Author Contribution	47
3	Absolutely calibrated lifetime-imaging voltage sensing in developing zebrafish embryos	55
3.1	Introduction	56
3.2	Results	59
3.2.1	A calibrated FLIM framework and cell-based analysis pipeline for developmental voltage imaging	59

3.2.2	Voltage dependence of Ace2N-mNeon fluorescence lifetime in HEK293T cells	60
3.2.3	Quantitative fluorescence lifetime analysis reveals resting membrane potential differences across cell types in zebrafish embryos	62
3.2.4	Membrane potential dynamics in different cell types across zebrafish development	65
3.3	Discussion	69
3.3.1	Biological insights into developmental resting potentials	69
3.3.2	Methodological implications for calibrated in vivo voltage imaging	71
3.4	Methods	73
3.4.1	Zebrafish husbandry	73
3.4.2	Plasmid construction and RNA synthesis	73
3.4.3	Zebrafish sample preparation	73
3.4.4	HEK293T cell culture.	74
3.4.5	Whole-cell patch-clamp electrophysiology for lifetime calibration.	74
3.4.6	Fluorescence lifetime data acquisition	74
3.4.7	Principle of lifetime–voltage transduction	75
3.4.8	Cell-based FLIM data processing and quality control	76
3.4.9	Statistical analysis	76
3.4.10	Cell-based FLIM data visualization	78
3.5	Supplementary Materials	78
3.5.1	Supplementary figures and additional data	78
3.5.2	Supplementary methods: cell-based FLIM analysis and quality control pipeline	86
4	Engineering FRET-based GEVIs for quantitative absolute voltage imaging: constraints and design principles	109
4.1	Introduction	110
4.2	Results	111
4.2.1	Design of the eFRET-GEVI for FLIM	111
4.2.2	Characterization of mNeonGR in HEK293T Cells.	112
4.2.3	Control Experiments: instrument noise and optical bleed-through	114

4.2.4	Spectral perturbation analysis of GR-D115N-mediated donor polarity reversal	116
4.3	Discussion	119
4.3.1	Spectral perturbation model for donor polarity reversal	120
4.3.2	Design limitations and future directions	121
4.4	Methods	122
4.4.1	Plasmid construction and mNeonGR linker variants	122
4.4.2	HEK cell culture and transfection	123
4.4.3	Whole-cell voltage clamp and fluorescence imaging	123
4.4.4	Fluorescence intensity analysis	124
4.4.5	Spectral perturbation simulations	124
5	Conclusions, future outlook, and societal impact	135
5.1	Key scientific contributions	136
5.1.1	Genetic and experimental access for in vivo voltage imaging during embryogenesis (Chapter 2)	136
5.1.2	Cell-based FLIM framework for absolutely calibrated membrane potential mapping in developing zebrafish (Chapter 3)	137
5.1.3	Engineering constraints and design principles for next-generation lifetime-readable eFRET voltage indicators (Chapter 4)	137
5.2	Future outlook	138
5.2.1	Technical advances in absolute voltage imaging	138
5.2.2	Biological applications	139
5.2.3	Cross-species translation	140
5.2.4	Integration with other imaging techniques	140
5.3	Societal impact	140
5.3.1	Reduced animal experiments	140
5.3.2	Toward precision bioelectric phenotyping	140
5.3.3	Developmental disorders	141
5.3.4	Sample-to-sample comparison of noisy lifetime readouts in industry	141
5.4	Conclusion	141

A	Used theory and conventions	147
A.1	Bioelectric origin of resting membrane potential: Goldman-Hodgkin-Katz framework and assumptions	148
A.2	Fluorescence photophysics	148
A.3	Lifetime as a FRET readout in eFRET voltage indicators.	150
A.4	Practical lifetime acquisition: TCSPC, TTTR and IRF	151
A.5	Lifetime definition in this thesis.	153
	Acknowledgements	159
	Curriculum Vitae	163
	List of Publications	165

SUMMARY

The role of membrane potential signaling, which is fundamental to brain function, remains unclear in many other areas of biology, including embryonic development. Developmental bioelectricity spans fast transients in excitable tissues and slower changes in resting membrane potential that evolve alongside morphogenesis. Fast activity can be observed with established approaches, but calibrated comparisons of resting membrane potential across cell types and developmental stages *in vivo* remain difficult. Live embryos introduce photon-limited imaging, optical heterogeneity, motion, and heterogeneous indicator expression, making it hard to compare relative intensity readouts across samples. This dissertation establishes an integrated *in vivo* voltage imaging framework for developing zebrafish embryos. It combines genetic access with high-speed intensity imaging for fast activity and an absolutely calibrated, cell-resolved FLIM readout for comparable mapping of resting membrane potential across tissues and developmental time.

[Chapter 1](#) motivates the need for quantitative developmental voltage mapping and defines the conceptual distinctions that guide the thesis, including the separation between fast activity readouts and calibrated sensing of resting membrane potential. It also defines the scope of live embryos and explains why lifetime-based measurements are attractive when intensity is confounded by heterogeneous expression and optical conditions. Since lifetime readouts are not straightforward, [Appendix A](#) contains an introduction to lifetime measurements and the basic definitions we use in our measurements and analyses.

[Chapter 2](#) shows that early, cell-resolved voltage measurements in live embryos depend on reliable genetic access and robust membrane-localized indicator expression. This chapter establishes a zebrafish toolkit for the genetically encoded voltage indicator (GEVI) Ace2N-mNeon that supports both ubiquitous and promoter-driven targeting across multiple embryonic tissues, with membrane-localized fluorescence detectable from early developmental stages. Using neurons and cardiomyocytes as representative examples, I demonstrate *in vivo* voltage readouts in early embryos, including synchronous activity during primary neurogenesis and cardiac electrical activity before clear chamber morphology, with propagation features that mature from 1 to 4 days post-fertilization. These results provide practical guidance on where *in vivo* voltage imaging is feasible and what types of early electrical phenomena can be measured using existing tools.

[Chapter 3](#) presents the core methodological contribution of this thesis, aiming for absolutely calibrated lifetime imaging of voltage sensing in live zebrafish embryos. I

introduce a calibrated, cell-based FLIM workflow, based on fluorescence lifetime readout of the genetically encoded voltage indicator (GEVI) Ace2N-mNeon, designed to compare resting membrane potentials in living embryos under photon-limited and heterogeneous conditions. This chapter develops an analysis pipeline from TTR data handling through membrane-focused segmentation and photon summing, multi-component fitting with explicit quality control, and cell-based visualization that conveys tissue context in directly interpretable units, providing a clearer biological reading than pixel-level maps. By calibrating a cell-integrated lifetime–voltage relation using controlled electrophysiology and applying consistent acquisition and analysis, the framework enables calibrated comparisons of resting potential distributions across cell types and across developmental time. This chapter shows that, with state-of-the-art sensors and imaging technologies, systematic differences on the order of 10 mV can be resolvable *in vivo*. Together, this framework converts qualitative voltage patterns into quantitative measurements that can be compared across embryos and stages.

Given the limitations in the state of the art outlined in [Chapter 3](#), [Chapter 4](#) investigates the possibility of engineering an improved GEVI with higher sensitivity for encoding membrane voltage into fluorescence lifetime. Building on design principles exemplified by Ace2N-mNeon, this chapter designs and screens alternative eFRET constructs in HEK293T cells. I obtain surprisingly weak and inverted-polarity responses to voltage changes. To explain this, I provide a theoretical framework that shows how these responses can arise from likely coupling strengths and voltage-induced spectral changes. Together, these results define practical constraints and design principles that guide future GR-based eFRET indicators toward higher effective sensitivity in lifetime-based voltage readouts.

[Chapter 5](#) discusses how the combination of an expression library, calibrated cell-based FLIM, and indicator engineering contributes to quantifying the relationship between membrane voltage signaling and embryonic development. The future outlook focuses on necessary improvements to enable broad adoption of the developed technique and quantitative lifetime imaging in general, including increasing the sensitivity and dynamic range of lifetime-readable indicators, aligning analysis protocols, and improving hardware to increase photon efficiency and stability *in vivo*. It also outlines directions for biological applications, cross-species translation, and integration with complementary imaging modalities. The societal impact focuses on enabling reduced animal use through open, comparable workflows, establishing calibrated voltage changes as a functional biomarker for preclinical and precision-medicine studies, supporting quantitative voltage phenotyping and screening in developmental-disorder models, and extending lifetime-based standardization toward metrology applications in industry.

SAMENVATTING

De rol van signaaloverdracht via membraanpotentialen, die fundamenteel is voor de hersenfunctie, blijft in veel andere gebieden van de biologie, waaronder de embryonale ontwikkeling, onduidelijk. Electriciteit in de ontwikkelingsbiologie omvat kortdurende signalen in exciteerbare weefsels en langzamere veranderingen in het rustmembraan-potentiaal die zich parallel aan de morfogenese ontwikkelen. Snelle activiteit kan met bestaande technieken worden waargenomen, maar gekalibreerde vergelijkingen van het rustmembraanpotentiaal tussen celtypen en ontwikkelingsstadia in vivo blijven moeilijk. Levende embryo's brengen foton-beperkte beeldvorming, optische heterogeniteit, beweging en heterogene indicator-expressie met zich mee, waardoor het lastig is om relatieve op lichtintensiteit gebaseerde video-opnames tussen monsters te vergelijken. Dit proefschrift ontwikkelt een geïntegreerd in vivo optogeneticaraamwerk voor ontwikkelende zebraisembryo's. Het combineert genetische toegang met snelle video-opnames voor kortdurende signalen en een absoluut gekalibreerde FLIM-uitlezingsmethode met resolutie op celniveau voor vergelijkbare mapping van de rustmembraanpotentiaal in verschillende weefsels in verschillende ontwikkelingsstadia.

Hoofdstuk 1 onderbouwt de noodzaak van het kwantitatief in kaart brengen van voltage in de ontwikkeling en definieert de concepten die het proefschrift sturen, waaronder het onderscheid tussen uitlezingen van snelle activiteit en gekalibreerde meting van het rustmembraanpotentiaal. Het definieert ook de reikwijdte van metingen in levende embryo's en legt uit waarom op vervaltijd gebaseerde metingen aantrekkelijk zijn wanneer intensiteit wordt verstoord door heterogene expressie en wisselende optische omstandigheden. Omdat vervaltijdmetingen niet vanzelfsprekend zijn, bevat **Bijlage A** een inleiding tot vervaltijdmetingen en de basisdefinities die wij in onze metingen en analyses gebruiken.

Hoofdstuk 2 laat zien dat vroege spanningsmetingen op celniveau in levende embryo's afhangen van betrouwbare genetische toegang en robuuste, membraan-gelokaliseerde indicator-expressie. Dit hoofdstuk ontwikkelt een zebravistoolkit voor de genetisch geco-deerde spanningsindicator (GEVI) Ace2N-mNeon, die zowel universele als promotor-gestuurde expressie in meerdere embryonale weefsels ondersteunt, met membraan-gelokaliseerde fluorescentie die vanaf vroege ontwikkelingsstadia detecteerbaar is. Met neuronen en cardiomyocyten als representatieve voorbeelden demonstreer ik in vivo spanningsuitlezingen in vroege embryo's, waaronder synchrone activiteit tijdens primaire neurogenese en cardiale elektrische activiteit vóórdat duidelijke kamer-morfologie aanwezig is, met signaalkenmerken die ontwikkelen van 1 tot 4 dagen na bevruchting.

Deze resultaten bieden praktische richtlijnen voor waar in vivo spanningsmetingen haalbaar zijn en welke typen vroege elektrische fenomenen kunnen worden gemeten met bestaande hulpmiddelen.

Hoofdstuk 3 toont de belangrijkste methodologische bijdrage van dit proefschrift, gericht op absoluut gekalibreerde vervaltijdbeeldvorming van spanningsmeting in levende zebrafisembryo's. Ik introduceer een gekalibreerde, cel-gebaseerde FLIM-workflow, gebaseerd op fluorescentie-vervaltjduitreading van de genetisch gecodeerde spanningsindicator (GEVI) Ace2N-mNeon, ontworpen om rustmembraanpotentialen in levende embryo's te vergelijken onder foton-beperkte en heterogene omstandigheden. Dit hoofdstuk ontwikkelt een analysepipeline, van TTR-data-afhandeling via membraan-gerichte segmentatie en foton-somming, multicomponenten-fitting met expliciete kwaliteitscontrole, tot cel-gebaseerde visualisatie die weefselcontext weergeeft in direct interpreteerbare eenheden, en daarmee een duidelijker biologische interpretatie biedt dan kaarten op pixel-niveau. Door een cel-geïntegreerde vervaltijd-spanningsrelatie te kalibreren met gecontroleerde elektrofysiologie en consistente acquisitie en analyse toe te passen, maakt het raamwerk gekalibreerde vergelijkingen van rustpotentiaalverdelingen mogelijk tussen celtypen en over ontwikkelingsduur. Dit hoofdstuk laat zien dat, met state-of-the-art sensoren en beeldvormingstechnologieën, systematische verschillen in de orde van 10 mV in vivo te onderscheiden zijn. Samen zet dit raamwerk kwalitatieve spanningspatronen om in kwantitatieve metingen die tussen embryo's en stadia kunnen worden vergeleken.

Gegeven de beperkingen in de stand van de techniek zoals uiteengezet in **Hoofdstuk 3**, onderzoekt **Hoofdstuk 4** de mogelijkheid om een verbeterde GEVI te ontwerpen met hogere gevoeligheid voor het meetbaar maken van membraanpotentiaal in fluorescentie-vervaltijd. Voortbouwend op ontwerpprincipes die worden geïllustreerd door Ace2N-mNeon, wordt in dit hoofdstuk beschreven hoe alternatieve eFRET-constructen ontworpen en getest worden. Ik verkrijg verrassend zwakke en omgekeerde polariteitsreacties op spanningsveranderingen. Om dit te verklaren, presenteer ik een theoretisch raamwerk dat laat zien hoe deze reacties kunnen ontstaan uit waarschijnlijke koppelingssterktes en spanningsgeïnduceerde spectrale veranderingen. Samen definiëren deze resultaten praktische beperkingen en ontwerpprincipes die kunnen helpen om toekomstige GR-gebaseerde eFRET-indicatoren met een hogere effectieve gevoeligheid in vervaltijd-gebaseerde spanningsuitlezingen te ontwerpen.

Hoofdstuk 5 bespreekt hoe de combinatie van een expressiebibliotheek, gekalibreerde cel-gebaseerde FLIM en indicator-engineering bijdraagt aan het kwantificeren van de relatie tussen signaaloverdracht via membraanpotentialen en embryonale ontwikkeling. De toekomstvisie richt zich op noodzakelijke verbeteringen om brede adoptie van de ontwikkelde techniek en kwantitatieve vervaltijdbeeldvorming in het algemeen mogelijk te maken, waaronder het vergroten van de gevoeligheid en het dynamisch bereik van indicatoren waarmee vervaltijd kan worden gemeten, het afstemmen van analyseprotocollen en het verbeteren van hardware om de fotonefficiëntie en stabiliteit in vivo te

verhogen, en het uitbreiden van het raamwerk naar biologische toepassingen, translatie naar andere diersoorten en integratie met complementaire beeldvormingsmodaliteiten. De maatschappelijke impact richt zich op het verminderen van de behoefte aan proefdieren via open, vergelijkbare workflows, het vaststellen van gekalibreerde spanningsveranderingen als een functionele biomarker voor preklinische en precisiegeneeskunde-studies, het ondersteunen van kwantitatieve fenotypering via membraanpotentialen en screening in modellen van ontwikkelingsstoornissen, en het uitbreiden van robuuste, vervaltijd-gebaseerde standaardisatie niet alleen in de biologie maar ook voor metrologie-toepassingen in de industrie.

1

INTRODUCTION

1.1. DEVELOPMENTAL BIOELECTRICITY IN EMBRYOGENESIS, FROM FAST ELECTRICAL ACTIVITY TO RESTING MEMBRANE POTENTIAL

EMBRYOGENESIS depends on coordinated positional information that orchestrates proliferation, migration, and differentiation as tissues and organs emerge.¹ Most developmental frameworks emphasize biochemical morphogens and mechanical cues as the dominant coordinating signals; it remains unclear whether, and how, bioelectricity contributes through cell-level differences in membrane potential (V_m) that persist and evolve over developmental time.^{2,3} Although multiple studies have reported spatiotemporal voltage patterns in morphogenesis, regeneration, and disease, these observations often remain difficult to interpret mechanistically. A major reason is measurement: existing approaches cannot provide absolute, cell-resolved maps of V_m in developing organisms, with sufficient spatiotemporal resolution to relate specific bioelectrical events to defined developmental events.^{2,4,5} Patch-clamp electrophysiology provides quantitative membrane voltage but samples few cells at a time and is not suitable for resolving spatial patterns, whereas microelectrode array (MEA) recordings can capture population-level activity but are difficult to apply to three-dimensional, rapidly changing embryonic tissues.^{6,7} Optical voltage imaging can reveal spatial patterns without mechanical perturbation, yet commonly used intensity-based readouts only resolve transient changes in single cell voltage, so they do not support quantitative comparisons of V_m between cells.^{6,8} A central technical barrier is that we still lack an *in vivo* method to map absolute resting V_m at cellular resolution over extended developmental periods.^{2,9}

To address this gap, this thesis develops an *in vivo* imaging and analysis framework that converts optical measurements into absolutely calibrated estimates of membrane voltage at cellular resolution, enabling comparisons across cell types, tissues, and developmental stages.

1.1.1. CONCEPTS AND MECHANISMS OF BIOELECTRICITY

At the level of individual cells, bioelectricity is often summarized by the membrane potential (V_m), defined as the voltage difference between the cytoplasm and the extracellular space across the plasma membrane.¹⁰ V_m reflects ion concentration gradients and their effective membrane permeabilities, which are dynamically set by channels, pumps, transporters, and electrical coupling.^{10,11} Because these permeability weights are remodelled during development, perturbing individual components, such as specific ion channels, transporters, and pumps, does not uniquely affect the V_m achieved in each cell. This emphasizes the need for direct *in vivo* measurements that are cell-resolved and comparable across stages. For notation and the Goldman–Hodgkin–Katz convention used in this

thesis, see Appendix A.1.¹⁰

While V_m is a biophysical variable, it also interfaces with molecular and genetic control.^{12–14} Developmental programs tune the expression and localization of ion channels, and voltage-dependent signalling can in turn modulate cellular state, creating feedback that further reinforces the need for direct *in vivo* readout rather than inference from perturbation alone.^{15,16} Taken together, this suggests that bioelectric signals can participate in regulatory feedback with biochemical and mechanical cues, rather than being merely a passive byproduct of cellular physiology.¹⁷

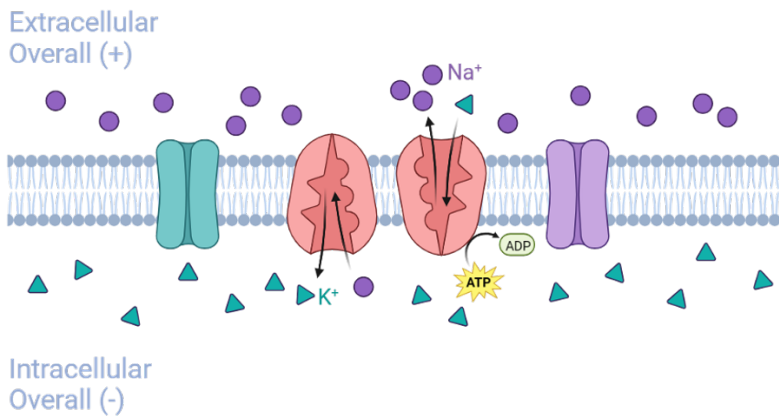


Figure 1.1: **Ion gradients and membrane potential across the plasma membrane.** The plasma membrane contains K^+ and Na^+ channels and the Na^+/K^+ ATPase, which exports Na^+ and imports K^+ to maintain high extracellular Na^+ , high intracellular K^+ , and a negative intracellular membrane potential. This schematic highlights representative contributors and is not exhaustive. Illustration made in BioRender.

1.1.2. SPATIOTEMPORAL ORGANIZATION AND THE ROLES OF BIOELECTRIC SIGNALS IN EMBRYONIC DEVELOPMENT

Developmental bioelectricity can be described on two practically relevant time scales.^{15,18} At fast time scales, excitable cells generate action potentials and other rapid voltage events, whereas at slower time scales, cells and tissues show gradual shifts in resting membrane potential during development, together with the emergence of tissue-level spatial patterns in V_m .^{15,19–21} Increasing evidence points to the role of resting V_m in regulating proliferation, migration, differentiation, and apoptosis.^{13,18,22,23} At larger scales, spatial

voltage patterns have been associated with coordinated morphogenetic outcomes, including axis specification, left-right patterning, and organogenesis.^{13,15,18,22,24,25} Sustained perturbations of these states have also been linked to disease-relevant phenotypes, from impaired regeneration to congenital structural defects.^{15,25–27}

In excitable tissues, fast electrical activity is overlaid on and can evolve with the slower resting membrane potential.^{11,28} The developing nervous system and heart are prominent examples, where spontaneous and evoked spikes occur alongside developmental shifts in resting V_m and excitability during organogenesis.^{28–30} For developmental interpretation, this means that fast events and slow resting membrane potentials may co-vary as tissues assemble and mature.^{2,4,31,32}

Bioelectric organization is also structured in space.¹⁵ At subcellular scales, membrane microdomains can host distinct complements of channels and receptors.³³ In this thesis, V_m is treated as a whole-cell variable, while noting that subcellular heterogeneity can exist and may matter in other contexts. Across cell types, resting membrane potentials differ substantially, with epithelia, neurons, skeletal muscle, and cardiomyocytes occupying characteristic V_m ranges.^{20,21,34} At multicellular scales, gap junction coupling and extracellular fields connect cells into bioelectric networks, enabling extended voltage domains and gradients across tissues and organs.^{15,34,35}

These observations raise the possibility that spatial patterns of V_m interact with, rather than merely accompany, chemical morphogen gradients and mechanical cues.^{14,15,18} To test this hypothesis *in vivo*, measurements must remain cell-resolved and comparable across cell types and developmental stages for resting V_m , while still being able to resolve fast electrical activity when it is biologically informative.^{6,36–38} This requirement motivates the dual emphasis of this thesis: high-speed optical readout of rapid voltage events and a workflow that supports millivolt-scale, cross-stage comparison of resting V_m across embryonic stages.

1.1.3. THE NEED TO MAP DEVELOPMENTAL BIOELECTRIC PATTERNS *IN VIVO*

The main challenge in interpreting developmental bioelectric perturbations is not simply detecting voltage changes, but assigning them to individual cells and defined cell types and relating them to a quantitatively comparable resting V_m within the same embryo across development.^{3,14,26} Interpreting these perturbation studies is especially challenging because many perturbations act broadly across tissues and time. Across pharmacological, genetic, and optogenetic approaches, researchers have changed bioelectric state by depolarizing or hyperpolarizing cells, modifying intercellular coupling through gap junctions, or introducing non-native voltage patterns.^{25,26,39,40} When bioelectric state is manipulated in these ways, reported outcomes include changes in patterning and body-plan features, as well as the rescue or redirection of developmental and regenerative programs, linking bioelectric state to developmental control *in vivo*.^{26,41} However,

the strength of this link often depends on how well the resulting electrical state can be measured and compared *in vivo*.

At the same time, these studies expose a practical limitation central to this thesis: without cell-resolved resting V_m readouts in live embryos, it often remains uncertain what voltage individual cells actually reach, how far voltage changes propagate through electrically coupled tissues, and how stable these changes are over developmental time.^{2,6,9} As a result, a reported “depolarization” or “hyperpolarization” can remain a relative contrast rather than an absolute value in millivolts, making it difficult to compare across embryos, tissues, or stages. This ambiguity limits the ability to distinguish genuine voltage remodeling from changes in indicator expression, optical background, or other readout artifacts.⁴² In addition, bioelectric networks can exhibit compensatory regulation, so perturbing one component may be buffered or redistributed, further complicating inference from perturbation alone.^{26,43}

Early vertebrate embryos such as zebrafish are well-suited to address this measurement gap.^{44–46} They develop externally and remain optically accessible at early stages, enabling longitudinal imaging in intact animals, and they exhibit functional neural and cardiac activity within a few days while remaining well-suited to genetic manipulation.^{45,47}

These observations raise a practical question: how can we quantify membrane voltage in intact embryos? The measurement must resolve voltage patterns at cellular resolution and support quantitative comparisons across cell types and developmental time. The next sections summarize the key readout constraints and motivate the approach used here: high-speed imaging for rapid electrical events, and absolutely calibrated, lifetime-based measurements for cross-stage comparison of resting V_m .

1.2. MEASURING MEMBRANE POTENTIAL IN DEVELOPING EMBRYOS: OPPORTUNITIES AND CONSTRAINTS

1.2.1. TRADITIONAL ELECTROPHYSIOLOGICAL APPROACHES AND THEIR LIMITATIONS

Electrophysiological recordings have long provided the most direct measurements of V_m , reporting absolute values with millisecond temporal resolution.^{6,7} Approaches such as intracellular microelectrodes and whole-cell patch clamp have yielded foundational insights into electrical signaling in cultured systems, acute slices, and mature preparations.^{7,48,49} However, using these methods to map V_m in early vertebrate embryos at single-cell resolution remains difficult. The mechanical strain of electrode penetration can perturb or damage delicate tissues, while ongoing cell rearrangements during morphogenesis undermine the stability of long-term recordings. Moreover, these single-recording cons-

traits are compounded by limited throughput: such workflows cannot provide the broad spatial and temporal coverage needed to characterize diverse cell populations across the entire embryo.^{7,30,49,50}

These limitations motivate minimally invasive optical approaches that can monitor V_m in parallel across many cells in live animals, while preserving spatial coverage and supporting longitudinal comparisons.^{6,36}

1.2.2. GENETICALLY ENCODED VOLTAGE INDICATORS FOR IN VIVO IMAGING

Voltage imaging reduces several practical limitations of electrode recordings by converting voltage changes into fluorescence.^{51,52} Genetically encoded voltage indicators (GEVIs) are protein-based sensors that can be targeted to the plasma membrane and expressed in defined cell populations.^{36,37,52} Because they are DNA-encoded, GEVIs can be introduced through transgenesis or transient expression, enabling cell-type-specific labeling and repeated in vivo measurements over time. In practice, GEVIs have enabled monitoring of fast electrical activity, particularly action potentials and other rapid transients, in parallel across many cells in intact tissues.⁵² However, most GEVI measurements rely on fluorescence intensity contrast, which provides a relative fractional change in fluorescence intensity ($\Delta F/F$) readout that is effective for detecting fast transients, but does not by itself yield an absolute V_m value that is comparable across embryos, cell types, or developmental stages.^{6,9,53}

This limitation arises because baseline fluorescence intensity is shaped by several sources of variation that are not directly related to membrane voltage.^{6,53} Biologically, expression heterogeneity and subcellular distribution set a cell-specific baseline that can vary across cells and over time.^{36,37} Instrumentally, fluctuations in excitation power and detection efficiency, together with photobleaching, can distort intensity measurements even when V_m is stable.^{54,55} Over development, growth and morphogenetic remodeling alter tissue geometry and the optical path, changing how much membrane contributes signal within the detection volume.⁵⁴ Consequently, baseline intensity fluctuations cannot be interpreted as differences in resting membrane potential, and comparisons across embryos, developmental stages, or imaging sessions remain difficult using fluorescence intensity alone.^{6,9} Bridging this gap requires readouts that are robust to intensity inhomogeneity and can report membrane voltage on an absolute scale.^{6,53}

1.3. FLUORESCENCE LIFETIME IMAGING AND eFRET-BASED ABSOLUTELY CALIBRATED VOLTAGE SENSING

1.3.1. PRINCIPLES OF FLIM AND LIFETIME-BASED READOUTS

Fluorescence lifetime imaging microscopy (FLIM) reduces the dependence of voltage readout on intensity inhomogeneity by using fluorescence lifetime (τ_{fl}) as the primary contrast.^{56–59} τ_{fl} is the average time a fluorophore remains in its excited state before returning to the ground state. It is set by the balance between radiative emission and non-radiative relaxation pathways.^{60,61} Unlike intensity, τ_{fl} is largely set by the fluorophore's photophysics and its local microenvironment,^{56,60,61} and is therefore often less sensitive to factors that mainly influence intensity, such as fluorophore concentration, excitation power, optical path, scattering, and moderate photobleaching, given that acquisition settings and analysis conventions are consistent.^{56–58,62} Nonetheless, lifetime estimates can be shifted by background and analysis choices, so consistency of acquisition and processing remains essential.^{58,62} This relative decoupling is particularly valuable in embryos, where expression heterogeneity, optical inhomogeneity, and developmental remodeling make it difficult to compare baseline intensities across cells and stages.

Prior work has shown that two-photon lifetime imaging can report membrane voltage in cultured cells under voltage-clamp conditions, enabling absolutely calibrated measurements with millivolt sensitivity.⁸ These results establish a quantitative basis for using fluorescence lifetime as a calibrated voltage readout. Importantly, lifetime is also directly sensitive to Förster resonance energy transfer (FRET); because of this, voltage-dependent FRET-based quenching can be expressed as lifetime contrast and then linked to voltage through calibration.^{60,61,63} Decay models and definitions for computing lifetime for this thesis are summarized in Appendix A.2.

1.3.2. eFRET-BASED GEVIS AND LIFETIME-VOLTAGE TRANSDUCTION

FRET is a non-radiative energy transfer process between a fluorescent donor and an acceptor.^{60,63,64} Following donor excitation, energy can be dissipated by photon emission or transferred to the acceptor through dipole-dipole coupling.^{65,66} FRET becomes efficient when the donor and acceptor are brought within a few nanometers and when donor emission overlaps with acceptor absorption, with additional dependence on dipole orientation.^{61,63,65} Because FRET introduces an additional non-radiative relaxation pathway for the donor, it shortens the donor fluorescence lifetime.^{63,67} Accordingly, in FLIM-FRET, the donor lifetime provides a single-valued readout of donor quenching, supporting quantitative comparison without relying on intensity normalization.^{56,61,65} The lifetime-FRET relations and notation are summarized in Appendix A.3.

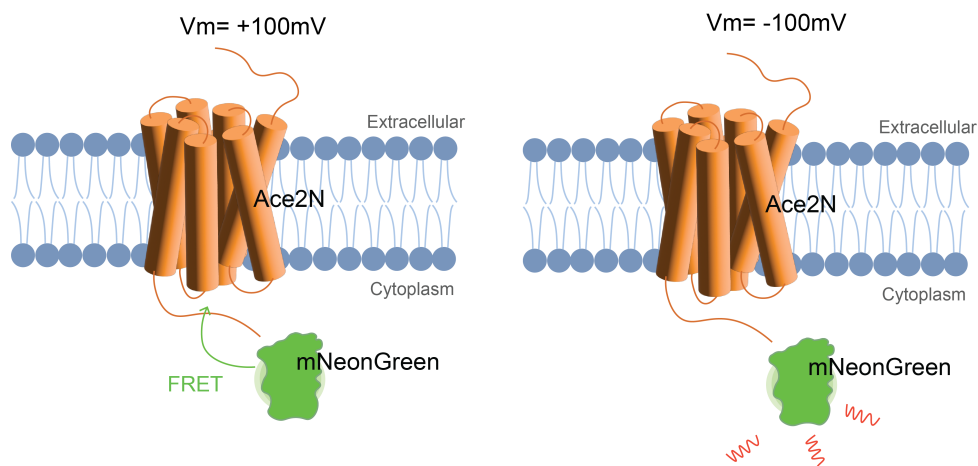


Figure 1.2: **Schematic illustration of the eFRET voltage-sensing mechanism in Ace2N-mNeon.** The seven-transmembrane Ace rhodopsin is embedded in the plasma membrane and functions as the voltage-sensitive acceptor, while mNeonGreen (mNeon) acts as the fluorescent donor. Changes in membrane potential reshape the absorption spectrum of Ace within the mNeonGreen emission band. Under depolarizing conditions (schematic example, $V_m = +100$ mV), increased Ace absorption enhances donor quenching via eFRET, leading to reduced donor fluorescence and a shortened donor τ_{fl} . Under hyperpolarizing conditions (schematic example, $V_m = -100$ mV), reduced Ace absorption weakens quenching, resulting in increased donor emission and a longer τ_{fl} .

Among commonly used GEVI architectures, voltage can be coupled to fluorescence either through sensors that change conformation (voltage-sensing-domain, VSD-based) or through *microbial rhodopsins* with strongly voltage-dependent optical properties.^{68–70} This thesis focuses on an electrochromic FRET (eFRET)-based GEVI, as voltage-dependent rhodopsin absorption modulates donor quenching, allowing direct readout as a lifetime change.^{71,72}

eFRET-based GEVIs adapt this principle to voltage sensing by pairing a bright fluorescent protein donor with a voltage-sensitive *microbial rhodopsin* acceptor.^{69,72,73} Membrane voltage shifts the rhodopsin absorption spectrum, thereby changing the spectral overlap with donor emission and modulating donor quenching, producing corresponding changes in donor intensity and donor lifetime.^{68,71,72} For in vivo embryonic imaging, a key practical benefit is that voltage can be read out from the donor lifetime alone, while the rhodopsin acceptor remains optically dim.^{36,51} This keeps the detected signal in a bright donor channel while retaining voltage sensitivity through the rhodopsin, which is advantageous under scattering and photon-limited conditions.^{62,64}

In this thesis, the eFRET indicator Ace2N-mNeon serves as a practical platform for probing developmental bioelectric dynamics in zebrafish embryos, supported by robust membrane targeting, millisecond kinetics, and sufficient donor brightness in vivo.⁷² Keeping the indicator constant across chapters shifts comparisons toward biological and

developmental differences rather than sensor-behavior variability, such as expression, localization, and photophysics, and clarifies the interpretation of voltage dynamics across tissues and developmental time. In Ace2N-mNeon, the seven-transmembrane *Ace rhodopsin* provides the voltage-sensitive acceptor, paired with mNeonGreen as the fluorescent donor (Fig. 1.2).⁷² Consistent with electrochromic quenching, depolarization shortens the donor τ_{fl} , whereas hyperpolarization prolongs it.^{8,64,72,74} This donor lifetime-voltage relation can be established under controlled electrophysiological conditions and then used as a calibration basis for quantitative interpretation of in vivo measurements.^{8,72}

1.3.3. TECHNICAL CHALLENGES FOR IN VIVO FLIM IN DEVELOPING ZEBRAFISH

Prior work has established calibrated lifetime-voltage relationships in cultured cells.^{6,8} In live embryos, lifetime-based voltage imaging can in principle support cell-resolved, millivolt-resolution mapping of resting membrane potential as tissues remodel during embryogenesis.^{15,75} In practice, implementing this approach in vivo remains challenging because embryos limit photon collection, introduce strong optical heterogeneity, and make cell-level attribution difficult.^{6,8,53,56,58}

In live embryos, in vivo FLIM is constrained by photon statistics, depth-dependent attenuation, and motion.⁷⁶ Reliable lifetime estimation requires sufficient photon counts, yet developing zebrafish embryos are three-dimensional, scattering, and partially absorbing, so the signal decreases with imaging depth. Excitation power cannot be increased arbitrarily because phototoxicity must be minimized to preserve normal development during extended recordings.^{77–80} Moreover, morphogenetic movements and cardiac contractions can overlap with FLIM acquisition windows, mixing signals within the integration period and biasing decay estimates unless motion is explicitly addressed.^{58,62}

A second challenge is cell attribution, which is substantially harder in vivo than in cultured cells.^{37,81} Indicators such as Ace2N-mNeon can contribute intracellular fluorescence in addition to membrane-associated signal, and expression varies across cells, tissues, and developmental stages.^{32,72} Consequently, pixel-based lifetime maps can blend membrane-enriched and non-membrane contributions, and cell boundaries are often difficult to resolve in densely packed tissues.⁸² Without cell-level segmentation of membrane-enriched regions of interest (ROI), apparent lifetime differences remain ambiguous because they may reflect background fluorescence, intracellular signal mixing, or geometry and scattering effects rather than membrane voltage.^{81,82}

Quantitative interpretation also depends on matched calibration transfer from controlled electrophysiology in cells to in vivo acquisition and analysis.^{6,8,53} In live embryos, the measured lifetime is sensitive to both acquisition choices and analysis conventions, for example background subtraction, instrument response correction, the decay fitting model and fitting window, photon-limited estimation, and the specific lifetime metric

reported.^{6,58,76} For indicators with time-dependent responses or hysteresis, mismatches in timing or sampling windows between calibration and in vivo recordings can introduce additional bias in the lifetime assigned to a given voltage.^{32,74} In principle the calibration remains valid, but in vivo values are only interpretable when procedures are matched and key parameters are documented.

Together, these constraints motivate the need for a standardized framework that aligns acquisition, calibration, and analysis conventions for cell-resolved voltage readout to remain comparable across embryos, tissues, and stages.

1.4. MOTIVATION AND OUTLINE OF THIS THESIS

1.4.1. MOTIVATION

Understanding embryogenesis depends on our ability to visualize pattern formation in intact embryos and to identify the signals that drive it.^{2,4} Bioelectricity, reflected in membrane potential, has been implicated in developmental patterning, yet linking these observations to mechanism requires measurements that are both temporally and spatially precise, so that rapid electrical events and slower shifts in resting V_m can be interpreted within the same developmental context.^{2,4,15} Existing voltage imaging approaches can capture fast transients in excitable tissues; however, their commonly used intensity readouts do not readily support absolute calibration to membrane voltage, and are not well suited to reliably quantify long-term, gradual changes in membrane potential across embryonic development.^{6,8,9} As a result, this leaves two practical gaps. First, in early embryos, cross-stage datasets that track fast dynamics with defined cell-type attribution remain relatively limited.^{83–85} Most importantly, for the slow regime, we still lack an in vivo method that can map resting V_m on an absolute scale at cellular resolution over extended developmental times.^{6,9}

Therefore, this thesis develops a 3D, cellular-resolution FLIM imaging and analysis framework for absolutely calibrated measurements of resting V_m that remain interpretable under photon-limited and optically heterogeneous conditions, enabling comparisons across cell types, tissues, developmental stages, and individuals. To place these absolutely calibrated resting V_m measurements in the broader bioelectric landscape of the embryo, high-speed intensity imaging is used in parallel to record rapid activity in early embryos, so fast electrical events can be examined alongside slower changes in resting V_m .

1.4.2. OUTLINE OF THIS THESIS

The research is organized into four major chapters to address the genetic, analytical, and biophysical challenges of *in vivo* voltage imaging.

Chapter 2 develops and validates a zebrafish Ace2N-mNeon genetic toolkit for cell-type-specific voltage imaging in early embryos.³² Across 4 hpf to 5 dpf, it maps membrane-targeted expression and establishes practical signal quality benchmarks across multiple tissues. Using this platform, the chapter reports *in vivo* recordings of rapid voltage activity in forming neurons and cardiomyocytes, including patterns indicative of coordinated neuronal activity and developmental changes associated with cardiac conduction maturation.³²

Chapter 3 builds on this toolkit to introduce a calibrated, cell-based FLIM framework.^{6,53} It develops an analysis and visualization workflow for photon-limited, optically inhomogeneous embryo data, allowing reproducible longitudinal comparisons of resting membrane potential across tissues. This framework is evaluated by testing whether it recovers expected bioelectric hierarchies across cell types and by tracking developmental trends from 1 to 4 dpf, demonstrating that it supports consistent, interpretable *in vivo* voltage measurements.

Chapter 4 focuses on improving quantitative accuracy and practical sensitivity for absolutely calibrated, *in vivo* voltage sensing using FLIM by examining eFRET indicator engineering in this context.^{8,72,86} Using systematic electrophysiology recordings under voltage clamp together with a simple spectral-perturbation model, it dissects the factors that set the lifetime–voltage coupling, and maps key design constraints related to sensor geometry and donor selection. Together, these results provide design principles for next-generation, lifetime-readable voltage indicators with improved sensitivity.

Chapter 5 integrates the methodological and biological outcomes of the thesis and looks ahead to future work, including broader cell-type coverage, improved robustness *in vivo*, and experiments that combine voltage readouts with targeted perturbations to test causal links.

For reference, Appendix A summarizes the core definitions, symbols, and minimal equations used throughout this thesis. It also describes the TCSPC-TTTR timing conventions used in this thesis, the FRET-lifetime relations, and the definition of the computed fluorescence lifetime.

BIBLIOGRAFIE

- [1] Jeremy B. A. Green en James Sharpe. “Positional information and reaction-diffusion: two big ideas in developmental biology combine”. In: *Development* 142 (7 apr 2015), p. 1203–1211. ISSN: 1477-9129. DOI: [10.1242/dev.114991](https://doi.org/10.1242/dev.114991).
- [2] Michael Levin. “Molecular bioelectricity in developmental biology: New tools and recent discoveries”. In: *BioEssays* 34 (3 mrt 2012), p. 205–217. ISSN: 02659247. DOI: [10.1002/bies.201100136](https://doi.org/10.1002/bies.201100136). PMID: 22237730.
- [3] Juanita Mathews en Michael Levin. “The body electric 2.0: recent advances in developmental bioelectricity for regenerative and synthetic bioengineering”. In: *Current Opinion in Biotechnology* 52 (aug 2018), p. 134–144. ISSN: 09581669. DOI: [10.1016/j.copbio.2018.03.008](https://doi.org/10.1016/j.copbio.2018.03.008).
- [4] Laura Faith George en Emily Anne Bates. “Mechanisms Underlying Influence of Bioelectricity in Development”. In: *Frontiers in Cell and Developmental Biology* 10 (feb 2022). ISSN: 2296-634X. DOI: [10.3389/fcell.2022.772230](https://doi.org/10.3389/fcell.2022.772230).
- [5] D. Delisi, N. Eskandari en S. Gentile. “Membrane potential: A new hallmark of cancer”. In: deel 164. Epub 2024-05-15. 2024, p. 93–110. DOI: [10.1016/bs.acr.2024.04.010](https://doi.org/10.1016/bs.acr.2024.04.010).
- [6] Julia R. Lazzari-Dean, Anneliese M.M. Gest en Evan W. Miller. “Measuring Absolute Membrane Potential Across Space and Time”. In: *Annual Review of Biophysics* 50 (1 mei 2021), p. 447–468. ISSN: 1936-122X. DOI: [10.1146/annurev-biophys-062920-063555](https://doi.org/10.1146/annurev-biophys-062920-063555).
- [7] Alan D. Wickenden. “Overview of Electrophysiological Techniques”. In: *Current Protocols in Pharmacology* 11 (1 dec 2000). ISSN: 1934-8282. DOI: [10.1002/0471141755.ph1101s64](https://doi.org/10.1002/0471141755.ph1101s64).
- [8] Daan Brinks, Aaron J. Klein en Adam E. Cohen. “Two-Photon Lifetime Imaging of Voltage Indicating Proteins as a Probe of Absolute Membrane Voltage”. In: *Biophysical Journal* 109 (5 sep 2015), p. 914–921. ISSN: 15420086. DOI: [10.1016/j.bpj.2015.07.038](https://doi.org/10.1016/j.bpj.2015.07.038). PMID: 26331249.
- [9] Dmitrii M. Nikolaev e.a. “Fluorescence Imaging of Cell Membrane Potential: From Relative Changes to Absolute Values”. In: *International Journal of Molecular Sciences* 24 (3 jan 2023), p. 2435. ISSN: 1422-0067. DOI: [10.3390/ijms24032435](https://doi.org/10.3390/ijms24032435).

- [10] David E. Goldman. "POTENTIAL, IMPEDANCE, AND RECTIFICATION IN MEMBRANES". In: *Journal of General Physiology* 27 (1 sep 1943), p. 37–60. ISSN: 1540-7748. DOI: [10.1085/jgp.27.1.37](https://doi.org/10.1085/jgp.27.1.37).
- [11] Bertil Hille. *Ion channels of excitable membranes*. 3rd ed. Sunderland, Mass: Sinauer, 2001, p. 814.
- [12] Michael Levin. "Bioelectric signaling: Reprogrammable circuits underlying embryogenesis, regeneration, and cancer". In: *Cell* 184 (8 2021), p. 1971–1989.
- [13] Wendy Scott Beane et al. "Bioelectric signaling regulates head and organ size during planarian regeneration". In: *Development (Cambridge)* 140 (2 2013), p. 313–322. ISSN: 09501991. DOI: [10.1242/dev.086900](https://doi.org/10.1242/dev.086900). PMID: [23250205](https://pubmed.ncbi.nlm.nih.gov/23250205/).
- [14] Michael Levin. "Bioelectrical approaches to cancer as a problem of the scaling of the cellular self". In: *Progress in Biophysics and Molecular Biology* 165 (okt 2021), p. 102–113. ISSN: 00796107. DOI: [10.1016/j.pbiomolbio.2021.04.007](https://doi.org/10.1016/j.pbiomolbio.2021.04.007).
- [15] Michael Levin. "Molecular bioelectricity: How endogenous voltage potentials control cell behavior and instruct pattern regulation in vivo". In: *Molecular Biology of the Cell* 25 (24 dec 2014), p. 3835–3850. ISSN: 19394586. DOI: [10.1091/mbc.E13-12-0708](https://doi.org/10.1091/mbc.E13-12-0708). PMID: [25425556](https://pubmed.ncbi.nlm.nih.gov/25425556/).
- [16] Barbara Rosati en David McKinnon. "Regulation of Ion Channel Expression". In: *Circulation Research* 94 (7 apr 2004), p. 874–883. ISSN: 0009-7330. DOI: [10.1161/01.RES.0000124921.81025.1F](https://doi.org/10.1161/01.RES.0000124921.81025.1F).
- [17] Matthew P. Harris. "Bioelectric signaling as a unique regulator of development and regeneration". In: *Development* 148 (10 mei 2021). ISSN: 0950-1991. DOI: [10.1242/dev.180794](https://doi.org/10.1242/dev.180794).
- [18] James M. Harris, Andy Yu-Der Wang en Paola Arlotta. "Optogenetic axon guidance in embryonic zebrafish". In: *STAR Protocols* 2 (4 dec 2021). ISSN: 26661667. DOI: [10.1016/j.xpro.2021.100947](https://doi.org/10.1016/j.xpro.2021.100947). PMID: [34841275](https://pubmed.ncbi.nlm.nih.gov/34841275/).
- [19] Michael H Grider, Rishita Jessu en Rian Kabir. "Physiology, Action Potential." In: Treasure Island (FL): StatPearls Publishing, 2023.
- [20] Steven M. Chrysafides, Stephen J. Bordes en Sandeep Sharma. "Physiology, Resting Potential". In: Treasure Island (FL): StatPearls Publishing, 2023.
- [21] Lina Abdul Kadir, Michael Stacey en Richard Barrett-Jolley. "Emerging Roles of the Membrane Potential: Action Beyond the Action Potential". In: *Frontiers in Physiology* 9 (nov 2018). ISSN: 1664-042X. DOI: [10.3389/fphys.2018.01661](https://doi.org/10.3389/fphys.2018.01661).

- [22] Min Zhao. “Electrical fields in wound healing—An overriding signal that directs cell migration”. In: *Seminars in Cell and Developmental Biology* 20 (6 2009). Regenerative Biology and Medicine: II and Patterning and Evolving the Vertebrate Forebrain, p. 674–682. ISSN: 1084-9521. DOI: <https://doi.org/10.1016/j.semcdb.2008.12.009>. URL: <https://www.sciencedirect.com/science/article/pii/S1084952108001535>.
- [23] Sarah Sundelacruz, Michael Levin en David L. Kaplan. “Role of Membrane Potential in the Regulation of Cell Proliferation and Differentiation”. In: *Stem Cell Reviews and Reports* 5 (3 sep 2009), p. 231–246. ISSN: 1550-8943. DOI: [10.1007/s12015-009-9080-2](https://doi.org/10.1007/s12015-009-9080-2).
- [24] Michael Levin e.a. *Asymmetries in H⁺/K⁺-ATPase and cell membrane potentials comprise a very early step in left-right patterning*. 4 okt 2002. DOI: [10.1016/S0092-8674\(02\)00939-X](https://doi.org/10.1016/S0092-8674(02)00939-X).
- [25] Dany S. Adams, Alessio Masi en Michael Levin. “H⁺ pump-dependent changes in membrane voltage are an early mechanism necessary and sufficient to induce *Xenopus* tail regeneration”. In: *Development* 134 (7 apr 2007), p. 1323–1335. ISSN: 1477-9129. DOI: [10.1242/dev.02812](https://doi.org/10.1242/dev.02812).
- [26] Vaibhav P. et al. “Transmembrane voltage potential controls embryonic eye patterning in *Xenopus laevis*”. In: *Development* 139 (2 jan 2012), p. 313–323. ISSN: 1477-9129. DOI: [10.1242/dev.073759](https://doi.org/10.1242/dev.073759).
- [27] Ming Yang en William J. Brackenbury. “Membrane potential and cancer progression”. In: *Frontiers in Physiology* 4 (2013). ISSN: 1664-042X. DOI: [10.3389/fphys.2013.00185](https://doi.org/10.3389/fphys.2013.00185).
- [28] Nicholas C. Spitzer. “Electrical activity in early neuronal development”. In: *Nature* 444 (7120 dec 2006), p. 707–712. ISSN: 0028-0836. DOI: [10.1038/nature05300](https://doi.org/10.1038/nature05300).
- [29] Hidekazu et al. “Visualizing voltage dynamics in zebrafish heart”. In: *Journal of Physiology* 588 (12 jun 2010), p. 2017–2021. ISSN: 00223751. DOI: [10.1113/jphysiol.2010.189126](https://doi.org/10.1113/jphysiol.2010.189126). PMID: [20421282](https://pubmed.ncbi.nlm.nih.gov/20421282/).
- [30] Michiko Watanabe e.a. “Probing the Electrophysiology of the Developing Heart”. In: *Journal of Cardiovascular Development and Disease* 3 (1 mrt 2016), p. 10. ISSN: 2308-3425. DOI: [10.3390/jcdd3010010](https://doi.org/10.3390/jcdd3010010).
- [31] Peter Kirwan e.a. “Development and function of human cerebral cortex neural networks from pluripotent stem cells in vitro”. In: *Development* 142 (18 sep 2015), p. 3178–3187. ISSN: 1477-9129. DOI: [10.1242/dev.123851](https://doi.org/10.1242/dev.123851).
- [32] ZhenZhen Wu e.a. *Exploring Bioelectricity with Ace2N-mNeon during Zebrafish Embryogenesis*. Dec 2024. DOI: [10.1101/2024.12.12.628143](https://doi.org/10.1101/2024.12.12.628143).
- [33] Steven L. Jones en Tatyana M. Svitkina. “Axon Initial Segment Cytoskeleton: Architecture, Development, and Role in Neuron Polarity”. In: *Neural Plasticity* 2016 (2016), p. 1–19. ISSN: 2090-5904. DOI: [10.1155/2016/6808293](https://doi.org/10.1155/2016/6808293).

- [34] Costas A. Anastassiou e.a. “The Effect of Spatially Inhomogeneous Extracellular Electric Fields on Neurons”. In: *The Journal of Neuroscience* 30 (5 feb 2010), p. 1925–1936. ISSN: 0270-6474. DOI: [10.1523/JNEUROSCI.3635-09.2010](https://doi.org/10.1523/JNEUROSCI.3635-09.2010).
- [35] Javier Cervera e.a. “Bioelectrical coupling in multicellular domains regulated by gap junctions: A conceptual approach”. In: *Bioelectrochemistry* 123 (okt 2018), p. 45–61. ISSN: 15675394. DOI: [10.1016/j.bioelechem.2018.04.013](https://doi.org/10.1016/j.bioelechem.2018.04.013).
- [36] Helen H. Yang en François St-Pierre. “Genetically encoded voltage indicators: Opportunities and challenges”. In: *Journal of Neuroscience* 36 (39 sep 2016), p. 9977–9989. ISSN: 15292401. DOI: [10.1523/JNEUROSCI.1095-16.2016](https://doi.org/10.1523/JNEUROSCI.1095-16.2016). PMID: [27683896](https://pubmed.ncbi.nlm.nih.gov/27683896/).
- [37] Yuki et al. “Comparative Evaluation of Genetically Encoded Voltage Indicators”. In: *Cell Reports* 26 (3 jan 2019), 802–813.e4. ISSN: 22111247. DOI: [10.1016/j.celrep.2018.12.088](https://doi.org/10.1016/j.celrep.2018.12.088). PMID: [30650368](https://pubmed.ncbi.nlm.nih.gov/30650368/).
- [38] Reyhaneh Shakibi e.a. “From resting potential to dynamics: advances in membrane voltage indicators and imaging techniques”. In: *Quarterly Reviews of Biophysics* 58 (jan 2025), e7. ISSN: 0033-5835. DOI: [10.1017/S0033583524000210](https://doi.org/10.1017/S0033583524000210).
- [39] Michael Levin en Mark Mercola. “Gap junction-mediated transfer of left-right patterning signals in the early chick blastoderm is upstream of Shh asymmetry in the node”. In: *Development* 126 (21 nov 1999), p. 4703–4714. ISSN: 0950-1991. DOI: [10.1242/dev.126.21.4703](https://doi.org/10.1242/dev.126.21.4703).
- [40] Maya Emmons-Bell en Iswar K Hariharan. “Membrane potential regulates Hedgehog signalling in the Drosophila wing imaginal disc”. In: *EMBO reports* 22 (4 apr 2021). ISSN: 1469-221X. DOI: [10.15252/embr.202051861](https://doi.org/10.15252/embr.202051861).
- [41] Néstor J. Oviedo e.a. “Long-range neural and gap junction protein-mediated cues control polarity during planarian regeneration”. In: *Developmental Biology* 339 (1 mrt 2010), p. 188–199. ISSN: 00121606. DOI: [10.1016/j.ydbio.2009.12.012](https://doi.org/10.1016/j.ydbio.2009.12.012).
- [42] Thomas Knöpfel en Chenchen Song. “Optical voltage imaging in neurons: moving from technology development to practical tool”. In: *Nature Reviews Neuroscience* 20 (12 dec 2019), p. 719–727. ISSN: 1471-003X. DOI: [10.1038/s41583-019-0231-4](https://doi.org/10.1038/s41583-019-0231-4).
- [43] Javier Cervera, Michael Levin en Salvador Mafe. “Multicellular adaptation to electrophysiological perturbations analyzed by deterministic and stochastic bioelectrical models”. In: *Scientific Reports* 14 (1 nov 2024), p. 27608. ISSN: 2045-2322. DOI: [10.1038/s41598-024-79087-7](https://doi.org/10.1038/s41598-024-79087-7).
- [44] Jordan T. Shin en Mark C. Fishman. “From Zebrafish to human: modular medical models”. In: *Annual Review of Genomics and Human Genetics* 3 (1 sep 2002), p. 311–340. ISSN: 1527-8204. DOI: [10.1146/annurev.genom.3.031402.131506](https://doi.org/10.1146/annurev.genom.3.031402.131506).
- [45] Tae-Young Choi et al. “Zebrafish as an animal model for biomedical research”. In: *Experimental and Molecular Medicine* 53 (3 mrt 2021), p. 310–317. ISSN: 1226-3613. DOI: [10.1038/s12276-021-00571-5](https://doi.org/10.1038/s12276-021-00571-5).

- [46] Sebastiaan A. Brittiijn e.a. “Zebrafish development and regeneration: new tools for biomedical research”. In: *The International Journal of Developmental Biology* 53 (5-6 2009), p. 835–850. ISSN: 0214-6282. DOI: [10.1387/ijdb.082615sb](https://doi.org/10.1387/ijdb.082615sb).
- [47] Catherine T. Nguyen e.a. “Zebrafish as a model for cardiovascular development and disease”. In: *Drug Discovery Today: Disease Models* 5 (3 sep 2008), p. 135–140. ISSN: 17406757. DOI: [10.1016/j.ddmod.2009.02.003](https://doi.org/10.1016/j.ddmod.2009.02.003).
- [48] Sodikdjon A. Kodirov. “Whole-cell patch-clamp recording and parameters”. In: *Biophysical Reviews* 15 (2 apr 2023), p. 257–288. ISSN: 1867-2450. DOI: [10.1007/s12551-023-01055-8](https://doi.org/10.1007/s12551-023-01055-8).
- [49] Mladen Barbic e.a. “Detachable glass microelectrodes for recording action potentials in active moving organs”. In: *American Journal of Physiology-Heart and Circulatory Physiology* 312 (6 jun 2017), H1248–H1259. ISSN: 0363-6135. DOI: [10.1152/ajpheart.00741.2016](https://doi.org/10.1152/ajpheart.00741.2016).
- [50] Rong-wei Zhang en Jiu-lin Du. “In Vivo Whole-Cell Patch-Clamp Recording in the Zebrafish Brain”. In: 2016, p. 281–291. DOI: [10.1007/978-1-4939-3771-4_19](https://doi.org/10.1007/978-1-4939-3771-4_19).
- [51] Adam E. Cohen en Veena Venkatachalam. “Bringing Bioelectricity to Light”. In: *Annual Review of Biophysics* 43 (1 mei 2014), p. 211–232. ISSN: 1936-122X. DOI: [10.1146/annurev-biophys-051013-022717](https://doi.org/10.1146/annurev-biophys-051013-022717).
- [52] Yongxian Xu, Peng Zou en Adam E Cohen. “Voltage imaging with genetically encoded indicators”. In: *Current Opinion in Chemical Biology* 39 (aug 2017), p. 1–10. ISSN: 13675931. DOI: [10.1016/j.cbpa.2017.04.005](https://doi.org/10.1016/j.cbpa.2017.04.005).
- [53] Julia R Lazzari-Dean, Anneliese MM Gest en Evan W Miller. “Optical estimation of absolute membrane potential using fluorescence lifetime imaging”. In: *eLife* 8 (sep 2019). ISSN: 2050-084X. DOI: [10.7554/eLife.44522](https://doi.org/10.7554/eLife.44522).
- [54] Jennifer C. Waters. “Accuracy and precision in quantitative fluorescence microscopy”. In: *Journal of Cell Biology* 185 (7 jun 2009), p. 1135–1148. ISSN: 1540-8140. DOI: [10.1083/jcb.200903097](https://doi.org/10.1083/jcb.200903097).
- [55] Tingying Peng e.a. “A BaSiC tool for background and shading correction of optical microscopy images”. In: *Nature Communications* 8 (1 jun 2017), p. 14836. ISSN: 2041-1723. DOI: [10.1038/ncomms14836](https://doi.org/10.1038/ncomms14836).
- [56] Klaus Suhling e.a. “Fluorescence lifetime imaging (FLIM): Basic concepts and some recent developments”. In: *Medical Photonics* 27 (mei 2015), p. 3–40. ISSN: 2213-8846. DOI: [10.1016/J.MEDPHO.2014.12.001](https://doi.org/10.1016/J.MEDPHO.2014.12.001).
- [57] W. BECKER. “Fluorescence lifetime imaging – techniques and applications”. In: *Journal of Microscopy* 247 (2 aug 2012), p. 119–136. ISSN: 0022-2720. DOI: [10.1111/j.1365-2818.2012.03618.x](https://doi.org/10.1111/j.1365-2818.2012.03618.x).

- [58] Rupsa Datta e.a. “Fluorescence lifetime imaging microscopy: fundamentals and advances in instrumentation, analysis, and applications”. In: *Journal of Biomedical Optics* 25 (07 mei 2020), p. 1. ISSN: 1083-3668. DOI: [10.1117/1.JBO.25.7.071203](https://doi.org/10.1117/1.JBO.25.7.071203).
- [59] Alessandro Esposito en Fred S. Wouters. “Fluorescence Lifetime Imaging Microscopy”. In: *Current Protocols in Cell Biology* 25 (1 dec 2004). ISSN: 1934-2500. DOI: [10.1002/0471143030.cb0414s25](https://doi.org/10.1002/0471143030.cb0414s25).
- [60] Joseph R. Lakowicz. *Principles of Fluorescence Spectroscopy*. Red. door Joseph R. Lakowicz. Boston, MA: Springer US, 2006. ISBN: 978-0-387-31278-1. DOI: [10.1007/978-0-387-46312-4](https://doi.org/10.1007/978-0-387-46312-4).
- [61] Mikhail Y. Berezin en Samuel Achilefu. “Fluorescence Lifetime Measurements and Biological Imaging”. In: *Chemical Reviews* 110 (5 mei 2010), p. 2641–2684. ISSN: 0009-2665. DOI: [10.1021/cr900343z](https://doi.org/10.1021/cr900343z).
- [62] Mohamadreza Fazel e.a. “Fluorescence microscopy: A statistics-optics perspective”. In: *Reviews of Modern Physics* 96 (2 jun 2024), p. 025003. ISSN: 0034-6861. DOI: [10.1103/RevModPhys.96.025003](https://doi.org/10.1103/RevModPhys.96.025003).
- [63] Horst Wallrabe en Ammasi Periasamy. “Imaging protein molecules using FRET and FLIM microscopy”. In: *Current Opinion in Biotechnology* 16 (1 feb 2005), p. 19–27. ISSN: 09581669. DOI: [10.1016/j.copbio.2004.12.002](https://doi.org/10.1016/j.copbio.2004.12.002).
- [64] Klaus Suhling, Paul M. W. French en David Phillips. “Time-resolved fluorescence microscopy”. In: *Photochemical and Photobiological Sciences* 4 (1 jan 2005), p. 13–22. ISSN: 1474-905X. DOI: [10.1039/b412924p](https://doi.org/10.1039/b412924p).
- [65] Ágnes Szabó, János Szöllösi en Peter Nagy. “Principles of Resonance Energy Transfer”. In: *Current Protocols* 2 (12 dec 2022). ISSN: 2691-1299. DOI: [10.1002/cpz1.625](https://doi.org/10.1002/cpz1.625).
- [66] Rahul Roy, Sungchul Hohng en Taekjip Ha. “A practical guide to single-molecule FRET”. In: *Nature Methods* 5 (6 jun 2008), p. 507–516. ISSN: 1548-7091. DOI: [10.1038/nmeth.1208](https://doi.org/10.1038/nmeth.1208).
- [67] Elizabeth A Jares-Erijman en Thomas M Jovin. “FRET imaging”. In: *Nature Biotechnology* 21 (11 nov 2003), p. 1387–1395. ISSN: 1087-0156. DOI: [10.1038/nbt896](https://doi.org/10.1038/nbt896).
- [68] Hidekazu Tsutsui e.a. “Improving membrane voltage measurements using FRET with new fluorescent proteins”. In: *Nature Methods* 5 (8 aug 2008), p. 683–685. ISSN: 1548-7091. DOI: [10.1038/nmeth.1235](https://doi.org/10.1038/nmeth.1235).
- [69] François St-Pierre e.a. “High-fidelity optical reporting of neuronal electrical activity with an ultrafast fluorescent voltage sensor”. In: *Nature Neuroscience* 17 (6 2014), p. 884–889. ISSN: 15461726. DOI: [10.1038/nn.3709](https://doi.org/10.1038/nn.3709). PMID: [24755780](https://pubmed.ncbi.nlm.nih.gov/24755780/).
- [70] Daniel R. Hochbaum e.a. “All-optical electrophysiology in mammalian neurons using engineered microbial rhodopsins”. In: *Nature Methods* 11 (8 2014), p. 825–833. ISSN: 15487105. DOI: [10.1038/NMETH.3000](https://doi.org/10.1038/NMETH.3000). PMID: [24952910](https://pubmed.ncbi.nlm.nih.gov/24952910/).

- [71] Yiyang Gong e.a. “Imaging neural spiking in brain tissue using FRET-opsin protein voltage sensors”. In: *Nature Communications* 5 (apr 2014). ISSN: 20411723. DOI: [10.1038/ncomms4674](https://doi.org/10.1038/ncomms4674). PMID: 24755708.
- [72] Peng Zou e.a. “Bright and fast multicoloured voltage reporters via electrochromic FRET”. In: *Nature Communications* 5 (aug 2014). ISSN: 20411723. DOI: [10.1038/ncomms5625](https://doi.org/10.1038/ncomms5625). PMID: 25118186.
- [73] Daniel J. Liput e.a. “A Guide to Fluorescence Lifetime Microscopy and Förster’s Resonance Energy Transfer in Neuroscience”. In: *Current Protocols in Neuroscience* 94 (1 dec 2020). ISSN: 1934-8584. DOI: [10.1002/cpns.108](https://doi.org/10.1002/cpns.108).
- [74] Dougal Maclaurin e.a. “Mechanism of voltage-sensitive fluorescence in a microbial rhodopsin”. In: *Proceedings of the National Academy of Sciences* 110 (15 apr 2013), p. 5939–5944. ISSN: 0027-8424. DOI: [10.1073/pnas.1215595110](https://doi.org/10.1073/pnas.1215595110).
- [75] Alexis Pietak en Michael Levin. “Bioelectrical control of positional information in development and regeneration: A review of conceptual and computational advances”. In: *Progress in Biophysics and Molecular Biology* 137 (sep 2018), p. 52–68. ISSN: 00796107. DOI: [10.1016/j.pbiomolbio.2018.03.008](https://doi.org/10.1016/j.pbiomolbio.2018.03.008).
- [76] Alex J. Walsh e.a. “Temporal binning of time-correlated single photon counting data improves exponential decay fits and imaging speed”. In: *Biomedical Optics Express* 7 (4 apr 2016), p. 1385. ISSN: 2156-7085. DOI: [10.1364/BOE.7.001385](https://doi.org/10.1364/BOE.7.001385).
- [77] Alexander Netaev, Nicolas Schierbaum en Karsten Seidl. “Advantages and Limitations of Fluorescence Lifetime Measurements Using Single-Photon Avalanche Diode (SPAD) Array Detector: A Comprehensive Theoretical and Experimental Study”. In: *Sensors* 22 (10 mei 2022), p. 3822. ISSN: 1424-8220. DOI: [10.3390/s22103822](https://doi.org/10.3390/s22103822).
- [78] Binglin Shen e.a. “Overcoming photon and spatiotemporal sparsity in fluorescence lifetime imaging with SparseFLIM”. In: *Communications Biology* 7 (1 okt 2024), p. 1359. ISSN: 2399-3642. DOI: [10.1038/s42003-024-07080-x](https://doi.org/10.1038/s42003-024-07080-x).
- [79] Lara Carvalho en Carl-Philipp Heisenberg. “Imaging Zebrafish Embryos by Two-Photon Excitation Time-Lapse Microscopy”. In: 2009, p. 273–287. DOI: [10.1007/978-1-60327-977-2_17](https://doi.org/10.1007/978-1-60327-977-2_17).
- [80] Chris Xu e.a. “Multiphoton fluorescence microscopy for in vivo imaging”. In: *Cell* 187 (17 aug 2024), p. 4458–4487. ISSN: 00928674. DOI: [10.1016/j.cell.2024.07.036](https://doi.org/10.1016/j.cell.2024.07.036).
- [81] Rishikesh U. Kulkarni en Evan W. Miller. “Voltage Imaging: Pitfalls and Potential”. In: *Biochemistry* 56 (39 okt 2017), p. 5171–5177. ISSN: 0006-2960. DOI: [10.1021/acs.biochem.7b00490](https://doi.org/10.1021/acs.biochem.7b00490).
- [82] Sebastian Nilsson e.a. “Fluorescence lifetime imaging through scattering media”. In: *Scientific Reports* 13 (1 feb 2023), p. 3066. ISSN: 2045-2322. DOI: [10.1038/s41598-023-30055-7](https://doi.org/10.1038/s41598-023-30055-7).

- [83] Asuka Shiraishi e.a. “In vivo long-term voltage imaging by genetically encoded voltage indicator reveals spatiotemporal dynamics of neuronal populations during development”. In: (mei 2023). DOI: [10.1101/2023.05.25.540669](https://doi.org/10.1101/2023.05.25.540669).
- [84] Lilach Avitan e.a. “Spontaneous and evoked activity patterns diverge over development”. In: *eLife* 10 (2021). ISSN: 2050084X. DOI: [10.7554/ELIFE.61942](https://doi.org/10.7554/ELIFE.61942). PMID: [33871351](https://pubmed.ncbi.nlm.nih.gov/33871351/).
- [85] Bill Z. Jia e.a. “A bioelectrical phase transition patterns the first vertebrate heartbeats”. In: *Nature* 622 (7981 okt 2023), p. 149–155. ISSN: 0028-0836. DOI: [10.1038/s41586-023-06561-z](https://doi.org/10.1038/s41586-023-06561-z).
- [86] Ahmed S. Abdelfattah e.a. “A general approach to engineer positive-going eFRET voltage indicators”. In: *Nature Communications* 11 (1 dec 2020). ISSN: 20411723. DOI: [10.1038/s41467-020-17322-1](https://doi.org/10.1038/s41467-020-17322-1). PMID: [32651384](https://pubmed.ncbi.nlm.nih.gov/32651384/).

2

A ZEBRAFISH ACE2N-mNEON EXPRESSION LIBRARY FOR IN VIVO VOLTAGE IMAGING OF NEURONAL SYNCHRONY AND CARDIAC MATURATION

Early, cell-resolved voltage measurements in intact embryos depend critically on reliable genetic access and robust expression of membrane-localized indicators. This chapter establishes a zebrafish expression library for the genetically encoded voltage indicator (GEVI) Ace2N-mNeon, enabling membrane-localized fluorescence from 4 hours post-fertilization (hpf) and supporting both ubiquitous and promoter-driven targeting to specific cell types. The toolkit spans multiple embryonic tissues, and we present neurons and cardiomyocytes as representative use cases. Using high-speed in vivo voltage imaging, we demonstrate early neuronal and cardiac voltage readouts, including motor-neuron synchrony during primary neurogenesis and developmental sharpening of chamber-specific cardiac propagation from 1 to 4 days post-fertilization (dpf).

This chapter has been published as: **Z. Wu**, R. Oliveira Silva, R. Houssein, F. Marques Trujillo, J. Gotti, S. Ganapathy, Z. Gao, D. Brinks, *Zebrafish Ace2N-mNeon expression toolkit for in vivo voltage imaging of neuronal synchrony and cardiac maturation*, Neurophotonics, Vol. 13, Issue S2, S23205 (2026).

2.1. INTRODUCTION

BIOELECTRICITY, defined as the voltage changes across and ionic currents through cellular membranes, is a fundamental biophysical mechanism that regulates a wide range of developmental processes, including cellular differentiation, pattern formation, and morphogenesis.¹⁻⁴ These electrical signals span multiple timescales, from millisecond-scale action potentials in excitable cells (neurons and myocytes),⁵ to slower membrane voltage (V_m) dynamics that evolve over minutes to days across diverse tissues.^{1,2} Understanding these dynamic bioelectric signals is important for elucidating their roles during embryogenesis.^{1-4,6}

Neuronal action potentials, also known as spikes, encode and transmit information essential for processes such as sensory perception, motor control, and cognition,⁵ whereas cardiac action potentials coordinate contraction and reflect functional maturation of the heart.⁷ To advance our understanding of these bioelectric signals during embryogenesis, it is crucial to monitor V_m dynamics *in vivo* across multiple cell types at early stages. However, achieving cellular resolution with millisecond timing in developing embryos remains difficult: electrophysiology is invasive and has limited capacity for simultaneous multi-cell recordings.^{8,9} Recent advances in genetically encoded voltage indicators (GEVIs) enable non-invasive, real-time visualization of V_m dynamics through fluorescence changes,¹⁰⁻¹³ making *in vivo* monitoring of early developmental activity feasible.¹⁴ Zebrafish, with optical transparency and rapid development, are particularly well suited for high-speed *in vivo* voltage imaging during early embryogenesis.^{15,16} Nevertheless, despite several studies extending these approaches to early embryonic stages, systematic *in vivo* measurements at the earliest stages remain limited.^{14,17,18}

Among available GEVIs, Ace2N-mNeon offers a practical balance of sensitivity, kinetics, and brightness suitable for high-speed *in vivo* imaging.¹⁹ We therefore developed a zebrafish expression library for Ace2N-mNeon that yields membrane-localized fluorescence from the 512-cell stage and supports both ubiquitous and promoter-driven, cell-type-specific expression. The library achieves broad membrane targeting across embryonic tissues; here we document this coverage to guide future applications, while functional validation focuses on neurons and cardiomyocytes. Using high-speed *in vivo* voltage imaging, we examined activity across multiple neuronal classes at 25 hours post-fertilization (hpf), with a targeted analysis of spinal cord motor neuronal synchronous activity during the transition from primary to secondary neurogenesis. In parallel, we evaluated atrial and ventricular optical action potentials from 25 to 102 hpf, detecting signals prior to overt chamber delineation and observing developmental sharpening of waveforms and increased rates.

Collectively, these findings establish the Ace2N-mNeon expression library as a practical tool for cell-resolved, millisecond-scale *in vivo* voltage imaging during early embryogenesis and demonstrate cross-tissue generalizability. This resource provides a foundation

for studies linking membrane-voltage dynamics to emergent circuit-level properties at single-cell resolution.

2.2. RESULTS

2.2.1. ACE2N-mNEON PREDOMINANTLY LOCALIZES TO THE PLASMA MEMBRANE ACROSS DIVERSE CELL TYPES DURING ZEBRAFISH (*Danio rerio*) DEVELOPMENT

To study bioelectricity during early development, we established strategies to express Ace2N-mNeon across developmental stages. To capture the earliest expression, we injected Ace2N-mNeon mRNA into the cytoplasm of one-cell embryos (Fig. 2.1a). Membrane-localized fluorescence was detectable as early as 2.75 hpf, coincident with the onset of the blastula stage (Fig. 2.1b).

To follow expression throughout development, we used the Tol2 transposon system (Methods).²⁰ First, we studied the broad expression of Ace2N-mNeon using this system under the ubiquitin (*ubi*) promoter, which can drive robust and ubiquitous transgene expression throughout zebrafish development.²¹ We constructed a *ubi*:Ace2N-mNeon Tol2 plasmid (Fig. 2.1c) and co-injected it with Tol2 transposase mRNA into the yolk of one-cell embryos (Fig. 2.1d; Supplementary Figs. S2.1,S2.2).

Ace2N-mNeon was broadly expressed across cell types throughout development (Fig. 2.1e,f).^{22,23} Ace2N-mNeon-positive embryos could be detected starting from the sphere stage (4 hpf) using confocal microscopy. During gastrulation (50% epiboly, 5.3 hpf, to embryonic shield, 10 hpf), expression persisted in newly differentiating cells with strong membrane fluorescence (Fig. 2.1e, 4–8 hpf). From 10 hpf through the 21-somite stage (19.5 hpf), as segmentation began and somites formed (Fig. 2.1e, 10–12 hpf), the embryo developed a more defined body shape (Fig. 2.1f, 19.5 hpf). By the prim-6 stage (25 hpf), the embryo exhibited a recognizable body plan, including head, tail, and clear segmentation (Fig. 2.1f, 25 hpf). At this stage, multiple cell types were identifiable by morphology, including skeletal muscle, neural, and epithelial cells, with broad Ace2N-mNeon expression and strong localization to the cell membrane (Fig. 2.1g). This expression can be observed throughout development, at least 5 days post-fertilization (dpf). More detailed expression images from 1 to 5 dpf can be found in Supplementary Fig. S2.1.

Together, these findings demonstrate stable, widespread expression with predominant membrane localization of Ace2N-mNeon from gastrulation onward, persisting across diverse cell types through 5 dpf.

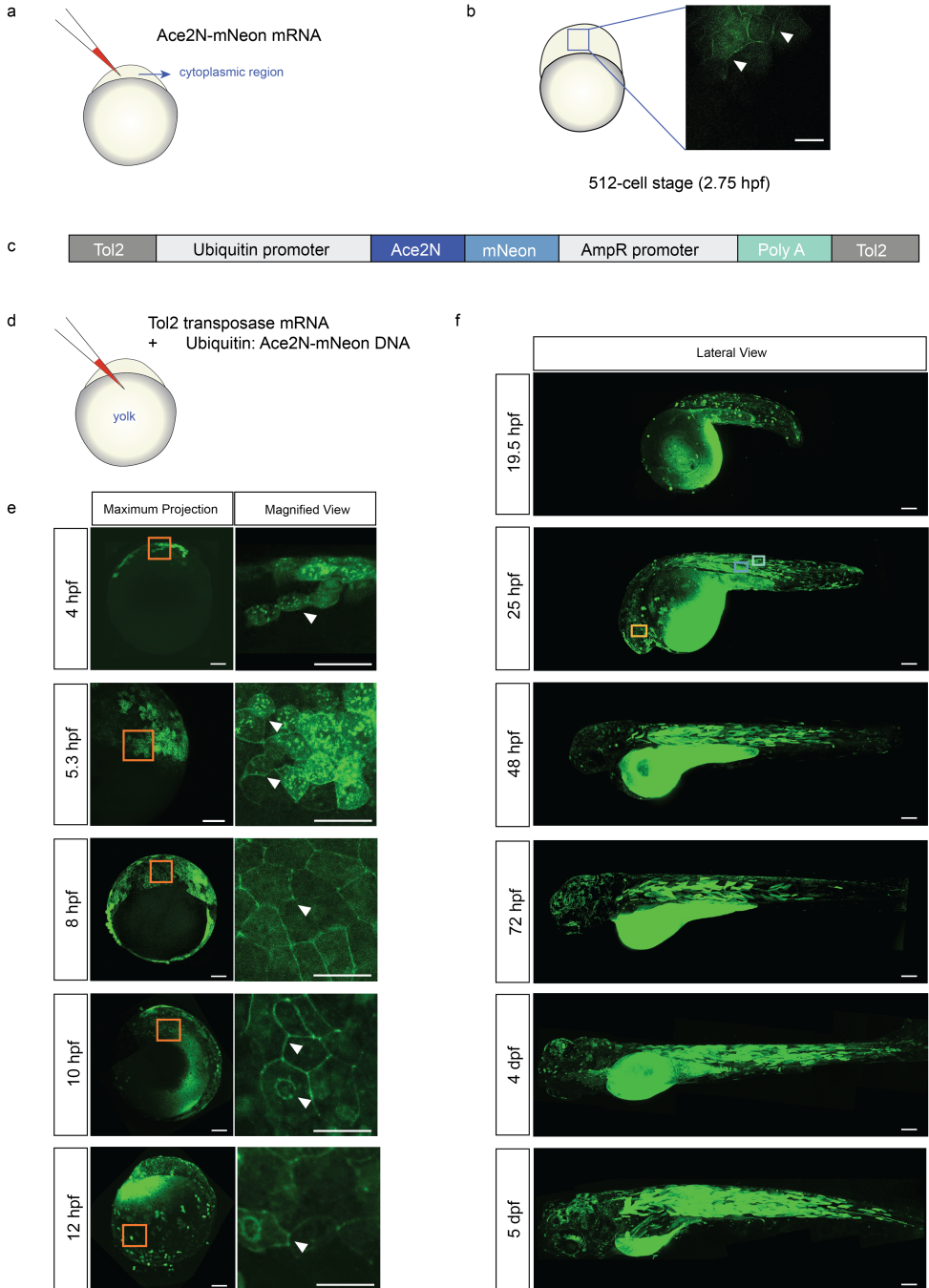


Figure 2.1

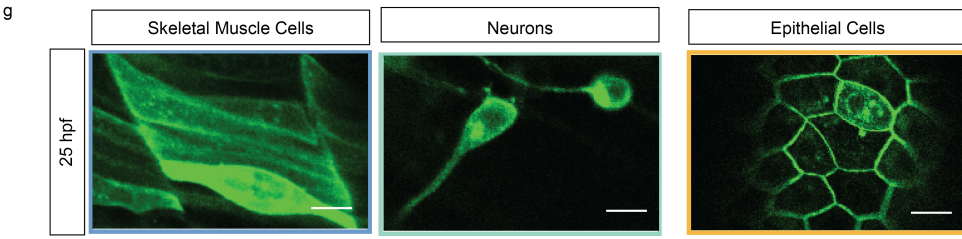


Figure 2.1: **Expression of Ace2N-mNeon in various cell types throughout development.** (a) Schematic of microinjection of Ace2N-mNeon mRNA into the cytoplasm of a 1-cell stage embryo. (b) Single z-plane confocal image of Ace2N-mNeon mRNA expression at the 512-cell stage. Membrane localization is observed at 2.75 hpf (white arrows). Scale bar = 20 μm . (c) Diagram of Tol2 constructs driving Ace2N-mNeon from the *ubi* promoter. (d) Schematic of co-injection of *ubi*:Ace2N-mNeon Tol2 plasmid and Tol2 transposase mRNA into the yolk at the 1-cell stage. (e-f) Maximum-intensity projections of *ubi*:Ace2N-mNeon expression from sphere stage (4 hpf) to 5 dpf. Ace2N-mNeon is widely expressed with predominant membrane localization across diverse cell types. (e) Early expression from 4–12 hpf. Left: maximum-intensity projection, scale bar = 100 μm . Right: magnified view showing membrane labeling, scale bar = 50 μm . (f) Lateral views of Ace2N-mNeon expression in multiple cell types from 1–5 dpf. Scale bar = 100 μm . (g) Single z-plane confocal image of Ace2N-mNeon expression at 25 hpf. Distinct cell types can be identified based on morphology, including skeletal muscle cells, neurons, and epithelial cells. Scale bar = 20 μm . **hpf**, hours post-fertilization; **dpf**, days post-fertilization; **ubi**, ubiquitin.

2.2.2. CELL-SPECIFIC PROMOTERS DRIVE DIFFERENTIAL ACE2N-mNEON EXPRESSION DURING ZEBRAFISH (*Danio rerio*) DEVELOPMENT

Table 2.1: Cell-specific promoters used to drive Ace2N-mNeon expression in zebrafish.

Promoter (gene)	Target cell types
503-bp <i>unc-45b</i>	skeletal and cardiac muscle cells
<i>acta2</i> (α -smooth muscle actin)	smooth muscle cells and pericytes
<i>cmlc2</i> (cardiac myosin light chain 2)	cardiomyocytes
<i>elavl3</i> (ELAV-like protein 3)	neurons
<i>neuroD</i> (neurogenic differentiation 1)	neurons

In our initial experiments, we established ubiquitous Ace2N-mNeon expression across zebrafish development, providing membrane-targeted labeling across multiple cell types and stages. We then built promoter-driven, cell-type-specific constructs, facilitating targeted investigation of bioelectrical activity in defined cell types (Table 2.1). Given the crucial roles of neurons and myocytes during development, our research primarily focused on these cell types. Neurons are essential for propagating bioelectric signals that orchestrate tissue and organogenesis,^{2,3} while myocytes are integral to motility, structural support, and cardiac functionality.²⁴

Zebrafish embryogenesis is marked by rapid development, with somite formation beginning around 16 hpf and the basic body plan and early organ systems forming by 19.5 hpf.²⁵ To investigate bioelectricity changes during this window, we assessed

promoter-driven expression from the 21-somite stage (19.5 hpf), a key point for early organogenesis.²⁵ As expected, constructs yielded cell-specific expression. Expression levels were mosaic and varied across embryos and cell types, consistent with Tol2-mediated transient transgenesis and promoter-dependent strength (Fig. 2.2 and Fig. 2.3).^{20,21}

ACE2N-mNEON EXPRESSION IN MUSCLE CELLS

Zebrafish musculature comprises smooth, skeletal, and cardiac muscle cells, each with distinct gene expression profiles and localizations.²⁴ The promoters used in this study allow the differentiation and independent analysis of these cell types.

Expression in cardiac muscle cells was driven by the promoter for cardiac myosin light chain 2 (*cmhc2*), a key cardiac contractile protein. The zebrafish *cmhc2* promoter drives specific expression in cardiomyocytes.^{26,27} Expression begins at 19.5 hpf and continues throughout development (Fig. 2.2a). By 4 dpf, distinct atrium (A) and ventricle (V) structures are observable (Fig. 2.2d), allowing separate recording of electrical dynamics.

To investigate skeletal muscle cells (skm), we used the promoter for *unc-45b*, a myosin chaperone important for correct assembly of the contractile apparatus in developing muscles.²⁸ In zebrafish, it is specifically expressed in striated muscle, including both cardiac and skeletal muscles, where it can help myosin fold during myofiber formation.^{28,29} At 19.5 hpf, the *unc-45b* promoter labels skm and adaxial cells (ad, progenitors of slow-twitch skm) (Fig. 2.2b, 19.5 hpf). These cells can be identified by their morphology (Fig. 2.2b,e). By 3 dpf, fluorescence was evident in head muscles (Fig. 2.2e).

Smooth muscle cells (SMCs) were labeled using the promoter for α -smooth muscle actin (*acta2*). *acta2* is one of the earliest markers for mural cell development in vertebrates, expressed in SMCs and pericytes.³⁰ In zebrafish, *acta2*:EGFP expression begins slightly later in development, initially in the myocardium, followed by visceral smooth muscle and skeletal muscle, and eventually in vascular smooth muscle.³⁰ At 19.5 hpf, *acta2* expression is faintly detectable in the myocardium and in a few skm (Fig. 2.2c, 19.5 hpf). More expression in skm could be observed from 25 hpf onwards (Fig. 2.2c, 25 hpf). By 48 hpf, the *acta2* signal was observed in the myocardium, consistent with early *acta2* reporter activity (Fig. 2.2c, 48 hpf). By 5 dpf, strong expression was observed in the myocardium and visceral smooth muscle of the gut (Fig. 2.2c,f, 5 dpf).

ACE2N-mNEON EXPRESSION IN NEURONS

During early somite formation, *elavl3*, an mRNA-binding protein broadly expressed in newly differentiated neurons,³¹ is detectable in the neural tube and forebrain of zebrafish embryos (Fig. 2.3 a). Under the *elavl3* promoter, Ace2N-mNeon labeling is prominent by 1 dpf in the spinal cord (SC) and telencephalon (T) (Fig. 2.3 a, 19.5 hpf and 25 hpf). At 25 hpf, distinct neuronal populations can be identified by location and morphology,

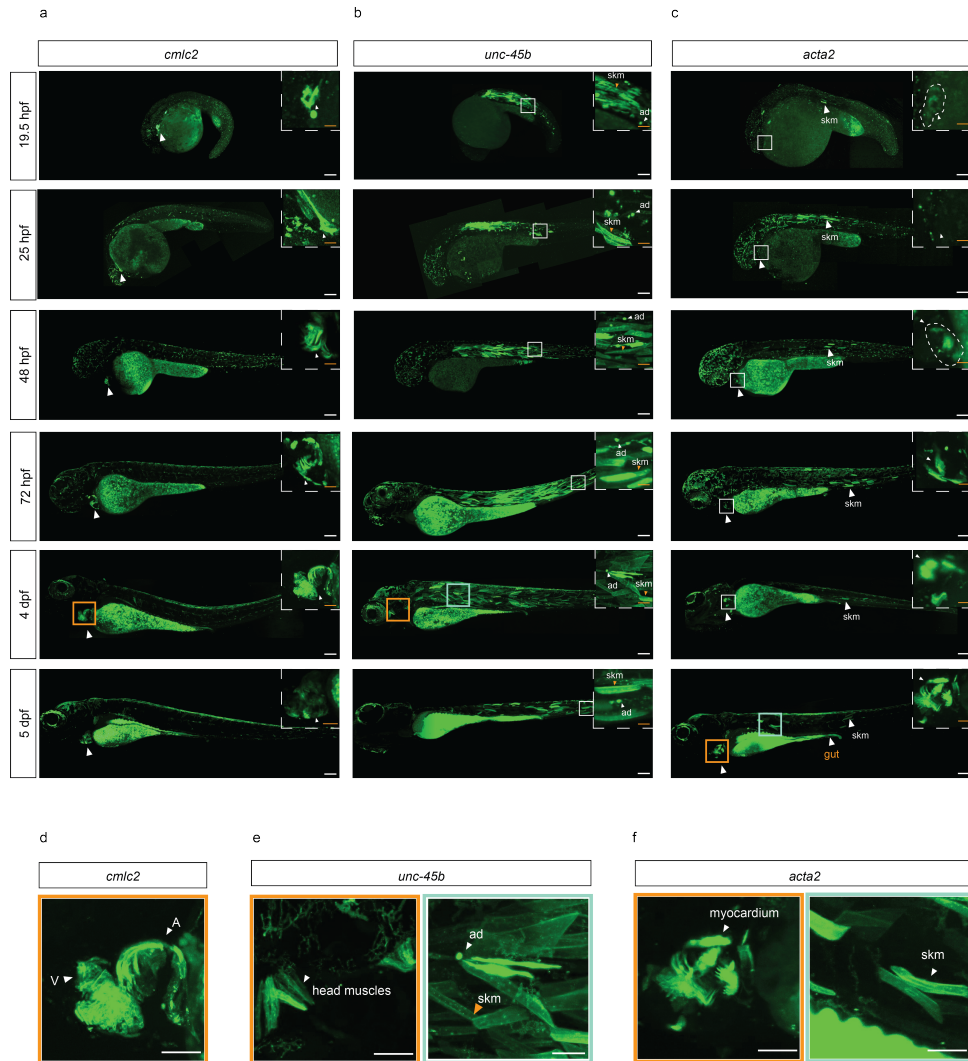
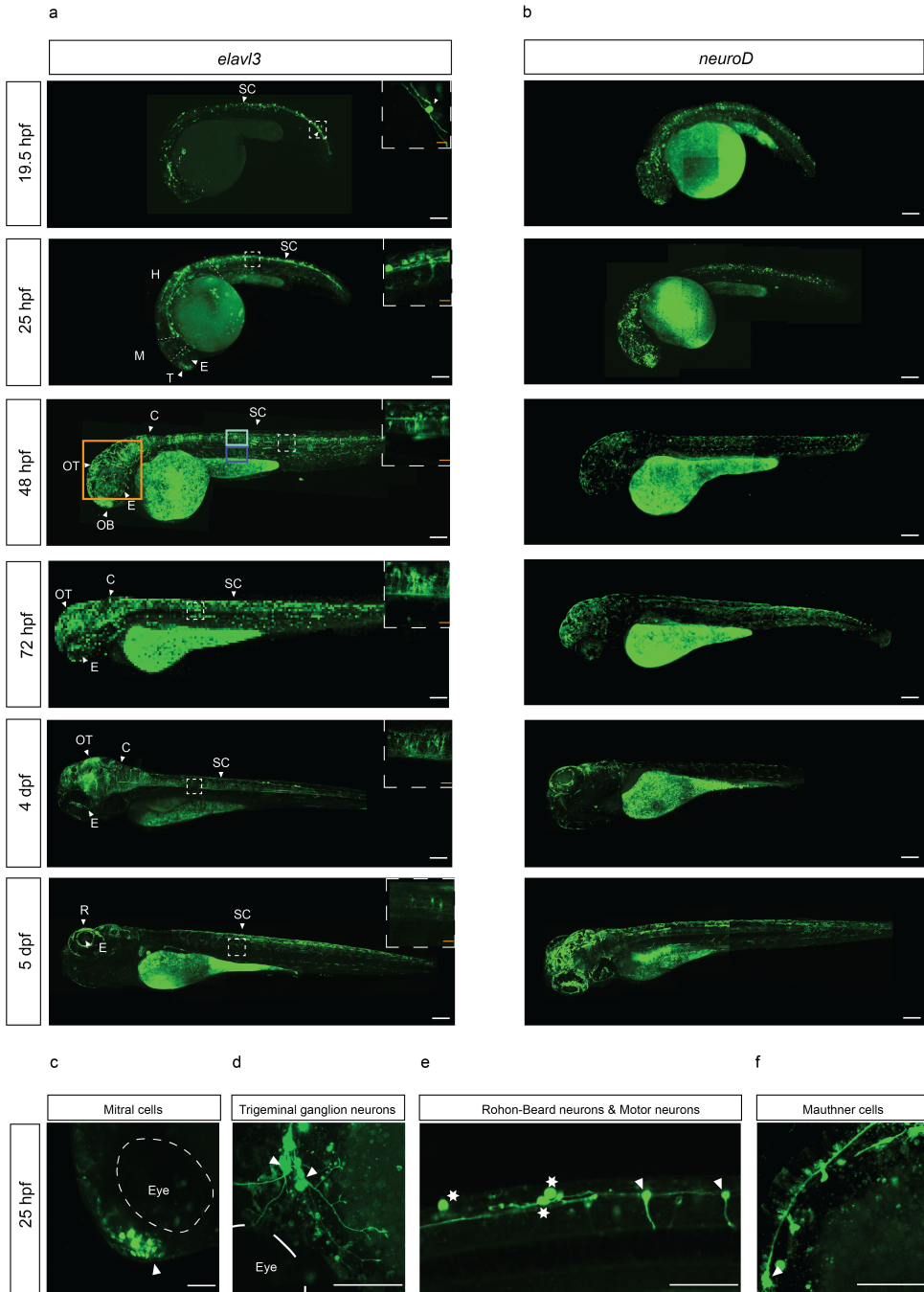


Figure 2.2: Ace2N-mNeon expression in muscle cell types across developmental stages. (a-c) Whole-embryo maximum-intensity projections of Ace2N-mNeon driven by the indicated promoters from 19.5 hpf to 5 dpf. Scale bar = 100 μ m. Boxed regions are shown at higher magnification (scale bar = 25 μ m). (a) *cmlc2*: cardiomyocytes labeled from the 21-somite stage (19.5 hpf), with progressively stronger signal over time. (b) *unc-45b*: stronger labeling in skm (orange arrows) and ad (white arrows); head musculature is visible by 4 dpf (orange box). (c) *acta2*: sparse labeling at 19.5 hpf; from 48 hpf, labeling appears in the myocardium, and by 5 dpf, a robust signal is present in the myocardium (orange box) and visceral smooth muscle of the gut (orange arrows). (d-f) Higher-magnification single z-plane images at later stages. Scale bar = 50 μ m. (d) *cmlc2* at 4 dpf: cardiomyocytes with clear labeling in the A and V. (e) *unc-45b* at 4 dpf: head muscles (orange box), skeletal muscle (green box; orange arrows), and ad (green box; white arrows). (f) *acta2* at 5 dpf: labeling in the myocardium (orange box) and visceral smooth muscle (green box). **hpf**: hours post-fertilization; **dpf**: days post-fertilization; **skm**: skeletal muscle cells; **ad**: adaxial cells; **A**: atrium; **V**: ventricle.

including mitral cells,³² trigeminal ganglion neurons,³³ Mauthner cells,³⁴ Rohon-Beard mechanosensory (RB) neurons,³⁵ and motor neurons³⁶ (Fig. 2.3 c to f).

By 2 dpf, Ace2N-mNeon labeling expands across the central nervous system (CNS). In addition, regions visible at 1 dpf show signals in the retina (R), optic tectum (OT), and cerebellum (C) (Fig. 2.3 a and g). At this stage, retinal ganglion cells (RGCs) are identifiable with centrally projecting axons (Fig. 2.3 h), and secondary motor neurons projecting to the ventral trunk muscles also become distinguishable (Fig. 2.3 i and j). From 2 to 4 dpf, labeling density increases in the OT, C, and SC; individual neurons become harder to resolve in maximum-intensity projections but remain distinguishable in single *z*-planes from 3D scans (Fig. 2.3 a, white dashed box). Ace2N-mNeon expression persists in the CNS at least through 5 dpf.

We compared *elavl3*- and *neuroD*-driven expression (Fig. 2.3 a and b).³⁷ Labeling under *elavl3* was denser than under *neuroD* (Fig. 2.3 a and b), consistent with their endogenous profiles: *elavl3* is broadly expressed in newly differentiated neurons,³⁸ whereas *neuroD* labels subsets and is not universal across neuronal classes.³⁹ These observations indicate that Ace2N-mNeon can be targeted to defined neuronal populations with membrane localization throughout early development.



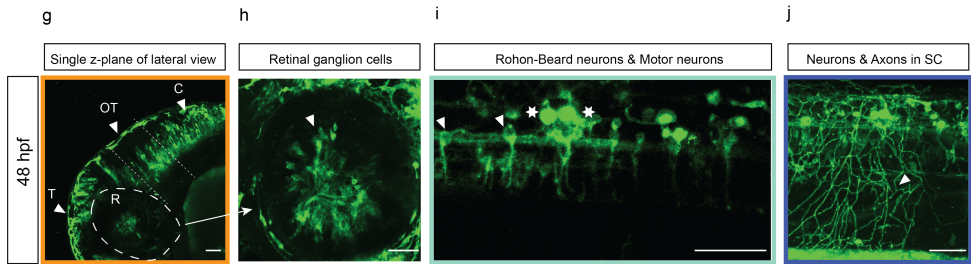


Figure 2.3: ***Ace2N-mNeon* expression in neurons across developmental stages.** (a,b) Whole-embryo maximum-intensity projections of *Ace2N-mNeon* driven by the indicated neuronal promoters from 19.5 hpf to 5 dpf. Scale bar = 100 μm . Boxed regions are shown at higher magnification as single z-plane confocal images from the indicated brain region. Scale bar = 20 μm . (a) *elavl3*: prominent labeling in the spinal cord (SC) by 19.5 hpf, extending to the telencephalon (T) and hindbrain (H) by 25 hpf, with increased labeling in the olfactory bulb (OB), retina (R), optic tectum (OT), and cerebellum (C) from 2–4 dpf. (b) *neuroD*: labeling is sparser compared to *elavl3*. (c–f) Single z-plane images at 25 hpf showing identifiable neuronal populations by location and morphology. Scale bar = 50 μm . (c) Mitral cell in the telencephalon (T) (white arrows). (d) Trigeminal ganglion neurons (white arrows). (e) Rohon-Beard (RB) mechanosensory neurons (white stars) and motor neurons (white arrows). (f) Mauthner cells (white arrows). (g–j) Single z-plane images at 48 hpf. Scale bar = 50 μm . (g) Labeling in the retina (R), optic tectum (OT), and cerebellum (C) [region indicated by the orange box in (a)]. (h) Retinal ganglion cells (RGCs) with centrally projecting axons. (i) Neurons and axons in the spinal cord [regions indicated by the green box in (a)]. (j) Secondary motor neuron axons projecting to ventral trunk muscles. **hpf**, hours post-fertilization; **dpf**, days post-fertilization; **SC**, spinal cord; **T**, telencephalon; **H**, hindbrain; **OB**, olfactory bulb; **R**, retina; **OT**, optic tectum; **C**, cerebellum; **RB**, Rohon-Beard; **RGCs**, retinal ganglion cells.

2.2.3. *ACE2N-mNeon* VOLTAGE IMAGING REVEALS NEUROGENESIS-SPECIFIC ELECTRICAL ACTIVITY

To validate the library for studying neural development *in vivo*, we performed high-speed imaging of identified neuronal types and analyzed activity traces using a standard motion correction and spike extraction workflow.^{40–43} We co-injected the *elavl3:Ace2N-mNeon* construct with Tol2 transposase mRNA into one-cell-stage embryos and selected labeled embryos for high-speed imaging in defined brain regions from 24 to 28 hpf.

For voltage imaging, we targeted three identifiable neuronal classes based on morphology and location: RB mechanosensory neurons, spinal motor neurons, and mitral cells in the olfactory bulb. Along the tail, motor neurons were recognized by axons projecting to the ventral myotome,³⁶ and RB neurons by laterally extended axons (Fig. 2.4 b). In the rostral bulb near the eyes, mitral cells were located adjacent to the medial olfactory tract (Fig. 2.4 c).³² Voltage transients were detectable at 25 hpf in all three classes (Fig. 2.4 d to f).

During zebrafish neurogenesis, a primary scaffold precedes secondary neurogenesis, which involves axonal and dendritic elaboration and the emergence of early synapses.^{44–46} To examine activity across this transition, we imaged sparsely labeled spinal motor neurons at 1 and 3 dpf, identifying individual cells in the recording plane. Across embryos,

neighboring motor neurons showed more frequent synchronized activity at ~25 hpf that appeared reduced or absent at 3 dpf (Fig. 2.4 g and h), indicating distinct activity patterns across primary versus secondary neurogenesis.^{45,46} Additionally, we obtained recordings from denser regions in the head (Supplementary Fig. S2.3 a to c). These observations indicate that Ace2N-mNeon supports *in vivo* voltage recordings across neuronal classes during early development and can reveal qualitative changes in motor network synchronization during neurogenesis.

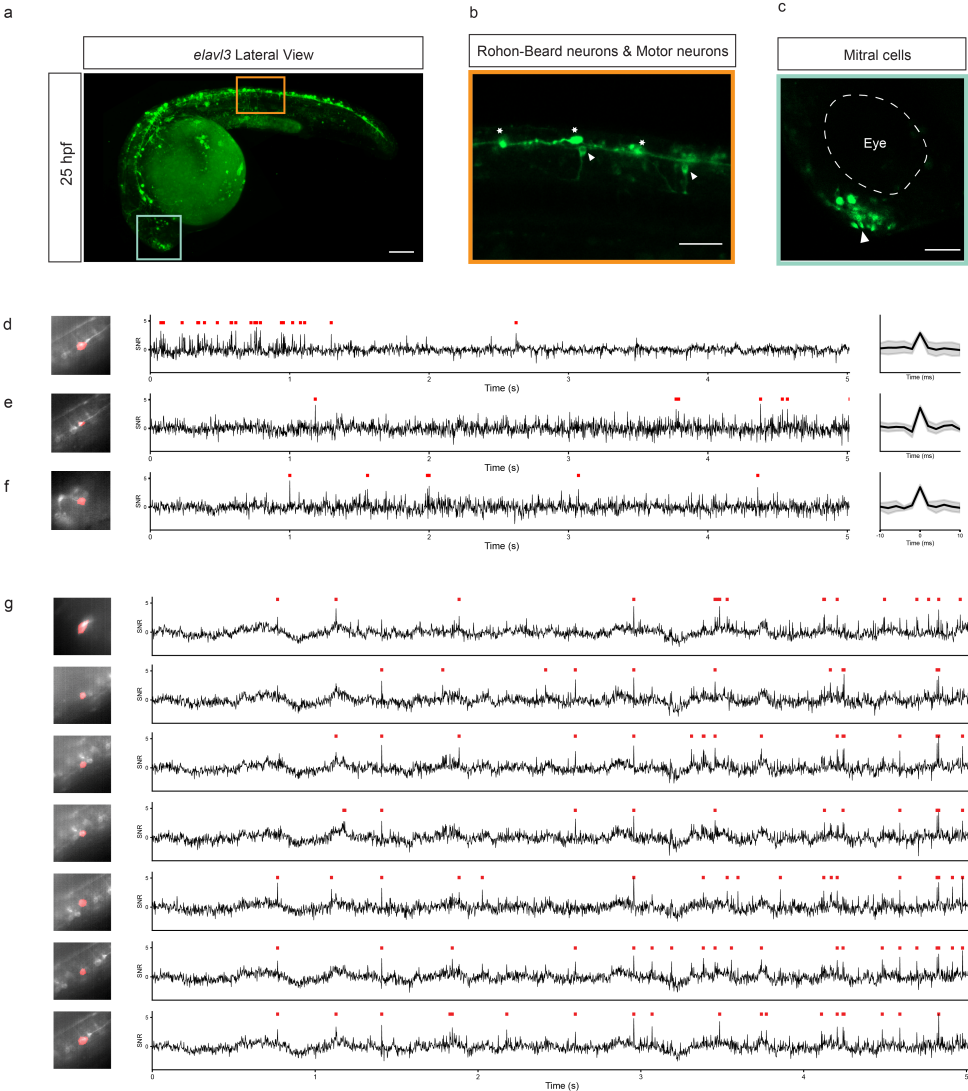


Figure 2.4

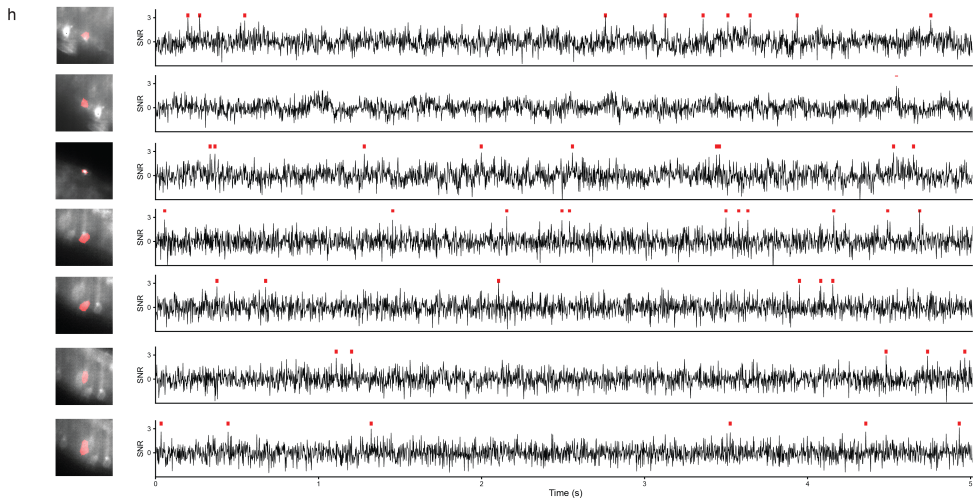


Figure 2.4: *Ace2N-mNeon* voltage across neuronal classes during early development. (a) Whole-embryo maximum-intensity projections of *Ace2N-mNeon* driven by *elavl3* at 25 hpf. Scale bar = 100 μm . Orange and green boxes indicate regions shown at higher magnification in (b) and (c). (b) Single z-plane in the spinal cord showing motor neurons (white arrows) and RB neurons (white stars). Scale bar = 50 μm . (c) Single z-plane in the olfactory bulb showing mitral cells (white arrow). Scale bar = 50 μm . (d-f) Voltage recordings at 25 hpf from the three neuronal classes. Left: mean image of the recording with spatial footprint. Center: example fluorescence traces. Right: average spike waveform with standard deviation from detected events. (d) Motor neuron. (e) RB neuron. (f) Mitral cell. (g, h) Voltage recordings from multiple motor neurons in the same field of view at about 25 hpf (g) and 3 dpf (h). Left: mean with spatial footprints, ROI was manually annotated in red. For all traces, red ticks indicate detected spikes. **RB**: Rohon-Beard; **ROI**: region of interest; **hpf**: hours post-fertilization; **dpf**: days post-fertilization.

2.2.4. DETECTION OF DEVELOPMENT-DEPENDENT VOLTAGE DYNAMICS IN THE ZEBRAFISH HEART

Using the same expression resource applied to neurons, *cmhc2:Ace2N-mNeon* showed strong membrane labeling in cardiomyocytes from the 21-somite stage (Fig. 2.2a), enabling in vivo optical readout of cardiac activity. At 4 dpf, lateral views reveal persistent and pronounced membrane localization, with a visibly stronger signal than at earlier stages (Fig. 2.5a,b).

To study cardiac AP dynamics during early development, we imaged *cmhc2:Ace2N-mNeon* positive embryos of the zebrafish heart at 25, 48, and 102 hpf (Fig. 2.5c-e), using different embryos at each time point. To minimize motion artifacts caused by heart contractions, embryos were incubated with para-aminobenzocaine (pAB, 100 μM) for 4 h before imaging.⁴⁷ Illumination was kept low to avoid blue-light inactivation of pAB, and beating resumed promptly upon brief high-intensity blue light after each recording, confirming viability during the session (Supplementary Movies 1-3).

At 25 hpf, the heart presents as a narrow tube without an overt anatomical division

(Fig. 2.5c, top), yet distinctive atrial- and ventricular-type optical APs were detectable, with atrial-to-ventricular propagation (Fig. 2.5c, bottom). By 48 hpf, the atrium (A) and ventricle (V) are anatomically delineated (Fig. 2.2a, 48 hpf), and both compartments exhibit sharper waveforms and higher frequency (Fig. 2.5d). This sharpening and acceleration continue through development until 102 hpf (Fig. 2.5e), while maintaining a clear A–V propagation pattern (Fig. 2.5e,f).

These *in vivo* optical recordings were consistent with prior patch-clamp measurements on explanted hearts,^{48,49} demonstrating that chamber-specific cardiac APs arise before overt morphological chamber formation. Together with the neuronal recordings, the cardiac results demonstrate the cross-tissue applicability of the Ace2N-mNeon expression library for cell-resolved, early embryonic voltage imaging.

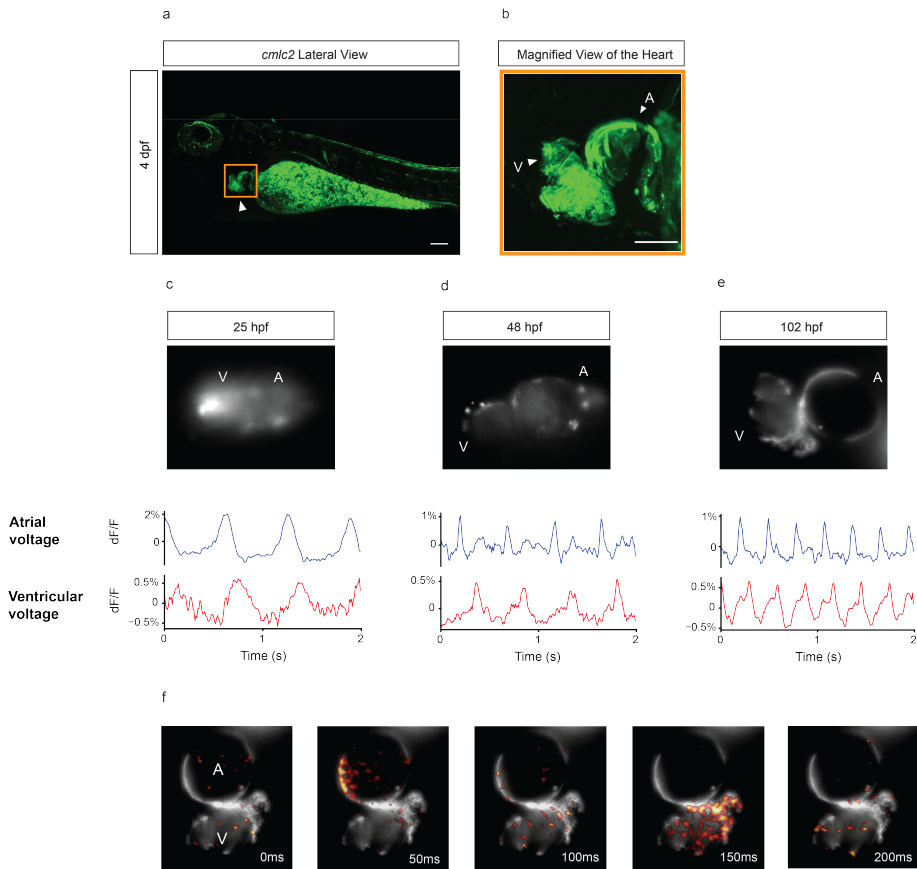


Figure 2.5: **Atrial and ventricular voltage dynamics in the embryonic zebrafish heart.** (a) Maximum-intensity projections of Ace2N-mNeon driven by *cm1c2* at 4 dpf. Scale bar = 100 μ m. (b) Higher-magnification view of the boxed region in (a), showing membrane localization and delineation of atrium (A) and ventricle (V) at 4 dpf. Scale bar = 50 μ m. (c-e) Developmental series of A and V optical voltage recordings at 25, 48, and 102 hpf. Top: fluorescence images of recorded hearts. Bottom: optical voltage traces ($\Delta F/F$). (f) Voltage-time footprint (temporal-maximum F/F) over a 200 ms window at 102 hpf. **hpf**: hours post-fertilization; **dpf**: days post-fertilization; **A**: atrium; **V**: ventricle; **pAB**: para-aminoblebbistatin; **ROI**: region of interest.

2.3. DISCUSSION

GEVIs have revolutionized the study of bioelectric signals, but applications in early embryogenesis remain comparatively limited.^{14,17,18} Here we introduce a zebrafish Ace2N-mNeon expression library that delivers membrane-targeted fluorescence from the 512-cell stage and supports promoter-driven, cell-specific expression at later stages, enabling cell-resolved, millisecond-scale *in vivo* voltage imaging during early development. To our knowledge, this work presents the first demonstration of Ace2N-mNeon expression

across multiple cell types in zebrafish,⁵⁰ documenting neurons, cardiomyocytes, mural cells, and skeletal muscle cells, thereby providing a unified library for cross-tissue *in vivo* voltage imaging.

A primary application of this library is tracking neuronal activity in the early developing brain. Zebrafish neurogenesis comprises a primary phase (to ~2 dpf) that establishes a transient scaffold, followed by secondary neurogenesis with axonal and dendritic elaboration and the emergence of early synapses.^{45,46,51} During primary neurogenesis, developing neural networks often exhibit spontaneous patterned activity, synchrony has been reported to occur with phases of axon outgrowth and the emergence of early synapses.^{46,51,52} Prior approaches have provided important insights, but simultaneously, cell-resolved voltage readouts in early embryos remain challenging.⁵³ In this study, we have shown that adjacent spinal cord motor neurons exhibit synchronous activity during primary neurogenesis and appear absent by 3 dpf across embryos, consistent with the transition from primary to secondary neurogenesis. These observations highlight the feasibility of *in vivo* voltage imaging to probe activity motifs across neurogenesis.

While much of the progress in voltage imaging has centered on neural signals, Ace2N-mNeon also captured the longer-duration APs of cardiomyocytes. Here, we observed atrial and ventricular voltage activity as early as 25 hpf, even before a clearly visible anatomical division between the chambers. Moreover, as development proceeded, both atrial and ventricular action potentials exhibited sharper waveforms and higher frequency, which is consistent with the rise in embryonic heart rate^{54,55} and likely reflects maturation of ion-channel composition and coupling, possible contributors include increased expression of the cardiac sodium channel Nav1.5.⁵⁶ Our optical recordings align with prior electrophysiological measurements in embryonic preparations, supporting the view that electrophysiological maturation precedes morphological partitioning.^{48,49,57} Together with the neuronal data, this supports the cross-tissue applicability of our Ace2N-mNeon library.

Beyond fast spiking in excitable cells, slow V_m changes in non-excitable cells potentially function as endogenous cues for growth and morphogenesis, influencing both individual cell behavior and anatomical features.^{2,3,50,58} Although calibrated V_m measurements *in vivo* remain challenging,^{59–62} the early, membrane-targeted, and broadly distributed expression achieved by our library provides a practical entry point for future studies of slow bioelectric signaling during embryogenesis as optical voltage methodologies continue to advance.

This study has several limitations. First, neuronal analyses were qualitative and drawn from sparsely labeled fields. Second, expression declined by 3 dpf, restricting longitudinal tracking primarily to motor neurons. Third, Tol2-mediated transient expression produced embryo-to-embryo mosaicism, reducing comparability across individuals.²⁰ These constraints can be mitigated by generating stable Ace2N-mNeon transgenic lines and using compartment-targeted or more cell-type-specific promoters to achieve

controlled-density labeling and reduce mosaicism. Combining this resource with volumetric light-sheet microscopy and faster detectors would expand the field of view while preserving temporal resolution. Adopting standardized synchrony metrics and shared analysis pipelines will facilitate cross-stage and cross-lab comparisons. In addition, all-optical paradigms, pairing this library with optogenetic pacing or perturbations, may help establish causality in early circuit assembly and cardiac conduction.¹⁴ Finally, extending functional assays to additional cell types already represented in the panel will test and broaden its cross-tissue applicability.

Together, the Ace2N-mNeon expression library enables *in vivo* voltage imaging across neuronal and cardiac tissues in early embryogenesis, establishes feasibility and cross-tissue applicability, and provides a practical path to chart how membrane-voltage dynamics evolve from cells to circuits in the intact embryo.

2.4. METHODS

2.4.1. ZEBRAFISH HUSBANDRY

All experiments used Casper zebrafish (*Danio rerio*).⁶³ Adults were maintained in recirculating systems at the Delft University of Technology fish facility under a 14 h light/10 h dark cycle at 28°C and pH 7.5.

2.4.2. PLASMID CONSTRUCTION

Ace2N-mNeon was amplified from YA1611:mNeon-Ace (a gift from Adam Cohen) and fused to various promoters in Tol2 backbones. Inserts were generated by overlap-extension PCR using Phusion high-fidelity DNA polymerase (NEB), and promoter-containing backbones were amplified with KOD Xtreme Hot Start DNA Polymerase (Merck Sigma). Fragments were assembled with Gibson Assembly Master Mix (NEB) and transformed into NEB[®] 5-alpha competent *E. coli*. Primer sequences are listed in Table S2.1, and all plasmids generated in this study are listed in Table S2.2.

2.4.3. TOL2 TRANSPOSON SYSTEM

The Tol2 system mediates cut-and-paste genomic integration and supports stable transgene expression in zebrafish.²⁰ Following microinjection, Tol2 transposase mRNA drives integration of the Tol2-flanked expression cassette, improving expression breadth compared to episomal plasmids.²⁰

2.4.4. RNA SYNTHESIS

Ace2N-mNeon was subcloned downstream of an SP6 promoter (from pCS2FA-CO-Tol2-TPase, Addgene #133032). Tol2 transposase mRNA was transcribed directly from pCS2FA-CO-Tol2-TPase. In vitro transcription was performed using the mMESSAGE mMACHINE[®] Kit (Thermo Fisher Scientific) following the manufacturer's protocol. The synthesized RNA was purified and quantified before subsequent microinjections.

2.4.5. MICROINJECTION

Fertilized eggs were collected at the 1-cell stage immediately after spawning. For mRNA injections, Ace2N-mNeon mRNA (100 ng/ μ L) with 0.1% phenol red (Sigma-Aldrich, P0290) was injected into the cytoplasm at the 1–4 cell stage (~1 nL). For DNA injections, 1-cell-stage embryos were co-injected into the yolk with ~1 nL containing 50 ng/ μ L plasmid DNA, 100 ng/ μ L Tol2 transposase mRNA, and 0.1% phenol red. After injection, embryos were incubated in egg water (Instant Ocean salts, 60 μ g/mL) containing 0.0002% methylene blue. Unfertilized or dead eggs were removed at 6 h and 24 h post-injection.

2.4.6. CONFOCAL IMAGING SAMPLE PREPARATION

Embryos at 2.75–12 hpf were imaged directly in a drop of egg water. Embryos from 19.5 hpf to 5 dpf were manually dechorionated (before 2 dpf) and mounted in 1.5% agarose (Sigma-Aldrich, A4018) containing 0.03% tricaine (Sigma-Aldrich, A5040). Embryos imaged at each developmental stage were separate individuals. Before and after imaging, embryos were checked for heartbeat, overall health, and gross morphology.

2.4.7. CONFOCAL IMAGING SETUP

Confocal imaging was performed on a Nikon Ti C2si inverted microscope with 485 nm excitation (illumination power ~3.35 mW). The system was equipped with a 405/488/561/640 quad-band dichroic (Nikon, MHE46410), and imaging used the 488 nm channel with a 525/50 emission filter (Nikon, MHE46710). Images were acquired with a 20 \times /0.75 NA objective (Nikon CFI Plan Fluor 20XC MI). Data acquisition was performed using NIS-Elements, and analysis was conducted with ImageJ. All voltage recordings (neuronal and cardiac) in this study were performed on a single *z*-plane at the recording plane; whole-embryo maximum-intensity projections were used only for anatomical orientation in expression figures.

2.4.8. VOLTAGE IMAGING OF NEURONS

Embryos at 24–28 hpf and 3 dpf were paralyzed with α -bungarotoxin (1 mg/mL, Sigma-Aldrich, 203980; 15 min) to block nicotinic receptors and suppress motion artifacts during imaging. Embryos were mounted in 1.5% low-melting agarose (Sigma-Aldrich, A4018). Single-photon voltage imaging was performed on a Nikon A1RMP microscope using a $25\times/1.1$ NA water-immersion objective (Nikon CFI75 Apo, 25XC W). Illumination was provided by a white LED (SOLA Light Engine, Lumencor; $20\text{--}50$ mW/mm²) filtered with a 504/12 excitation filter (Semrock FF01-504/12-25), an FF518-Di01 dichroic (Semrock), and a 532/18 emission filter (Semrock FF01-532/18-25). Images were acquired at 500 frames per second (fps) on a Kinetix sCMOS camera (Teledyne Photometrics) via Micro-Manager, with 2×2 or 4×4 binning, for 20–30 s per recording. All neuronal voltage recordings were acquired on a single z -plane at the recording plane.

2.4.9. NEURONAL VOLTAGE IMAGING ANALYSIS

Recordings were motion-corrected using rigid NoRMCorre within CaImAn^{40–42} and denoised with the SUPPORT pipeline⁴³ (100 training iterations on a 5000-frame zebrafish tail dataset, 10 s). Regions of interest (ROIs) corresponding to individual cells were manually annotated and processed using the VolPy pipeline.⁴² VolPy parameters followed defaults except for a 1 Hz high-pass filter to optimize spike detection. Cells with well-defined spatial footprints after VolPy processing were retained for subsequent analysis. For visualization in Fig. 2.4, traces were high-pass filtered at 1 Hz for baseline correction and plotted as SNR (spike-peak amplitude divided by baseline standard deviation).

2.4.10. VOLTAGE IMAGING OF HEART DYNAMICS

Embryos at 25, 48, and 102 hpf (separate individuals at each stage) were reared in egg water. Embryos at 25 and 48 hpf were manually dechorionated, and embryos at 25, 48, and 102 hpf were incubated with 100 μ M para-aminoblebbistatin (pAB) (MCE, HY-111474) for 4 h to inhibit heart contractions. During early development, zebrafish can remain healthy even with inhibited heart contraction;⁶⁴ a drop of pAB was added 5 min before recording. Embryos were mounted in 3% low-melting agarose (Sigma-Aldrich, A4018). Single-photon imaging was performed on a Nikon A1RMP microscope with a $25\times/1.1$ NA water-immersion objective (Nikon CFI75 Apo, 25XC W). Illumination was provided by a white LED at $0.6\text{--}1.5$ mW/mm² (SOLA Light Engine, Lumencor) and filtered with a 504/12 excitation filter (Semrock FF01-504/12-25), an FF518-Di01 dichroic (Semrock), and a 532/18 emission filter (Semrock FF01-532/18-25). Images were acquired at 100 fps on a Kinetix sCMOS camera (Teledyne Photometrics) via Micro-Manager, with 2×2 binning for 10 s per recording, on a single z -plane at the recording plane. For traces in Fig. 2.5, photobleaching was corrected with a 1.5 s rolling mean, followed by 30 ms rol-

ling mean smoothing. To verify viability and demonstrate blue-light reversibility of pAB, hearts were illuminated at 10 mW/mm^2 through a Nikon FITC cube (480/30 excitation, 505 dichroic, 535/45 emission) for 10 s at the end of each session to observe resumption of contractions.⁴⁷ Activity extraction used a unified pipeline (NoRMCorre motion correction,⁴⁰ SUPPORT denoising,⁴³ VolPy event detection⁴²). For footprint visualizations, cardiac voltage-time maps were computed as the temporal maximum $\Delta F/F$ within a 200 ms window (see Discussion and the caption of Fig. 2.5 for interpretation).

2.4.11. ANESTHESIA AND EUTHANASIA COMPLIANCE

For zebrafish embryos > 3 dpf, euthanasia was performed by overdose immersion in buffered tricaine (250–500 mg/L, pH 7.0–7.5) with exposure maintained for ≥ 30 min, followed by rapid chilling (2–4 °C) to ensure irreversibility, in accordance with the AVMA Guidelines for the Euthanasia of Animals (2020).⁶⁵

2.5. SUPPLEMENTARY MATERIALS

2.5.1. SUPPLEMENTARY TABLES

2

Table S2.1: Primer sequences used in this study. Sequences are listed 5'–3'. Uppercase denotes engineered sequence (e.g., restriction site/linker/overlap), lowercase denotes the template-annealing region.

Primer name	Target / Notes	Sequence (5'–3')
Ace2N-mNeon-fwd (<i>cmlc2</i>)	Insert (Ace2N-mNeon) for <i>cmlc2</i> construct	gccggccctccaaatcagcagacttaac
Ace2N-mNeon-rev (<i>cmlc2</i>)	Insert (Ace2N-mNeon) for <i>cmlc2</i> construct	atttggagGGCCGGCCCAACTTTTCTATAC
<i>cmlc2</i> -fwd	<i>cmlc2</i> promoter	cagccatCCATGGTGGCGATTCTCC
<i>cmlc2</i> -rev	<i>cmlc2</i> promoter	gcgcgccGTTCAGTGTCTGCTTTGC
Ace2N-mNeon-fwd (<i>unc45b</i>)	Insert (Ace2N-mNeon) for punc503 / <i>unc45b</i> construct	atttggagGGCCGGCCCAACTTTTCTATAC
Ace2N-mNeon-rev (<i>unc45b</i>)	Insert (Ace2N-mNeon) for punc503 / <i>unc45b</i> construct	acgtcagccatGGTCCAGCCTGCTT
<i>unc45b</i> -fwd (punc503)	<i>unc45b</i> 503-bp promoter	aggtgtaaACCCAGCTTTCTTGACAAAAG
<i>unc45b</i> -rev (punc503)	<i>unc45b</i> 503-bp promoter	acgtcagccatGGTCCAGCCTGCTT
Ace2N-mNeon-fwd (<i>acta2</i>)	Insert (Ace2N-mNeon) for <i>acta2</i> construct	gctggaccATGGCTGACGTGGA AAC
Ace2N-mNeon-rev (<i>acta2</i>)	Insert (Ace2N-mNeon) for <i>acta2</i> construct	agctgggtTTACACCTCGTTCTCGTAG
<i>acta2</i> -fwd	<i>acta2</i> promoter	aggtgtaaACCCAGCTTTCTTGACAAAAG
<i>acta2</i> -rev	<i>acta2</i> promoter	cagccatGGTCCAGCCTGCTTTTTTG
Ace2N-mNeon-fwd (<i>elavl3</i>)	Insert (Ace2N-mNeon) for <i>elavl3</i> construct	ctgcagataattaccggtATGGCTGACGTGGA AAC
Ace2N-mNeon-rev (<i>elavl3</i>)	Insert (Ace2N-mNeon) for <i>elavl3</i> construct	ccagatccaccggtTTACACCTCGTTCTCGTAG
<i>elavl3</i> -fwd	<i>elavl3</i> promoter	ACCGGTGGATCCTGGCCG
<i>elavl3</i> -rev	<i>elavl3</i> promoter	ACCGTAATTATCTGCAGGTGG
Ace2N-mNeon-fwd (<i>neuroD</i>)	Insert (Ace2N-mNeon) for <i>neuroD</i> construct	gcgccaccATGGGGACCTGGATGCTG
Ace2N-mNeon-rev (<i>neuroD</i>)	Insert (Ace2N-mNeon) for <i>neuroD</i> construct	agctgggtTTACACCTCGTTCTCGTAG
<i>neuroD</i> -fwd	<i>neuroD</i> promoter	aggtgtaaACCCAGCTTTCTTGACAAAAGTGG
<i>neuroD</i> -rev	<i>neuroD</i> promoter	tcccatGGTGGCGCAGCCTGCTTTTTTG

Table S2.2: Supplementary Table S2. Plasmids are constructed in this study.

Plasmid name	Promoter	Insert	Backbone / system	Notes
pTol2pA2_ubi_Ace2N-mNeon	ubi	Ace2N-mNeon	Tol2pA2	Ubiquitous expression
pTol2pA2_cmlc2_Ace2N-mNeon	cmlc2	Ace2N-mNeon	Tol2pA2	Cardiomyocytes
pTol2pA2_punc503_Ace2N-mNeon	unc45b (503-bp; punc503)	Ace2N-mNeon	Tol2pA2	Skeletal muscle / adaxial
pTol2pA2_acta2_Ace2N-mNeon	acta2	Ace2N-mNeon	Tol2pA2	Smooth muscle / pericytes
pTol2pA2_elavl3_Ace2N-mNeon	elavl3	Ace2N-mNeon	Tol2pA2	Pan-neuronal (postmitotic)
pTol2pA2_neuroD_Ace2N-mNeon	neuroD	Ace2N-mNeon	Tol2pA2	Neuronal subsets

2.5.2. SUPPLEMENTARY FIGURES

2

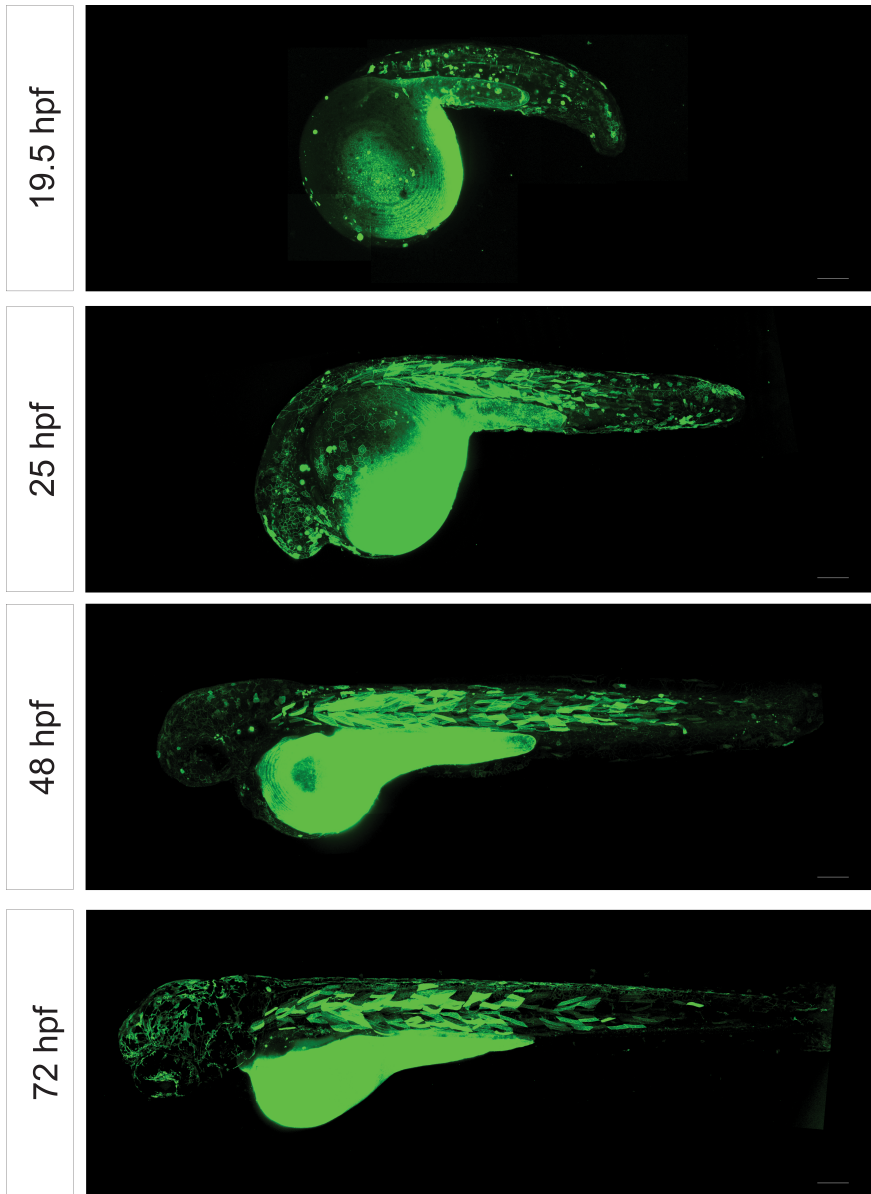


Figure S2.1

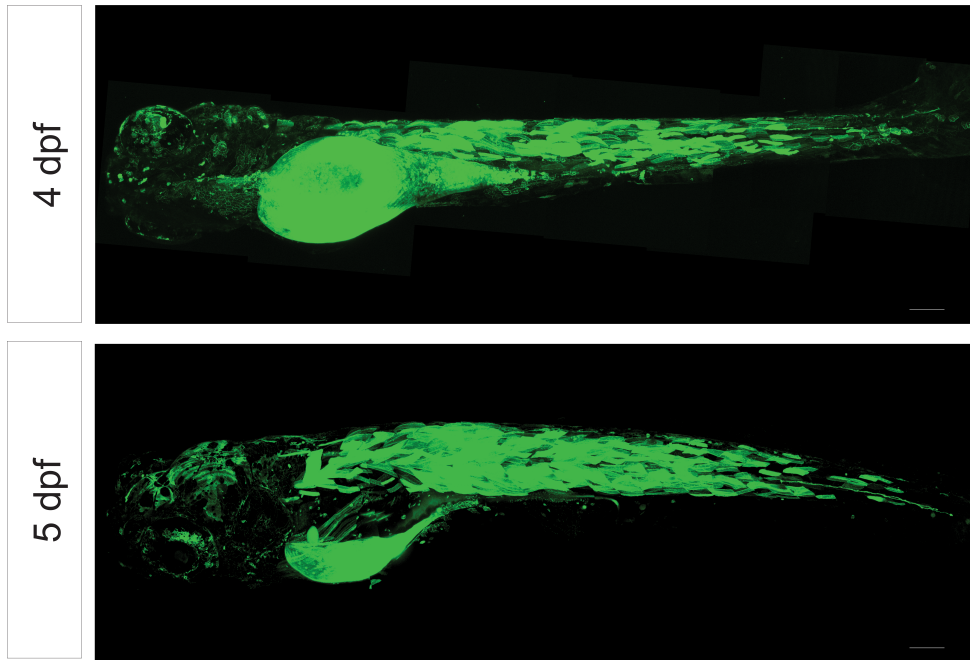


Figure S2.1: **Higher-magnification views of Ace2N-mNeon expression driven by the ubiquitin promoter.** Single z-plane confocal images at the indicated developmental stages illustrate membrane-localized fluorescence across multiple embryonic tissues under the *ubi* promoter. Scale bar = 100 μm . **ubi**: ubiquitin; **hpf**: hours post-fertilization; **dpf**: days post-fertilization.

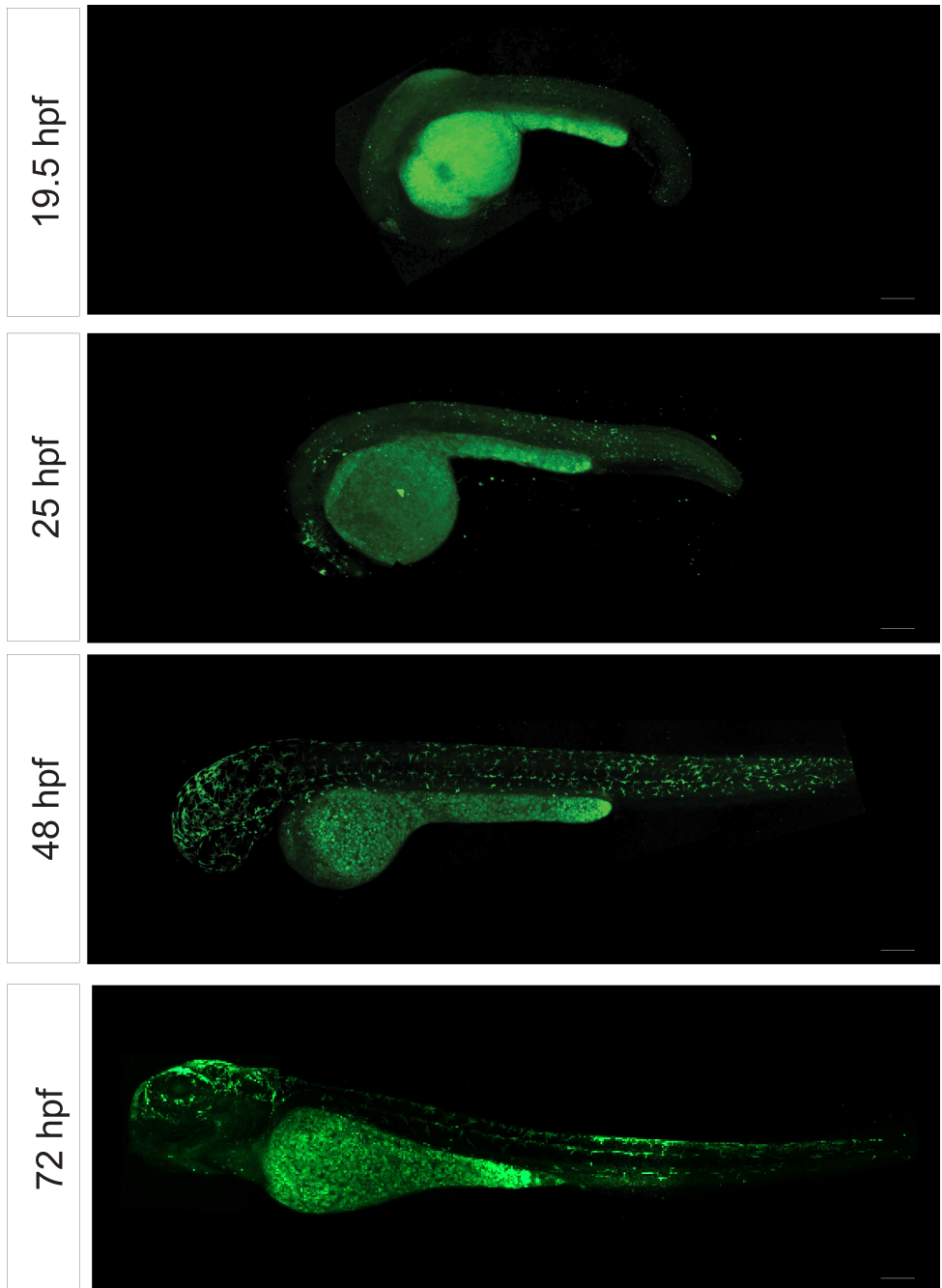


Figure S2.2

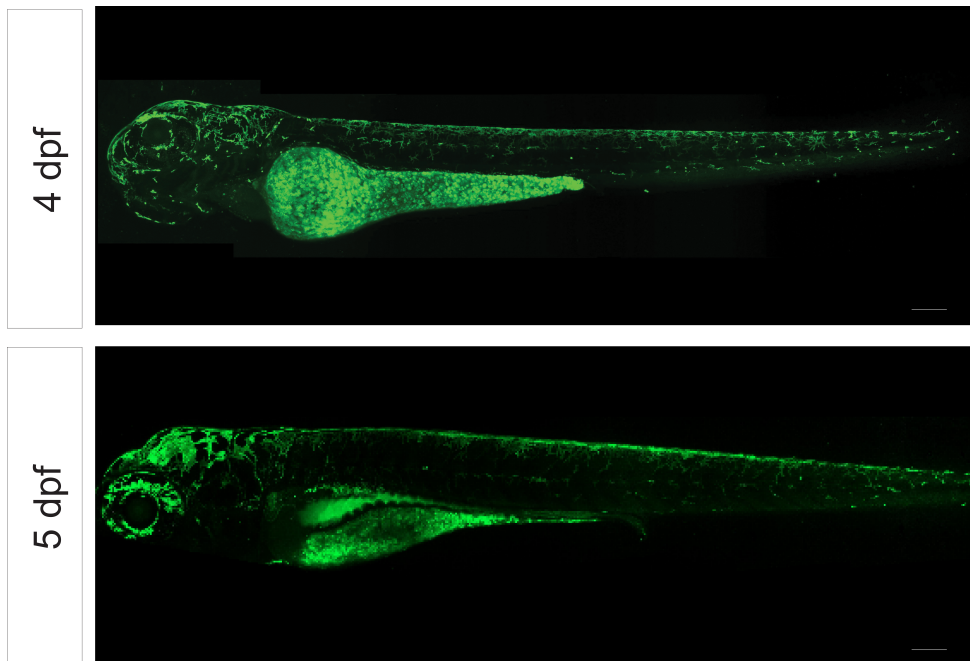


Figure S2.2: **Yolk-sac autofluorescence in uninjected and injected embryos across development.** Representative images showing fluorescence in the yolk sac observed in uninjected controls and in embryos injected with different constructs. This yolk-sac signal was classified as autofluorescence and excluded from Ace2N-mNeon expression scoring. Scale bar = 100 μm . **hpf**: hours post-fertilization; **dpf**: days post-fertilization.

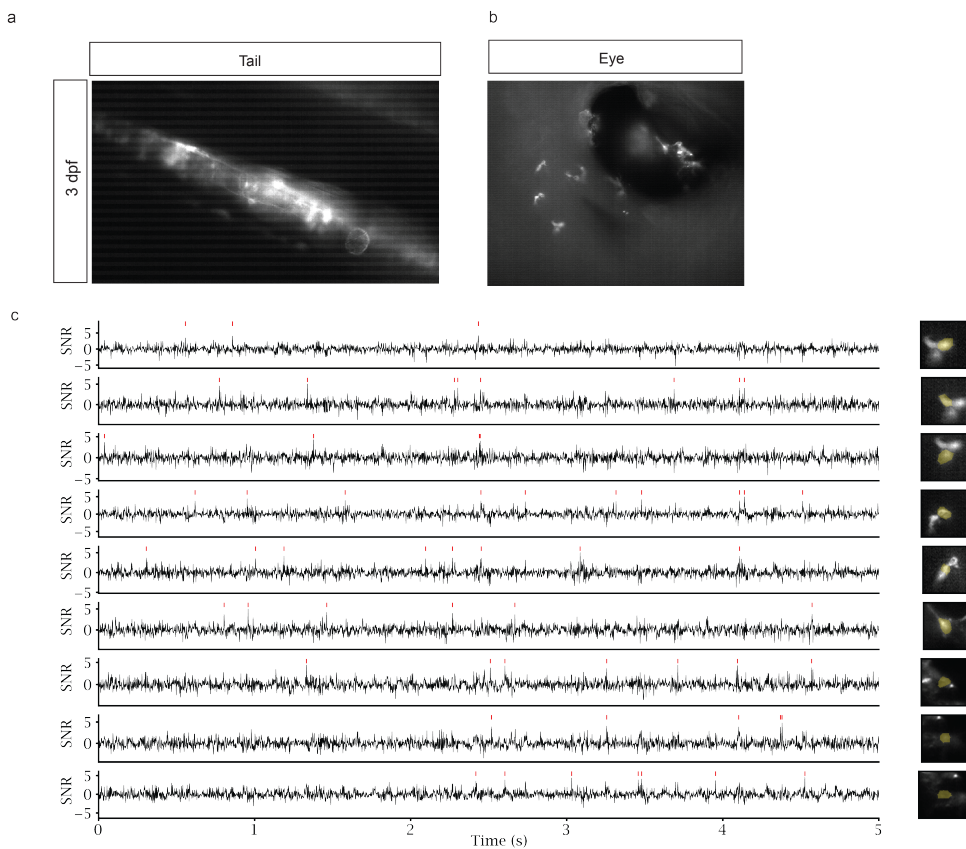


Figure S2.3: Voltage imaging in densely labeled neuronal fields. (a–b) Representative FOVs at 3 dpf. (a) Tail: single-photon image showing high background and dense labeling, which limits suitability for voltage recording. (b) Head: single-photon image near the eye with neurons whose identity could not be confirmed based on morphology alone. (c) Example voltage traces extracted from several ROIs in panel b, red ticks indicate detected spikes. Right panels show the time-averaged image of the recording with manually annotated spatial footprints (shaded orange). Recordings were acquired as single z-planes, processing followed NoRMCorre, SUPPORT, and VolPy as described in Methods. Scale bar = 50 μm . **FOV**: field of view; **ROI**: region of interest; **dpf**: days post-fertilization; **SNR**: signal-to-noise ratio.

2.6. AUTHOR CONTRIBUTION

Conceptualization: Daan Brinks, **ZhenZhen Wu**, Rui Oliveira Silva. **Plasmids preparation:** **ZhenZhen Wu (lead)**, Srividya Ganapathy, Ruya Houssein, Fabiola Marques Trujillo, Jordan Gotti. **Experiment in expression toolkit:** **ZhenZhen Wu (lead)**, Ruya Houssein. **Expression toolkit data analysis Visualization:** **ZhenZhen Wu (lead)**, Ruya Houssein. **Experiments in voltage imaging:** Rui Oliveira Silva (lead), **ZhenZhen Wu**. **Voltage imaging analysis Visualization:** Rui Oliveira Silva (lead), **ZhenZhen Wu**. **Resources:** Daan Brinks (lead), Zhenyu Gao. **Funding, project administration, and supervision:** Daan Brinks. **Writing-original draft preparation:** **ZhenZhen Wu**, Rui Oliveira Silva, Daan Brinks. **Writing-review and editing:** Daan Brinks (lead), **ZhenZhen Wu (lead)**, Rui Oliveira Silva (lead), Ruya Houssein, Fabiola Marques Trujillo, Jordan Gotti, Srividya Ganapathy, Zhenyu Gao. All authors have read and agreed to the published version of the manuscript.

BIBLIOGRAFIE

- [1] Michael Levin. “Molecular bioelectricity in developmental biology: New tools and recent discoveries”. In: *BioEssays* 34 (3 mrt 2012), p. 205–217. ISSN: 02659247. DOI: [10.1002/bies.201100136](https://doi.org/10.1002/bies.201100136). PMID: 22237730.
- [2] Michael Levin. “Molecular bioelectricity: How endogenous voltage potentials control cell behavior and instruct pattern regulation in vivo”. In: *Molecular Biology of the Cell* 25 (24 dec 2014), p. 3835–3850. ISSN: 19394586. DOI: [10.1091/mbc.E13-12-0708](https://doi.org/10.1091/mbc.E13-12-0708). PMID: 25425556.
- [3] Laura Faith George en Emily Anne Bates. “Mechanisms Underlying Influence of Bioelectricity in Development”. In: *Frontiers in Cell and Developmental Biology* 10 (feb 2022). ISSN: 2296-634X. DOI: [10.3389/fcell.2022.772230](https://doi.org/10.3389/fcell.2022.772230).
- [4] Zoe Schofield e.a. “Bioelectrical understanding and engineering of cell biology”. In: *Journal of The Royal Society Interface* 17 (166 mei 2020), p. 20200013. ISSN: 1742-5689. DOI: [10.1098/rsif.2020.0013](https://doi.org/10.1098/rsif.2020.0013).
- [5] Bruce P. Bean. “The action potential in mammalian central neurons”. In: *Nature Reviews Neuroscience* 8 (6 jun 2007), p. 451–465. ISSN: 1471-003X. DOI: [10.1038/nrn2148](https://doi.org/10.1038/nrn2148).
- [6] Michael Levin. “Bioelectric signaling: Reprogrammable circuits underlying embryogenesis, regeneration, and cancer”. In: *Cell* 184 (8 2021), p. 1971–1989.
- [7] Luis F. Santana, Edward P. Cheng en W. Jonathan Lederer. “How does the shape of the cardiac action potential control calcium signaling and contraction in the heart?” In: *Journal of Molecular and Cellular Cardiology* 49 (6 dec 2010), p. 901–903. ISSN: 00222828. DOI: [10.1016/j.yjmcc.2010.09.005](https://doi.org/10.1016/j.yjmcc.2010.09.005).
- [8] Gerard A. Marchal e.a. “Recent advances and current limitations of available technology to optically manipulate and observe cardiac electrophysiology”. In: *Pflügers Archiv - European Journal of Physiology* 475 (11 nov 2023), p. 1357–1366. ISSN: 0031-6768. DOI: [10.1007/s00424-023-02858-0](https://doi.org/10.1007/s00424-023-02858-0).
- [9] Edith Chorev e.a. “Electrophysiological recordings from behaving animals—going beyond spikes”. In: *Current Opinion in Neurobiology* 19 (5 okt 2009), p. 513–519. ISSN: 09594388. DOI: [10.1016/j.conb.2009.08.005](https://doi.org/10.1016/j.conb.2009.08.005).
- [10] Thomas Knöpfel en Chenchen Song. “Optical voltage imaging in neurons: moving from technology development to practical tool”. In: *Nature Reviews Neuroscience* 20 (12 dec 2019), p. 719–727. ISSN: 1471-003X. DOI: [10.1038/s41583-019-0231-4](https://doi.org/10.1038/s41583-019-0231-4).

- [11] Adam E. Cohen en Veena Venkatachalam. “Bringing Bioelectricity to Light”. In: *Annual Review of Biophysics* 43 (1 mei 2014), p. 211–232. ISSN: 1936-122X. DOI: [10.1146/annurev-biophys-051013-022717](https://doi.org/10.1146/annurev-biophys-051013-022717).
- [12] Akash Pal en Lin Tian. “Imaging voltage and brain chemistry with genetically encoded sensors and modulators”. In: *Current Opinion in Chemical Biology* 57 (aug 2020), p. 166–176. ISSN: 13675931. DOI: [10.1016/j.cbpa.2020.07.006](https://doi.org/10.1016/j.cbpa.2020.07.006).
- [13] Yongxian Xu, Peng Zou en Adam E Cohen. “Voltage imaging with genetically encoded indicators”. In: *Current Opinion in Chemical Biology* 39 (aug 2017), p. 1–10. ISSN: 13675931. DOI: [10.1016/j.cbpa.2017.04.005](https://doi.org/10.1016/j.cbpa.2017.04.005).
- [14] Bill Z. Jia e.a. “A bioelectrical phase transition patterns the first vertebrate heartbeats”. In: *Nature* 622 (7981 okt 2023), p. 149–155. ISSN: 0028-0836. DOI: [10.1038/s41586-023-06561-z](https://doi.org/10.1038/s41586-023-06561-z).
- [15] Tae-Young Choi et al. “Zebrafish as an animal model for biomedical research”. In: *Experimental and Molecular Medicine* 53 (3 mrt 2021), p. 310–317. ISSN: 1226-3613. DOI: [10.1038/s12276-021-00571-5](https://doi.org/10.1038/s12276-021-00571-5).
- [16] Jordan T. Shin en Mark C. Fishman. “From Zebrafish to human: modular medical models”. In: *Annual Review of Genomics and Human Genetics* 3 (1 sep 2002), p. 311–340. ISSN: 1527-8204. DOI: [10.1146/annurev.genom.3.031402.131506](https://doi.org/10.1146/annurev.genom.3.031402.131506).
- [17] Asuka Shiraishi e.a. “In vivo long-term voltage imaging by genetically encoded voltage indicator reveals spatiotemporal dynamics of neuronal populations during development”. In: (mei 2023). DOI: [10.1101/2023.05.25.540669](https://doi.org/10.1101/2023.05.25.540669).
- [18] Lilach Avitan e.a. “Spontaneous and evoked activity patterns diverge over development”. In: *eLife* 10 (2021). ISSN: 2050084X. DOI: [10.7554/ELIFE.61942](https://doi.org/10.7554/ELIFE.61942). PMID: [33871351](https://pubmed.ncbi.nlm.nih.gov/33871351/).
- [19] Y. Gong e.a. “High-speed recording of neural spikes in awake mice and flies with a fluorescent voltage sensor”. In: *Science* 350 (6266 dec 2015), p. 1361–1366. ISSN: 0036-8075. DOI: [10.1126/science.aab0810](https://doi.org/10.1126/science.aab0810).
- [20] Koichi Kawakami. *Tol2: A versatile gene transfer vector in vertebrates*. Okt 2007. DOI: [10.1186/gb-2007-8-s1-s7](https://doi.org/10.1186/gb-2007-8-s1-s7). PMID: [18047699](https://pubmed.ncbi.nlm.nih.gov/18047699/).
- [21] Christian Mosimann e.a. “Ubiquitous transgene expression and Cre-based recombination driven by the ubiquitin promoter in zebrafish”. In: *Development* 138 (1 jan 2011), p. 169–177. ISSN: 09501991. DOI: [10.1242/dev.059345](https://doi.org/10.1242/dev.059345). PMID: [21138979](https://pubmed.ncbi.nlm.nih.gov/21138979/).
- [22] Abhinav Sur e.a. “Single-cell analysis of shared signatures and transcriptional diversity during zebrafish development”. In: *Developmental Cell* 58 (24 dec 2023), 3028–3047.e12. ISSN: 15345807. DOI: [10.1016/j.devcel.2023.11.001](https://doi.org/10.1016/j.devcel.2023.11.001).
- [23] Jeffrey A. Farrell e.a. “Single-cell reconstruction of developmental trajectories during zebrafish embryogenesis”. In: *Science* 360 (6392 jun 2018). ISSN: 0036-8075. DOI: [10.1126/science.aar3131](https://doi.org/10.1126/science.aar3131).

- [24] Thibaut Brunet e.a. “The evolutionary origin of bilaterian smooth and striated myocytes”. In: *eLife* 5 (dec 2016). ISSN: 2050-084X. DOI: [10.7554/eLife.19607](https://doi.org/10.7554/eLife.19607).
- [25] Sebastiaan A. Brittijn e.a. “Zebrafish development and regeneration: new tools for biomedical research”. In: *The International Journal of Developmental Biology* 53 (5-6 2009), p. 835–850. ISSN: 0214-6282. DOI: [10.1387/ijdb.082615sb](https://doi.org/10.1387/ijdb.082615sb).
- [26] P Silver, L Buja en J Stull. “Frequency-dependent myosin light chain phosphorylation in isolated myocardium”. In: *Journal of Molecular and Cellular Cardiology* 18 (1 jan 1986), p. 31–37. ISSN: 00222828. DOI: [10.1016/S0022-2828\(86\)80980-4](https://doi.org/10.1016/S0022-2828(86)80980-4).
- [27] Chiu-Ju et al. Huang. “Germ-line transmission of a myocardium-specific GFP transgene reveals critical regulatory elements in the cardiac myosin light chain 2 promoter of zebrafish”. In: *Developmental Dynamics* 228 (1 sep 2003), p. 30–40. ISSN: 1058-8388. DOI: [10.1002/dvdy.10356](https://doi.org/10.1002/dvdy.10356).
- [28] José M et al. Barral. “Role of the Myosin Assembly Protein UNC-45 as a Molecular Chaperone for Myosin”. In: *Science* 295 (5555 jan 2002), p. 669–671. ISSN: 0036-8075. DOI: [10.1126/science.1066648](https://doi.org/10.1126/science.1066648).
- [29] Letitia Etheridge, Philip Diiorio en Charles G. Sagerström. “A zebrafish unc-45-related gene expressed during muscle development”. In: *Developmental Dynamics* 224 (4 aug 2002), p. 457–460. ISSN: 1058-8388. DOI: [10.1002/dvdy.10123](https://doi.org/10.1002/dvdy.10123).
- [30] Thomas R. Whitesell e.a. “An -smooth muscle actin (*acta2/sma*) zebrafish transgenic line marking vascular mural cells and visceral smooth muscle cells”. In: *PLoS ONE* 9 (3 mrt 2014). ISSN: 19326203. DOI: [10.1371/journal.pone.0090590](https://doi.org/10.1371/journal.pone.0090590). PMID: [24594685](https://pubmed.ncbi.nlm.nih.gov/24594685/).
- [31] Cheol-Hee Kim e.a. “Zebrafish *elav/HuC* homologue as a very early neuronal marker”. In: *Neuroscience Letters* 216 (1996), p. 109–112. DOI: [10.1016/0304-3940\(96\)13021-4](https://doi.org/10.1016/0304-3940(96)13021-4).
- [32] Cynthia L. Fuller, Holly K. Yettaw en Christine A. Byrd. “Mitral cells in the olfactory bulb of adult zebrafish (*Danio rerio*): Morphology and distribution”. In: *Journal of Comparative Neurology* 499 (2 nov 2006), p. 218–230. ISSN: 00219967. DOI: [10.1002/cne.21091](https://doi.org/10.1002/cne.21091). PMID: [16977629](https://pubmed.ncbi.nlm.nih.gov/16977629/).
- [33] Alvaro et al. Sagasti. “Repulsive interactions shape the morphologies and functional arrangement of zebrafish peripheral sensory arbors”. In: *Current Biology* 15 (9 mei 2005), p. 804–814. ISSN: 09609822. DOI: [10.1016/j.cub.2005.03.048](https://doi.org/10.1016/j.cub.2005.03.048). PMID: [15886097](https://pubmed.ncbi.nlm.nih.gov/15886097/).
- [34] Masaharu Takahashi, Madoka Narushima en Yoichi Oda. “In Vivo Imaging of Functional Inhibitory Networks on the Mauthner Cell of Larval Zebrafish”. In: *The Journal of Neuroscience* 22 (10 mei 2002), p. 3929–3938. ISSN: 0270-6474. DOI: [10.1523/JNEUROSCI.22-10-03929.2002](https://doi.org/10.1523/JNEUROSCI.22-10-03929.2002).

- [35] José L. Juárez-Morales e.a. “Zebrafish transgenic constructs label specific neurons in *Xenopus laevis* spinal cord and identify frog V0v spinal neurons”. In: *Developmental Neurobiology* 77.8 (2017), p. 1007–1020. ISSN: 1932-846X. DOI: [10.1002/dneu.22490](https://doi.org/10.1002/dneu.22490). PMID: 28188691.
- [36] James M. Harris, Andy Yu-Der Wang en Paola Arlotta. “Optogenetic axon guidance in embryonic zebrafish”. In: *STAR Protocols* 2 (4 dec 2021). ISSN: 26661667. DOI: [10.1016/j.xpro.2021.100947](https://doi.org/10.1016/j.xpro.2021.100947). PMID: 34841275.
- [37] Thomas Mueller en Mario F. Wullimann. *Expression domains of neuroD (nrd) in the early postembryonic zebrafish brain*. 2002. DOI: [10.1016/S0361-9230\(01\)00694-3](https://doi.org/10.1016/S0361-9230(01)00694-3).
- [38] Sataree et al. Khuansuwan. “A novel transgenic zebrafish line allows for in vivo quantification of autophagic activity in neurons”. In: *Autophagy* 15 (8 aug 2019), p. 1322–1332. ISSN: 1554-8627. DOI: [10.1080/15548627.2019.1580511](https://doi.org/10.1080/15548627.2019.1580511).
- [39] Akira et al. Sato. “Neuronal Subtypes Are Specified by the Level of neurod Expression in the Zebrafish Lateral Line”. In: *The Journal of Neuroscience* 33 (2 jan 2013), p. 556–562. ISSN: 0270-6474. DOI: [10.1523/JNEUROSCI.4568-12.2013](https://doi.org/10.1523/JNEUROSCI.4568-12.2013).
- [40] Eftychios A. Pnevmatikakis en Andrea Giovannucci. “NoRMCorre: An online algorithm for piecewise rigid motion correction of calcium imaging data”. In: *Journal of Neuroscience Methods* 291 (nov 2017), p. 83–94. ISSN: 1872678X. DOI: [10.1016/j.jneumeth.2017.07.031](https://doi.org/10.1016/j.jneumeth.2017.07.031). PMID: 28782629.
- [41] Andrea Giovannucci e.a. “CaImAn: an open source tool for scalable calcium imaging data analysis”. In: *eLife* 8 (2019), e38173. DOI: [10.7554/eLife.38173](https://doi.org/10.7554/eLife.38173).
- [42] Changjia Cai e.a. “VolPy: Automated and scalable analysis pipelines for voltage imaging datasets”. In: *PLoS Computational Biology* 17 (4 apr 2021). ISSN: 15537358. DOI: [10.1371/journal.pcbi.1008806](https://doi.org/10.1371/journal.pcbi.1008806). PMID: 33852574.
- [43] Minhho Eom e.a. “Statistically unbiased prediction enables accurate denoising of voltage imaging data”. In: *Nature Methods* 20 (10 okt 2023), p. 1581–1592. ISSN: 15487105. DOI: [10.1038/s41592-023-02005-8](https://doi.org/10.1038/s41592-023-02005-8). PMID: 37723246.
- [44] Jonathan Boulanger-Weill en Germán Sumbre. “Functional Integration of Newborn Neurons in the Zebrafish Optic Tectum”. In: *Frontiers in Cell and Developmental Biology* 7 (apr 2019). ISSN: 2296-634X. DOI: [10.3389/fcell.2019.00057](https://doi.org/10.3389/fcell.2019.00057).
- [45] Prisca Chapouton en Laure Bally-Cuif. “Neurogenesis”. In: *deel* 76. 2004, p. 163–206. DOI: [10.1016/S0091-679X\(04\)76010-0](https://doi.org/10.1016/S0091-679X(04)76010-0).
- [46] M. F. Wullimann. “Secondary neurogenesis and telencephalic organization in zebrafish and mice: a brief review”. In: *Integrative Zoology* 4 (1 mrt 2009), p. 123–133. ISSN: 1749-4877. DOI: [10.1111/j.1749-4877.2008.00140.x](https://doi.org/10.1111/j.1749-4877.2008.00140.x).

- [47] Boglárka H. Várkuti e.a. “A highly soluble, non-phototoxic, non-fluorescent blebbistatin derivative”. In: *Scientific Reports* 6 (mei 2016). ISSN: 20452322. DOI: [10.1038/srep26141](https://doi.org/10.1038/srep26141). PMID: 27241904.
- [48] Neil C. Chi e.a. “Genetic and physiologic dissection of the vertebrate cardiac conduction system”. In: *PLoS Biology* 6 (5 mei 2008), p. 1006–1019. ISSN: 15449173. DOI: [10.1371/journal.pbio.0060109](https://doi.org/10.1371/journal.pbio.0060109). PMID: 18479184.
- [49] N. et al Petros. “Adult zebrafish heart as a model for human heart? An electrophysiological study”. In: *Journal of Molecular and Cellular Cardiology* 48 (1 jan 2010), p. 161–171. ISSN: 00222828. DOI: [10.1016/j.yjmcc.2009.08.034](https://doi.org/10.1016/j.yjmcc.2009.08.034).
- [50] Martin R. Silic en GuangJun Zhang. “Bioelectricity in Developmental Patterning and Size Control: Evidence and Genetically Encoded Tools in the Zebrafish Model”. In: *Cells* 12 (8 apr 2023), p. 1148. ISSN: 2073-4409. DOI: [10.3390/cells12081148](https://doi.org/10.3390/cells12081148).
- [51] Rebecca Schmidt, Uwe Strähle en Steffen Scholpp. “Neurogenesis in zebrafish, from embryo to adult”. In: *Neural Development* 8 (21 feb 2013), p. 3. DOI: [10.1186/1749-8104-8-3](https://doi.org/10.1186/1749-8104-8-3).
- [52] Erica Warp e.a. “Emergence of patterned activity in the developing zebrafish spinal cord”. In: *Current Biology* 22 (2 jan 2012), p. 93–102. ISSN: 09609822. DOI: [10.1016/j.cub.2011.12.002](https://doi.org/10.1016/j.cub.2011.12.002). PMID: 22197243.
- [53] Martin R. Silic e.a. “Zebrafish Embryos Display Characteristic Bioelectric Signals during Early Development”. In: *Cells* 11 (22 nov 2022), p. 3586. ISSN: 2073-4409. DOI: [10.3390/cells11223586](https://doi.org/10.3390/cells11223586).
- [54] Fiorency Santoso e.a. “An Overview of Methods for Cardiac Rhythm Detection in Zebrafish”. In: *Biomedicines* 8 (9 sep 2020), p. 329. ISSN: 2227-9059. DOI: [10.3390/biomedicines8090329](https://doi.org/10.3390/biomedicines8090329).
- [55] Elisa De Luca e.a. “ZebraBeat: a flexible platform for the analysis of the cardiac rate in zebrafish embryos”. In: *Scientific Reports* 4 (1 mei 2014), p. 4898. ISSN: 2045-2322. DOI: [10.1038/srep04898](https://doi.org/10.1038/srep04898).
- [56] M. B. Rook e.a. “Biology of cardiac sodium channel Nav1.5 expression”. In: *Cardiovascular Research* 93 (1 jan 2012), p. 12–23. ISSN: 0008-6363. DOI: [10.1093/cvr/cvr252](https://doi.org/10.1093/cvr/cvr252).
- [57] V. Biasci e.a. “Optogenetic manipulation of cardiac electrical dynamics using sub-threshold illumination: dissecting the role of cardiac alternans in terminating rapid rhythms”. In: *Basic Research in Cardiology* 117 (1 dec 2022), p. 25. ISSN: 0300-8428. DOI: [10.1007/s00395-022-00933-8](https://doi.org/10.1007/s00395-022-00933-8).
- [58] Michael Levin. “Bioelectrical approaches to cancer as a problem of the scaling of the cellular self”. In: *Progress in Biophysics and Molecular Biology* 165 (okt 2021), p. 102–113. ISSN: 00796107. DOI: [10.1016/j.pbiomolbio.2021.04.007](https://doi.org/10.1016/j.pbiomolbio.2021.04.007).

- [59] Daan Brinks, Aaron J. Klein en Adam E. Cohen. “Two-Photon Lifetime Imaging of Voltage Indicating Proteins as a Probe of Absolute Membrane Voltage”. In: *Biophysical Journal* 109 (5 sep 2015), p. 914–921. ISSN: 15420086. DOI: [10.1016/j.bpj.2015.07.038](https://doi.org/10.1016/j.bpj.2015.07.038). PMID: 26331249.
- [60] Julia R Lazzari-Dean, Anneliese MM Gest en Evan W Miller. “Optical estimation of absolute membrane potential using fluorescence lifetime imaging”. In: *eLife* 8 (sep 2019). ISSN: 2050-084X. DOI: [10.7554/eLife.44522](https://doi.org/10.7554/eLife.44522).
- [61] Julia R. Lazzari-Dean, Anneliese M.M. Gest en Evan W. Miller. “Measuring Absolute Membrane Potential Across Space and Time”. In: *Annual Review of Biophysics* 50 (1 mei 2021), p. 447–468. ISSN: 1936-122X. DOI: [10.1146/annurev-biophys-062920-063555](https://doi.org/10.1146/annurev-biophys-062920-063555).
- [62] Philipp Rühl e.a. “An Ultrasensitive Genetically Encoded Voltage Indicator Uncovers the Electrical Activity of Non-Excitable Cells”. In: *Advanced Science* 11 (20 mei 2024). ISSN: 2198-3844. DOI: [10.1002/advs.202307938](https://doi.org/10.1002/advs.202307938).
- [63] Richard Mark White e.a. “Transparent Adult Zebrafish as a Tool for In Vivo Transplantation Analysis”. In: *Cell Stem Cell* 2 (2 feb 2008), p. 183–189. ISSN: 19345909. DOI: [10.1016/j.stem.2007.11.002](https://doi.org/10.1016/j.stem.2007.11.002). PMID: 18371439.
- [64] J. Bakkers. “Zebrafish as a model to study cardiac development and human cardiac disease”. In: *Cardiovascular Research* 91 (2 jul 2011), p. 279–288. ISSN: 0008-6363. DOI: [10.1093/cvr/cvr098](https://doi.org/10.1093/cvr/cvr098).
- [65] Steven L. Leary. *AVMA guidelines for the euthanasia of animals : 2020 edition*. American Veterinary Medical Association, 2020, p. 121. ISBN: 9781882691098.

3

ABSOLUTELY CALIBRATED LIFETIME-IMAGING VOLTAGE SENSING IN DEVELOPING ZEBRAFISH EMBRYOS

This chapter establishes a calibrated fluorescence lifetime imaging framework that uses the eFRET-based GEVI Ace2N-mNeon to report approximate, physiologically anchored membrane potentials in live zebrafish embryos at single cell resolution. We combine TTTR-based FLIM acquisition in embryos, a patch clamp derived lifetime-voltage relation in cultured cells, and a standardized cell-based analysis pipeline that includes membrane-targeted segmentation, photon pooling, multi-component lifetime fitting, and stringent quality control to extract reliable lifetime values for individual cells in intact tissues and place them on a shared voltage scale that does not depend on fluorescence intensity. Using this framework, we map how resting potentials are distributed across major cell types and how they evolve from 1 to 4 days post fertilization, showing that fluorescence lifetimes follow the expected hierarchy of resting potential among epithelial cells, neurons, skeletal muscle cells, and cardiomyocytes and that these patterns are reproducible across embryos at both single cell and per fish levels. Together, these results provide a practical in vivo platform for quantitatively tracking developmental bioelectric patterns across tissues and developmental stages using calibrated lifetime-based voltage imaging that is robust to optical inhomogeneity and sensitive to relative and approximate absolute differences in membrane potential on the order of tens of millivolts.

This chapter is based on: Z. Wu, A. João Falcão Neves, M. Post, R. Liu, T. Luciani, T. Höppener, X. Meng, D. Brinks, *Absolutely calibrated lifetime-imaging voltage sensing in developing zebrafish embryos*. In preparation.

3.1. INTRODUCTION

EMBRYOGENESIS is a highly complex process in which numerous cells coordinate precisely to form specific tissues and organs. Growing evidence indicates that bioelectricity, defined as membrane voltage (V_m) generated by ion fluxes across cell membranes, plays a crucial role in this process.¹⁻³ Unlike the rapid, millisecond-scale action potentials in excitable neurons and cardiomyocytes,⁴ developmental bioelectricity is dominated by resting membrane potentials that change gradually over minutes to days across many cell types.^{1,2} Emerging as early as the two-cell stage in vertebrates, these relatively stable bioelectric signals regulate diverse processes such as cell proliferation,⁵ differentiation,⁶ polarization,⁷ and apoptosis.³ Moreover, by integrating with other physiological signals, developmental bioelectricity helps establish morphological features and anatomical identity^{1,8-10} and drives critical developmental events, such as neural tube closure⁵ and limb regeneration.¹¹

Although bioelectric signals in non-excitable cells are closely linked to growth and development, their regulatory mechanisms at the cellular and tissue levels remain unclear.^{1-3,9} Current research primarily relies on manipulating bioelectric activity, for example by modulating ion channel function and inducing morphological changes.^{1,12,13} However, these perturbative approaches often introduce off-target effects and compensatory responses, leading to context-dependent and sometimes unpredictable outcomes.^{1,12,13} Therefore, a quantitative, minimally perturbative approach that can map long-term V_m dynamics at single-cell resolution in intact embryos and place these dynamics on a shared voltage scale is essential to clarify how bioelectricity shapes cell behavior and development.

In vivo, quantitative measurements of V_m dynamics are particularly challenging, especially for capturing subtle changes in resting potentials. Traditional electrophysiological techniques provide high temporal resolution but are invasive and low throughput, limiting their suitability for long-term in vivo studies and for repeated measurements in the same preparations.¹⁴ Voltage imaging with genetically encoded voltage indicators (GEVIs) enables non-invasive, real-time monitoring^{15,16} and has been widely used to track rapid action potentials in neurons^{17,18} and cardiomyocytes.¹⁹⁻²¹ However, fluorescence intensity-based readouts are influenced by factors such as fluorophore concentration, intracellular transport, optical path variations, and detection efficiency.^{22,23} These factors lead to large baseline signal variations over minutes to hours, so calibrations made on one cell at a given time cannot be reliably extended to other cells or even to the same cell later, which precludes straightforward measurement of absolute V_m . Although alternative optical methods, including ratio-based and pump-probe approaches, have been explored to address these limitations, challenges such as optical interference and weak signals reduce their reliability.²⁰ Consequently, a method to spatially map quantitative V_m in biological systems over extended periods is still lacking.

Recent advances in fluorescence lifetime imaging (FLIM) present a promising approach for quantitative V_m readout in biological systems.^{15,20,22-25} Unlike intensity-based voltage imaging, FLIM measures a fluorophore's fluorescence lifetime (τ_{fl}), the time a probe remains in its excited state before emitting a photon, which is largely independent of excitation intensity and overall probe concentration, making it more robust to common imaging artifacts than intensity-based readout.^{26,27} As a result, τ_{fl} behaves as a

cell-independent physical quantity that can be compared directly across cells, fields of view, and animals, providing a natural common scale for pooling measurements from different experiments. Once a lifetime–voltage relation has been calibrated, this shared lifetime scale can be used as a quantitative voltage ruler, so that differences in τ_{fl} are translated into membrane potential differences with a defined magnitude rather than remaining as unscaled relative optical changes.

Previous studies have validated the microbial rhodopsin-based GEVI CAESR, demonstrating that its voltage-sensitive absorption shifts exhibit an approximately linear relationship with τ_{fl} , thus enabling calibration of τ_{fl} to absolute V_m in cultured cells.^{22,24} These proof-of-principle experiments establish that lifetime-based GEVIs can be used to derive absolute estimates of V_m under well-controlled conditions, and suggest that similar strategies might be extended to more complex biological preparations. However, despite this potential, the complexity of live tissues, characterized by light scattering, heterogeneity, and autofluorescence, together with the need for advanced instrumentation, precise calibration, and sophisticated data analysis for high-resolution FLIM, makes long-term in vivo validation extremely challenging.²²

To address the technical challenges of long-term in vivo V_m measurement in dynamic embryonic environments, we established a time-correlated single-photon counting (TCSPC)-based FLIM system and analysis framework optimized for tracking calibrated scales of V_m during zebrafish embryogenesis. Zebrafish were selected as the animal model due to their external development, high reproductive capacity, and transparent embryos, which make them ideally suited for optical imaging studies and for following defined cell populations throughout early patterning and organogenesis.^{28,29} Although previous work using CAESR has demonstrated the feasibility of using FLIM for absolute V_m quantification in cultured cells,²⁴ CAESR's limited precision, with variability of approximately 20 mV, and insufficient brightness render it unsuitable for long-term in vivo recordings.^{24,25} In contrast, we chose the Förster resonance energy transfer (FRET)-based GEVI Ace2N-mNeon for its higher sensitivity and brightness for long-term in vivo imaging and its robust τ_{fl} readout.³⁰ Ace2N-mNeon exhibits voltage-dependent responses with distinct instantaneous and steady-state optical components, and its optical behavior in cultured cells suggests that the lifetime readout remains well behaved over the subthreshold range most relevant for resting membrane potentials.³⁰

Our previous work established a zebrafish expression library for Ace2N-mNeon and characterized its spatiotemporal expression at the cellular level, providing a platform to interrogate bioelectric signals in neurons, cardiomyocytes, epithelial cells, and skeletal muscle within the same embryo.³¹ As a FRET-based GEVI, Ace2N-mNeon relies on voltage-dependent modulation of energy transfer between the mNeonGreen donor and an Ace2-derived *microbial rhodopsin* domain, which belongs to the same broad class of *microbial rhodopsin* as Arch, and this coupling leads to corresponding changes in τ_d .^{20,24,30,32} Because Ace2N-mNeon and CAESR are both *microbial rhodopsin*-based GEVIs that couple voltage-dependent changes in rhodopsin absorption to a fluorescent protein reporter, we anticipated that Ace2N-mNeon would exhibit a monotonic and approximately linear dependence of τ_d on V_m in HEK293T cells over the voltage range relevant for resting membrane potentials, allowing us to use a patch clamp derived τ_d – V_m slope as an external calibration to interpret in vivo lifetime differences on a shared voltage

scale, while accepting small deviations from strict linearity at the extremes of the tested range.^{20,30}

Beyond sensor choice, the analysis framework is equally important for *in vivo* FLIM. Many conventional TCSPC-FLIM analysis tools rely on pixel-wise lifetime fitting and visualization.^{27,32,33} While this approach works well for samples with high signal-to-noise ratios (SNR) or in controlled optical environments, it poses difficulties in developing embryos, where GEVI labeling is often sparse, expression levels vary across cells, and tissues are highly heterogeneous. Although many pixel-based analysis methods offer region-of-interest (ROI)-based analysis, they often struggle to effectively distinguish membrane-localized GEVI signals from cytoplasmic fluorescence, out-of-focus structures, and tissue autofluorescence. As a result, cytoplasmic and other non-membrane regions may inadvertently be included in the lifetime calculations and visualizations, which dilutes true V_m differences between cell types and reduces our ability to resolve biologically meaningful patterns. Standard noise filtering techniques, such as intensity-based thresholding and unconstrained multi-exponential fitting, can further remove weak but informative signals in samples where membrane fluorescence is low or unevenly distributed, as is often the case in early zebrafish embryos expressing GEVIs. Furthermore, most FLIM studies to date have been limited to two-dimensional (2D) lifetime visualization. Although 2D FLIM is widely used, it has notable limitations when investigating complex tissues or multilayer structures. Specifically, 2D FLIM captures only a single optical section, which is insufficient for accurately reflecting the electrophysiological dynamics in three-dimensional tissues, so critical information regarding cross-layer electrical signal propagation can be lost. In thick tissues, such as the brain and myocardium, 2D FLIM is further constrained by focal plane limitations, scattering, and light absorption effects, which hinder the resolution of deep tissue signals. Because bioelectric signals, including V_m changes, often propagate through three-dimensional (3D) structures, there is a clear need for analysis strategies that can reconstruct and interpret *in vivo* lifetime patterns in 3D.

To overcome these limitations, we developed a cell-based analysis pipeline tailored for living organisms. Our approach applies strict segmentation criteria to accurately define membrane regions, thereby reducing interference from non-membrane signals, and sums photons from all membrane pixels of each cell into a single decay curve for fitting, which stabilizes τ_{fl} estimates under low-photon conditions without discarding biologically significant signals. This is followed by a multistep filtering process that eliminates noise and background components, ensuring that the voltage-sensitive signal is retained, and lifetime values are then summarized by cell type to link the optical measurements directly to defined biological populations. In addition to these computational steps, our method enhances interpretability by selectively visualizing membrane-localized lifetime values at the cell level in both two and three dimensions, providing intuitive comparisons within and across tissues and facilitating effective communication of bioelectric patterns *in vivo*.

Collectively, our study establishes a FLIM-based framework that enables quantitative, long-term recordings of calibrated membrane-potential scales in living embryos. We first measured the $\tau_{fl} - V_m$ relation of Ace2N-mNeon in HEK293T cells, consistent with previous characterizations of this sensor, providing a robust slope for converting lifetime changes into calibrated voltage differences with an effective precision on the order of

several tens of millivolts.³⁰ By comparing the τ_{fl} of cell types with well characterized resting potential ranges in zebrafish embryos at a given stage, and using the cell-derived slope together with these physiological anchors, we show that our method can resolve cell type specific resting membrane potentials *in vivo* and yields calibrated effective V_m values that fall within expected ranges, so that the framework is best suited for quantifying calibrated differences in V_m across cell types, embryos, and developmental stages rather than exact millivolt readouts for individual cells.

Moreover, by tracking τ_{fl} dynamics in both excitable and non-excitable cells throughout early zebrafish development, we map distinct bioelectrical trends in different cell types. We find that the V_m of neurons and cardiomyocytes gradually depolarizes as their excitability increases,²⁸ consistent with a role for resting-potential depolarization in promoting the emergence of spontaneous and evoked activity, whereas skeletal muscle cells exhibit an initial hyperpolarization followed by partial depolarization, in line with previous observations that transient hyperpolarization is an important step in muscle maturation. Together, these results provide direct *in vivo* evidence that precisely regulated V_m dynamics accompany the functional maturation of diverse cell types during embryogenesis and establish a foundation for using calibrated voltage imaging to investigate how bioelectric signals contribute to development, circuit assembly, and disease.

3.2. RESULTS

3.2.1. A CALIBRATED FLIM FRAMEWORK AND CELL-BASED ANALYSIS PIPELINE FOR DEVELOPMENTAL VOLTAGE IMAGING

Building on the Ace2N-mNeon expression library described in [Chapter 2](#), we next asked whether Ace2N-mNeon fluorescence lifetime can be used to follow membrane potential in defined cell types during zebrafish embryogenesis.³¹ Using the same Ace2N-mNeon construct in HEK293T cells and in zebrafish embryos on a single TCSPC-based FLIM setup, we first established an experimental relation between Ace2N-mNeon τ_{fl} and V_m in HEK293T cells by combining TCSPC with whole-cell voltage clamp, and then used this relation as an external calibration for lifetime measurements *in vivo* to place zebrafish τ_{fl} values on a shared, calibrated membrane-potential scale (Fig. 3.1a). In this way, lifetime differences observed between cell types and across developmental stages in zebrafish can be interpreted in voltage units for the same sensor under defined conditions, rather than relying solely on qualitative intensity changes or uncalibrated lifetime differences. This calibrated framework is best suited for quantifying membrane-potential differences across cell types, embryos, and developmental stages and provides the basis for the long-term, cell-type-resolved voltage imaging experiments described in the remainder of this chapter.

To make Ace2N-mNeon lifetime measurements interpretable in the context of developing embryos, we replaced conventional pixel-based FLIM analysis with a membrane-focused, cell-based pipeline tailored to *in vivo* imaging (Fig. 3.1b). In sparsely labeled, heterogeneous tissues, pixel-wise lifetime fitting is sensitive to low photon counts and to contamination from cytoplasmic fluorescence, out-of-focus structures, and tissue autofluorescence.

luorescence, which dilute the membrane-localized GEVI signal. In our analysis pipeline, cell membranes are first segmented into defined membrane masks. Photons from all membrane pixels belonging to a given cell are summed into a single decay histogram and fitted as one decay, followed by multiple quality-control steps, yielding one τ_{fl} value per cell that is directly assigned to a defined biological cell type. This strategy reduces the influence of low photon counts, minimizes contributions from non-membrane regions, and expresses the data at the level at which biological questions are posed, namely individual cells and cell types, while keeping all lifetime values on the same calibrated voltage scale.

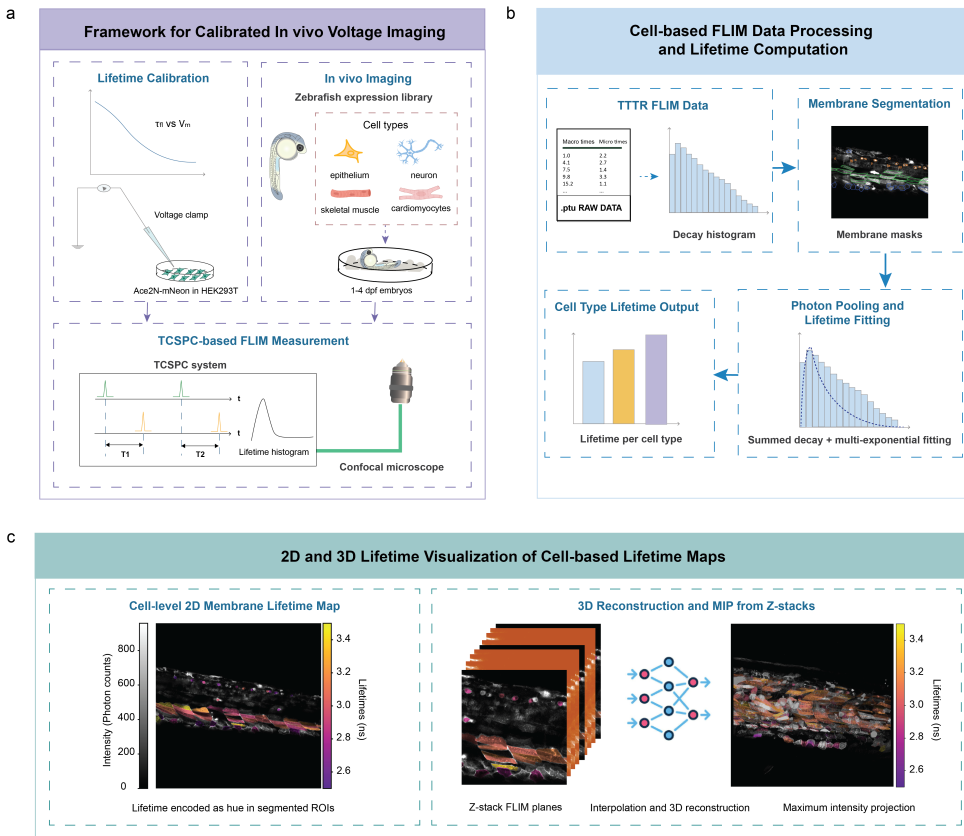
The resulting lifetimes are visualized as membrane-based pseudocolor maps in two-dimensional planes and as three-dimensional reconstructions from z -stacks (Fig. 3.1c), revealing tissue-scale bioelectric patterns while preserving single-cell resolution. A more detailed schematic of the acquisition and analysis pipeline, including TTTR data handling, membrane segmentation, and multi-component lifetime fitting, is provided in Supplementary Fig. S3.1 and Supplementary Methods Section 3.5.2. Throughout the following Results sections, this calibrated, cell-based representation of τ_{fl} serves as the common readout for quantifying resting-potential differences between cell types and for following their developmental trajectories in vivo.

3.2.2. VOLTAGE DEPENDENCE OF Ace2N-mNEON FLUORESCENCE LIFETIME IN HEK293T CELLS

Previous work on CAESR showed that the lifetime–voltage relation in HEK cells is monotonic and approximately linear over a 200 mV range, with only small deviations from linearity at the most hyperpolarized and depolarized potentials.^{24,30} In contrast, for Ace2N-mNeon, the intensity–voltage relation in neurons displays a more pronounced nonlinear profile with distinct peak and steady-state components.³⁰ On this basis, we next characterized the relation between Ace2N-mNeon τ_{fl} and V_m in HEK293T cells to obtain an experimental calibration for the same sensor used in vivo.

HEK293T cells were transiently transfected with Ace2N-mNeon, and cells with clear membrane-localized fluorescence were selected for simultaneous whole-cell patch clamp and TCSPC-based FLIM recordings (Fig. 3.2a). A step-voltage protocol from -100 mV to $+100$ mV in 50 mV increments (total range 200 mV) was applied while τ_{fl} was measured continuously (Fig. 3.2b). For each cell, τ_{fl} was averaged over the steady portion of every voltage step and plotted as a function of V_m . In individual cells, τ_{fl} decreased monotonically and was well described by an approximately linear function of V_m over the tested range, with only mild deviations from strict linearity at the most depolarized voltages, as illustrated by the representative cell in Fig. 3.2c.

To obtain a combined calibration, we recorded five cells over the same voltage range and averaged τ_{fl} across cells at each holding potential. These mean τ_{fl} values with their standard errors are shown in Fig. 3.2d. A linear regression fitted to all individual cell measurements yielded a slope of approximately -6.1×10^{-4} ns per mV, corresponding to a τ_{fl} change of about 0.06 ns over 100 mV. The root-mean-square deviation of the data from this linear fit was approximately 0.025 ns, corresponding to a voltage-equivalent noise of about 40 mV under our recording conditions. The pooled τ_{fl} – V_m relation shows a



slight curvature at the extremes of the tested voltage range, with a modest reduction in apparent sensitivity at the most depolarized steps. This shallow nonlinearity is consistent with the steady-state intensity–voltage behavior of Ace2N-mNeon reported by Gong *et al.* in neurons and is therefore expected rather than a calibration artifact.³⁰

In summary, these calibration experiments demonstrate that Ace2N-mNeon exhibits a monotonic and well-defined $\tau_{fl}-V_m$ dependence in HEK293T cells that can be approximated by a linear relation over the subthreshold range spanning the resting potentials of the zebrafish cell types studied here. Therefore, we used the linear fit as a first-order description of the $\tau_{fl}-V_m$ relation, providing a calibrated voltage scale with an effective precision of several tens of millivolts for individual lifetime measurements, while recognizing that mild deviations from strict linearity at the extremes are an intrinsic and previously documented feature of Ace2N-mNeon.³⁰ In the following sections, we use this experimentally determined $\tau_{fl}-V_m$ relation as an external scaling factor to interpret lifetime differences measured in zebrafish embryos in terms of underlying membrane-potential differences, with the calibration best suited for quantifying voltage differences across cell types, embryos, and developmental stages rather than for reporting exact voltages of individual cells.

3.2.3. QUANTITATIVE FLUORESCENCE LIFETIME ANALYSIS REVEALS RESTING MEMBRANE POTENTIAL DIFFERENCES ACROSS CELL TYPES IN ZEBRAFISH EMBRYOS

Based on our calibration data (Fig. 3.2), we next asked whether Ace2N-mNeon could resolve the expected hierarchy of resting potentials across different cell types in early zebrafish embryos. Resting potentials differ systematically between cell classes that fulfill distinct physiological roles, with skeletal muscle cells typically more hyperpolarized than neurons, and epithelial cells reported to be the most depolarized in many developing tissues.^{2,34–36} Therefore, we focused on epithelial cells, neurons, and skeletal muscle cells at 2 dpf, which can be readily distinguished within the same embryo and field of view (FOV), and used their τ_{fl} values to test whether our calibrated FLIM approach can separate cell types with known differences in resting potential. Table 3.1 summarizes literature-based resting-potential ranges that we use as physiological anchors in our interpretation.

Table 3.1: Literature-based resting membrane potential ranges used as physiological anchors for interpreting calibrated τ_{fl} differences across cell types at 2 dpf.

Cell type	Resting potential range
Skeletal muscle cells	–80 to –90 mV
Neurons	–60 to –70 mV
Epithelial cells	–30 to –50 mV

To achieve ubiquitous expression of Ace2N-mNeon, we used the ubiquitin (*ubi*) promoter and co-injected the plasmid with Tol2 transposase mRNA at the one-cell stage.³⁷ At 2 dpf, these cell types were easily distinguished by their morphology within the same

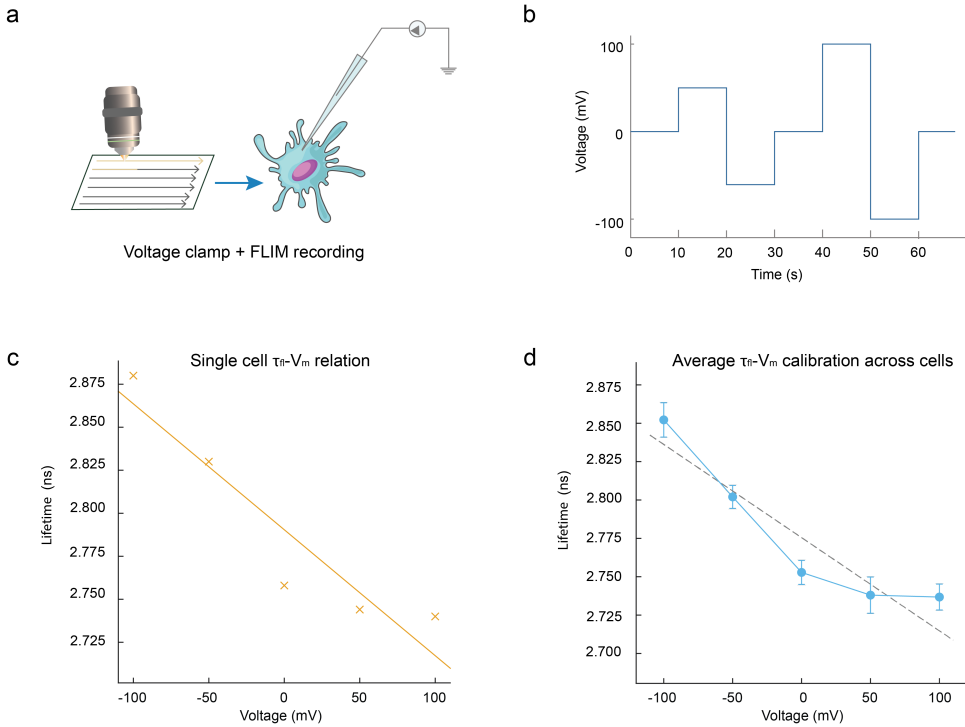


Figure 3.2: Calibration of Ace2N-mNeon fluorescence lifetime versus membrane potential in HEK293T cells. (a) Schematic of the calibration experiment. HEK293T cells expressing Ace2N-mNeon were recorded under whole-cell voltage clamp, while τ_{fl} was measured with a TCSPC-based FLIM setup. (b) Step-voltage protocol applied during calibration, from -100 mV to $+100$ mV in 50 mV increments. (c) Example τ_{fl} - V_m relation from a single HEK293T cell. Each point represents the average τ_{fl} during the steady state of a voltage step, with a linear fit illustrating the approximately monotonic decrease of τ_{fl} with depolarization. (d) Average τ_{fl} - V_m calibration across cells. Points show mean lifetime \pm SEM at each voltage ($n = 5$ cells). The dashed line is a linear regression fitted to all individual cell measurements, yielding a slope of approximately -6.1×10^{-4} ns per mV, corresponding to a τ_{fl} change of about 0.06 ns per 100 mV ($p < 0.0001$) and an estimated voltage-equivalent RMS noise of roughly 40 mV. Small deviations from the regression line at the most depolarized voltages reflect a mild nonlinearity that is consistent with previously reported intensity-voltage relations of Ace2N-mNeon.³⁰ RMS: root mean square; τ_{fl} : fluorescence lifetime.

embryo,³¹ as described in [Chapter 2](#). Positive embryos were selected for FLIM imaging, and TCSPC data were processed with our membrane-focused, cell-based analysis pipeline to obtain one τ_{fl} value per morphologically identified cell.

In the intensity images, epithelial cells, neurons, and skeletal muscle cells were identified based on their distinct morphologies (Fig. 3.3a). For each embryo, τ_{fl} values were quantified at the single-cell level and compared between cell types. The resulting 2D τ_{fl} maps displayed clearly separable pseudocolor patterns for each cell population within individual embryos (Fig. 3.3b,c), and statistical analysis confirmed significant differences between epithelial cells and neurons ($p = 0.0389$), neurons and skeletal muscle cells ($p = 1.39 \times 10^{-8}$), and epithelial cells and skeletal muscle cells ($p = 1.20 \times 10^{-9}$) (Fig. 3.3d).

The ordering of τ_{fl} values, with epithelial cells showing the shortest lifetimes, neurons intermediate values, and skeletal muscle cells the longest lifetimes, matches the expected progression from more depolarized to more hyperpolarized resting potentials in Table 3.1. Using the slope obtained from the HEK293T calibration, these lifetime differences correspond to voltage differences on the order of several tens of millivolts between cell types, consistent with their reported resting potential ranges on the calibrated scale.

To assess reproducibility, we repeated this analysis in five 2 dpf embryos and consistently observed significant τ_{fl} differences among the three cell types ($p < 0.01$ for all pairwise comparisons) (Fig. 3.3e). Across embryos, the relative ordering and approximate spacing of τ_{fl} between epithelial cells, neurons, and skeletal muscle cells were preserved, indicating that the calibrated lifetime readout robustly reports cell-type-specific resting-potential levels within and across fish.

We further extended these measurements across multiple developmental stages and additional cell types in a larger cohort of embryos and analyzed τ_{fl} both at the single-cell level and as mean values per fish (Supplementary Fig. S3.4). Across 1 to 4 dpf, skeletal muscle cells and cardiomyocytes consistently displayed longer τ_{fl} than neurons and epithelial cells, and this ordering was preserved when lifetimes were averaged per embryo rather than per cell, indicating that the cell-type-specific differences reported in Fig. 3.3 generalize across animals and developmental time. In our zebrafish recordings (Figs. 3.3 and 3.4; Supplementary Figs. S3.3 and S3.4), lifetime differences between cell types and developmental stages typically range from about 0.03 to 0.1 ns, that is, several tens of millivolts on the calibrated scale. By averaging many cells per cell type and per embryo, we therefore improve the precision of the estimated mean resting potentials beyond the single-cell calibration noise established in Fig. 3.2.

Because the same pattern emerges when comparing single cells and when comparing per-fish averages, these differences are robust to both cell-to-cell and fish-to-fish variability and are not driven by a few outlier animals or fields of view. Pairwise comparisons between cell types were almost all highly significant, with p values typically smaller than 0.0001 and in many cases smaller than 10^{-10} (Supplementary Fig. S3.4), supporting the use of Ace2N-mNeon lifetime as a quantitative proxy for resting-potential differences in vivo when interpreted through the HEK-derived calibration slope and physiologically plausible voltage ranges. Moreover, because τ_{fl} can be summarized at the single-cell level and aggregated by anatomical region or whole embryo, the same dataset can be interrogated at single-cell, population, and tissue scales, enabling the analysis of spatially patterned bioelectric signals during embryonic development.

Finally, to evaluate the impact of our analysis strategy, we compared τ_{fl} measurements obtained with the cell-based FLIM pipeline to those obtained with a standard pixel-based analysis in neurons and skeletal muscle cells from five 2 dpf embryos (5 to 8 cells per type per embryo). Using pixel-based fitting, τ_{fl} distributions for neurons and skeletal muscle cells overlapped substantially, and their mean values did not differ significantly. In contrast, the cell-based analysis, which sums photons from segmented membrane regions into a single decay per cell and suppresses cytoplasmic and background contributions, yielded a clear and statistically significant separation between neuronal and skeletal muscle τ_{fl} that matches the resting-potential hierarchy established in Fig. 3.3 (Supplementary Fig. S3.2). Thus, for sparsely labeled, heterogeneous in vivo datasets,

Table 3.2: Cell-type-specific promoters used to drive Ace2N-mNeon expression for longitudinal τ_{fl} measurements from 1 to 4 dpf.

Promoter	Target cell type(s)
503-bp <i>unc-45b</i> promoter	Skeletal muscle cells
<i>cmhc2</i> (cardiac myosin light chain 2)	Cardiomyocytes
<i>elavl3</i> (ELAV-like protein 3)	Neurons

analysis strategy is as important as sensor choice for preserving voltage-sensitive contrast and resolving biologically meaningful differences in resting potential.

Together, these results demonstrate that calibrated, cell-based Ace2N-mNeon FLIM can distinguish cell types in zebrafish embryos based on their resting-potential hierarchy and can do so reproducibly across animals. Rather than providing single-millivolt precision, our measurements resolve biologically meaningful differences in resting potential on the scale of several tens of millivolts, and Supplementary Fig. S3.2 underlines that reaching this level of contrast depends not only on the sensor and the optics, but also on the choice of analysis framework, establishing a practical framework for mapping developmental bioelectric patterns at both the single-cell and population levels in vivo.

3.2.4. MEMBRANE POTENTIAL DYNAMICS IN DIFFERENT CELL TYPES ACROSS ZEBRAFISH DEVELOPMENT

Building on our demonstration that Ace2N-mNeon can reliably distinguish cells with different resting potentials (Fig. 3.3), we next explored its capacity to track developmental changes in V_m across early zebrafish development. Using the τ_{fl} versus V_m relation measured in HEK293T cells (Fig. 3.2), we interpret τ_{fl} shifts in embryos as approximate changes in V_m , using the calibrated relation primarily to quantify relative changes and differences in membrane potential rather than to report exact voltages for individual cells. Existing evidence suggests that less differentiated cells tend to be more depolarized (closer to 0 mV), whereas terminally differentiated cells maintain more hyperpolarized resting potentials (more negative potentials).^{2,38} However, these observations largely stem from cell-culture studies because current in vivo measurement methods are limited.² To address this gap, we monitored τ_{fl} from 1 to 4 dpf in three distinct cell populations: two excitable cell types, neurons and cardiomyocytes,^{34,35} and one electrically active cell type whose primary function is not rapid spike generation, skeletal muscle cells.³⁶ This allows us to characterize how their estimated V_m evolves during early zebrafish development on the calibrated lifetime scale.

To overcome variable expression levels and potential fluorescence interference associated with the *ubi* promoter, we used Ace2N-mNeon constructs driven by cell-type-specific promoters that label skeletal muscle cells, cardiomyocytes, and neurons, respectively (Table 3.2 and Chapter 2 for details³¹). These plasmids were co-injected with Tol2 transposase mRNA at the one-cell stage, and positive embryos were imaged by TCSPC-based FLIM from 1 to 4 dpf. The resulting data were processed with our cell-based analysis pipeline to obtain single-cell τ_{fl} values for each cell type and developmental stage (Fig. 3.4).

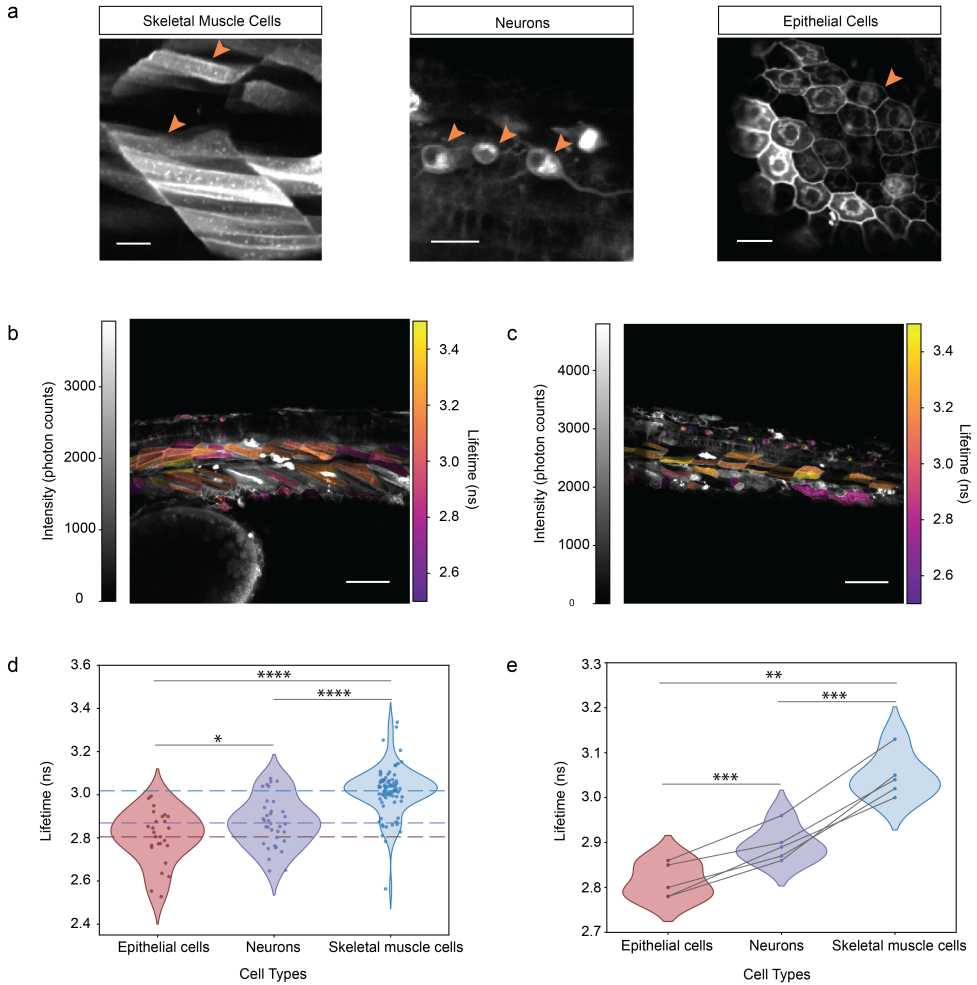


Figure 3.3: Quantitative lifetime analysis resolves resting membrane potential differences among cell types in zebrafish embryos. (a) Representative fluorescence intensity images in skeletal muscle cells, neurons, and epithelial cells in 2 dpf zebrafish embryos. Arrowheads indicate example cells. Scale bar = 20 μm . (b, c) 2D membrane lifetime maps in distinct regions of a 2 dpf embryo: (b) trunk and (c) tail. Grayscale encodes photon counts, and the color scale encodes τ_{fl} for segmented membrane regions, revealing distinct τ_{fl} distributions across cell types. Scale bar = 50 μm . (d) Single-cell τ_{fl} distributions for epithelial cells ($n = 26$ cells), neurons ($n = 36$), and skeletal muscle cells ($n = 80$) pooled across embryos. Violin plots show the distribution, and individual dots represent single cells. Dashed horizontal lines indicate mean τ_{fl} for each cell type (epithelial cells, 2.84 ns; neurons, 2.91 ns; skeletal muscle cells, 3.02 ns). Pairwise comparisons (unpaired t -tests): epithelial vs neurons, $p = 0.0389$; neurons vs skeletal muscle, $p = 1.39 \times 10^{-8}$; epithelial vs skeletal muscle, $p = 1.20 \times 10^{-9}$. (e) τ_{fl} values averaged per embryo confirm reproducible differences between cell types across five 2 dpf embryos. Violin plots show the distribution of embryo means for each cell type (epithelial cells, $n = 5$ embryos; neurons, $n = 5$; skeletal muscle cells, $n = 5$). Dots represent embryo means, and gray lines connect measurements from the same fish. Pairwise comparisons (paired t -tests): epithelial vs neurons, $p = 6.68 \times 10^{-4}$; neurons vs skeletal muscle, $p = 3.61 \times 10^{-4}$; epithelial vs skeletal muscle, $p = 1.55 \times 10^{-3}$. **dpf**: days post-fertilization; τ_{fl} : fluorescence lifetime.

SKELETAL MUSCLE CELLS

Zebrafish skeletal muscle development proceeds through distinct phases,³⁹ including myoblast generation during somitogenesis (10 to 24 hours post-fertilization, hpf),⁴⁰ primary muscle-fiber maturation (1 to 2 dpf), secondary muscle-fiber formation (2 to 3 dpf), and overall muscle maturation (3 to 5 dpf).^{39,41} Previous studies indicate that myoblast differentiation and fusion are promoted by hyperpolarized resting potentials mediated primarily by the inward-rectifier K⁺ channel Kir2.1,^{36,42–44} although its direct necessity for fusion remains unclear because quantitative *in vivo* evidence is still lacking.

In our experiments, skeletal muscle cells showed the longest τ_{fl} at 1 dpf, which was significantly higher than at later stages (Fig. 3.4a,b), consistent with a more hyperpolarized state during periods of active myoblast fusion and primary fiber formation, as reported in human and chicken embryonic muscle cells.^{42,43,45} Between 2 and 4 dpf, τ_{fl} decreased and remained at a lower level compared with 1 dpf, indicating a relative depolarization that coincides with secondary fiber formation and progressive fiber maturation.³⁹ A modest increase in τ_{fl} at 4 dpf suggests a slight repolarization in more mature muscle, which may help stabilize excitability during repetitive contraction.

Taken together, the τ_{fl} trajectory in skeletal muscle cells supports a model in which an early hyperpolarized phase accompanies myoblast fusion and early fiber assembly, followed by partial depolarization as fibers mature. Within the limits of our calibration, these trends are consistent with developmental changes in resting potential inferred from previous electrophysiological studies and illustrate that our method can follow V_m dynamics in a non-neuronal tissue *in vivo* with a resolution on the order of several tens of millivolts.

NEURONS AND CARDIOMYOCYTES

In neurons, action potential (AP) initiation is driven by the opening of voltage-gated sodium channels (Na_V), resulting in rapid depolarization, followed by repolarization mediated by voltage-gated potassium channels (K_V) and stabilization by Kir channels.^{4,35} Our previous work has shown that the excitability of both neurons and cardiomyocytes increases during early zebrafish development,^{31,34,35,46} suggesting that these cells remain relatively immature and highly active at this stage. This heightened excitability may result from underdeveloped Kir conductances together with the upregulation of excitatory channels, such as Na_V channels and glutamate receptors including AMPA and NMDA receptors, which collectively contribute to more depolarized resting potentials.⁴⁶

Consistent with this picture, neuronal τ_{fl} decreased progressively from 1 to 4 dpf (Fig. 3.4c,d), indicating a gradual shift toward shorter lifetimes that, under our calibration, corresponds to a modest depolarization of the resting potential. Similarly, embryonic cardiomyocytes exhibited relatively stable τ_{fl} at 2 and 3 dpf compared with 1 dpf, followed by a significant reduction at 4 dpf (Fig. 3.4e,f), again consistent with a developmental depolarization as cardiac excitability and conduction mature.³⁴ These reductions in τ_{fl} during early development suggest that, for both neurons and cardiomyocytes, resting V_m moves closer to spike threshold as excitability increases, thereby facilitating the emergence of spontaneous and evoked activity.

Supplementary Fig. S3.4 shows that the developmental trajectories we report for

skeletal muscle cells, neurons, and cardiomyocytes are evident at both the single-cell and per-embryo level, indicating that these trends are reproducible across individual fish rather than being driven by a subset of recordings. In the same analysis, epithelial cells do not show a clear lifetime shift between 1 and 2 dpf (Supplementary Fig. S3.4g,h), suggesting that their resting potential is relatively stable over this time window, or that any changes are smaller than the effective resolution of our current calibration and noise level. Supplementary Fig. S3.5 provides a global summary of mean τ_{fl} values across developmental stages and cell types, highlighting that, across all time points, the relative ordering of τ_{fl} , and thus resting potential, is conserved while absolute values shift in a manner consistent with the known maturation of each lineage.

Overall, by quantitatively monitoring τ_{fl} in defined cell populations over time, our calibrated FLIM framework reveals distinct bioelectric maturation trajectories in skeletal muscle cells, neurons, and cardiomyocytes during early zebrafish development on a shared, calibrated membrane-potential scale and provides a basis for linking cell-type-specific V_m dynamics to emerging physiological function in vivo.

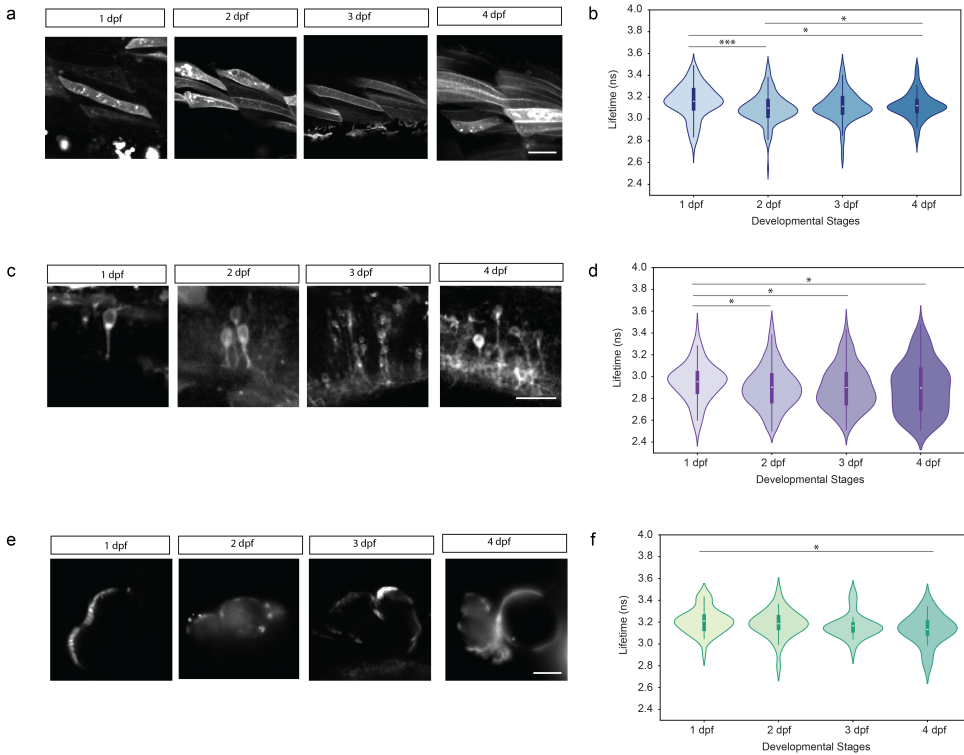


Figure 3.4: Developmental trajectories of Ace2N-mNeon fluorescence lifetime in skeletal muscle, neurons, and cardiomyocytes. (a,c,e) Representative fluorescence intensity images of (a) skeletal muscle cells, (c) neurons, and (e) cardiomyocytes in the heart tube or early chambers in zebrafish embryos at 1–4 dpf. Scale bar = 20 μm . (b) Fluorescence lifetime distributions of skeletal muscle cells across development. Violin plots show single-cell τ_{fl} values pooled across embryos at each stage (fish: 1 dpf $n = 19$, 2 dpf $n = 21$, 3 dpf $n = 9$, 4 dpf $n = 18$; cells: 1 dpf $n = 188$, 2 dpf $n = 653$, 3 dpf $n = 145$, 4 dpf $n = 203$). Inner box plots indicate the median and interquartile range, whiskers extend to 1.5 times the interquartile range. Mean τ_{fl} is highest at 1 dpf and significantly reduced at later stages, consistent with an early hyperpolarized phase followed by partial depolarization during muscle maturation. (d) Fluorescence lifetime distributions of neurons (fish: 1 dpf $n = 11$, 2 dpf $n = 28$, 3 dpf $n = 8$, 4 dpf $n = 9$; cells: 1 dpf $n = 92$, 2 dpf $n = 711$, 3 dpf $n = 189$, 4 dpf $n = 142$). Neuronal τ_{fl} shows a gradual decrease from 1–4 dpf, indicating a modest developmental depolarization of the resting potential as excitability increases. (f) Fluorescence lifetime distributions of cardiomyocytes (fish: 1 dpf $n = 8$, 2 dpf $n = 8$, 3 dpf $n = 9$, 4 dpf $n = 6$; cells: 1 dpf $n = 43$, 2 dpf $n = 29$, 3 dpf $n = 33$, 4 dpf $n = 28$). Cardiomyocyte τ_{fl} remains relatively stable between 1 and 3 dpf and decreases significantly by 4 dpf, consistent with further depolarization during cardiac maturation. For (b,d,f), horizontal bars indicate significant pairwise differences between stages (two-sided t -tests; * $p < 0.05$, ** $p < 0.01$, *** $p < 0.001$). **dpf**: days post-fertilization; τ_{fl} : fluorescence lifetime.

3.3. DISCUSSION

3.3.1. BIOLOGICAL INSIGHTS INTO DEVELOPMENTAL RESTING POTENTIALS

Recent work has highlighted that bioelectric signals influence cell proliferation, differentiation, and morphogenesis, and that experimental modulation of V_m can even rescue

some developmental defects.^{1,47} However, most quantitative studies of resting potential have been carried out in cultured cells or isolated preparations, so how resting potentials are distributed across cell types and change over time in an intact developing vertebrate embryo has remained largely unknown.^{22,23} In this context, our study introduces a calibrated FLIM framework that uses Ace2N-mNeon to read out approximate, calibrated membrane-potential levels in live zebrafish embryos at single-cell resolution. By combining an experimentally determined $\tau_{fl}-V_m$ relation from HEK293T cells with cell-type-resolved lifetime measurements in embryos, we map how resting potentials are distributed across tissues and how they evolve during early development.

In our calibration experiments, the $\tau_{fl}-V_m$ relation had a slope of about -6.1×10^{-4} ns per mV and a root-mean-square (RMS) lifetime residual of roughly 0.025 ns, corresponding to a single-cell voltage-equivalent noise on the order of 40 mV. In zebrafish recordings, the τ_{fl} differences we observe between cell types and developmental stages are typically 0.03 to 0.1 ns, that is, several tens of millivolts on this scale. To our knowledge, this represents the first application of a calibrated, lifetime-based GEVI to follow resting membrane-potential dynamics across multiple cell types during vertebrate embryogenesis, providing an *in vivo* counterpart to earlier cultured-cell-based studies of developmental bioelectricity.²³ These cell-type-specific trajectories are summarized in Supplementary Fig. S3.5, which highlights that across all stages, the relative ordering of τ_{fl} , and thus resting potential, is conserved while the absolute values shift in a manner consistent with the known maturation of each lineage.

We focused on four representative cell populations that play distinct roles in embryogenesis and have well-described resting-potential ranges from *ex vivo* work, namely surface epithelial cells, spinal neurons, and trunk skeletal muscle cells, and additionally examined embryonic cardiomyocytes.^{2,34-36} At 2 dpf, epithelial cells, neurons, and skeletal muscle cells showed clearly separated τ_{fl} distributions, in an order that matches their expected resting-potential hierarchy, with epithelial cells most depolarized, neurons at intermediate values, and skeletal muscle most hyperpolarized.^{34-36,43,44} Using the calibrated slope from HEK293T cells, these lifetime separations correspond to voltage differences of several tens of millivolts between cell types, consistent with the reported resting-potential ranges for these classes.^{2,34-36} This agreement between *in vivo* τ_{fl} ordering and established *in vitro* electrophysiology supports the idea that lifetime can be used as a quantitative proxy for resting potential in intact embryos and provides a first cell-type-resolved bioelectric map within a single zebrafish.

Extending these measurements across developmental time revealed distinct V_m trajectories for each cell class. Skeletal muscle cells displayed their longest lifetimes at 1 dpf, consistent with a strongly hyperpolarized state during active myoblast fusion and primary fiber formation, followed by a partial and sustained depolarization as fibers expand and mature.^{36,42,44} This pattern agrees with previous observations that Kir-mediated hyperpolarization promotes myogenic differentiation, whereas later stages require a balance between excitability and stability.^{42,44} Neurons showed a more modest but significant decrease in τ_{fl} from 1 to 4 dpf, indicating gradual depolarization as excitatory conductances increase and Kir conductance is not yet fully established, a shift that likely lowers the threshold for spontaneous and evoked activity.^{31,35} Embryonic cardiomyocytes exhibited relatively stable lifetimes between 1 and 3 dpf, with a detectable depolarizing

shift at 4 dpf, which may reflect electrical remodeling as the embryonic heart transitions toward more mature action-potential waveforms.^{31,34,48} Together, these trajectories suggest that precise, cell-type-specific tuning of resting potential is an integral part of functional maturation in both excitable and non-excitable tissues and that our calibrated lifetime measurements are sensitive to these developmental changes on the scale of several tens of millivolts. These interpretations are consistent with the assumption, based on prior characterizations of Ace2N-mNeon and its mNeonGreen fluorophore, that the local photophysical environment of the indicator within a given cell type does not change dramatically over the 1 to 4 dpf window, so that developmental shifts in τ_{fl} primarily reflect changes in membrane potential rather than large environment-induced lifetime changes.³⁰

3.3.2. METHODOLOGICAL IMPLICATIONS FOR CALIBRATED IN VIVO VOLTAGE IMAGING

Methodologically, our work demonstrates that lifetime-based GEVIs can be used for calibrated voltage imaging in the complex environment of a developing embryo when combined with an appropriate analysis strategy. The $\tau_{fl}-V_m$ relation measured in HEK293T cells provides a reproducible slope that converts lifetime changes into voltage differences, while known resting-potential ranges for specific zebrafish cell types serve as physiological anchors that constrain absolute values. Our cell-based pipeline, which sums photons within segmented membrane masks into a single decay per cell and reports lifetimes at the level of individual cells and cell types, mitigates key challenges for in vivo FLIM, including low photon counts, contamination from cytoplasmic fluorescence, and tissue autofluorescence. The resulting 2D and 3D membrane lifetime maps enable visualization of bioelectric patterns across entire embryos while preserving single-cell resolution. For sparsely labeled, heterogeneous in vivo datasets, this makes the analysis strategy as critical as the sensor itself for preserving voltage-sensitive contrast and resolving biologically meaningful differences in resting potential. For indicators such as Ace2N-mNeon, which show pronounced time-dependent responses and hysteresis, the timing of data acquisition becomes an additional determinant of effective voltage sensitivity and is directly linked to how the calibration is interpreted.³⁰

At the same time, several limitations must be considered when interpreting the calibrated values. When we combine the calibrated $\tau_{fl}-V_m$ relation with literature resting membrane potentials, the lifetimes expected for zebrafish cell types are lower than the measured values by roughly 0.1 to 0.2 ns, while the relative ordering across cell types is preserved. We therefore examined which aspects of our calibration and imaging scheme are most likely to account for these offsets. Although local biochemical environment and tissue optics can influence fluorescence lifetime, the magnitude and direction of the discrepancies are difficult to attribute solely to such factors, especially since HEK cells and embryos were imaged at comparable temperature and pH and Ace2N-mNeon is tethered to the cytoplasmic side of the membrane rather than buried in the lipid bilayer.^{30,49} Instead, we consider it more likely that our optical sampling interrogates different dynamical components of the Ace2N-mNeon response in the two samples.³⁰

In the HEK293T calibration, we used small fields of view (FOV), for example, about 40

by $40\ \mu\text{m}$, sampled at 128×128 pixels with a frame time of about 1.2 s. Under these conditions, the pixel dwell time is on the order of tens of microseconds, and each membrane region is scanned multiple times during each multi-second voltage step. As a result, each pixel experiences tens of milliseconds of effective excitation, and the indicator approaches a quasi-steady state before the lifetime is read out. In zebrafish embryos, we image a larger field of view, approximately $300\ \mu\text{m}$ across, sampled at 1024×1024 pixels with frame times of about 2 s, which reduces the dwell time to a few microseconds per pixel and greatly lowering the illumination duty cycle, so individual membrane pixels receive only a few short excitation bursts separated by millisecond-scale dark intervals, and the readout mainly samples the instantaneous response.

Because Ace2N-mNeon and related Ace based indicators are known to exhibit a fast peak and a slower steady state component in their optical response to voltage steps, we interpret these offsets as arising from a mismatch between the steady state regime sampled in the HEK293T calibration and the more instantaneous regime sampled in zebrafish imaging.³⁰ Consequently, in the present work we use the cell derived $\tau_{\text{fl}}-V_{\text{m}}$ relation primarily to set the voltage scale for in vivo lifetime differences, rather than as a source of exact per cell voltages.

Within this context, our framework is best viewed as a method for resolving systematic resting-potential differences of several tens of millivolts between cell types and developmental stages, rather than for reporting precise voltages of single cells. The main biological conclusions of this study rely on the relative ordering of resting potentials across cell types and on developmental shifts within each population, both of which are robust to moderate offsets in absolute τ_{fl} . Additional technical constraints also shape the scope of the method. In cardiomyocytes, dense packing and motion artifacts necessitated a population-level analysis, which reduces spatial resolution compared with single-cell measurements in neurons and skeletal muscle. Moreover, our imaging parameters are optimized for slowly varying resting potentials, so the suitability of this approach for resolving fast action-potential waveforms in vivo remains to be established. Addressing these points, for example by using brighter and more stable lifetime-readable GEVIs, improved motion correction, and parallel imaging modalities, should further strengthen calibrated voltage imaging in intact embryos.^{22,23}

These considerations suggest several concrete routes for future refinement. On the calibration side, HEK293T datasets could be reanalyzed by explicitly separating early and late segments of each voltage step, for example by fitting τ_{fl} using only an initial time window and comparing this early-state calibration to the conventional steady-state fit. On the in vivo side, analogous analyses that restrict τ_{fl} estimation to earlier parts of each acquisition, or that employ scan parameters more closely matched to those used in HEK cells, could test whether sampling comparable portions of the Ace2N-mNeon response trajectory reduces offsets between calibrated and zebrafish lifetimes. Jointly applying these calibration-side and in vivo-side adjustments would clarify how acquisition timing and indicator kinetics interact to shape absolute τ_{fl} . More generally, the same framework should be easier to apply to brighter, more stable, and less hysteretic lifetime-readable GEVIs, where kinetic complications are reduced and absolute calibration becomes more straightforward.

Despite these methodological constraints, calibrated lifetime imaging coupled with

genetically targeted expression opens the door to a wide range of biological investigations in developmental bioelectricity.^{1,2} Applying this framework to additional cell types, such as glia, endothelium, or neural crest derivatives, could reveal how bioelectric patterns coordinate across germ layers during organogenesis.^{2,50} Coupling lifetime-based voltage readout to optogenetic or pharmacological perturbations may help disentangle causal links between resting potential, gene expression, and tissue morphogenesis. Systematic measurements in disease models could clarify how electrical maturation is altered in congenital muscle and heart disorders.^{21,51} More broadly, the experimental and analytical strategy presented here provides a practical path toward quantitative, cell-type-resolved voltage imaging *in vivo* and establishes a foundation for future studies that seek to integrate bioelectric signals into a more complete understanding of vertebrate development.

3.4. METHODS

3.4.1. ZEBRAFISH HUSBANDRY

All experiments were conducted using Casper strain zebrafish (*Danio rerio*).⁵² Adult zebrafish were raised and bred in recirculating systems at the Delft University of Technology fish facility under a 14 h light/10 h dark cycle, maintained at pH 7.5 and 28°C. Adults aged 3–24 months were intercrossed, and embryos were collected at the one-cell stage in egg water containing Instant Ocean salts (60 µg/mL) and 0.0002% methylene blue. After injection, embryos were incubated at 28°C and euthanized at 5 dpf after the experiment.

3.4.2. PLASMID CONSTRUCTION AND RNA SYNTHESIS

The Ace2N-mNeon insert (a gift from Adam Cohen's lab) was amplified and assembled with different promoters in Tol2 backbones using Gibson Assembly (Gibson Assembly Master Mix, NEB).⁵³ The full list of plasmids and primers is available in our published work.³¹ Tol2 transposase mRNA was transcribed from pCS2FA-CO-Tol2-TPase (Addgene #133032) using the mMACHINE[®] Kit (Thermo Fisher Scientific), then purified and quantified before use.

3.4.3. ZEBRAFISH SAMPLE PREPARATION

Fertilized eggs were co-injected at the one-cell stage with ~1 nL of a solution containing 50 ng/µL plasmid DNA, 100 ng/µL Tol2 transposase mRNA, and 0.1% phenol red (P0290, Sigma-Aldrich) into the yolk. Embryos were incubated at 28°C, and dead eggs were removed at 6 and 24 h post-injection. Chorions of embryos at 1–2 dpf were mechanically removed using precision tweezers. Embryos were anesthetized with 0.03% tricaine (A5040, Sigma-Aldrich) and immobilized in 1.5% low-melting agarose (A4018, Sigma-Aldrich) on glass-bottom imaging dishes (D35-14-1.5 N, Cellvis). Embryos were maintained at 28.5°C during imaging and regularly monitored for health.

3.4.4. HEK293T CELL CULTURE

HEK293T cells were cultured at 37°C with 5–10% CO₂ in DMEM (D6429, Sigma-Aldrich) supplemented with 10% fetal bovine serum (FBS, Seradigm) and penicillin-streptomycin (P4333, Sigma-Aldrich). Cells were transfected at ~80% confluency with 1500 ng plasmid DNA and 6 μL TransIT-293 (MIR 2705, Mirus Bio) transfection reagent. The next day, transfected cells were split onto 35 mm glass-bottom dishes (D35-14-1.5 N, Cellvis) coated with human plasma fibronectin (FC010 5MG, Sigma-Aldrich).

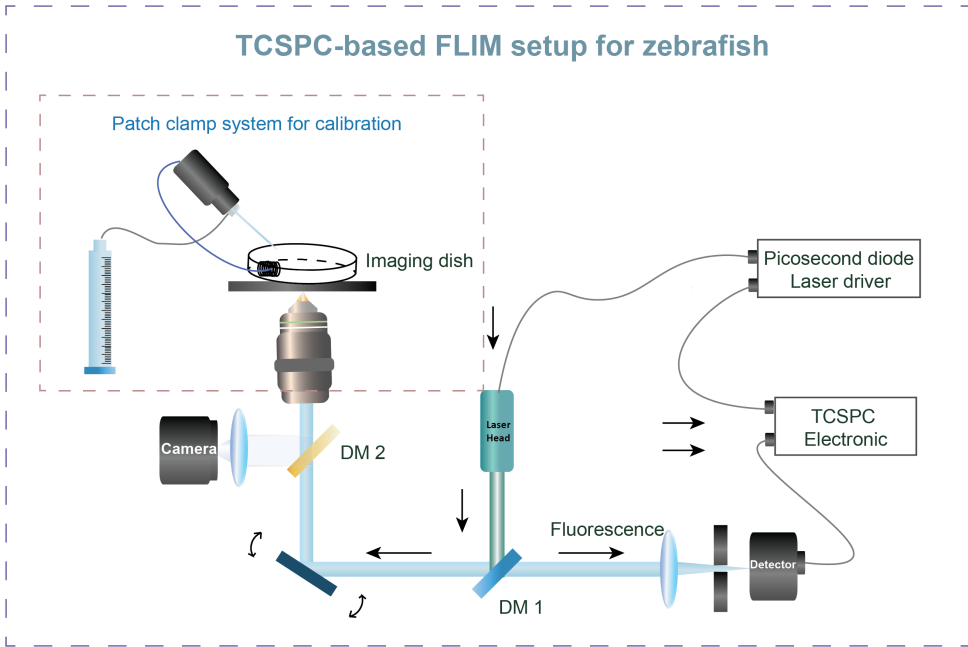
3.4.5. WHOLE-CELL PATCH-CLAMP ELECTROPHYSIOLOGY FOR LIFETIME CALIBRATION

Whole-cell voltage-clamp recordings were performed 48–72 h post-transfection at room temperature (25°C). Cells were washed and perfused with extracellular buffer (pH 7.3, 310 mOsmol/L) containing 125 mM NaCl, 15 mM HEPES, 2.5 mM KCl, 1 mM CaCl₂, 1 mM MgCl₂, and 30 mM glucose. Micropipettes were pulled from borosilicate glass capillaries (1.5 mm outer diameter, 0.84 mm inner diameter, World Precision Instruments) using a micropipette puller (P-1000, Sutter Instrument) to a resistance of 5–10 MΩ. The intracellular pipette solution (pH 7.3, 295 mOsmol/L) contained 125 mM potassium gluconate, 0.1 mM CaCl₂, 0.6 mM MgCl₂, 1 mM EGTA, 10 mM HEPES, 4 mM ATP magnesium salt, 0.4 mM GTP sodium salt, and 8 mM NaCl. Micropipettes were positioned using a micromanipulator (S-PS-7000C, Scientifica).

Voltage-lifetime calibration experiments were performed in voltage-clamp mode with simultaneous FLIM acquisition. Voltage steps from –100 to +100 mV were applied using a patch-clamp amplifier (Model 2400, AM Systems). Holding potentials were applied in pseudorandom order, and a seal test was performed between steps to verify recording stability and quality. Software controlling the patch-clamp hardware was custom written in Python.⁵⁴

3.4.6. FLUORESCENCE LIFETIME DATA ACQUISITION

FLIM was performed on an inverted confocal microscope (Ti C2si, Nikon) equipped with a 405/488/561/640 quad-band dichroic (MHE46410, Nikon) and a 20× objective (CFI Plan Fluor 20XC MI, numerical aperture 0.75, Nikon), integrated with a PicoQuant Compact Lifetime upgrade and the patch-clamp setup. The FLIM system included a 40 MHz pulsed 485 nm laser (LDH-DC 485 dual-mode, PicoQuant), an HC475/28 cleanup filter, a TCSPC unit (MH150, PicoQuant), and a single-photon detector (PMA Hybrid 40, PicoQuant). The same optical path and detection chain were used for both zebrafish and HEK293T recordings to ensure consistent excitation and detection conditions. Fluorescence lifetime data were acquired using SymPhoTime 64 (v2.6, PicoQuant). Data were recorded with 25 time bins in the analog-to-digital converter and with spatial sampling of either 1024×1024 or 512×512 pixels for zebrafish embryo FLIM, and 128×128 pixels for HEK293T lifetime calibration.



Scheme 3.1: Schematic of the TCSPC-based FLIM setup for zebrafish embryos with patch-clamp calibration.

3.4.7. PRINCIPLE OF LIFETIME–VOLTAGE TRANSDUCTION

Ace2N-mNeon is a FRET-based genetically encoded voltage indicator (GEVI) in which the mNeonGreen donor transfers excitation energy to a *microbial rhodopsin* acceptor. Changes in V_m reshape the absorption spectrum of the rhodopsin domain, thereby modulating the energy-transfer rate $k_{ET}(V_m)$, the FRET efficiency $E(V_m)$, and consequently the donor lifetime $\tau_{fl}(V_m)$.^{20,24,30} Over a sufficiently restricted voltage range, this dependence can be approximated as linear:^{24,25}

$$\tau_{fl}(V_m) \approx \tau_0 + s(V_m - V_0), \quad (3.1)$$

where s is the lifetime–voltage slope and (V_0, τ_0) denote a reference voltage and its corresponding lifetime under the calibration condition. In HEK293T cells, whole-cell voltage clamp combined with FLIM yielded

$$s \approx -6.1 \times 10^{-4} \text{ ns mV}^{-1}, \quad (3.2)$$

corresponding to ~ 0.06 ns per 100 mV and a root mean square (RMS) lifetime residual of ~ 0.025 ns, that is, a single-cell voltage-equivalent noise of ~ 40 mV (Fig. 3.2). In zebrafish embryos, we use this slope as an external scaling factor and estimate voltage differences from lifetime differences as

$$\Delta V_m \approx \frac{\Delta \tau_{fl}}{s}, \quad (3.3)$$

interpreting Ace2N-mNeon lifetimes as reporting calibrated membrane-potential differences on the scale of several tens of millivolts rather than exact millivolt values for individual cells.

3.4.8. CELL-BASED FLIM DATA PROCESSING AND QUALITY CONTROL

FLIM data were stored in time-tagged time-resolved (TTTR) format (PTU, PicoQuant) and processed using a custom Python library, `readPTU_FLIM`.⁵⁵ The complete processing workflow is summarized in Supplementary Fig. S3.1. In brief, all datasets were analyzed with a standardized cell-based workflow comprising four steps: TTTR data structuring, membrane segmentation, photon pooling, and multi-component lifetime fitting to obtain cell-type-specific lifetime outputs.

For each acquisition, the TTTR event stream was converted into a four-dimensional (4D) array indexed by spatial coordinates (x, y), microtime within the laser period (decay histogram), and frame index. Intensity images were obtained by integrating photon counts over the decay dimension and were used as inputs for cell segmentation. Segmentation was performed using Cellpose 2.0.⁵⁶ The resulting cell masks were refined using morphological operations to generate narrow membrane masks, and each mask was inspected and, when necessary, manually corrected. Only cells meeting predefined, stringent inclusion criteria were retained for downstream analysis.

Photon events from pixels within each membrane mask were summed to generate one fluorescence decay histogram per cell. The instrument response function (IRF) was corrected to account for system-induced temporal broadening, and τ_{fl} fitting was performed on a cell-by-cell basis. Multi-component decay models were used to identify and iteratively exclude fast noise and background-related components, after which a simplified model was fitted to extract the voltage-sensitive lifetime component. The full quality-control and fitting procedure is summarized as a decision tree in Supplementary Fig. S3.6. Fits that did not meet predefined quality criteria, for example based on χ^2 statistics, were discarded. Final τ_{fl} values were assigned to individual cells and grouped by cell type for downstream visualization and statistical analysis. In brief, cells were required to pass a biological lifetime range check and a reduced chi-square gate (e.g., χ^2_v within 0.8–1.5), with full decision logic in Supplementary Methods Section 3.5.2.

3.4.9. STATISTICAL ANALYSIS

All statistical analyses were performed on τ_{fl} values obtained from the membrane-focused, cell-based FLIM pipeline described above (Section 3.4.8). For zebrafish experiments, we used two complementary levels of analysis: pooled single-cell datasets and per-fish averages.

Pooled single-cell analyses were used to visualize the full spread of τ_{fl} values within a given cell type and developmental stage, and to test for overall differences between groups. In these cases, all cells of a given type and condition were treated as independent observations, and unpaired two-sided t -tests were applied to compare lifetime distributions between cell types or developmental stages (for example, Fig. 3.3d and Fig. 3.4b,d,f).

Per-fish analyses were used to assess reproducibility across animals and to account for

the fact that multiple cells can be recorded from the same embryo. For these comparisons, a mean τ_{fl} value was first computed for each cell type within each fish, and these per-fish means were then compared between cell types or stages. When cell types were compared within the same embryos, paired two-sided t -tests were used (for example, Fig. 3.3e and Supplementary Fig. S3.4). When developmental stages were compared and different embryos contributed to each stage, unpaired two-sided t -tests were applied to the corresponding per-fish means.

For HEK293T calibration experiments, the relation between τ_{fl} and V_m was quantified by linear regression on pooled single-cell measurements across holding potentials, and the significance of the slope was assessed by the associated p -value (Fig. 3.2d). Unless otherwise specified in the figure legends, all tests were two-sided, a significance level of $\alpha = 0.05$ was used, and exact p -values are reported in the main text or figure legends.

3.4.10. CELL-BASED FLIM DATA VISUALIZATION

2D VISUALIZATION

Final τ_{fl} values for each cell were visualized using the HSV (hue, saturation, value) color model. In this model, hue encodes fluorescence lifetime by mapping the lifetime of each cell to a distinct color. Saturation was fixed at 1 to ensure consistent color representation, and value represents brightness, derived from the corresponding intensity image by summing photon counts within each segmented cell (details in the Supplementary Materials). Lifetime maps were overlaid on the underlying intensity images so that only membrane regions belonging to segmented cells were shown in color, whereas non-membrane regions were displayed in grayscale. This representation emphasizes membrane-localized GEVI signals while preserving anatomical context.

3D VISUALIZATION

For 3D visualization, z -stack FLIM was performed with a $3\ \mu\text{m}$ layer interval, capturing 30 to 60 layers per field of view for each zebrafish embryo. Individual 2D visualizations were generated for each layer, and a neural-network-based interpolation method (FILM) was applied to generate intermediate optical sections between acquired planes.⁵⁷ The interpolated stack was then used to reconstruct volumetric lifetime images and maximum intensity projections. All volumetric visualizations were generated in ImageJ using the interpolated z -stacks, and additional implementation details are provided in the Supplementary Materials.

3.5. SUPPLEMENTARY MATERIALS

3.5.1. SUPPLEMENTARY FIGURES AND ADDITIONAL DATA

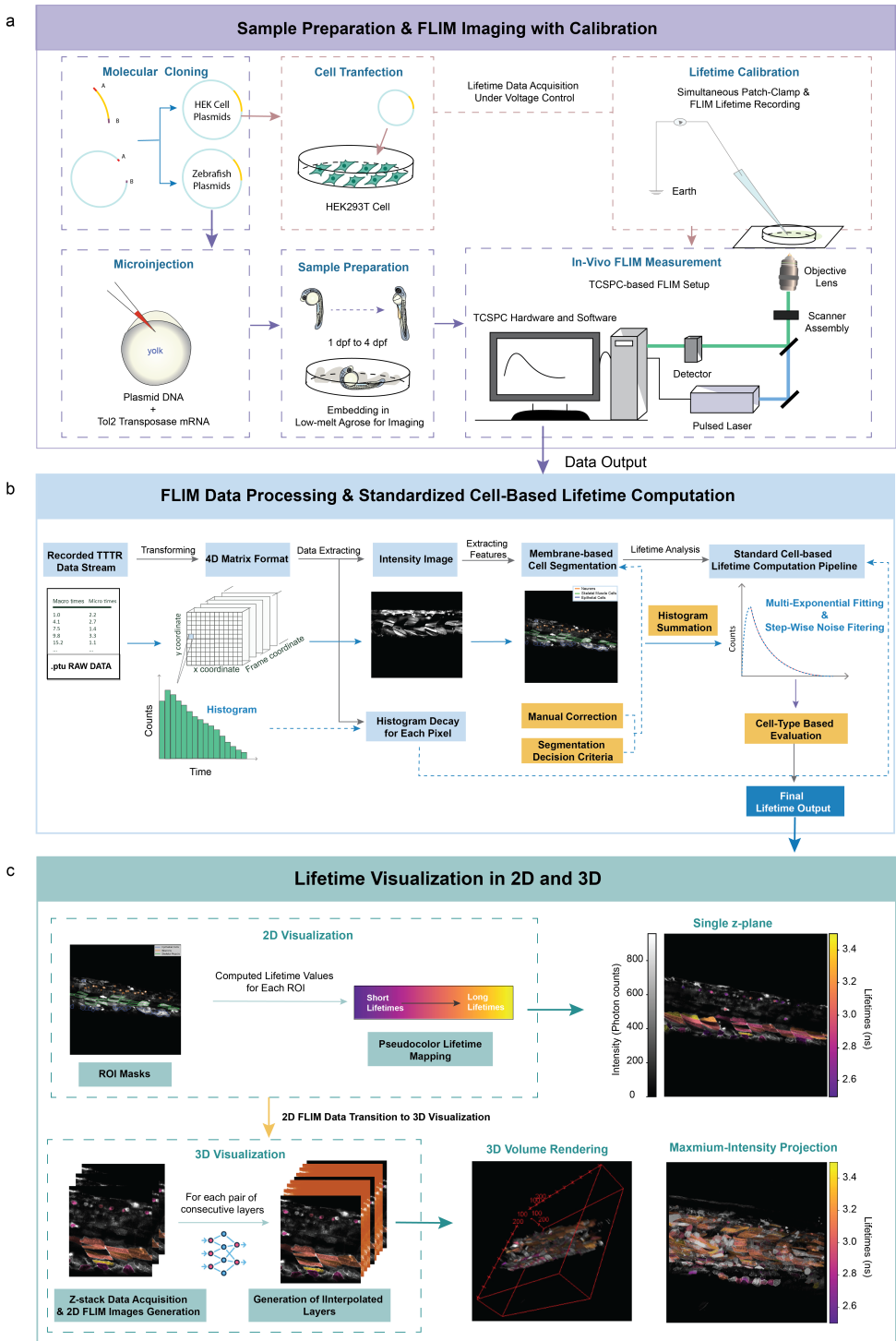


Figure S3.1

Figure S3.1: **Detailed workflow for calibrated Ace2N-mNeon FLIM acquisition and cell-based analysis.** (a) Sample preparation and calibrated FLIM imaging. Molecular cloning, HEK293T transfection, and zebrafish microinjection are used to express Ace2N-mNeon in HEK cells and in zebrafish embryos. Whole-cell voltage clamp in HEK293T cells is combined with TCSPC-based FLIM to establish the $\tau_{fl}-V_m$ relation, which is then applied to in vivo measurements in zebrafish embryos using the same FLIM setup. (b) FLIM data processing and standardized cell-based lifetime computation. Recorded TTR data are converted into 4D decay histograms, intensity images are generated, and cell membranes are segmented using a CellPose-based workflow with manual correction. For each cell, photon counts within the membrane mask are pooled, decay histograms are summed, and multi-component fitting with stepwise noise filtering is performed to obtain a single τ_{fl} value per cell, which is then assigned to a defined cell type. (c) Lifetime visualization in 2D and 3D. Cell-based τ_{fl} values are displayed as membrane-level pseudocolor maps in 2D planes, using intensity as brightness. For z-stack data, 2D FLIM layers are combined with interpolated intermediate layers to generate 3D lifetime volumes and maximum intensity projections, revealing tissue-scale bioelectric patterns while preserving single-cell resolution. τ_{fl} , fluorescence lifetime; V_m , membrane voltage.

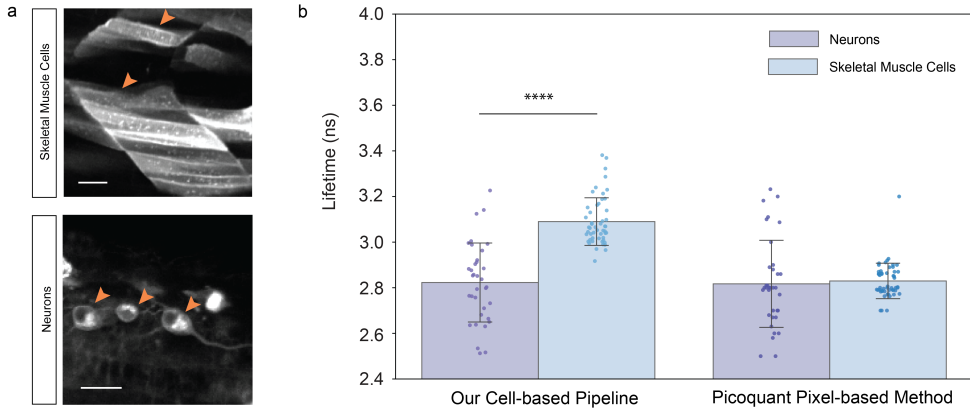


Figure S3.2: Comparison of cell-based and pixel-based FLIM analysis. (a) Representative fluorescence intensity images of skeletal muscle cells (top) and spinal neurons (bottom) in a 2 dpf zebrafish embryo expressing Ace2N-mNeon. Arrowheads indicate individual neurons. Scale bar = 10 μm . (b) Comparison of τ_{fl} for neurons and skeletal muscle cells using our cell-based pipeline (left) and a pixel-based analysis (right). Each dot represents a single cell (skeletal muscle, $n = 51$; neurons, $n = 35$ from five 2 dpf embryos), bars show mean \pm s.d. Our cell-based analysis resolves a significant difference in τ_{fl} between neurons and skeletal muscle cells, whereas the pixel-based method does not (unpaired two-sided t -test; **** $p < 0.0001$, n.s., not significant). **dpf**, days post-fertilization; τ_{fl} , fluorescence lifetime.

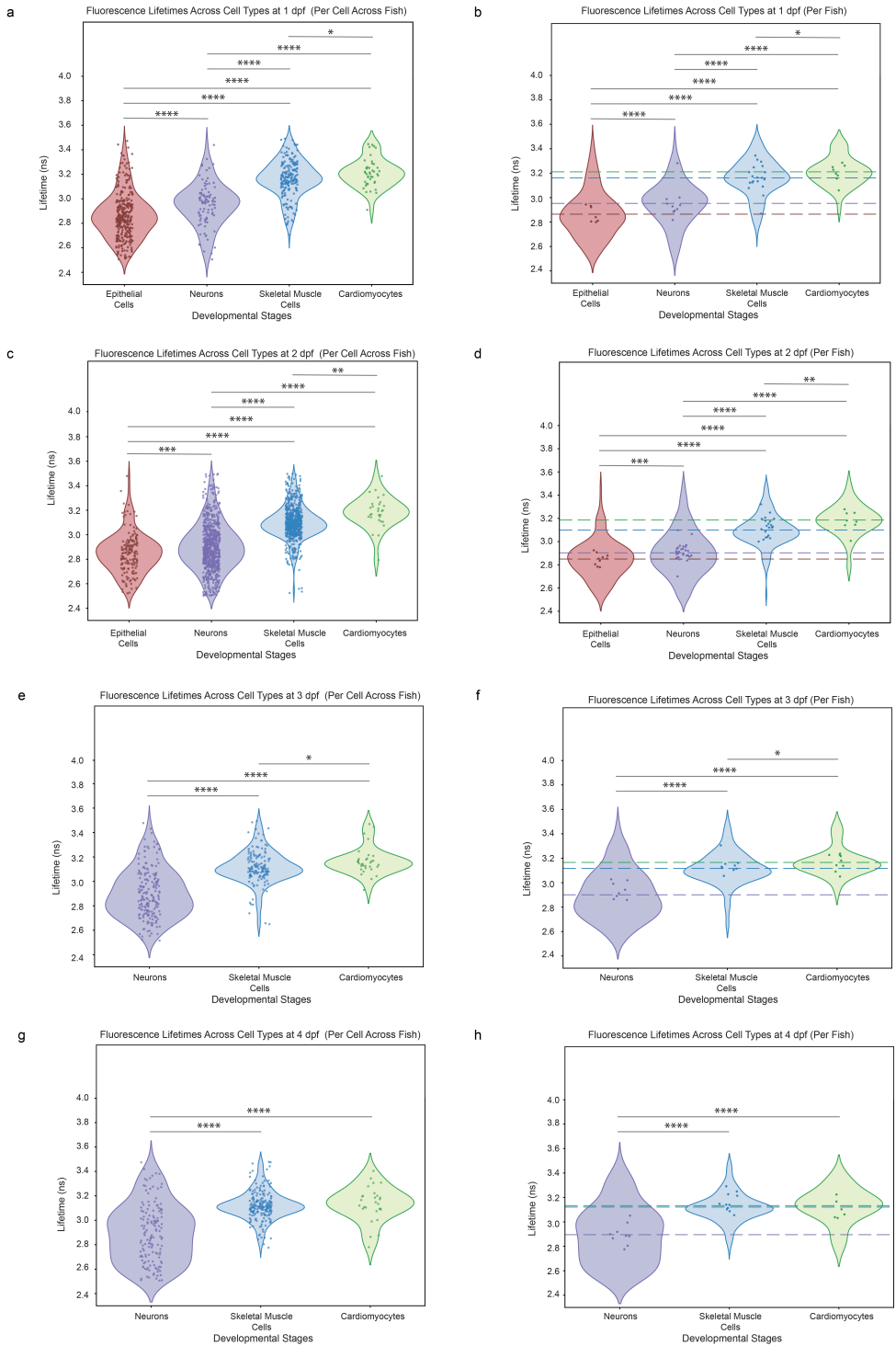


Figure S3.3

Figure S3.3: **Fluorescence lifetimes of major cell types across developmental stages.** (a,b) Fluorescence lifetimes of epithelial cells, neurons, skeletal muscle cells, and cardiomyocytes at 1 dpf. (a) Violin plots of single-cell τ_{fl} values (epithelial, 315 cells from 7 fish; neurons, 92 cells from 11 fish; skeletal muscle, 188 cells from 18 fish; cardiomyocytes, 43 cells from 8 fish). Unpaired two-sided t -tests: $p = 5.77 \times 10^{-5}$ (epithelial vs neurons), $p = 3.77 \times 10^{-61}$ (epithelial vs skeletal muscle), $p = 1.76 \times 10^{-27}$ (epithelial vs cardiomyocytes), $p = 6.10 \times 10^{-18}$ (neurons vs skeletal muscle), $p = 9.04 \times 10^{-18}$ (neurons vs cardiomyocytes), and $p = 2.15 \times 10^{-2}$ (skeletal muscle vs cardiomyocytes). (b) Mean τ_{fl} per fish, each point represents one embryo. At this stage, skeletal muscle cells and cardiomyocytes show longer lifetimes than neurons and epithelial cells, consistent with a more hyperpolarized resting potential. (c,d) τ_{fl} distributions at 2 dpf for the same four cell types (epithelial, 162 cells from 10 fish; neurons, 712 cells from 28 fish; skeletal muscle, 652 cells from 21 fish; cardiomyocytes, 29 cells from 8 fish), shown as single-cell values (c) and mean per fish (d). The separation between skeletal muscle cells or cardiomyocytes and the more depolarized epithelial cells and neurons remains highly significant, with p values as follows: $p = 3.17 \times 10^{-4}$ (epithelial vs neurons), $p = 1.16 \times 10^{-44}$ (epithelial vs skeletal muscle), $p = 2.72 \times 10^{-16}$ (epithelial vs cardiomyocytes), $p = 4.64 \times 10^{-87}$ (neurons vs skeletal muscle), $p = 5.66 \times 10^{-13}$ (neurons vs cardiomyocytes), and $p = 1.45 \times 10^{-3}$ (skeletal muscle vs cardiomyocytes). (e,f) τ_{fl} at 3 dpf for neurons, skeletal muscle cells, and cardiomyocytes (neurons, 189 cells from 8 fish; skeletal muscle, 145 cells from 9 fish; cardiomyocytes, 33 cells from 9 fish), shown as single cells (e) and mean per fish (f). Muscle and cardiomyocytes remain more hyperpolarized than neurons, with all pairwise comparisons significant: $p = 9.65 \times 10^{-27}$ (neurons vs skeletal muscle), $p = 5.56 \times 10^{-17}$ (neurons vs cardiomyocytes), and $p = 3.44 \times 10^{-2}$ (skeletal muscle vs cardiomyocytes). (g,h) τ_{fl} at 4 dpf for neurons, skeletal muscle cells, and cardiomyocytes (neurons, 142 cells from 9 fish; skeletal muscle, 203 cells from 11 fish; cardiomyocytes, 28 cells from 6 fish), shown as single cells (g) and mean per fish (h). Lifetime differences between neurons and the two muscle populations remain strongly significant, with p values as follows: $p = 1.58 \times 10^{-20}$ (neurons vs skeletal muscle) and $p = 1.27 \times 10^{-9}$ (neurons vs cardiomyocytes). Across all stages, the ordering of τ_{fl} matches the expected resting potential hierarchy. **dpf**, days post-fertilization; τ_{fl} , fluorescence lifetime.

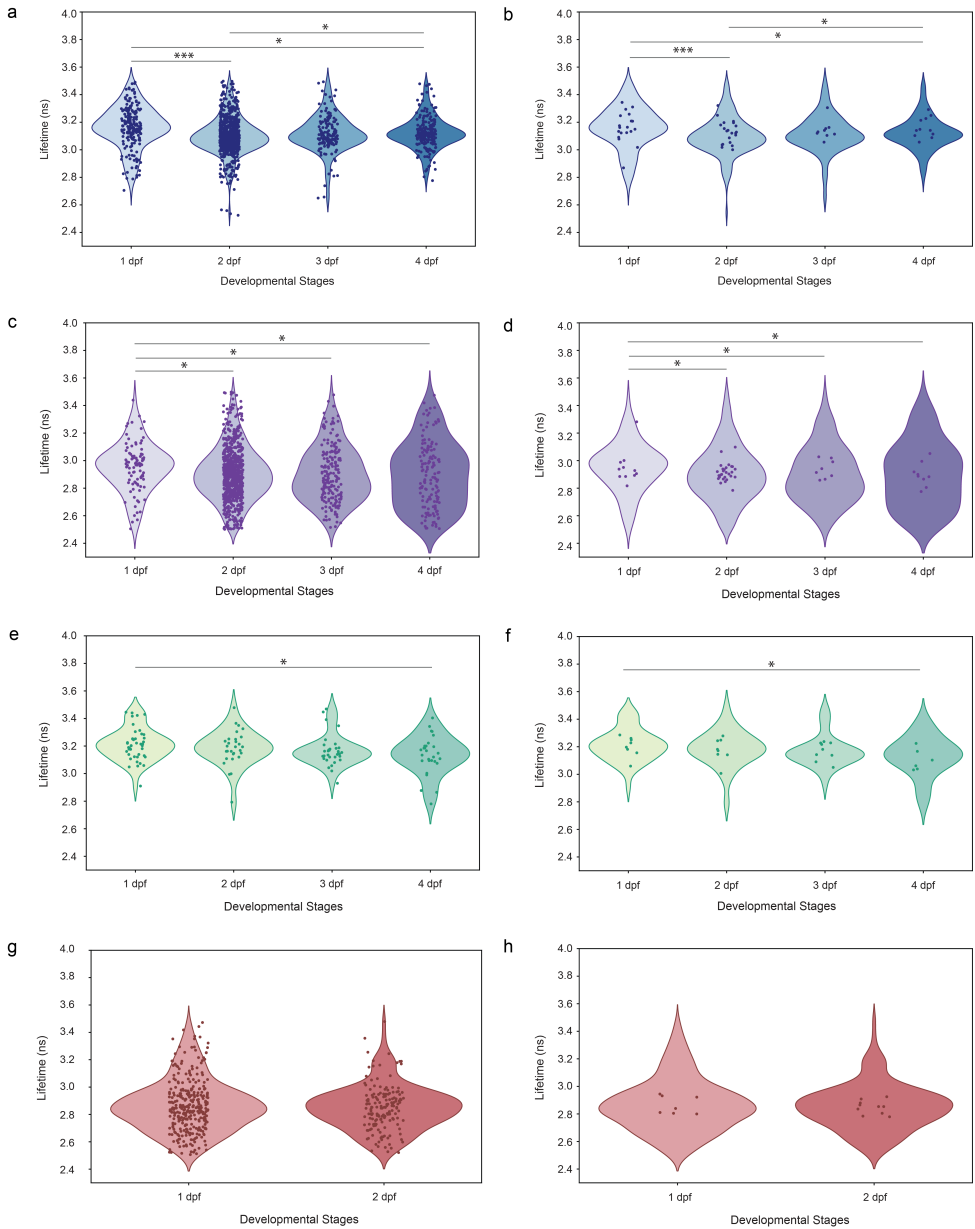


Figure S3.4

Figure S3.4: **Developmental trajectories of fluorescence lifetime for individual cell types.** (a, b) Skeletal muscle cells. (a) Violin plots of single-cell τ_{fl} values from 1 to 4 dpf. Each point represents one cell. Sample sizes: 1 dpf, 188 cells from 19 fish; 2 dpf, 653 cells from 21 fish; 3 dpf, 145 cells from 9 fish; 4 dpf, 203 cells from 18 fish. Unpaired two-sided t -tests: $p = 1.04 \times 10^{-7}$ (1 vs 2 dpf), $p = 5.23 \times 10^{-3}$ (1 vs 3 dpf), $p = 2.55 \times 10^{-3}$ (1 vs 4 dpf), and $p = 4.78 \times 10^{-2}$ (2 vs 4 dpf). (b) Mean τ_{fl} per fish for the same groups, each point represents one embryo. (c, d) Neurons. (c) Violin plots of single-cell τ_{fl} values from 1 to 4 dpf: 1 dpf, 92 cells from 11 fish; 2 dpf, 711 cells from 28 fish; 3 dpf, 189 cells from 8 fish; 4 dpf, 142 cells from 9 fish. Unpaired two-sided t -tests: $p = 2.36 \times 10^{-2}$ (1 vs 2 dpf), $p = 3.67 \times 10^{-2}$ (1 vs 3 dpf), and $p = 4.84 \times 10^{-2}$ (1 vs 4 dpf). (d) Mean τ_{fl} per fish for the same groups, each point represents one embryo. (e, f) Cardiomyocytes. (e) Violin plots of single-cell τ_{fl} values from 1 to 4 dpf: 1 dpf, 43 cells from 8 fish; 2 dpf, 29 cells from 8 fish; 3 dpf, 33 cells from 9 fish; 4 dpf, 28 cells from 6 fish. Unpaired two-sided t -test: $p = 1.40 \times 10^{-2}$ (1 vs 4 dpf). (f) Mean τ_{fl} per fish for the same groups, each point represents one embryo. (g, h) Epithelial cells. (g) Violin plots of single-cell τ_{fl} values at 1 and 2 dpf: 1 dpf, 315 cells from 7 fish; 2 dpf, 162 cells from 10 fish. (h) Mean τ_{fl} per fish for the same groups, each point represents one embryo. **dpf**: days post fertilization; τ_{fl} : fluorescence lifetime.

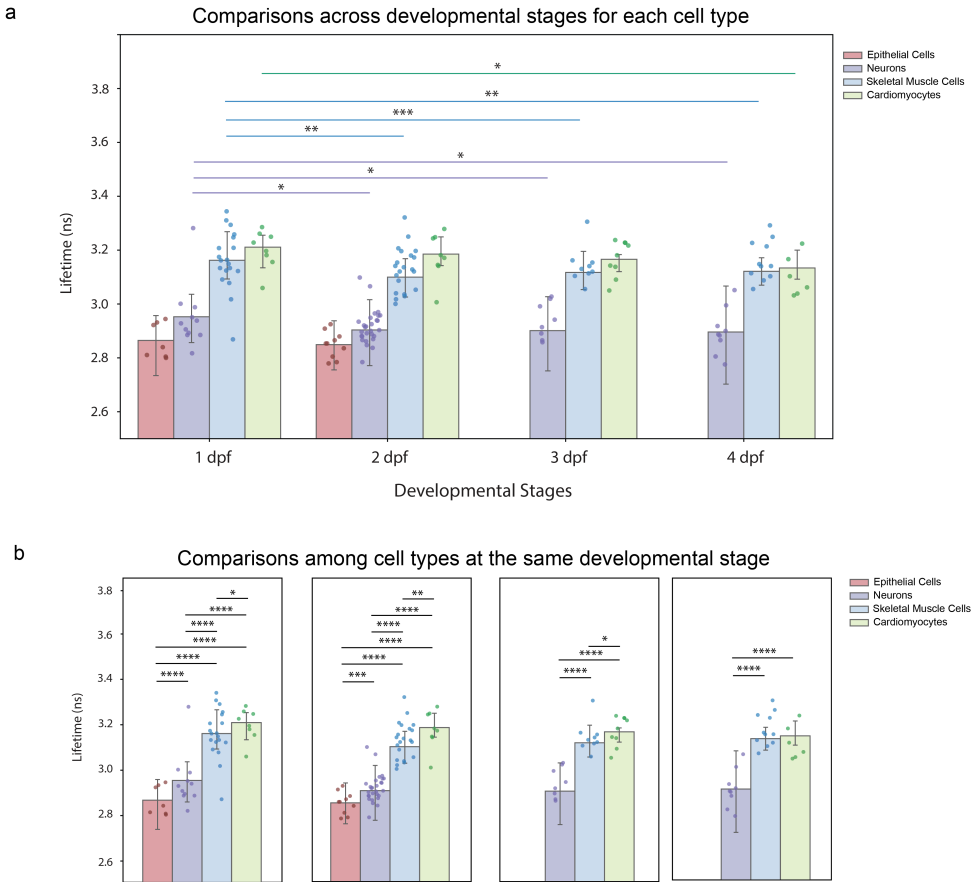


Figure S3.5: **Summary of fluorescence lifetime variation across developmental stages and cell types.** (a) Bar plots of mean τ_{fl} for epithelial cells, neurons, skeletal muscle cells, and cardiomyocytes from 1 to 4 dpf. Each point represents one embryo; bars show the mean \pm s.e.m. Horizontal lines indicate statistically significant differences across developmental stages within the same cell type (color-coded by cell type). (b) Bar plots comparing mean τ_{fl} among the four cell types at each developmental stage. Each point represents one embryo; bars show the mean \pm s.e.m. Horizontal lines indicate statistically significant differences between cell types at the same time point. **dpf**: days post fertilization; τ_{fl} : fluorescence lifetime.

3.5.2. SUPPLEMENTARY METHODS: CELL-BASED FLIM ANALYSIS AND QUALITY CONTROL PIPELINE

To complement the brief description in the main Methods, this section provides a detailed account of the membrane focused, cell-based FLIM analysis pipeline used throughout this chapter. Supplementary Fig. S3.6 summarizes the complete workflow, from TTTR data structuring and membrane segmentation to per cell lifetime computation and quality control.

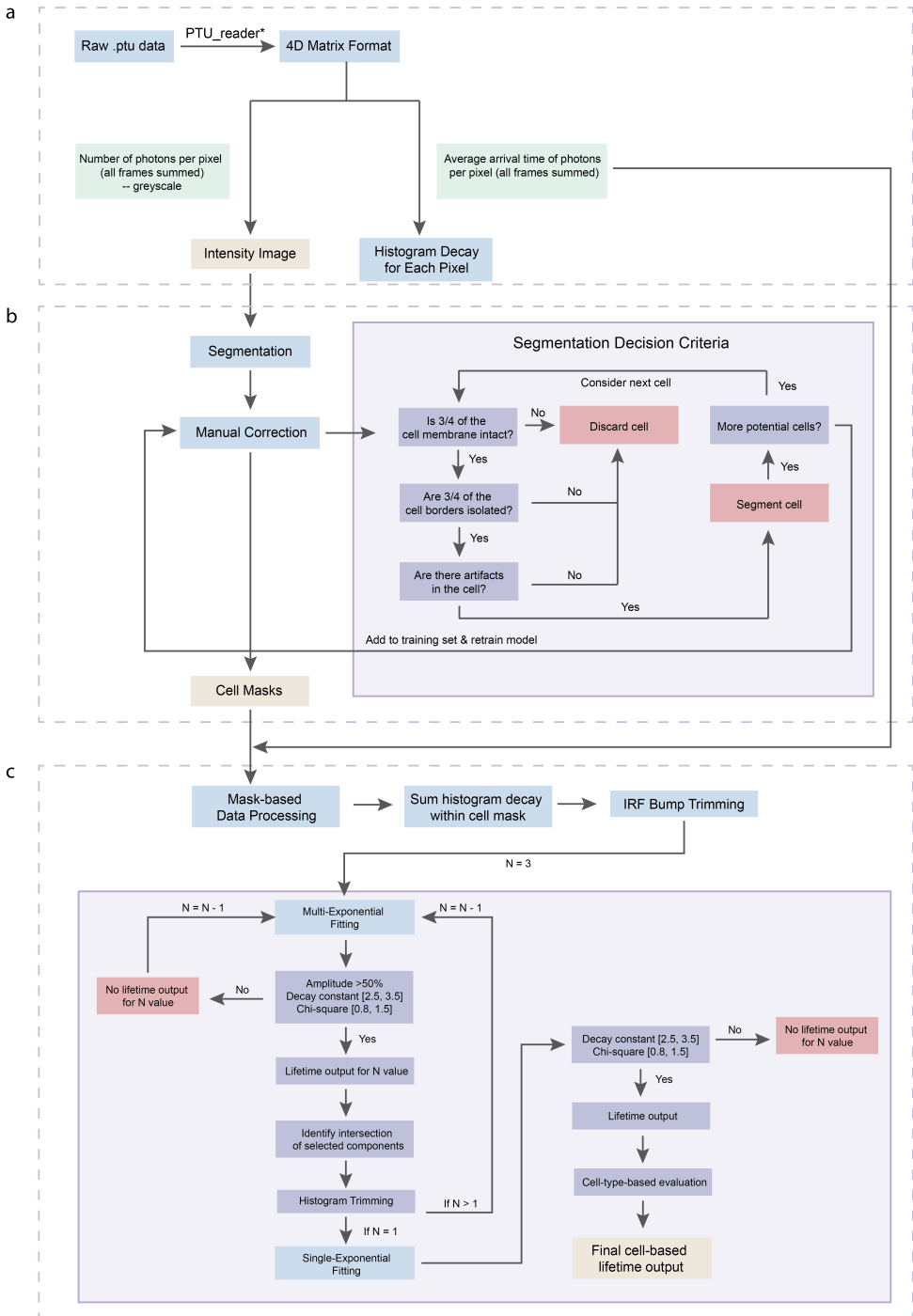


Figure S3.6

Figure S3.6: **Overview of the cell-based FLIM analysis and quality control pipeline.** (a) Raw TTTR data are converted into 4D matrices to generate intensity images and per-pixel decay histograms, followed by membrane segmentation, manual curation, and downstream decision steps with multi-exponential fitting to obtain per-cell lifetime outputs. (b) Segmentation QC: Cellpose 2.0 masks are reviewed and corrected using standardized criteria (membrane continuity, separation from neighbouring cells, absence of obvious artefacts); accepted masks proceed to lifetime analysis and are added for iterative model refinement, whereas rejected masks are discarded. (c) Lifetime computation: for each accepted cell, membrane-photon decays are processed by IRF trimming, multi-component fitting and noise handling, and a final single-exponential fit to report one lifetime value per cell.

TTTR DATA PROCESSING AND STRUCTURING

FLIM datasets were stored in a time-tagged time-resolved (TTTR) format, in which every detected photon is written as an individual event. For each event, the file contains three key quantities:^{33,55} macro time, which reports the elapsed time from the start of the acquisition and therefore the order of photon arrivals; micro time, which reports the arrival time of the photon within the current laser excitation period; and special event markers, which encode scanner and hardware events such as the start of a frame or line. The raw TTTR stream was saved in PicoQuant PTU files, where spatial coordinates are reconstructed from the scanning and synchronization markers rather than stored explicitly.

To convert these PTU files into a structured format suitable for downstream analysis, we used the open source Python library `readPTU_FLIM`.⁵⁵ This library parses the TTTR event list, extracts macro time, micro time, detector channel, event markers and acquisition parameters, and reorganizes the data into a four dimensional (4D) matrix with axes (x , y , time bin, frame). Photon arrival times are binned along the decay axis to produce a fluorescence decay histogram for each pixel. Photon counts are then summed across all time bins and frames to construct a 2D intensity matrix (x , y), which serves as the basis for cell segmentation, initial quality control and data visualization, whereas the per-pixel decay histograms serve as the input for subsequent lifetime fitting (Supplementary Fig. S3.6a). A schematic timing interpretation of micro time, macro time and markers is provided in Appendix A.4.

CELL SEGMENTATION

Cell segmentation is a critical preprocessing step in our pipeline, because τ_{fl} values are interpreted only from membrane regions where V_m -sensitive indicators are located. However, live zebrafish embryos present several challenges that make standard segmentation methods unreliable. Autofluorescence from structures such as yolk and muscle, non-membrane background fluorescence, and scattering in deeper tissue reduce contrast and blur membrane boundaries, so that simple intensity thresholding, edge detection, or ridge enhancement filters cannot isolate cell contours in a robust way.^{58–60} In addition, early embryos contain densely packed cells with irregular shapes that change over developmental time, which further complicates automatic segmentation across stages.

To identify a segmentation strategy that met the precision requirements of this project, we systematically benchmarked conventional approaches and machine-learning-based

tools and then built a CellPose 2.0-based workflow with human-in-the-loop correction.⁵⁶

Benchmarking conventional and Ilastik-based segmentation

We first tested a set of conventional image processing methods, including local contrast enhancement followed by Sato or Hessian filters and morphological operations, as well as several pre-trained neural network models from BioImage.io that were originally designed for nuclear segmentation.^{58–60} Across epithelial and neuronal datasets, these approaches frequently misclassified non-membrane fluorescence, failed to close cell contours, or interpreted yolk autofluorescence as signal, illustrating that fixed-threshold and global strategies are not suitable for membrane-specific analysis in our samples (Supplementary Fig. S3.7). Advanced instance segmentation frameworks, such as Mask R-CNN, would in principle be applicable, but they require large manually annotated training sets that were not practical to generate for multiple cell types and developmental stages in this study.⁶¹

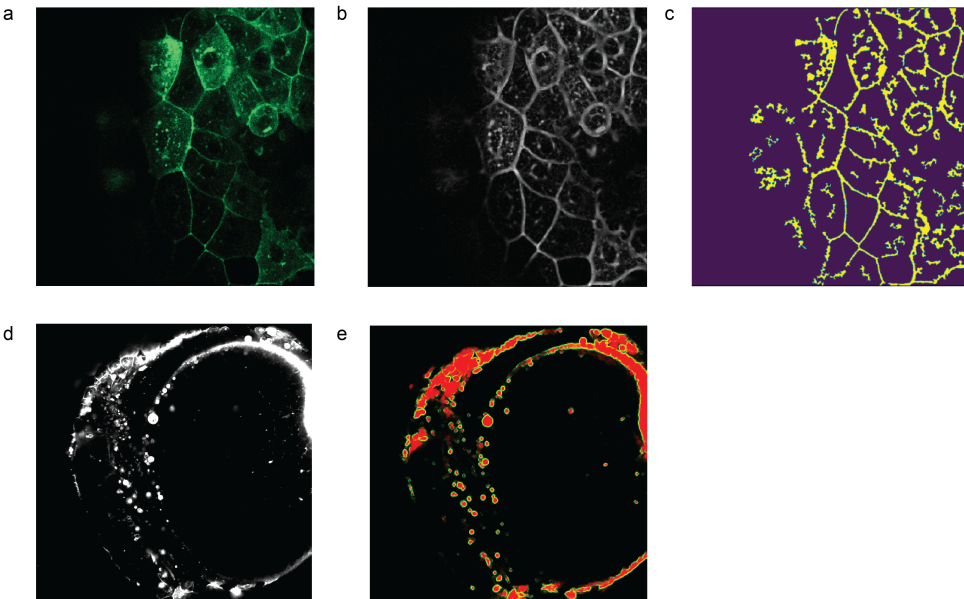


Figure S3.7: **Performance of conventional and generic segmentation methods on membrane localized Ace2N-mNeon images.** (a) Representative intensity image of zebrafish epithelial cells used to test conventional segmentation algorithms. (b) Segmentation result after local contrast enhancement followed by a Sato ridge filter. (c) Segmentation result after a Hessian-based filter and subsequent morphological operations. In both (b) and (c), non-membrane fluorescence is misclassified, and epithelial cell borders are incompletely captured. (d) Representative intensity image of a zebrafish head region containing neurons and surrounding yolk. (e) Prediction from a pre-trained neural network model from BioImage.io applied to the image in (d), which incorrectly labels yolk autofluorescence as neuronal signal, illustrating the limitations of generic nuclear segmentation networks for this membrane-specific application.

Given these limitations, we next evaluated Ilastik, a machine learning based pixel classification tool that can work with relatively small training sets and is often robust at low signal to noise ratios (SNR).⁶² For neuronal images, we trained Ilastik on manually annotated examples and generated probability maps that were converted to binary masks,

while independent ground truth masks were drawn in ImageJ. Using these masks we computed Intersection over Union (IoU) scores for individual cells and a simple precision like score defined as $TP / (TP + FN + FP)$, where true positives (TP) are correctly segmented cells, false negatives (FN) are missed cells, and false positives (FP) are spurious segments. In neuron rich fields, Ilastik reached a mean IoU of approximately 0.69 (Supplementary Fig. S3.8e), indicating reasonable but not near perfect agreement with ground truth and implying that substantial manual correction would still be required to reach the desired accuracy. Moreover, Ilastik does not provide an integrated environment for interactive mask editing, so corrections must be performed in external software and are difficult to feed back into the model in a systematic way. When we qualitatively tested Ilastik on epithelial and skeletal muscle images, performance deteriorated further, with frequent under segmentation in densely packed regions. Taken together, these benchmarks showed that Ilastik alone could not provide the level of accuracy and workflow integration needed for our multi-cell type, multi-stage dataset.

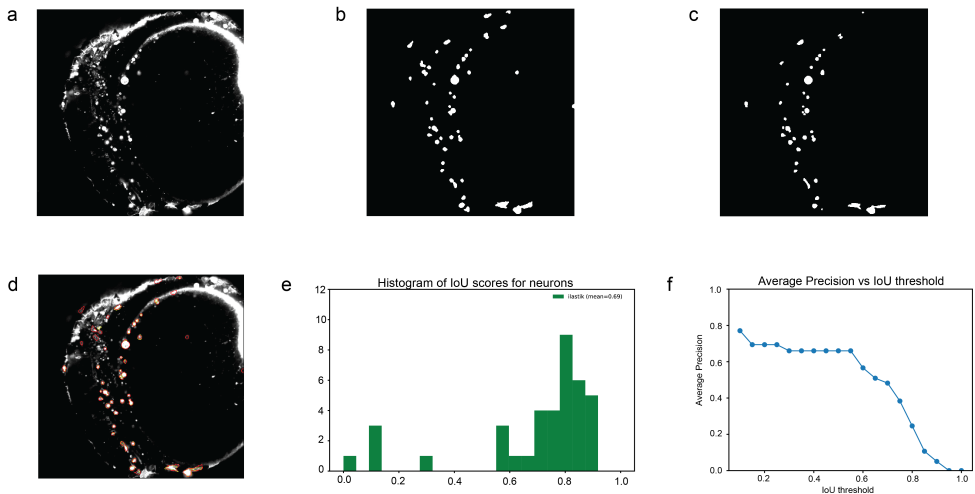


Figure S3.8: Evaluation of Ilastik for neuronal segmentation. (a) Representative intensity image of zebrafish neurons used for segmentation testing. (b) Binary masks predicted by the Ilastik classifier. (c) Ground truth masks manually annotated in ImageJ. (d) Overlay of predicted (red) and ground truth (yellow) contours. (e) Histogram of IoU scores across all annotated neurons (mean IoU = 0.69). (f) Average precision as a function of IoU threshold, illustrating that performance drops rapidly at stricter IoU criteria.

CellPose 2.0 based workflow and decision rules

Based on these tests, we adopted CellPose 2.0 as the core segmentation engine for this project. CellPose 2.0 uses a deep learning model that performs well on morphologically complex biological images and, importantly for our application, supports small-sample training, iterative refinement, and a graphical interface that allows users to correct masks and add them back into the training set.⁵⁶

We evaluated CellPose 2.0 on epithelial and skeletal muscle images before and after additional training on manually curated masks. For epithelial cells, the mean IoU im-

proved from 0.734 with the pre-trained cyto3 model to 0.874 after training. For skeletal muscle cells, the mean IoU increased from 0.299 to 0.433 (Supplementary Fig. S3.9). A similar improvement was observed in the associated precision-like scores across a range of IoU thresholds, indicating that model fine-tuning substantially reduced both missed and spurious cells.

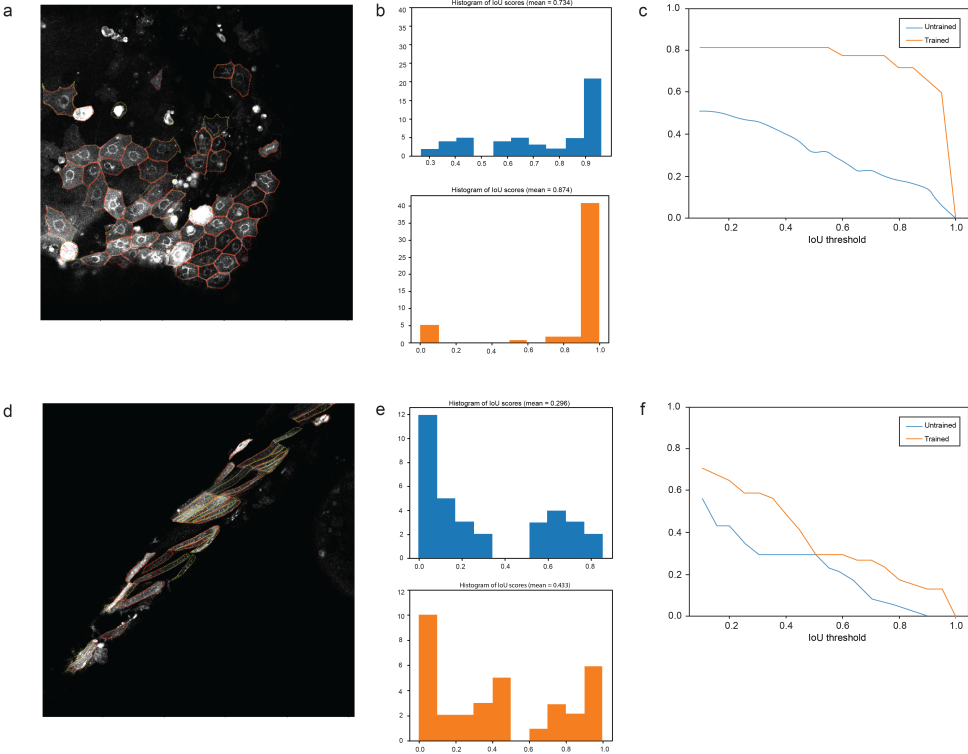


Figure S3.9: **CellPose 2.0 segmentation performance before and after model retraining for epithelial and skeletal muscle cells.** (a) Epithelial cell segmentation result with CellPose 2.0 after retraining. Ground-truth cell outlines are shown in yellow and CellPose predictions in red. (b) Histograms of IoU scores for epithelial cells before (top, blue) and after (bottom, orange) retraining. The mean IoU improves from 0.734 (untrained) to 0.874 (trained). (c) Precision, computed as $TP/(TP + FP + FN)$, as a function of IoU threshold for epithelial cell segmentation, comparing the untrained (blue) and trained (orange) models. (d) Skeletal muscle cell segmentation result with CellPose 2.0 after retraining, ground truth in yellow and predictions in red. (e) Histograms of IoU scores for skeletal muscle cells before (top, blue) and after (bottom, orange) retraining. The mean IoU increases from 0.299 (untrained) to 0.433 (trained). (f) Precision as a function of IoU threshold for skeletal muscle cell segmentation, for the untrained (blue) and trained (orange) models.

To integrate CellPose into a reproducible workflow, we implemented the following human-in-the-loop segmentation procedure (Supplementary Fig. S3.6b).

- 1. Initial segmentation.** Fluorescence intensity images were segmented with the CellPose `cyto3` model to generate preliminary whole-cell masks.
- 2. Cell selection.** Candidate cells were screened according to standardized decision

rules: at least three-quarters of the membrane contour had to be present within the field of view, borders needed to be clearly separated from neighbors, and masks containing obvious artifacts such as debris or saturated pixels were rejected.

3. **Manual correction.** Remaining segmentation errors were corrected interactively by deleting incorrect masks, adjusting boundaries, and adding missed cells using the CellPose graphical interface.
4. **Model retraining.** Corrected masks were added to the training set and used to retrain the CellPose model, improving performance on subsequent images from the same cell type and developmental stage.
5. **Final mask export.** The manually curated masks were exported as NumPy (.npy) arrays and passed to the downstream lifetime analysis.

In total, we evaluated 196 images across cell types and stages using this procedure. Although segmentation remains the main manual step in the pipeline, the combination of CellPose 2.0 with targeted retraining allows us to reach near-complete coverage of analyzable cells while keeping the amount of hand annotation manageable. Future work will focus on expanding the training set and implementing a more formal test routine to further reduce manual effort and to better quantify generalization across datasets.

Membrane extraction and mask output

After TTTR data had been structured and whole-cell masks were obtained, we restricted the analysis to membrane regions, since Ace2N-mNeon is most informative for V_m at the cell surface. For each segmented cell, membrane masks were generated by morphological operations: an eroded version of the cell mask was subtracted from a dilated version, yielding a narrow ring that follows the cell perimeter. The inner and outer widths of this ring could be adjusted by the user. In practice, we used one pixel on either side of the contour for neurons and two pixels for the other cell types.

These membrane masks were then used to zero out all pixels outside the membrane region in the decay data, ensuring that subsequent τ_{fl} calculations were driven solely by membrane-localized photons. For each field of view, the final masks were saved as .npy files with matrix dimensions matching the corresponding intensity image. Background pixels were assigned a value of zero, and membrane pixels were given unique integer labels (1, 2, 3, ...) so that individual cells could be tracked unambiguously through the downstream FLIM processing pipeline.

CELL-BASED LIFETIME COMPUTATION

The cell-based lifetime computation starts from the structured TTTR data and the membrane masks obtained from the segmentation pipeline. For each segmented cell, photon arrival-time histograms from all membrane pixels within the mask were summed to generate a single decay histogram per cell, which improves SNR by averaging out photon shot noise and local intensity fluctuations. Only these membrane-restricted decay curves were used for τ_{fl} estimation, ensuring that the analysis focuses on voltage-sensitive regions of the cell.

In practice, the measured decay contains contributions from four sources: (i) the instrument response function (IRF) of the TCSPC system, (ii) background and detection noise, (iii) sample autofluorescence, and (iv) the true fluorescence decay of Ace2N-mNeon. Therefore, our pipeline proceeds in three stages. First, IRF-related broadening is reduced by trimming the leading part of the histogram. Second, multi-exponential fitting is used to decompose the remaining decay into putative biological and non-biological components and to remove obvious noise-dominated contributions. Third, a simplified, mostly single-exponential model is fitted to the cleaned decay to extract the τ_{fl} value assigned to each cell. The main steps are described below and summarized in Supplementary Fig. S3.6c.

Preprocessing: reduction of instrument response function contributions

As a first preprocessing step, we reduce the influence of the instrument response function (IRF) by trimming the decay histogram around its peak. Starting from the maximum of the histogram, all bins that fall within the full width at half maximum (FWHM) of the independently measured IRF are removed from the leading edge of the decay. This time-domain trimming is less computationally demanding than full deconvolution, yet is sufficient for the predominantly single-exponential decays observed for Ace2N-mNeon under our conditions. An example of the trimming procedure and its effect on the decay shape is shown in Supplementary Fig. S3.10. After trimming, the remaining decay is used for multi-component fitting.

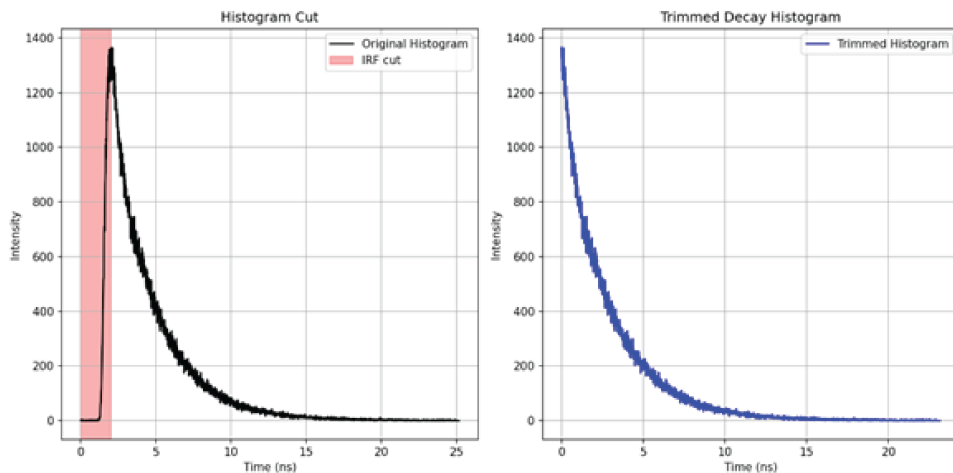


Figure S3.10: **Example of histogram trimming for IRF correction.** (a) Raw fluorescence decay histogram for a single cell, with the IRF region shaded in red. (b) Trimmed decay histogram obtained after removing data points up to the full width at half maximum of the IRF peak. The trimmed histogram is used as input for subsequent multi-exponential fitting. IRF: instrument response function.

Step 1. Multi-exponential fitting and component classification

The trimmed decay of each cell is first fitted with a three-component exponential model,⁶³

$$I(t) = \sum_{i=1}^3 A_i \exp(-t/\tau_i), \quad (3.4)$$

to capture contributions from the biological signal, autofluorescence, and residual background. Each component is characterized by a decay constant τ_i and a relative amplitude A_i . To identify the component corresponding to the voltage-sensitive Ace2N-mNeon signal, we apply the following criteria:⁶³

- **Biological range:** candidate lifetimes must fall within the experimentally calibrated range of 2.5 to 3.5 ns.
- **Amplitude dominance:** the amplitude of the biological component must contribute more than 50% of the total fitted amplitude.
- **Goodness of fit:** the reduced chi-square of the fit must lie between 0.8 and 1.5, consistent with an adequate description of the data at the measured photon counts.⁶⁴

If these criteria are not met for any component in the initial three-exponential fit, the model order is reduced and the decay is refitted with a bi-exponential model. Components that clearly fall outside the biological range or have very small amplitudes are interpreted as autofluorescence or background and are excluded from further consideration.

In practice, several typical situations occur:

- **Ideal case:** a single component lies within 2.5 to 3.5 ns, has the largest amplitude, and the overall fit satisfies the chi-square criterion. In this case, the corresponding τ_i is provisionally accepted as the cell lifetime.
- **No biological component:** none of the components fall within the biological range. The decay is considered dominated by noise or non-specific signals, and no lifetime is assigned.
- **Ambiguous case:** more than one component lies within the biological range, or the putative biological component does not dominate the amplitude. These decays are carried forward to the next step for additional refinement and noise removal rather than being immediately accepted.

Examples of three- and bi-exponential fits, together with their parameter tables and chi-square values, are shown in Supplementary Fig. S3.11 and Supplementary Fig. S3.12.

Step 2. Noise removal on logarithmic decays

To further suppress contributions from autofluorescence and background, the fitted components and the measured decay are examined on a semi-logarithmic scale, where exponential decays appear as straight segments. Using the fits from Step 1, we locate intersection points between the putative biological component and the faster or slower

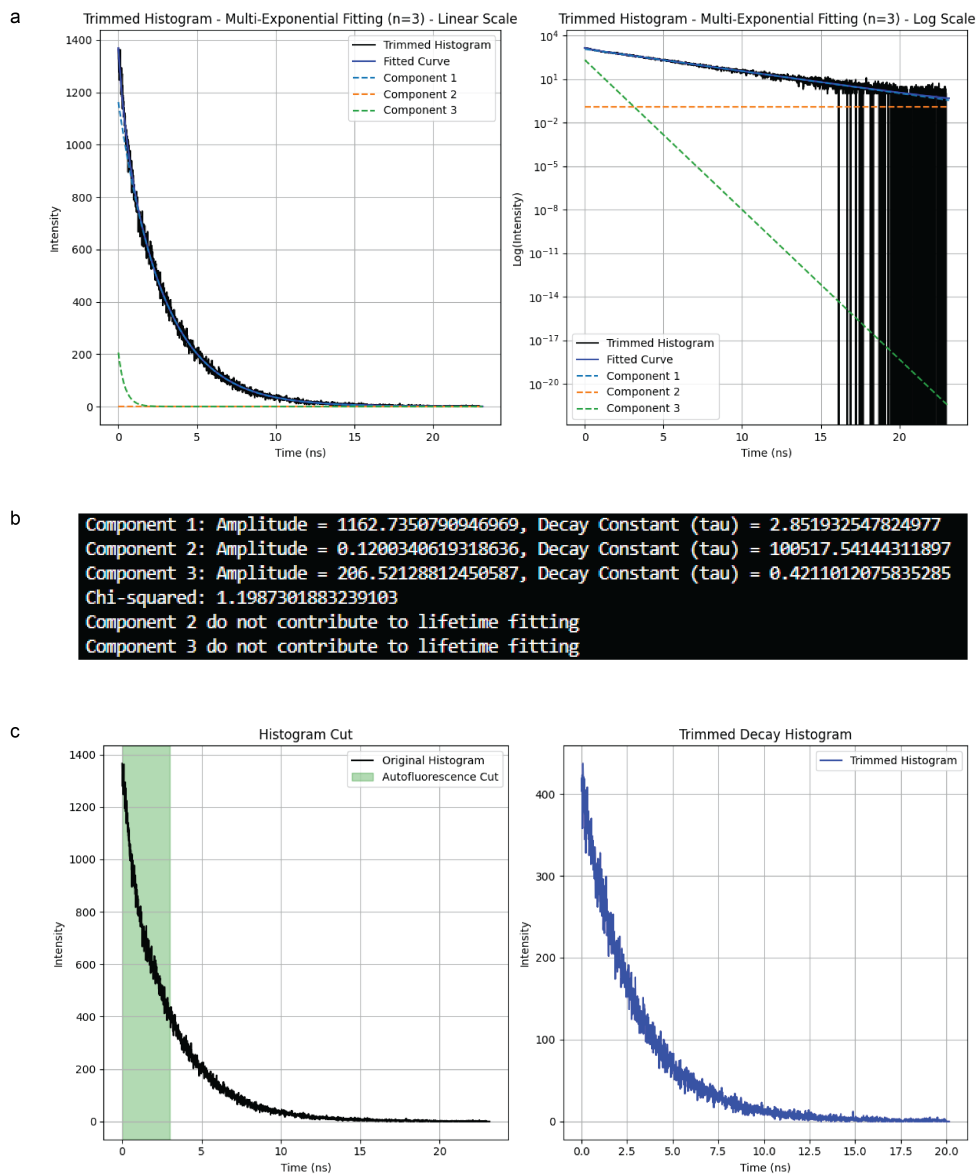


Figure S3.11: **Tri-component fitting and removal of fast autofluorescence.** (a) Trimmed decay histogram fitted with a tri-exponential model, shown on linear (left) and logarithmic (right) scales. Individual decay components and the overall fit are plotted separately. (b) Example of fitted parameters for the three components, including amplitudes, decay constants and reduced chi-square, illustrating that only one component lies within the biologically relevant lifetime range. (c) Illustration of early-time truncation used to remove the fast autofluorescence dominated component, with the removed region shaded in green and the resulting trimmed histogram shown on the right.

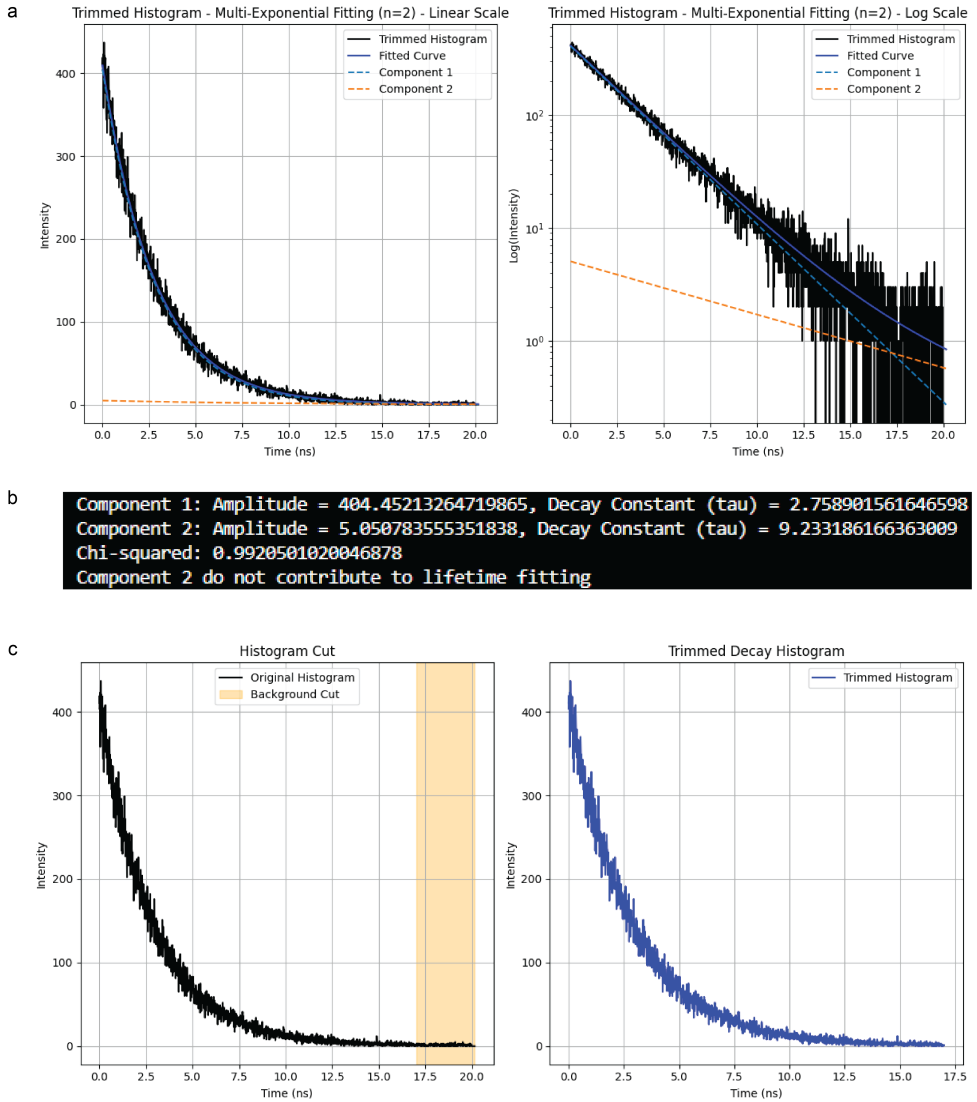


Figure S3.12: **Bi-exponential fitting and removal of late background noise.** (a) Bi-exponential fit to the trimmed decay histogram on linear (left) and logarithmic (right) scales, after removal of the fast autofluorescence component. (b) Example of fitted parameters for the two remaining components, showing that the long lived, low amplitude component is attributed to residual background. (c) Illustration of late-time truncation used to remove background dominated tail contributions, with the removed region shaded in yellow and the final trimmed histogram shown on the right.

components attributed to autofluorescence or background. These intersection points define candidate boundaries for trimming the measured histogram:

- If an intersection is detected on the rising side of the biological component, the earlier time bins are removed to eliminate fast, short-lifetime contributions.
- If an intersection is detected on the tail, the late bins are removed to suppress long-lived, background-dominated photons.
- If no clear intersection can be identified, the decay is left untrimmed at that end to avoid overcorrection.

This procedure, illustrated in Supplementary Fig. [S3.11](#) and Supplementary Fig. [S3.12](#), yields a refined decay that is expected to be dominated by a single biological component and is suitable for final single-exponential fitting.

Step 3. Single exponential fitting and quality criteria

After noise removal, the remaining histogram for each cell is fitted with a single exponential model,

$$I(t) = A \exp(-t/\tau_{fl}), \quad (3.5)$$

to obtain the final τ_{fl} estimate (Supplementary Fig. S3.13). The resulting fit is evaluated using two criteria:

- **Biological range:** τ_{fl} must lie within 2.5 to 3.5 ns.
- **Goodness of fit:** the reduced chi-square must be between 0.8 and 1.5.⁶³

If both criteria are satisfied, the fitted decay constant is accepted as the lifetime value for that cell. If not, the cell is marked as having no reliable lifetime estimate and is excluded from downstream quantitative analyses.

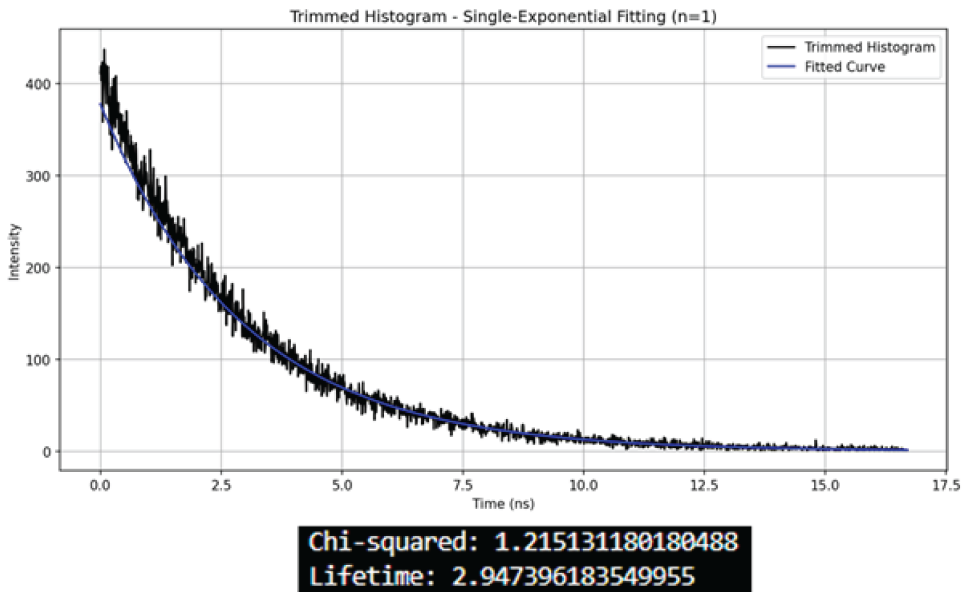


Figure S3.13: **Final single-exponential fit used to extract cell-based fluorescence lifetimes.** Trimmed decay histogram for one example cell (black) together with the best single exponential fit (blue). The reported lifetime and reduced chi-square values correspond to the voltage-sensitive component that passes all predefined quality criteria.

Step 4. Cell type specific model selection

During method development, we observed that the optimal lifetime feature for separating cell populations depends on both the fitting model and the cell type. To formalize this observation, we assembled τ_{fl} values obtained from single-, bi-, and tri-exponential fits for each cell, and performed principal component analysis on this multidimensional

feature set. Clustering with k -means on the PCA-transformed data yielded cell type classification accuracies ranging from 70% to 100%, with F1 scores ranging from 65% to 100%, indicating that no single model order is universally optimal.

Based on these analyses and on the known optical properties of different tissues, we adopted a cell type specific assignment strategy:

- **Cardiomyocytes and skeletal muscle cells** are assigned the lifetime obtained from the single exponential fit, which adequately describes their relatively homogeneous membrane signals.
- **Epithelial cells** retain the lifetime associated with the dominant component of the tri-exponential model, which better captures their complex membrane and submembrane structure.
- **Neurons** are assigned lifetimes from the bi-exponential fit, reflecting the frequent presence of a second, slower component that likely arises from local background and fine neuronal processes.

Cells that fail the quality criteria for all fitting models are discarded, as they are likely contaminated by motion artefacts, segmentation errors, or very low photon counts. In this way, each accepted cell is associated with a single biologically interpretable τ_{fl} value, while the overall pipeline maintains strict control over fitting quality. The complete computation workflow is summarized in Supplementary Fig. S3.6c.

REFINEMENTS AND FUTURE DIRECTIONS FOR OUR ANALYSIS PIPELINE

Our current analysis pipeline was deliberately designed to be conservative. Across datasets, only about 65% of segmented and pre-selected cells pass all lifetime computation criteria and are included in the final statistics. This strict filtering helps ensure that reported τ_{fl} values are robust, but it also limits sample size and may discard cells that visually appear well segmented and reasonably bright. Below, we briefly outline potential refinements that might increase data retention while preserving reliability. These refinements were not applied to the analyses presented in this chapter and are therefore discussed as future directions rather than as part of the validated pipeline.

Tiered classification rather than hard exclusion

Instead of treating the quality criteria as absolute pass or fail thresholds, cells can be grouped into three categories. **Category 1** contains cells that fully meet the biological-range and chi-square criteria and are used for primary statistical analyses. **Category 2** contains cells that fail a single criterion by a small margin, for example, slightly elevated chi-square despite a clear membrane signal, and can be retained for exploratory or sensitivity analyses with appropriate marking as lower-confidence measurements. **Category 3** contains cells with obvious artefacts, poor segmentation or extremely low photon counts and remains excluded. This tiered scheme would make the filtering more transparent and could reduce unnecessary loss of usable data in future implementations.

Adaptive use of fitted components and histogram trimming

Currently, histogram trimming is only applied when fitted components exhibit clear separation. In some cases, this conservative rule may prevent the removal of weak but distinct noise components. A possible refinement is to introduce a minimum contribution threshold for secondary components, for example, between 5% and 40%, and to allow trimming when a component exceeds this threshold, even if its lifetime partially overlaps with that of the biological component. Such thresholds would need to be calibrated empirically, for example by parameter sweeps on representative datasets and by comparing lifetime distributions before and after trimming, and ambiguous cases could be flagged for manual inspection instead of being automatically rejected.⁶³

Improved membrane pixel selection

The current membrane extraction uses fixed dilation and erosion widths for each cell type, which may not be optimal for very small or very large cells. A more adaptive approach would select membrane pixels based on a fraction of the cell area and could assign lower weights to pixels further from the segmented membrane when summing decay histograms. This type of adaptive weighting could further reduce contamination from cytoplasmic or background fluorescence, particularly in regions with strong intensity gradients, but will require careful benchmarking to avoid introducing bias.

Context-dependent relaxation of the chi-square thresholds and secondary review

Our present chi-square acceptance window of 0.8 to 1.5 is intentionally narrow. Preliminary tests suggest that modestly relaxing the upper bound to values around 2.0, combined with explicit flagging of these higher chi-square fits, would increase the number of usable cells without markedly changing the overall lifetime distributions. In parallel, storing basic metadata for rejected cells, such as photon counts, segmentation scores and fitted parameters, would enable systematic secondary review and help identify recurring reasons for failure. Simple machine learning or clustering analyses on this metadata could guide further algorithmic improvements.

Taken together, these planned refinements aim to make the pipeline more adaptive while preserving its core strengths. In particular, combining tiered quality labels, more flexible use of fitted components, improved membrane pixel selection and structured review of borderline or rejected cells should, after proper validation, allow higher data inclusion rates and more representative statistics without compromising the biological interpretability of the extracted τ_{fl} values.

CELL-BASED FLUORESCENCE LIFETIME VISUALIZATION

2D visualization

To integrate fluorescence lifetime information into spatial maps, we used a composite representation based on the HSV (Hue, Saturation, Value) color model. Segmented cells were first assigned a single τ_{fl} value by the analysis pipeline described above, and these per-cell lifetimes were then combined with the corresponding intensity images. In this representation,

- **Hue (H)** encodes fluorescence lifetime, mapping the continuous range of τ_{fl} values to colors along a perceptually ordered colormap.
- **Saturation (S)** is fixed to 1 to maintain vivid colors across the image.
- **Value (V)** represents brightness and is derived from the underlying intensity image using normalized photon counts so that local contrast is preserved.

This approach enables simultaneous visualization of spatial intensity and lifetime variation at the single-cell level. A schematic of the 2D mapping workflow is shown in Supplementary Fig. S3.14.

To map lifetime values effectively, the colormap must (i) provide clearly distinguishable tones across the τ_{fl} range, (ii) maintain approximately uniform brightness so that color does not confound the intensity channel, and (iii) be continuous, since τ_{fl} varies over a range rather than discrete classes. We evaluated several commonly used perceptually uniform colormaps from Matplotlib and found that truncated versions of Viridis and Plasma offered a good compromise between contrast and uniformity.⁶⁵ Cells with lifetimes close to the minimum tended to be mapped to very dark colors, which reduced contrast against the black background. To mitigate this, we used a truncated Plasma colormap in which the darkest approximately 30% of the scale was removed, and the remaining part was linearly rescaled. This preserves smooth color transitions while enhancing contrast for low τ_{fl} values.

Together, the HSV encoding and truncated Plasma colormap yield 2D maps in which lifetime differences across cells and tissues can be visually inspected without obscuring underlying intensity structure, while all quantitative analyses are performed on the underlying numerical τ_{fl} values rather than on the color representation.

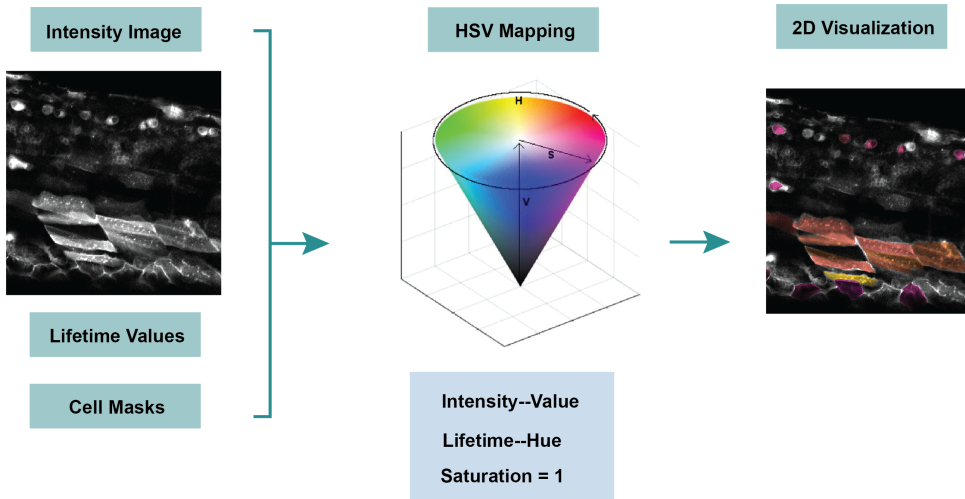


Figure S3.14: **Schematic of 2D cell-based fluorescence lifetime visualization.** Intensity images, cell masks, and per-cell lifetime values are combined using an HSV mapping, where lifetime is encoded in hue, intensity in value, and saturation is fixed to 1.

3D visualization

While confocal FLIM provides z-stacks of depth-resolved layers, conventional 2D projections are often insufficient to appreciate tissue-scale patterns and cell-cell relationships. Therefore, for selected datasets, we generated qualitative 3D renderings to visualize how cell-based τ_{fl} values are distributed across the embryo volume.⁵⁷

Z-stack FLIM images were acquired with a step size of 3 μm and reconstructed into volumetric datasets in ImageJ. Because the axial sampling is coarser than the lateral resolution and the number of acquired planes is limited, we used an interpolation-based strategy to increase the apparent z sampling before rendering. Intermediate layers were synthesized between consecutive FLIM planes using FILM, an open source neural network originally developed for video frame interpolation.⁵⁷ In our implementation, two consecutive lifetime images were provided as input, and a single intermediate plane was generated, which was then inserted between the originals to create a denser stack for visualization. Architectural details of FILM and its training procedure follow the original publication and were not modified for this work.⁵⁷

Using these interpolated stacks, we generated two types of 3D FLIM visualizations: volume renderings and maximum intensity projections, both with τ_{fl} encoded in color using the same HSV and Plasma-based scheme as in 2D. Typical examples are shown in Fig. 3.1c, where single planes, volume views, and projections of the trunk muscle are compared. In this work, 3D renderings are used only for qualitative illustration of tissue scale organization and not for any quantitative voltage analysis, so potential interpolation artefacts do not affect the main conclusions.

In practice, the 3D renderings are limited by the available z-sampling and signal at depth and are therefore used here only as qualitative illustrations. Taken together, the 2D and 3D visualization tools described above provide a way to view calibrated, cell-based τ_{fl} values from individual cells up to whole organs, while all numerical analyses are carried out in the 2D cell-based framework described above.

BIBLIOGRAFIE

- [1] Michael Levin. “Molecular bioelectricity in developmental biology: New tools and recent discoveries”. In: *BioEssays* 34 (3 mrt 2012), p. 205–217. ISSN: 02659247. DOI: [10.1002/bies.201100136](https://doi.org/10.1002/bies.201100136). PMID: [22237730](https://pubmed.ncbi.nlm.nih.gov/22237730/).
- [2] Michael Levin. “Molecular bioelectricity: How endogenous voltage potentials control cell behavior and instruct pattern regulation in vivo”. In: *Molecular Biology of the Cell* 25 (24 dec 2014), p. 3835–3850. ISSN: 19394586. DOI: [10.1091/mbc.E13-12-0708](https://doi.org/10.1091/mbc.E13-12-0708). PMID: [25425556](https://pubmed.ncbi.nlm.nih.gov/25425556/).
- [3] Laura Faith George en Emily Anne Bates. “Mechanisms Underlying Influence of Bioelectricity in Development”. In: *Frontiers in Cell and Developmental Biology* 10 (feb 2022). ISSN: 2296-634X. DOI: [10.3389/fcell.2022.772230](https://doi.org/10.3389/fcell.2022.772230).
- [4] Bruce P. Bean. “The action potential in mammalian central neurons”. In: *Nature Reviews Neuroscience* 8 (6 jun 2007), p. 451–465. ISSN: 1471-003X. DOI: [10.1038/nrn2148](https://doi.org/10.1038/nrn2148).
- [5] Vaibhav P. Pai e.a. “Endogenous Gradients of Resting Potential Instructively Pattern Embryonic Neural Tissue via Notch Signaling and Regulation of Proliferation”. In: *The Journal of Neuroscience* 35 (10 mrt 2015), p. 4366–4385. ISSN: 0270-6474. DOI: [10.1523/JNEUROSCI.1877-14.2015](https://doi.org/10.1523/JNEUROSCI.1877-14.2015).
- [6] Sarah Sundelacruz, Michael Levin en David L. Kaplan. “Role of Membrane Potential in the Regulation of Cell Proliferation and Differentiation”. In: *Stem Cell Reviews and Reports* 5 (3 sep 2009), p. 231–246. ISSN: 1550-8943. DOI: [10.1007/s12015-009-9080-2](https://doi.org/10.1007/s12015-009-9080-2).
- [7] Vaibhav P. Pai e.a. “HCN4 ion channel function is required for early events that regulate anatomical left-right patterning in a nodal and lefty asymmetric gene expression-independent manner”. In: *Biology Open* 6.10 (2017), p. 1445–1457. DOI: [10.1242/bio.026583](https://doi.org/10.1242/bio.026583).
- [8] Wendy Scott Beane et al. “Bioelectric signaling regulates head and organ size during planarian regeneration”. In: *Development (Cambridge)* 140 (2 2013), p. 313–322. ISSN: 09501991. DOI: [10.1242/dev.086900](https://doi.org/10.1242/dev.086900). PMID: [23250205](https://pubmed.ncbi.nlm.nih.gov/23250205/).
- [9] Alexis Pietak en Michael Levin. “Bioelectrical control of positional information in development and regeneration: A review of conceptual and computational advances”. In: *Progress in Biophysics and Molecular Biology* 137 (sep 2018), p. 52–68. ISSN: 00796107. DOI: [10.1016/j.pbiomolbio.2018.03.008](https://doi.org/10.1016/j.pbiomolbio.2018.03.008).
- [10] Martin R. Silic en GuangJun Zhang. “Bioelectricity in Developmental Patterning and Size Control: Evidence and Genetically Encoded Tools in the Zebrafish Model”. In: *Cells* 12 (8 apr 2023), p. 1148. ISSN: 2073-4409. DOI: [10.3390/cells12081148](https://doi.org/10.3390/cells12081148).

- [11] Lisa S. Jenkins, Bradley S. Duerstock en Richard B. Borgens. “Reduction of the Current of Injury Leaving the Amputation Inhibits Limb Regeneration in the Red Spotted Newt”. In: *Developmental Biology* 178 (2 sep 1996), p. 251–262. ISSN: 00121606. DOI: [10.1006/dbio.1996.0216](https://doi.org/10.1006/dbio.1996.0216).
- [12] Angela-S. Tseng e.a. “Induction of Vertebrate Regeneration by a Transient Sodium Current”. In: *The Journal of Neuroscience* 30.39 (2010), p. 13192–13200. DOI: [10.1523/JNEUROSCI.3315-10.2010](https://doi.org/10.1523/JNEUROSCI.3315-10.2010).
- [13] Dany S. Adams, Alessio Masi en Michael Levin. “H⁺ pump-dependent changes in membrane voltage are an early mechanism necessary and sufficient to induce *Xenopus* tail regeneration”. In: *Development* 134 (7 apr 2007), p. 1323–1335. ISSN: 1477-9129. DOI: [10.1242/dev.02812](https://doi.org/10.1242/dev.02812).
- [14] Edith Chorev e.a. “Electrophysiological recordings from behaving animals—going beyond spikes”. In: *Current Opinion in Neurobiology* 19 (5 okt 2009), p. 513–519. ISSN: 09594388. DOI: [10.1016/j.conb.2009.08.005](https://doi.org/10.1016/j.conb.2009.08.005).
- [15] Adam E. Cohen en Veena Venkatachalam. “Bringing Bioelectricity to Light”. In: *Annual Review of Biophysics* 43 (1 mei 2014), p. 211–232. ISSN: 1936-122X. DOI: [10.1146/annurev-biophys-051013-022717](https://doi.org/10.1146/annurev-biophys-051013-022717).
- [16] Thomas Knöpfel en Chenchen Song. “Optical voltage imaging in neurons: moving from technology development to practical tool”. In: *Nature Reviews Neuroscience* 20 (12 dec 2019), p. 719–727. ISSN: 1471-003X. DOI: [10.1038/s41583-019-0231-4](https://doi.org/10.1038/s41583-019-0231-4).
- [17] Zeguan Wang e.a. “Imaging the voltage of neurons distributed across entire brains of larval zebrafish”. In: *bioRxiv* (jan 2023), p. 2023.12.15.571964. DOI: [10.1101/2023.12.15.571964](https://doi.org/10.1101/2023.12.15.571964). URL: <http://biorxiv.org/content/early/2023/12/16/2023.12.15.571964.abstract>.
- [18] Kristin Scott e.a. “Fast two-photon imaging of subcellular voltage dynamics in neuronal tissue with genetically encoded indicators”. In: *Elife* 6 (2017).
- [19] V. Biasci e.a. “Optogenetic manipulation of cardiac electrical dynamics using sub-threshold illumination: dissecting the role of cardiac alternans in terminating rapid rhythms”. In: *Basic Research in Cardiology* 117 (1 dec 2022), p. 25. ISSN: 0300-8428. DOI: [10.1007/s00395-022-00933-8](https://doi.org/10.1007/s00395-022-00933-8).
- [20] Jennifer Hou et al. “Simultaneous mapping of membrane voltage and calcium in zebrafish heart in vivo reveals chamber-specific developmental transitions in ionic currents”. In: *Frontiers in Physiology* 5 (2014). ISSN: 1664042X. DOI: [10.3389/fphys.2014.00344](https://doi.org/10.3389/fphys.2014.00344).
- [21] Bill Z. Jia e.a. “A bioelectrical phase transition patterns the first vertebrate heartbeats”. In: *Nature* 622 (7981 okt 2023), p. 149–155. ISSN: 0028-0836. DOI: [10.1038/s41586-023-06561-z](https://doi.org/10.1038/s41586-023-06561-z).
- [22] Julia R. Lazzari-Dean, Anneliese M.M. Gest en Evan W. Miller. “Measuring Absolute Membrane Potential Across Space and Time”. In: *Annual Review of Biophysics* 50 (1 mei 2021), p. 447–468. ISSN: 1936-122X. DOI: [10.1146/annurev-biophys-062920-063555](https://doi.org/10.1146/annurev-biophys-062920-063555).

- [23] Dmitrii M. Nikolaev e.a. “Fluorescence Imaging of Cell Membrane Potential: From Relative Changes to Absolute Values”. In: *International Journal of Molecular Sciences* 24 (3 jan 2023), p. 2435. ISSN: 1422-0067. DOI: [10.3390/ijms24032435](https://doi.org/10.3390/ijms24032435).
- [24] Daan Brinks, Aaron J. Klein en Adam E. Cohen. “Two-Photon Lifetime Imaging of Voltage Indicating Proteins as a Probe of Absolute Membrane Voltage”. In: *Biophysical Journal* 109 (5 sep 2015), p. 914–921. ISSN: 15420086. DOI: [10.1016/j.bpj.2015.07.038](https://doi.org/10.1016/j.bpj.2015.07.038). PMID: [26331249](https://pubmed.ncbi.nlm.nih.gov/26331249/).
- [25] Julia R Lazzari-Dean, Anneliese MM Gest en Evan W Miller. “Optical estimation of absolute membrane potential using fluorescence lifetime imaging”. In: *eLife* 8 (sep 2019). ISSN: 2050-084X. DOI: [10.7554/eLife.44522](https://doi.org/10.7554/eLife.44522).
- [26] Mikhail Y. Berezin en Samuel Achilefu. “Fluorescence Lifetime Measurements and Biological Imaging”. In: *Chemical Reviews* 110 (5 mei 2010), p. 2641–2684. ISSN: 0009-2665. DOI: [10.1021/cr900343z](https://doi.org/10.1021/cr900343z).
- [27] Joseph R. Lakowicz. *Principles of Fluorescence Spectroscopy*. Red. door Joseph R. Lakowicz. Boston, MA: Springer US, 2006. ISBN: 978-0-387-31278-1. DOI: [10.1007/978-0-387-46312-4](https://doi.org/10.1007/978-0-387-46312-4).
- [28] Tae-Young Choi et al. “Zebrafish as an animal model for biomedical research”. In: *Experimental and Molecular Medicine* 53 (3 mrt 2021), p. 310–317. ISSN: 1226-3613. DOI: [10.1038/s12276-021-00571-5](https://doi.org/10.1038/s12276-021-00571-5).
- [29] Jordan T. Shin en Mark C. Fishman. “From Zebrafish to human: modular medical models”. In: *Annual Review of Genomics and Human Genetics* 3 (1 sep 2002), p. 311–340. ISSN: 1527-8204. DOI: [10.1146/annurev.genom.3.031402.131506](https://doi.org/10.1146/annurev.genom.3.031402.131506).
- [30] Y. Gong e.a. “High-speed recording of neural spikes in awake mice and flies with a fluorescent voltage sensor”. In: *Science* 350 (6266 dec 2015), p. 1361–1366. ISSN: 0036-8075. DOI: [10.1126/science.aab0810](https://doi.org/10.1126/science.aab0810).
- [31] ZhenZhen Wu e.a. *Exploring Bioelectricity with Ace2N-mNeon during Zebrafish Embryogenesis*. Dec 2024. DOI: [10.1101/2024.12.12.628143](https://doi.org/10.1101/2024.12.12.628143).
- [32] Klaus Suhling e.a. “Fluorescence lifetime imaging (FLIM): Basic concepts and some recent developments”. In: *Medical Photonics* 27 (mei 2015), p. 3–40. ISSN: 2213-8846. DOI: [10.1016/J.MEDPHO.2014.12.001](https://doi.org/10.1016/J.MEDPHO.2014.12.001).
- [33] Wolfgang Becker. *Advanced Time-Correlated Single Photon Counting Techniques*. Red. door A. W. Castleman, J. P. Toennies en W. Zinth. Deel 81. Berlin: Springer Berlin, Heidelberg, 2005. ISBN: 978-3-540-26047-9. DOI: [10.1007/3-540-28876-0](https://doi.org/10.1007/3-540-28876-0).
- [34] Jeanne M. Nerbonne en Robert S. Kass. “Molecular Physiology of Cardiac Repolarization”. In: *Physiological Reviews* 85 (4 okt 2005), p. 1205–1253. ISSN: 0031-9333. DOI: [10.1152/physrev.00002.2005](https://doi.org/10.1152/physrev.00002.2005).
- [35] Nicholas C. Spitzer. “Electrical activity in early neuronal development”. In: *Nature* 444 (7120 dec 2006), p. 707–712. ISSN: 0028-0836. DOI: [10.1038/nature05300](https://doi.org/10.1038/nature05300).
- [36] Bertil Hille. *Ion channels of excitable membranes*. 3rd ed. Sunderland, Mass: Sinauer, 2001, p. 814.

- [37] Christian Mosimann e.a. “Ubiquitous transgene expression and Cre-based recombination driven by the ubiquitin promoter in zebrafish”. In: *Development* 138 (1 jan 2011), p. 169–177. ISSN: 09501991. DOI: [10.1242/dev.059345](https://doi.org/10.1242/dev.059345). PMID: [21138979](https://pubmed.ncbi.nlm.nih.gov/21138979/).
- [38] Richard Binggeli en Roy C. Weinstein. “Membrane potentials and sodium channels: Hypotheses for growth regulation and cancer formation based on changes in sodium channels and gap junctions”. In: *Journal of Theoretical Biology* 123 (4 dec 1986), p. 377–401. ISSN: 00225193. DOI: [10.1016/S0022-5193\(86\)80209-0](https://doi.org/10.1016/S0022-5193(86)80209-0).
- [39] Charles B. Kimmel e.a. “Stages of embryonic development of the zebrafish”. In: *Developmental Dynamics* 203 (3 jul 1995), p. 253–310. ISSN: 1058-8388. DOI: [10.1002/aja.1002030302](https://doi.org/10.1002/aja.1002030302).
- [40] Heather L. Stickney, Michael J. F. Barresi en Stephen H. Devoto. “Somite development in zebrafish”. In: *Developmental Dynamics* 219.3 (nov 2000), p. 287–303. DOI: [10.1002/1097-0177\(200011\)219:3<287::AID-DVDY1065>3.0.CO;2-A](https://doi.org/10.1002/1097-0177(200011)219:3<287::AID-DVDY1065>3.0.CO;2-A).
- [41] Chris S. Blagden e.a. “Notochord induction of zebrafish slow muscle mediated by *Sonichedghog*”. In: *Genes and Development* 11 (17 sep 1997), p. 2163–2175. ISSN: 0890-9369. DOI: [10.1101/gad.11.17.2163](https://doi.org/10.1101/gad.11.17.2163).
- [42] Jacqueline Fischer-Lougheed en Laurent Bernheim. “Human Myoblast Fusion Requires Expression of Functional Inward Rectifier Kir2.1 Channels”. In: *J Cell Biol* 153 (4 2001), p. 677–686.
- [43] Stéphane Konig e.a. “Membrane Hyperpolarization Triggers Myogenin and Myocyte Enhancer Factor-2 Expression during Human Myoblast Differentiation”. In: *Journal of Biological Chemistry* 279 (27 jul 2004), p. 28187–28196. ISSN: 00219258. DOI: [10.1074/jbc.M313932200](https://doi.org/10.1074/jbc.M313932200).
- [44] Valérie Hinard e.a. “Initiation of human myoblast differentiation via dephosphorylation of Kir2.1 K⁺ channels at tyrosine 242”. In: *Development* 135 (5 mrt 2008), p. 859–867. ISSN: 1477-9129. DOI: [10.1242/dev.011387](https://doi.org/10.1242/dev.011387).
- [45] Jae-Yong Park e.a. “Role of Hyperpolarization Attained by Linoleic Acid in Chick Myoblast Fusion”. In: *Experimental Cell Research* 251 (2 sep 1999), p. 307–317. ISSN: 00144827. DOI: [10.1006/excr.1999.4579](https://doi.org/10.1006/excr.1999.4579).
- [46] Roman Tyzio e.a. “Membrane Potential of CA3 Hippocampal Pyramidal Cells During Postnatal Development”. In: *Journal of Neurophysiology* 90 (5 nov 2003), p. 2964–2972. ISSN: 0022-3077. DOI: [10.1152/jn.00172.2003](https://doi.org/10.1152/jn.00172.2003).
- [47] Vaibhav P. Pai e.a. “HCN2 Rescues brain defects by enforcing endogenous voltage pre-patterns”. In: *Nature Communications* 9 (1 mrt 2018), p. 998. ISSN: 2041-1723. DOI: [10.1038/s41467-018-03334-5](https://doi.org/10.1038/s41467-018-03334-5).
- [48] M. B. Rook e.a. “Biology of cardiac sodium channel Nav1.5 expression”. In: *Cardiovascular Research* 93 (1 jan 2012), p. 12–23. ISSN: 0008-6363. DOI: [10.1093/cvr/cvr252](https://doi.org/10.1093/cvr/cvr252).
- [49] Nathan C. Shaner e.a. “A bright monomeric green fluorescent protein derived from *Branchiostoma lanceolatum*”. In: *Nature Methods* 10 (5 mei 2013), p. 407–409. ISSN: 15487091. DOI: [10.1038/nmeth.2413](https://doi.org/10.1038/nmeth.2413). PMID: [23524392](https://pubmed.ncbi.nlm.nih.gov/23524392/).

- [50] Michael Levin, Giovanni Pezzulo en Joshua M Finkelstein. “Endogenous Bioelectric Signaling Networks: Exploiting Voltage Gradients for Control of Growth and Form”. In: *Annu Rev Biomed Eng* 19 (2017), p. 353–387.
- [51] Luis F. Santana, Edward P. Cheng en W. Jonathan Lederer. “How does the shape of the cardiac action potential control calcium signaling and contraction in the heart?” In: *Journal of Molecular and Cellular Cardiology* 49 (6 dec 2010), p. 901–903. ISSN: 00222828. DOI: [10.1016/j.yjmcc.2010.09.005](https://doi.org/10.1016/j.yjmcc.2010.09.005).
- [52] Richard Mark White e.a. “Transparent Adult Zebrafish as a Tool for In Vivo Transplantation Analysis”. In: *Cell Stem Cell* 2 (2 feb 2008), p. 183–189. ISSN: 19345909. DOI: [10.1016/j.stem.2007.11.002](https://doi.org/10.1016/j.stem.2007.11.002). PMID: 18371439.
- [53] Koichi Kawakami. *Tol2: A versatile gene transfer vector in vertebrates*. Okt 2007. DOI: [10.1186/gb-2007-8-s1-s7](https://doi.org/10.1186/gb-2007-8-s1-s7). PMID: 18047699.
- [54] Xin Meng e.a. “A compact microscope for voltage imaging”. In: *Journal of Optics* 24 (5 mei 2022), p. 054004. ISSN: 2040-8978. DOI: [10.1088/2040-8986/ac5dd5](https://doi.org/10.1088/2040-8986/ac5dd5).
- [55] Sumeet Rohilla. “readPTU_FLIM”. In: (n.d.). GitHub repository. URL: https://github.com/SumeetRohilla/readPTU_FLIM (bezocht op 05-01-2026).
- [56] Marius Pachitariu en Carsen Stringer. “Cellpose 2.0: how to train your own model”. In: *Nature Methods* 19 (12 dec 2022), p. 1634–1641. ISSN: 1548-7091. DOI: [10.1038/s41592-022-01663-4](https://doi.org/10.1038/s41592-022-01663-4).
- [57] Fitsum Reda e.a. “FILM: Frame Interpolation for Large Motion”. In: *arXiv:2202.04901* (2022).
- [58] Yu Qiao e.a. “Thresholding based on variance and intensity contrast”. In: *Pattern Recognition* 40 (2 feb 2007), p. 596–608. ISSN: 00313203. DOI: [10.1016/j.patcog.2006.04.027](https://doi.org/10.1016/j.patcog.2006.04.027).
- [59] Hassana Grema Kaganami en Zou Beiji. “Region-Based Segmentation versus Edge Detection”. In: IEEE, sep 2009, p. 1217–1221. ISBN: 978-1-4244-4717-6. DOI: [10.1109/IIH-MSP.2009.13](https://doi.org/10.1109/IIH-MSP.2009.13).
- [60] Yoshinobu Sato e.a. “Three-dimensional multi-scale line filter for segmentation and visualization of curvilinear structures in medical images”. In: *Medical Image Analysis* 2 (2 jun 1998), p. 143–168. ISSN: 13618415. DOI: [10.1016/S1361-8415\(98\)80009-1](https://doi.org/10.1016/S1361-8415(98)80009-1).
- [61] Kaiming He e.a. “Mask R-CNN”. In: *arXiv:1703.06870* (2017).
- [62] Anna Kreshuk en Chong Zhang. “Machine Learning: Advanced Image Segmentation Using ilastik”. In: 2019, p. 449–463. DOI: [10.1007/978-1-4939-9686-5_21](https://doi.org/10.1007/978-1-4939-9686-5_21).
- [63] Yahui Li e.a. “Investigations on Average Fluorescence Lifetimes for Visualizing Multi-Exponential Decays”. In: *Frontiers in Physics* 8 (okt 2020). ISSN: 2296-424X. DOI: [10.3389/fphy.2020.576862](https://doi.org/10.3389/fphy.2020.576862).
- [64] Darren A Smith e.a. “Analysis of time-correlated single photon counting data: a comparative evaluation of deterministic and probabilistic approaches”. In: *Methods and Applications in Fluorescence* 5 (4 okt 2017), p. 042001. ISSN: 2050-6120. DOI: [10.1088/2050-6120/aa8055](https://doi.org/10.1088/2050-6120/aa8055).

- [65] Matplotlib Development Team. “Choosing Colormaps in Matplotlib”. In: (n.d.). Matplotlib documentation. URL: <https://matplotlib.org/stable/users/explain/colors/colormaps.html>.

4

ENGINEERING FRET-BASED GEVIs FOR QUANTITATIVE ABSOLUTE VOLTAGE IMAGING: CONSTRAINTS AND DESIGN PRINCIPLES

This chapter aims to develop an electrochromic FRET-based voltage indicator that is compatible with the in vivo absolute voltage imaging framework presented in Chapter 3 and offers higher effective sensitivity than Ace2N-mNeon described in that chapter. We fused a bright fluorescent protein donor to the highly sensitive Gloeobacter rhodopsin (GR) mutant, built a focused linker library to tune donor-acceptor spacing, and characterized the resulting mNeonGR variants in HEK293T cells under whole cell voltage clamp with simultaneous fluorescence imaging. Although the constructs did not achieve the anticipated large negative-going voltage sensitivity, they consistently produced small positive donor responses. By combining control measurements with a minimal spectral perturbation model, we explain this polarity reversal, reveal how mutation and voltage reshape the GR absorption spectrum, and identify limitations in donor choice, FRET geometry, and screening strategy. These insights yield concrete design principles for next-generation GR-based voltage indicators that are optimized for absolute voltage FLIM and offer improved effective sensitivity.

This chapter is based on: *Engineering FRET-based GEVIs for quantitative absolute voltage imaging*, In preparation.

4.1. INTRODUCTION

BIOELECTRIC signals are key regulators of cell proliferation, migration, and tissue patterning throughout embryogenesis.^{1–3} Combining fluorescence lifetime imaging (FLIM) with genetically encoded voltage indicators (GEVIs) provides a promising route to quantitative readout of absolute membrane potential (V_m) in vivo, because fluorescence lifetime (τ_{fl}) is intrinsically ratiometric and largely independent of expression level and excitation intensity.^{4–8} In Chapter 3, we calibrated the τ_{fl} of Ace2N-mNeon as a function of V_m in HEK cells and applied this calibration to map resting V_m across multiple cell types in zebrafish embryos, demonstrating accurate in vivo reporting of absolute V_m during embryogenesis. However, indicators with higher effective sensitivity are required for millivolt (mV) scale tracking of V_m over hours to days in vivo, and this need remains a central limitation for broader and more precise use of absolute FLIM in development.

Most opsin-based GEVIs are impractical for in vivo FLIM because their emission is extremely dim and their fluorescence lifetimes are too short to be resolved clearly.^{9–11} Electrochromic FRET (eFRET) provides a route to these specifications by coupling an electrochromic opsin to a bright fluorescent donor while preserving the opsin voltage sensitivity.¹² Mechanistically, changes in V_m electrochromically shift opsin absorption and thereby modulate FRET and donor emission. These changes can be read out either as changes in donor intensity or as changes in donor lifetime (τ_D), and τ_D can be calibrated to absolute V_m .^{12–16}

However, existing eFRET-GEVIs remain limited for millivolt-scale tracking of resting potentials over hours to days.^{3,5} Ace2N-mNeon offers good brightness and lifetime accessibility, but provides only 8 to 13% $\Delta F/F$ per 100 mV, which constrains precision for small V_m shifts.^{5–7,16} More recently, Voltron2 (JF522 HaloTag) and Positron2 achieve substantially larger fractional fluorescence changes per 100 mV than the first generation eFRET GEVIs and excel at spike imaging.^{17,18} However, for the small (± 5 to 10 mV) fluctuations typical of non-excitabile cells and developing tissues, these amplitudes still translate into lifetime changes of only around 1%, which approaches the practical noise floor of high-speed, long-duration FLIM.^{5–7} In addition, dye-dependent designs require uniform, stable labeling in developing embryos and can be vulnerable to microenvironment-induced lifetime drifts that are unrelated to voltage.^{14,18} These constraints motivate the development of an eFRET-based GEVI with clearly improved effective sensitivity, sufficient baseline brightness, and an expanded voltage-dependent donor lifetime range suitable for developmental studies.

Gloeobacter rhodopsin (GR) from *Gloeobacter violaceus* is an attractive opsin scaffold due to its strong voltage-dependent electrochromism.^{19–21} In a directed-evolution screen, we identified GR-D115N, a variant that shows unusually large steady-state sensitivity, approximately 263.7% $\Delta F/F$ per 100 mV and roughly twentyfold higher than Ace2N-mNeon,^{16,22} with a dominant slow phase of around 40 ms that is acceptable for steady-state developmental readouts.²² However, GR-D115N is extremely dim at rest, and its intrinsic τ_{fl} is too short to be resolved with current single-photon detectors, which precludes direct τ_{fl} readout.²² To overcome this limitation, we adopted an eFRET design in which GR-D115N serves as the acceptor and a bright fluorescent donor is coupled to it, so that voltage-dependent changes in FRET render the signal accessible to FLIM while

retaining the intrinsic opsin sensitivity.²³

Building on prior eFRET opsin strategies, we designed and screened mNeonGreen-GR-D115N (mNeonGR) constructs.^{13,14,16} Unexpectedly, all variants produced small, positive donor signals on the order of 1 to 5% $\Delta F/F$ per 100 mV, instead of the robust negative-going responses expected for a conventional eFRET geometry, which prompted a mechanistic analysis of failure modes and design limitations.

In this chapter, we ask two questions: why does the highly sensitive electrochromic opsin GR-D115N fail to produce a negative eFRET readout when fused to mNeonGreen, and how do mutation- and voltage-driven spectral changes explain the observed polarity reversal. To address these questions, we combined high-speed voltage-clamp recordings with emission or absorption spectroscopy, and we built a minimal spectral perturbation model that maps mutation- and voltage-dependent spectral changes in GR-D115N onto the donor and acceptor signals. Our results reveal fundamental constraints on donor choice, FRET geometry, and screening strategy for high-sensitivity eFRET-GEVIs intended for absolute voltage FLIM. Based on these findings, we outline an evidence-driven, staged path toward a GR-based eFRET indicator that meets the required sensitivity, brightness, and lifetime for long-term in vivo FLIM of absolute V_m .

4.2. RESULTS

4.2.1. DESIGN OF THE eFRET-GEVI FOR FLIM

In a canonical electrochromic FRET voltage indicator, a depolarizing step enhances opsin absorption within the donor emission band, which increases the FRET efficiency (E_{FRET}) and quenches donor fluorescence. This produces a negative-going $\Delta F/F$ in the donor channel and a corresponding shortening of the donor lifetime (τ_D).^{14,16} Our goal was to engineer an eFRET-based GEVI that preserves the exceptional voltage sensitivity of GR-D115N while providing higher baseline brightness and a donor lifetime that can be read out by FLIM in vivo. Because E_{FRET} depends on voltage-dependent changes in opsin absorption and steeply on the center-to-center distance between donor and acceptor, scaling as r^{-6} , and on their relative dipole orientation through the Förster radius (R_0), typically a few nanometers for fluorescent protein pairs, we sought to maximize both the baseline E_0 and its voltage dependence by combining spectral matching with controlled geometry.^{12,24}

Spectral rationale. Because we did not measure the absorption spectrum of GR-D115N, our donor selection was guided by published spectra of wild-type GR (GR-WT), which shows broad absorption near 540 to 550 nm.²⁰ We therefore chose donors whose emission overlaps this band (Fig. 4.1b). Among the candidates, mNeonGreen, with an emission peak around 517 nm and a red shoulder, provided the best available overlap while offering high quantum yield and photostability.²⁵ This pairing was intended to raise the baseline E_0 and to provide a bright, lifetime-readable donor channel for FLIM measurements.

Geometry and linker library. To increase E_{FRET} , we shortened the distance between donor and acceptor by trimming predicted unstructured termini on both proteins. The

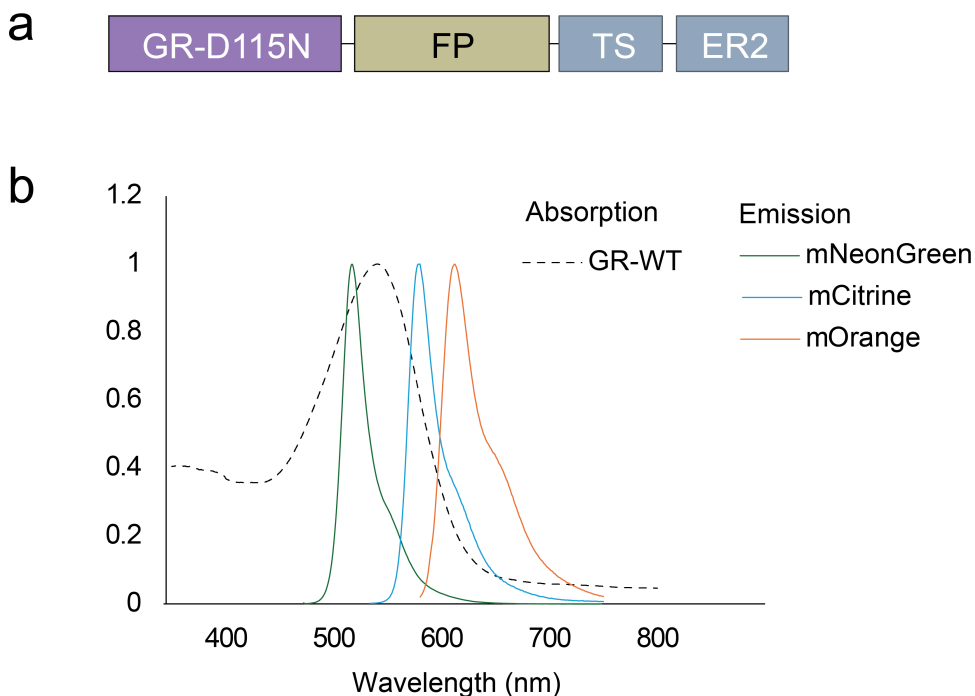


Figure 4.1: **Spectral matching for a GR-based eFRET-GEVI.** (a) Domain architecture. GR-D115N (acceptor) is fused to a fluorescent protein donor (FP), followed by a membrane trafficking sequence (TS) and an endoplasmic reticulum export motif (ER2). (b) Normalized spectra showing GR-WT absorption (dashed) and the emission of candidate donors (mNeonGreen, mCitrine, mOrange). mNeonGreen provides the greatest long-wavelength overlap with GR, motivating its selection as the donor. All spectra are peak-normalized for display.

carboxy (C) terminus of GR-D115N was truncated in single-residue steps, up to 24 residues, and the amino terminus of mNeonGreen was minimized based on prior work.^{16,20,25} The two domains were then joined with a short leucine-arginine (Leu-Arg) linker that had previously supported efficient FRET in a QuasAr2-mOrange construct.¹⁴ To sample a range of donor-to-acceptor spacings, we appended 1 to 9 additional residues after the donor minimal mNeonGreen amino terminus, generating a library that spans short, medium, and extended geometries (Fig. 4.2b).

Designs were screened with AlphaFold to confirm folding and membrane topology and to exclude gross clashes, not to infer donor-acceptor proximity.²⁶ We then tested whether these spectral and geometric choices yielded a high-efficiency, negative-going eFRET response in HEK293T cells.

4.2.2. CHARACTERIZATION OF mNEONGR IN HEK293T CELLS

To test whether mNeonGR variants could preserve the high voltage sensitivity of GR-D115N while producing the negative-going donor response expected for an eFRET geometry, we recorded donor signals from HEK293T cells expressing each construct under

6 cells per variant). Because additional variants fell within this same range and showed no qualitative differences, we presented three representative designs in Fig. 4.3, mNeonGR39, mNeonGR59, and mNeonGR65. Among the library variants, the best-performing variant, mNeonGR59, stood out because its donor response was reproducible, larger than those of the other variants, and showed clear kinetics. The steady-state amplitude of mNeonGR59 averaged approximately 4.5% $\Delta F/F$ per 100 mV, but was still much smaller than, and opposite in polarity to, the unfused GR-D115N acceptor response. Its donor waveform could be described by a biexponential fit with a dominant time constant on the order of 9 ms and a secondary faster component in the millisecond range (Fig. 4.3a-d). These kinetics are much faster than the approximately 40 ms slow phase of GR-D115N in the acceptor channel, consistent with a voltage-driven but modestly filtered signal.²²

Together, these data show that coupling mNeonGreen to GR-D115N did not yield the expected large, negative-going donor responses. Instead, all mNeonGR variants produced small positive donor signals, with mNeonGR59 providing the clearest but still low-amplitude example. This polarity reversal and limited effective sensitivity motivated the control experiments in Section 4.2.3, which quantify the contribution of instrument noise and optical bleed-through, and the spectral perturbation analysis in Section 4.2.4, which links mutation- and voltage-driven changes in the GR absorption spectrum to eFRET polarity and kinetics.

4.2.3. CONTROL EXPERIMENTS: INSTRUMENT NOISE AND OPTICAL BLEED-THROUGH

The mNeonGR recordings in Section 4.2.2 showed small, positive donor responses that were opposite in polarity to the negative-going signal expected from an eFRET indicator. To determine how much of these signals could arise from artifacts in the imaging system, we quantified two likely non-biological contributors: acceptor emission leaking into the donor detection channel and the optical and electronic noise floor of the instrument. Therefore, we performed three complementary control experiments using the same voltage protocol and detection settings as for mNeonGR.

Control 1. Acceptor only under 488 nm excitation, upper bound on leakage

Cells expressing GR-D115N alone were imaged with 488 nm excitation and donor-channel detection, matching the conditions used for the mNeonGR donor recordings. Under repeated 100 mV voltage steps from -70 mV to $+30$ mV, the donor-channel traces showed no resolvable voltage dependence and only small fluctuations of about 0.65% $\Delta F/F$ (Fig. 4.4a-c). We consider this an upper bound on direct acceptor-to-donor leakage in our setup, as any true donor contribution is absent under these conditions.

Control 2. Untransfected cells under 637 nm excitation, pure system floor

To measure system fluctuations in the absence of any fluorophore, untransfected HEK293T cells were imaged with 637 nm excitation while recording in the donor channel under the same voltage protocol and detection settings. These traces exhibited small synchronous changes of about 1.4% $\Delta F/F$ (Fig. 4.4d-f), reflecting the combined optical and electronic noise of the laser and detection path, as well as any voltage-locked motion or mechanical instability.

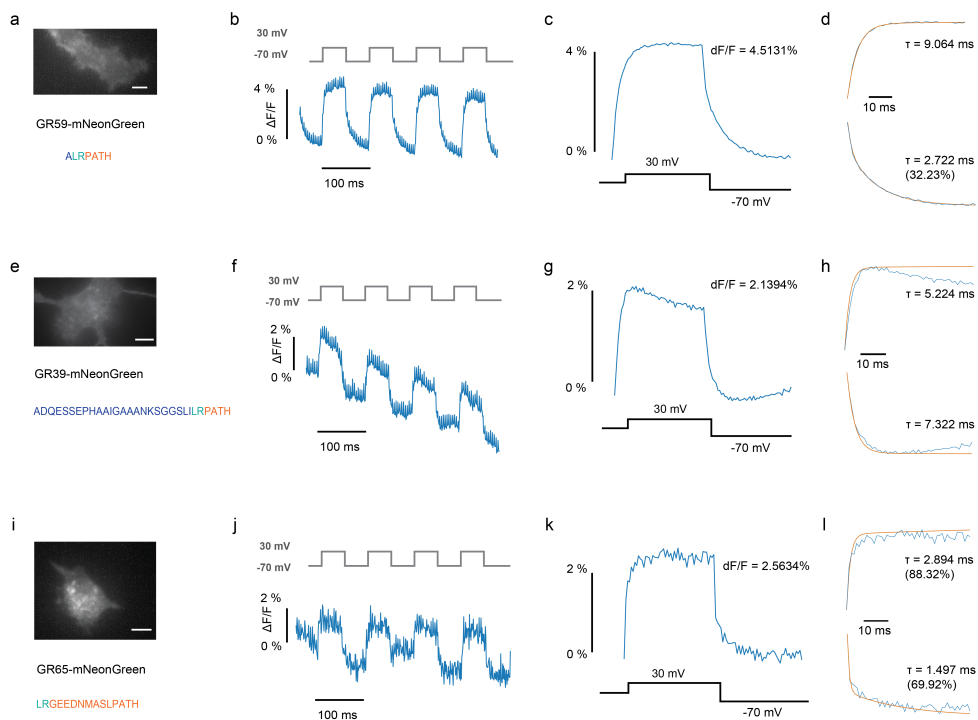


Figure 4.3: Representative responses of mNeonGR linker variants show small positive-going signals within the system noise floor. (a) Widefield fluorescence image of a HEK293T cell expressing mNeonGR59. Scale bar = 10 μm . (b) Single-trial donor-channel fluorescence response ($\Delta F/F$) of mNeonGR59 to repeated 100 mV voltage steps (from -70 mV to +30 mV, 488 nm excitation), recorded at 500 fps. (c) Averaged donor fluorescence response of mNeonGR59, with steady-state $\Delta F/F = 4.5131\%$. (d) Biexponential fit to rising and falling phases, $t_{\text{rise}} = 9.06$ ms, $t_{\text{fall}} = 2.72$ ms (32.23%). (e) Widefield fluorescence image of a HEK293T cell expressing mNeonGR39. Scale bar = 10 μm . (f) Single-trial donor-channel fluorescence response ($\Delta F/F$) of mNeonGR39 to repeated 100 mV voltage steps (from -70 mV to +30 mV, 488 nm excitation), recorded at 500 fps. (g) Averaged donor fluorescence response of mNeonGR39, with steady-state $\Delta F/F = +2.1394\%$. (h) Biexponential fit to rising and falling phases, $t_{\text{rise}} = 5.224$ ms, $t_{\text{fall}} = 7.322$ ms. (i) Widefield fluorescence image of a HEK293T cell expressing mNeonGR65. Scale bar = 10 μm . (j) Single-trial donor-channel fluorescence response ($\Delta F/F$) of mNeonGR65 to repeated 100 mV voltage steps (from -70 mV to +30 mV, 488 nm excitation), recorded at 500 fps. (k) Averaged donor fluorescence response of mNeonGR65, with steady-state $\Delta F/F = +2.5634\%$. (l) Biexponential fit to rising and falling phases, $t_{\text{rise}} = 2.894$ ms (88.32%), $t_{\text{fall}} = 1.497$ ms (69.92%).

Control 3. Cytosolic EGFP under 637 nm excitation, indirect noise floor with a fluorophore present

Finally, we imaged cells expressing cytosolic EGFP, which has negligible absorbance at 637 nm, again using 637 nm excitation and donor-channel detection. Under the same voltage steps, these recordings showed fluctuations of about 2.0% $\Delta F/F$ (Fig. 4.4g-i). Because EGFP contributes photons without true voltage sensitivity at this wavelength, this condition reports the effective noise floor of the system when a bright fluorophore is present, including any intensity changes driven by laser power or detection gain fluctuations.

Taken together, these controls constrain artifactual donor responses in our system to

approximately 2% $\Delta F/F$ per 100 mV, consisting of instrument noise on the order of 1 to 2% and minor optical bleed-through of about 0.65%. The associated traces are characteristically noisy, donor-positive, and lack clear rising or decaying phases, in contrast to the clean, biexponential waveforms observed for the best-performing construct mNeonGR59 in Section 4.2.2. Thus, while most 1 to 2% donor signals reported for the mNeonGR library can be explained by a combination of noise and bleed-through, the larger 3 to 5% steps and intermediate time constants of mNeonGR59 cannot. These discrepancies motivated the spectral perturbation analysis presented in Section 4.2.4, which tests whether mutation- and voltage-driven changes in the GR absorption spectrum can account for the observed polarity reversal and limited effective sensitivity.

4.2.4. SPECTRAL PERTURBATION ANALYSIS OF GR-D115N-MEDIATED DONOR POLARITY REVERSAL

To test whether changes in the GR absorption spectrum could account for the polarity reversal and limited donor sensitivity of mNeonGR, we constructed a minimal spectral perturbation model. The model links effective shifts of the GR spectrum to the steady-state voltage responses of both the unfused GR-D115N acceptor and the mNeonGR donor. We used the measured GR-WT absorption spectrum and the mNeonGreen emission spectrum to define the FRET overlap region and represented the combined effect of the D115N mutation and voltage as an effective spectral shift ($\Delta\lambda_{\text{mut},V}$) and an amplitude scaling ($\alpha_{\text{mut},V}$) applied to the GR-WT absorption.^{20,25}

Under voltage, we assumed that the same pair of perturbation parameters, $\Delta\lambda_{\text{mut},V}$ and $\alpha_{\text{mut},V}$, acts on GR-D115N in both configurations, the D115N-only condition excited at 639 nm and the mNeonGR FRET pair excited at 488 nm. In this minimal description, $\Delta\lambda_{\text{mut},V}$ and $\alpha_{\text{mut},V}$ summarize the combined spectral consequences of the D115N mutation and voltage and should therefore be interpreted as effective parameters rather than purely voltage-induced perturbations.

Baseline FRET efficiency at 0 mV (E_0) was taken from the Ace2N-mNeon calibration in HEK293T cells (Chapter 3 and Methods 3.4). For the spectral perturbation simulations, we therefore allowed baseline E_0 for mNeonGR to vary between 0.10 and 0.20, a range that brackets the calibrated value for Ace2N-mNeon and is broad enough to absorb plausible differences in baseline FRET efficiency arising from donor-acceptor distance, orientation, and local environment between constructs and cells.

We first used the GR-D115N acceptor-only recordings at 639 nm to constrain the space of admissible spectral perturbations. In this configuration, cells expressed GR-D115N without a donor and fluorescence was excited at 639 nm while applying a 100 mV step from -70 mV to $+30$ mV, so the voltage sensitivity is captured by the steady-state $\Delta F/F$ of acceptor intensity and depends directly on the extinction coefficient at 639 nm. A global change in absorption amplitude and a peak shift of the GR spectrum both alter the absorbance at this wavelength and therefore the steady-state $\Delta F/F$. Using a linearized description of the GR spectrum around the GR-WT shape, we expressed the D115N-only constraints as a family of straight lines in the $\Delta\lambda_{\text{mut},V}$ - $\alpha_{\text{mut},V}$ plane, each corresponding to a fixed fraction of the measured 263.7% $\Delta F/F$ response of GR-D115N at 639 nm. We restricted this fraction to the range 0.4 to 1.0, excluding solutions in which spectral effects

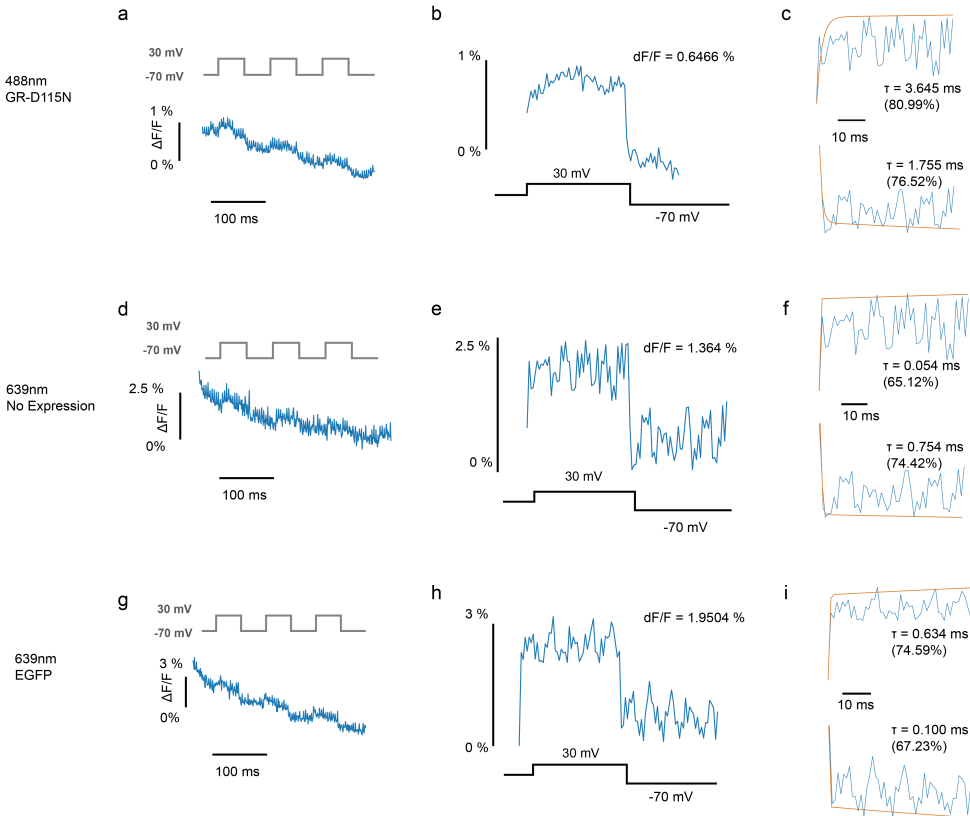


Figure 4.4: Representative control recordings reveal instrument noise and acceptor bleed-through as the source of small positive donor signals. (a) Donor-channel fluorescence response ($\Delta F/F$) from a HEK293T cell expressing GR-D115N only under repeated 100 mV voltage steps (from -70 mV to $+30$ mV, 488 nm excitation), recorded at 500 fps. (b) Averaged donor-channel response for the cell in (a), with steady-state $\Delta F/F = +0.6466\%$. (c) Biexponential fits to the rising and falling phases of (b), $t_{\text{rise}} = 3.645$ ms (80.99%), $t_{\text{fall}} = 1.755$ ms (76.52%). (d) Donor-channel $\Delta F/F$ from an untransfected HEK293T cell under the same voltage protocol, imaged with 637 nm excitation at 500 fps. (e) Averaged donor-channel response for the cell in (d), with steady-state $\Delta F/F = +1.364\%$. (f) Biexponential fits to the rising and falling phases of (e), $t_{\text{rise}} = 0.054$ ms (65.12%), $t_{\text{fall}} = 0.754$ ms (74.42%). (g) Donor-channel $\Delta F/F$ from a HEK293T cell expressing cytosolic EGFP (no voltage sensitivity) under 637 nm excitation at 500 fps. (h) Averaged donor-channel response for the cell in (g), with steady-state $\Delta F/F = +1.9504\%$. (i) Biexponential fits to the rising and falling phases of (h), $t_{\text{rise}} = 0.634$ ms (74.59%), $t_{\text{fall}} = 0.100$ ms (67.23%).

are only a minor contribution while still allowing a substantial residual component to arise from non-spectral mechanisms. The resulting family of lines forms a diagonal band in (Fig. 4.5b).

Then, each mNeonGR variant contributes an independent constraint from the donor side. For mNeonGR39, mNeonGR59, and mNeonGR65, the measured donor $\Delta F/F$ per 100 mV was converted into a normalized sensitivity that accounts for the baseline E_0 (Methods). Using a small-signal analysis of the spectral overlap integral, we showed that for small perturbations of the GR spectrum around the WT shape, each donor sensitivity

defines a straight line in the same $\Delta\lambda_{\text{mut},V}-\alpha_{\text{mut},V}$ plane. Physically admissible combinations of $\Delta\lambda_{\text{mut},V}$ and $\alpha_{\text{mut},V}$ are those that fall within the 639 nm band, so that a substantial fraction of the GR-D115N acceptor response is attributed to spectral perturbation, and lie on the donor constraint line for that variant, so that the measured donor $\Delta F/F$ is reproduced. Geometrically, this corresponds to the short segment where each donor line crosses the diagonal band in Fig. 4.5b.

To test how sensitive these inferences are to uncertainty in E_0 , we repeated the construction for several baseline E_0 spanning a plausible range for mNeonGR, from 0.10 through the Ace2N-mNeon-based central estimate of about 0.13 up to 0.20 (Fig. 4.5c). For each variant, varying E_0 from 0.10 to 0.20 generated a short trajectory in the $\Delta\lambda_{\text{mut},V}-\alpha_{\text{mut},V}$ plane. Across this range, all trajectories remained confined to a narrow region corresponding to large effective red shifts of approximately 25 to 30 nm and moderately negative amplitudes, with $\alpha_{\text{mut},V}$ between about 0 and -0.3 and only a few nanometers variation in $\Delta\lambda_{\text{mut},V}$.

Thus, under the assumptions of this model, reconciling the large GR-D115N response at 639 nm with the weak positive donor sensitivities of mNeonGR requires substantial red shifting and dimming of the effective GR absorption spectrum, and this conclusion is robust to reasonable uncertainty in the baseline E_0 . These constraints motivate the mechanistic interpretation and design implications that we develop in the Discussion.

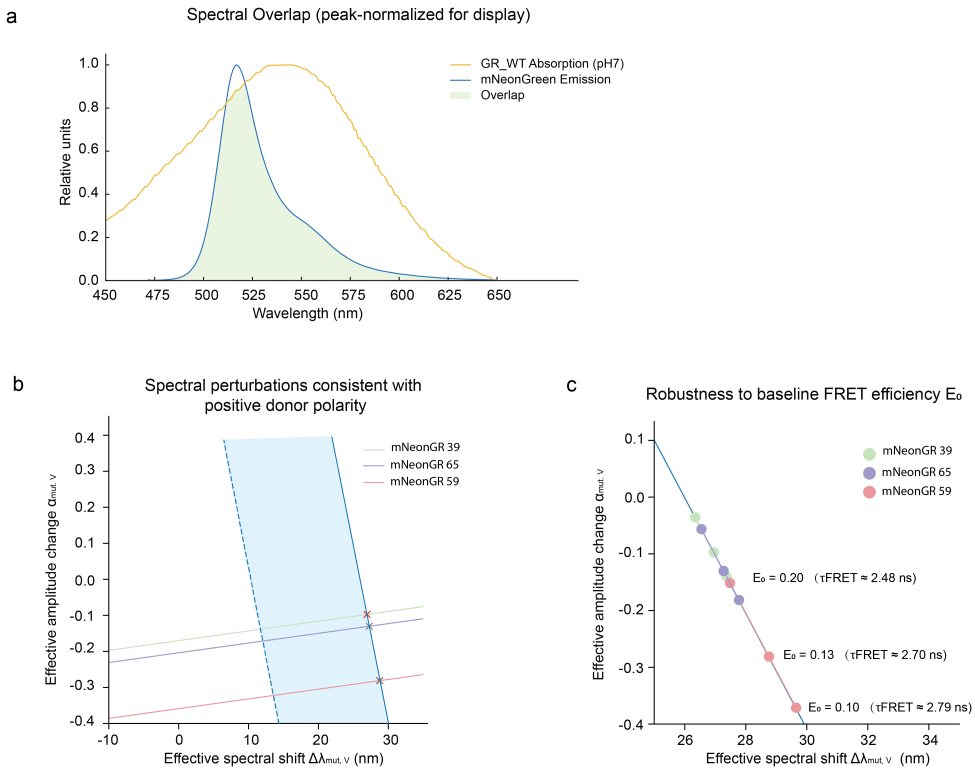


Figure 4.5: Spectral perturbation model for GR-D115N mediated donor polarity reversal. (a) Spectral overlap between GR-WT absorption (blue) and mNeonGreen emission (orange), both peak-normalized for display. The shaded region indicates the wavelength range contributing to the FRET overlap integral (J). (b) Joint spectral constraints on the effective perturbation under mutation plus voltage, expressed as amplitude change ($\alpha_{mut,V}$) versus spectral shift ($\Delta\lambda_{mut,V}$). The blue band denotes combinations of ($\alpha_{mut,V}$, $\Delta\lambda_{mut,V}$) that account for 40 to 100% of the GR-D115N only ($\Delta F/F$) at 639 nm. Colored lines show the donor constraints for three mNeonGR variants (mNeonGR39, mNeonGR59, mNeonGR65), derived from their measured 1 to 5% positive donor sensitivities. Crosses mark intersections of each donor line with the upper boundary of the 639 nm band, corresponding to spectral perturbations that both reproduce the GR-D115N only response and yield positive donor polarity. (c) Dependence of the inferred spectral perturbations on the baseline FRET efficiency (E_0). For each variant, points from bottom right to top left correspond to $E_0 = 0.10$, 0.13, and 0.20, respectively, with the associated FRET lifetimes indicated in parentheses. The trajectories remain confined to a narrow region of large red shifts and moderately negative amplitude changes, indicating that the inferred spectral perturbations required for positive donor polarity are robust to uncertainty in E_0 .

4.3. DISCUSSION

In [Chapter 3](#), we established a FLIM-based framework for absolute V_m imaging in developing embryos by calibrating fluorescence lifetime to resting V_m and applying these calibrations to track slow voltage shifts *in vivo*. Extending this framework to broader *in vivo* applications requires voltage indicators that combine sufficient baseline brightness, a lifetime that can be read reliably by FLIM, and substantially higher effective sensitivity than currently available tools. Motivated by these requirements, we fused the highly

sensitive but dim electrochromic rhodopsin GR-D115N as acceptor to the bright donor mNeonGreen, aiming to preserve the strong voltage response of GR-D115N while reporting voltage through changes in donor lifetime.

For a canonical eFRET indicator, a depolarizing step that strengthens acceptor absorption within the donor emission band should increase E_{FRET} and produce a negative-going donor response.^{14,16} Instead, we found that GR-D115N alone exhibited a very large positive sensitivity at 639 nm, whereas all mNeonGR linker variants produced only small positive donor signals. Control experiments constrained the artifactual floor in the donor channel to roughly 1 to 2% $\Delta F/F$ and revealed noisy, positive signals that lacked consistent kinetics. Together, these findings revealed a clear discrepancy in polarity between the expected donor quenching and the observed weak positive steps, which were only marginally above the artifact range. Under the conservative noise criteria applied in the earlier analysis, a subset of these recordings provided limited statistical support for definitive polarity assignment, and additional repeats will be needed to strengthen this conclusion.

To understand this discrepancy, we combined a spectral perturbation model with constraints from the GR-D115N-only measurements and the donor responses of several mNeonGR variants. The analysis indicates that substantial reshaping of the GR-D115N spectrum is required to reconcile the strong acceptor response with the weak positive donor signals. At the same time, the model points to limitations in donor selection, FRET geometry, and the screening pipeline that collectively prevented the present constructs from achieving the efficient, negative-polarity eFRET response needed for absolute voltage FLIM. In the following sections, we summarize the insights from the spectral perturbation analysis, discuss the design limitations it reveals, and outline a staged strategy for engineering improved GR-based eFRET indicators.

4.3.1. SPECTRAL PERTURBATION MODEL FOR DONOR POLARITY REVERSAL

We used a minimal spectral perturbation model to reconcile two observations: a large positive acceptor signal of GR-D115N at 639 nm and a small positive donor signal of mNeonGR under 488 nm excitation. In this model, the combined effect of mutation and voltage on the acceptor is summarized by an effective spectral shift ($\Delta\lambda_{\text{mut},V}$) and an amplitude change ($\alpha_{\text{mut},V}$). Our simulation results show that a combination of a large effective red shift of the GR-D115N absorption peak, about 25 to 30 nm, and a moderate decrease in its overall amplitude, with $\alpha_{\text{mut},V}$ between 0 and -0.3 , is sufficient to reproduce the observed polarity reversal of the donor response while matching the large positive 639 nm response of GR-D115N.

Intuitively, the D115N mutation reshapes the acceptor spectrum relative to GR-WT. A red-shifted, mildly attenuated spectrum increases absorption near 639 nm, which amplifies the acceptor-only readout, and reduces spectral overlap with mNeonGreen under 488 nm excitation, which weakens donor quenching and flips the expected negative eFRET response into a weak positive donor signal.

At the same time, the model has important limitations that restrict the interpretation of its outputs. First, it explicitly varies only the acceptor spectrum, through $\Delta\lambda_{\text{mut},V}$ and $\alpha_{\text{mut},V}$, and treats all other voltage-dependent processes, such as changes in nonradiative

decay, dark-state equilibria, or distance and orientation distributions, as being absorbed into the baseline E_0 and constant prefactors. In the present analysis, E_0 is treated as an effective parameter rather than being directly measured, and future work should estimate E_0 experimentally, for example by comparing the donor lifetime of mNeonGreen alone with that of the corresponding mNeonGR fusion under matched imaging conditions. Second, both the 639 nm constraint and the donor constraint are formulated in a linearized regime that uses first-order sensitivities of the 639 nm absorption and of the overlap integral to small spectral shifts and therefore do not capture higher-order or strongly nonlinear behavior. Third, we approximate the population of GR-D115N molecules by a single effective spectrum that is perturbed in the same way in the D115N-only and mNeonGR configurations, whereas in reality membrane microenvironment, expression level, and local pH may introduce cell-to-cell variability that is not represented in this description.

For these reasons, $\Delta\lambda_{\text{mut},V}$ and $\alpha_{\text{mut},V}$ are best viewed as effective parameters that summarize the net spectral consequences of mutation plus voltage rather than as a complete mechanistic description of GR-D115N photophysics. Therefore, the modeling does not exclude additional voltage-dependent changes in acceptor photophysics or conformation, which are likely required together with spectral perturbations to fully account for the magnitude and kinetics of the polarity reversal.

4.3.2. DESIGN LIMITATIONS AND FUTURE DIRECTIONS

Although the current mNeonGR constructs did not yield a functional eFRET voltage readout, the GR-D115N scaffold remains a strong basis for absolute voltage imaging. Its very high intrinsic voltage sensitivity, together with our modeling, indicates that D115N undergoes voltage-dependent spectral reshaping with a substantial red shift, which reduces overlap at 488 nm and can invert or weaken donor polarity. These results expose three coupled limitations in the present design: incomplete spectral information for GR-D115N during donor selection, suboptimal FRET geometry that likely produces a low baseline E_0 , and a screening pipeline that relied primarily on intensity-based readouts rather than lifetime or direct FRET metrics.

The first limitation concerns donor-acceptor pairing. mNeonGreen was selected based on the reported absorption maximum of wild-type GR near 538 nm in buffer,²⁵ under the assumption that the D115N mutation would preserve the overall spectral envelope. The modeling instead indicates that, in order to reconcile the strong GR-D115N-only response at 639 nm with the weak positive donor sensitivities, GR-D115N must be both substantially red shifted and moderately attenuated relative to GR-WT. This suggests that the true membrane-embedded spectrum of GR-D115N differs more strongly from the published wild-type spectrum than anticipated, and that reliance on inferred rather than measured spectra contributed to a spectral mismatch between mNeonGreen emission and D115N absorption. Resolving this limitation will require direct measurements of GR-D115N absorption and emission under imaging-relevant conditions, including membrane environment, pH, and ideally voltage dependence. Such data would allow the effective red shift and amplitude changes inferred by our model to be tested experimentally, provide a quantitative basis for donor selection, and enable

rational computation of overlap integrals and baseline E_0 for candidate donors.

The second limitation lies in the geometric design of the FRET pair. Although we used a short Leu-Arg linker that supports efficient FRET in other opsin-based sensors,¹⁴ the donor and acceptor in mNeonGR may not have resided within an optimal Förster distance or dipole orientation.^{8,12,23} Because FRET efficiency scales with the inverse sixth power of the donor-acceptor separation, even modest increases in effective distance, or excessive linker flexibility that averages over unfavorable orientations, can markedly depress the baseline E_0 .^{8,12} The simulations show that, even when the spectrum is displaced into a favorable D115N-like configuration, the donor sensitivities remain at the percent level, consistent with relatively low effective E_0 . This pattern suggests that the present architecture did not achieve a strongly coupled FRET geometry. Future designs should therefore treat higher baseline E_0 as an explicit target and use structural models of the fusion proteins and predicted membrane topology to propose geometries with tighter spacing and more constrained orientations. Strategies such as rigid or semi-rigid linkers, circularly permuted donors, or donor insertions into the opsin scaffold, which have proven effective in other rhodopsin-based indicators, are natural starting points.^{13,14,29,30} For each design, simple calculations of the expected Förster radius, feasible distances, and target E_0 can be used to filter constructs before experimental screening.

The third limitation is methodological. Linker variants were ranked primarily by patch-clamp $\Delta F/F$ in the donor channel, without an initial lifetime-based checkpoint to verify that voltage-modulated FRET was present. In the absence of independent spectral and lifetime information, small positive $\Delta F/F$ values near the 1 to 2% artifact floor were interpreted as either noise or weak reporter signals. Future screening pipelines should therefore integrate spectral and lifetime checkpoints alongside intensity measurements. Early characterization of each construct should include steady-state spectra for both donor and acceptor, and FLIM-based measurements of donor lifetime under voltage steps, to verify that changes in lifetime and FRET efficiency are present and of the expected polarity before patch-clamp imaging. Patch-clamp assays can then be used to reject constructs whose $\Delta F/F$ amplitudes remain at the artifact floor or whose kinetics mirror bleed-through and instrumental signals. The most promising variants can be advanced to the zebrafish FLIM pipeline established in Chapter 3 to test whether they can resolve gradual changes in resting membrane potential in vivo with higher sensitivity.

In this way, accurate spectral characterization, geometry-aware construct design, and staged functional validation together provide a practical blueprint for engineering next-generation FRET-opsin indicators that meet the requirements for brightness, sensitivity, and polarity in absolute voltage FLIM.

4.4. METHODS

4.4.1. PLASMID CONSTRUCTION AND mNEONGR LINKER VARIANTS

GR-D115N was derived from *Gloeobacter* rhodopsin as described previously.^{20,22} mNeonGreen was fused to the cytosolic C-terminus of GR-D115N.²⁵ To vary donor-acceptor spacing, we generated a panel of constructs with stepwise truncations of the predicted

unstructured GR-D115N C-terminus (1 to 24 residues removed) and with a shortened mNeonGreen N-terminus, retaining only the minimal sequence required for proper folding (based on Ace2N-mNeon designs).¹⁶ The two domains were connected by a Leu-Arg linker that has supported efficient FRET in earlier opsin-based indicators.¹⁴ Additional residues (1 to 9 amino acids) were inserted after the minimal mNeonGreen N-terminus to sample a range of linker lengths.

Fragments were amplified by overlapping PCR (Phusion High-Fidelity Master Mix, NEB). The vector backbone was amplified with KOD Xtreme Hot Start DNA Polymerase (Merck Sigma). GR-D115N and mNeonGreen fragments were assembled by Gibson Assembly (NEB Gibson Assembly Master Mix) and transformed into NEB[®] 5-alpha competent cells. Correct insert sequences and junctions were confirmed by sequencing.

GR-D115N alone and cytosolic EGFP were cloned in the same vector backbone and used in control experiments.

4.4.2. HEK CELL CULTURE AND TRANSFECTION

HEK293T cells were cultured in DMEM (D6429, Sigma-Aldrich) supplemented with 10% fetal bovine serum (Seradigm), 1% penicillin-streptomycin (P4333, Sigma-Aldrich), and 2 mM L-glutamine at 37 °C in 5% CO₂. Cells were maintained at subconfluent density and passaged every 2 to 3 days. At approximately 80% confluence, cells were transfected with 1500 ng plasmid DNA and 6 μL TransIT-293 (MIR 2705, Mirus Bio) per dish. After 24 h, cells were replated on 35-mm glass-bottom dishes (D35-14-1.5-N, Cellvis) coated with human plasma fibronectin (FC010-5MG, Sigma-Aldrich). Separate dishes were transfected with individual mNeonGR variants, GR-D115N only, or EGFP. Dishes were transferred to the recording chamber 48 to 72 h after transfection. Cells with bright membrane-localized fluorescence and healthy morphology were selected for patch clamp and imaging.

4.4.3. WHOLE-CELL VOLTAGE CLAMP AND FLUORESCENCE IMAGING

Recordings were performed at room temperature in an external solution (pH 7.3, 310 mOsm) containing (in mM): 125 NaCl, 15 HEPES, 2.5 KCl, 1 CaCl₂, 1 MgCl₂, and 30 glucose. Patch pipettes (borosilicate glass, outer diameter 1.5 mm, inner diameter 0.84 mm, WPI) had resistances of 5 MΩ to (numerical range) 10 MΩ and were filled with a K-based internal solution (pH 7.3, 295 mOsm) containing (in mM): 125 potassium gluconate, 0.1 CaCl₂, 0.6 MgCl₂, 1 EGTA, 10 HEPES, 4 Mg-ATP, 0.4 Na-GTP, and 8 NaCl. Liquid junction potentials were calculated and corrected offline. Pipettes were positioned with an S-PS-7000C micromanipulator (Scientifica), and recordings were made using a Model 2400 Patch Clamp Amplifier (A-M Systems). A 100 mV step from -70 to +30 mV was applied from a holding potential of -70 mV during simultaneous fluorescence imaging.

Fluorescence imaging was performed on a custom multimodal microscope integrated with a patch clamp.²⁷ Excitation was provided by a 488 nm laser (OBIS 488 LX, Coherent) at around 23 mW mm⁻² at the sample plane, as measured with a power meter after the 25× water-immersion objective (XLPLN25XWMP2, Olympus). Emission was collected through a 513 to 607 nm bandpass filter (FF01-560/94-25, Semrock) and a multiband dichroic (Di03-R405/488/532/635-t3-32×44, Semrock). Images were acquired using an

ORCA-Flash4.0 V3 sCMOS camera (Hamamatsu, 2048 × 2048, 6.5 μm pixel size) at 500 frames per second (fps). For GR-D115N-only and control measurements with 637 nm excitation, the same donor emission channel was used while switching excitation to 637 nm. Voltage command, laser control, and image acquisition were synchronized via a USB-6363 DAQ (National Instruments) and custom Python software.²²

4.4.4. FLUORESCENCE INTENSITY ANALYSIS

Fluorescence traces were extracted from videos using a multi-step pipeline.^{22,27,31} Regions devoid of cellular signal were used to estimate the background, which was subtracted frame-wise. A maximum-likelihood pixel-weighting procedure was applied to refine signal extraction. Photobleaching was corrected by fitting and removing a bi-exponential decay from each trace. Baseline (F_0) and steady-state (F_s) fluorescence were defined at rest and during voltage steps, respectively, and voltage sensitivity ($\Delta F/F_0$) was calculated as

$$\frac{\Delta F}{F_0} = \frac{F_s - F_0}{F_0}. \quad (4.1)$$

For kinetics, rising and falling phases were fitted with a single- or bi-exponential function:

$$F(t) = A(Ce^{-t/\tau_{\text{rise}}} + (1 - C)e^{-t/\tau_{\text{fall}}}), \quad (4.2)$$

where A is a scaling constant, C is the fast-component fraction, and τ_{rise} and τ_{fall} are the fast and slow time constants. This yielded amplitudes and time constants used to quantify response polarity and dynamics.

4.4.5. SPECTRAL PERTURBATION SIMULATIONS

SPECTRAL INPUTS

Spectral simulations were used to relate the voltage sensitivities measured in the GR-D115N-only 639 nm channel and in the mNeonGR donor channel to effective perturbations of the GR absorption spectrum. The GR-WT absorption spectrum, $\varepsilon_{A,WT}(\lambda)$, was digitized from published measurements in aqueous buffer and rescaled to arbitrary units, where λ denotes wavelength in nanometers.²⁰ The mNeonGreen emission spectrum, $f_D(\lambda)$, was obtained from FPbase and normalized to a peak value of 1.²⁵

Both spectra were interpolated onto a common wavelength grid from 350 to 750 nm with a step of 1 nm. The GR-WT absorption spectrum was peak-normalized to yield a dimensionless shape,

$$\tilde{\varepsilon}_{A,WT}(\lambda) = \frac{\varepsilon_{A,WT}(\lambda)}{\max_{\lambda} \varepsilon_{A,WT}(\lambda)}. \quad (4.3)$$

BASELINE FRET EFFICIENCY

The baseline FRET efficiency, E_0 at 0 mV, was estimated from the donor-only lifetime, τ_D , of mNeonGreen and the FRET-coupled lifetime, τ_{FRET} , of Ace2N-mNeon in HEK293T

cells using the standard relation

$$E_0 = 1 - \frac{\tau_{\text{FRET}}}{\tau_{\text{D}}}. \quad (4.4)$$

The donor-only lifetime τ_{D} was taken from FPbase, $\tau_{\text{D}} \approx 3.10$ ns, and the FRET-coupled lifetime of Ace2N-mNeon determined in Chapter 3 was $\tau_{\text{FRET}} \approx 2.71$ ns. Substituting these values yields a central baseline efficiency of $E_0 \approx 0.13$. In the spectral perturbation simulations, E_0 for mNeonGR was allowed to vary between 0.10 and 0.20. This interval brackets E_0 and is sufficiently broad to account for plausible variation in baseline FRET efficiency due to differences in donor-acceptor distance, orientation, and local membrane environment between constructs and cells.

EFFECTIVE SPECTRAL PERTURBATION UNDER MUTATION AND VOLTAGE

The combined effect of the D115N mutation and voltage on the GR spectrum was represented as an effective spectral perturbation, $(\Delta\lambda_{\text{mut},V}, \alpha_{\text{mut},V})$, where $\Delta\lambda_{\text{mut},V}$ is an effective spectral shift and $\alpha_{\text{mut},V}$ is an effective amplitude change. The perturbed acceptor spectrum was modeled as

$$\varepsilon_{\text{mut},V}(\lambda; \Delta\lambda_{\text{mut},V}, \alpha_{\text{mut},V}) = (1 + \alpha_{\text{mut},V}) \tilde{\varepsilon}_{\text{A,WT}}(\lambda - \Delta\lambda_{\text{mut},V}). \quad (4.5)$$

The same pair $(\Delta\lambda_{\text{mut},V}, \alpha_{\text{mut},V})$ was assumed to apply to both the D115N-only configuration excited at 639 nm and to the mNeonGR FRET pair under voltage.

D115N-ONLY 639 NM CONSTRAINT

Our goal in this part of the model was to translate the experimentally measured voltage response of GR-D115N in the 639 nm channel into a quantitative constraint on the spectral perturbation parameters $\Delta\lambda_{\text{mut},V}$ and $\alpha_{\text{mut},V}$. For GR-D115N recorded without a FRET donor, the sample was illuminated with a narrow-band 639 nm laser. Under these conditions, and assuming that fluorescence quantum yield and detection efficiency do not change with $\Delta\lambda_{\text{mut},V}$ or $\alpha_{\text{mut},V}$, the steady-state fluorescence intensity at 639 nm, F_{639} , is proportional to the effective absorption coefficient at 639 nm. Evaluating the spectral perturbation model at 639 nm and combining it with the proportionality between fluorescence and absorption gives

$$F_{639}(\Delta\lambda_{\text{mut},V}, \alpha_{\text{mut},V}) \propto (1 + \alpha_{\text{mut},V}) \tilde{\varepsilon}_{\text{A,WT}}(639 - \Delta\lambda_{\text{mut},V}). \quad (4.6)$$

Within the model, all other factors that influence fluorescence, such as laser power and detection efficiency, are absorbed into the proportionality constant and therefore drop out of the subsequent normalized analysis.

To describe the voltage-dependent change in the 639 nm signal in a normalized form, we defined the fractional change

$$B(\Delta\lambda_{\text{mut},V}, \alpha_{\text{mut},V}) = \frac{F_{639}(\Delta\lambda_{\text{mut},V}, \alpha_{\text{mut},V})}{F_{639}(0,0)} - 1. \quad (4.7)$$

Here $F_{639}(0,0)$ is the fluorescence intensity obtained from the unperturbed GR-WT spec-

trum, that is, with $\Delta\lambda_{\text{mut},V} = 0$ and $\alpha_{\text{mut},V} = 0$. This definition is equivalent to the usual $\Delta F/F$ and has the advantage that the unknown proportionality constant cancels between numerator and denominator. Using the expression for F_{639} above, this fractional change can be written explicitly as

$$B(\Delta\lambda_{\text{mut},V}, \alpha_{\text{mut},V}) = (1 + \alpha_{\text{mut},V}) \frac{\bar{\epsilon}_{\text{A,WT}}(639 - \Delta\lambda_{\text{mut},V})}{\bar{\epsilon}_{\text{A,WT}}(639)} - 1. \quad (4.8)$$

Around the GR-WT spectrum, we approximated the dependence of B on $\Delta\lambda_{\text{mut},V}$ and $\alpha_{\text{mut},V}$ by a first-order Taylor expansion. In other words, we assumed that the effective shift $\Delta\lambda_{\text{mut},V}$ and amplitude change $\alpha_{\text{mut},V}$ are small enough that B can be described by a linear function in their neighborhood. Expanding around $\Delta\lambda_{\text{mut},V} = 0$ and $\alpha_{\text{mut},V} = 0$ gives

$$B(\Delta\lambda_{\text{mut},V}, \alpha_{\text{mut},V}) \approx \alpha_{\text{mut},V} + s_{639} \Delta\lambda_{\text{mut},V}, \quad (4.9)$$

where the first term $\alpha_{\text{mut},V}$ represents the contribution from the overall amplitude scaling, and the second term $s_{639} \Delta\lambda_{\text{mut},V}$ represents the contribution from the spectral shift. The coefficient s_{639} is a numerical slope that relates small spectral shifts to relative changes in absorption at 639 nm. We obtained s_{639} by computing $B(\Delta\lambda, 0)$ for a set of small positive and negative values of $\Delta\lambda$ with $\alpha_{\text{mut},V} = 0$, and then fitting a straight line to these values; the slope of this line defines s_{639} .

In the D115N-only measurements, a 100 mV voltage step produced a large increase in the 639 nm fluorescence signal. Expressed as a fractional change, the measured response was

$$B_{\text{max}} \approx 2.637, \quad (4.10)$$

which corresponds to approximately 263.7% $\Delta F/F$ per 100 mV.²² We used this experimentally observed value as a reference for the spectral perturbation model. Rather than requiring the spectral perturbation alone to account for the entire response, we asked the model to explain only a fraction f of this change, with $0.4 \leq f \leq 1.0$. Values of f smaller than one allow for the possibility that additional voltage-dependent processes, such as changes in quantum yield or dark-state equilibria, also contribute to the observed signal.

In the linear approximation, imposing

$$B(\Delta\lambda_{\text{mut},V}, \alpha_{\text{mut},V}) \approx f B_{\text{max}} \quad (4.11)$$

and substituting the linear form of B yields

$$\alpha_{\text{mut},V} + s_{639} \Delta\lambda_{\text{mut},V} \approx f B_{\text{max}}, \quad (4.12)$$

which can be rearranged to

$$\alpha_{\text{mut},V} = f B_{\text{max}} - s_{639} \Delta\lambda_{\text{mut},V}. \quad (4.13)$$

For a fixed value of f , this equation describes a straight line in the $(\Delta\lambda_{\text{mut},V}, \alpha_{\text{mut},V})$ plane. As f varies between 0.4 and 1.0, these lines form a diagonal band of $(\Delta\lambda_{\text{mut},V}, \alpha_{\text{mut},V})$ combinations that are consistent with the D115N-only 639 nm response, as shown in

Fig. 4.5b. Additional simulations with f between 0.3 and 0.6 produced similar regions of intersection with the donor constraints, indicating that the main conclusions of the model do not depend sensitively on the precise choice of f within this range.

DONOR SENSITIVITIES AND NORMALIZATION

Donor sensitivities for mNeonGR39, mNeonGR59, and mNeonGR65 were taken from the patch-clamp imaging experiments described in Section 4.2.2. For each construct, the 100 mV donor response was first expressed as a fractional change in fluorescence intensity,

$$\frac{\Delta F}{F_0} = \frac{F_s - F_0}{F_0}, \quad (4.14)$$

where F_s and F_0 are the steady-state and baseline donor intensities, respectively. This definition is equivalent to the usual $\Delta F/F$ used to report voltage sensitivity.

To relate these intensity changes to changes in E_{FRET} , we used a simple model for a FRET-coupled donor. Under constant excitation and detection conditions, the steady-state donor intensity can be written as

$$F = K(1 - E_{\text{FRET}}), \quad (4.15)$$

where E_{FRET} is the FRET efficiency and K is a proportionality constant that collects all voltage-independent experimental factors, including excitation power, detection efficiency, and the number of donor molecules. The fractional change can then be written as

$$\frac{\Delta F}{F_0} = \frac{-K \Delta E}{K(1 - E_0)} = -\frac{\Delta E}{1 - E_0}. \quad (4.16)$$

Rearranging yields a normalized change in FRET efficiency,

$$\frac{\Delta E}{E_0} = -\frac{1 - E_0}{E_0} \frac{\Delta F}{F_0}. \quad (4.17)$$

Thus, for a FRET-coupled donor, the fractional intensity change $\Delta F/F_0$ provides a direct proxy for the fractional change in FRET efficiency $\Delta E/E_0$, up to the factor $(1 - E_0)/E_0$.

In our system, the baseline E_0 for Ace2N-mNeon in HEK293T cells is approximately $E_0 \approx 0.13$ (Chapter 3 and Methods 3.2.2), so that $1 - E_0 \approx 0.87$. Because this prefactor differs from one by less than 15% over the range of E_0 considered in the simulations, we approximated $1 - E_0 \approx 1$ when converting donor sensitivities into normalized quantities. Under this approximation,

$$\frac{\Delta E}{E_0} \approx -\frac{1}{E_0} \frac{\Delta F}{F_0}. \quad (4.18)$$

We therefore defined

$$A_{\text{norm}}(E_0) = -\frac{1}{E_0} \frac{\Delta F}{F_0}, \quad (4.19)$$

which provides a dimensionless measure of donor voltage sensitivity after accounting for the baseline E_0 . Positive values of $A_{\text{norm}}(E_0)$ correspond to negative-going donor responses, that is, to increases in E_{FRET} with depolarization, whereas negative values

correspond to positive-going donor signals.

DONOR CONSTRAINTS AND INTERSECTION ANALYSIS

To relate the measured donor sensitivities to spectral shifts, we performed a small-signal analysis of how the FRET overlap integral changes under an effective spectral shift $\Delta\lambda$. For each tested baseline efficiency E_0 , we first considered perturbations with $\alpha_{\text{mut},V} = 0$, so that only the wavelength axis is shifted while the overall amplitude is held fixed. In this case, the effective absorption spectrum entering the FRET overlap is $\varepsilon_{\text{mut},V}(\lambda; \Delta\lambda, 0)$, and the corresponding relative overlap integral is

$$J(\Delta\lambda) \propto \sum_{\lambda} \varepsilon_{\text{mut},V}(\lambda; \Delta\lambda, 0) f_{\text{D}}(\lambda) \lambda^4 \Delta\lambda_{\text{grid}}, \quad (4.20)$$

where $f_{\text{D}}(\lambda)$ denotes the donor emission spectrum and the factor λ^4 arises from the standard Förster expression for the spectral overlap. The sum is taken over a set of wavelengths that adequately sample the donor emission band, and $\Delta\lambda_{\text{grid}}$ denotes the wavelength step of the discretized grid.

Over a set of small $\Delta\lambda$ values we computed $J(\Delta\lambda)$ and defined the reference overlap $J_0 = J(0)$, corresponding to no spectral shift. We then introduced the normalized overlap

$$q(\Delta\lambda) = \frac{J(\Delta\lambda)}{J_0}, \quad (4.21)$$

which removes the overall proportionality constant and expresses each perturbed overlap as a fraction of the baseline value.

For a fixed donor-acceptor distance and orientation, the FRET efficiency can be written as a simple function of the overlap integral,

$$E(J) = \frac{J}{J + C}, \quad (4.22)$$

where C is a constant that collects the distance- and orientation-dependent contributions to the Förster denominator. We determined C by requiring that the efficiency at the baseline overlap J_0 equals the chosen baseline E_0 . Imposing $E(J_0) = E_0$ gives

$$C = J_0 \left(\frac{1}{E_0} - 1 \right). \quad (4.23)$$

Substituting $J(\Delta\lambda) = q(\Delta\lambda) J_0$ and this expression for C into the formula for $E(J)$ yields

$$E(\Delta\lambda) = \frac{q(\Delta\lambda)}{q(\Delta\lambda) + \left(\frac{1}{E_0} - 1 \right)}. \quad (4.24)$$

This expression describes how a small spectral shift $\Delta\lambda$ modifies E_{FRET} at a fixed baseline E_0 through the normalized overlap $q(\Delta\lambda)$.

We then propagated these changes in efficiency to donor intensity. As in the previous subsection, for a FRET-coupled donor the steady-state intensity scales approximately

with $1 - E$, so we took the donor intensity under a spectral shift $\Delta\lambda$ as

$$F_D(\Delta\lambda) \propto 1 - E(\Delta\lambda). \quad (4.25)$$

The corresponding fractional change in donor fluorescence at a given E_0 is

$$\left(\frac{\Delta F}{F}\right)_{\text{donor}}(\Delta\lambda) = \frac{F_D(\Delta\lambda)}{F_D(0)} - 1. \quad (4.26)$$

Using the same normalization as above, we formed

$$A(\Delta\lambda) = -\frac{1}{E_0} \left(\frac{\Delta F}{F}\right)_{\text{donor}}(\Delta\lambda), \quad (4.27)$$

which provides a dimensionless proxy for the normalized change in FRET efficiency, $\Delta E/E_0$, induced by the spectral shift $\Delta\lambda$ at that baseline E_0 .

For small $\Delta\lambda$, the dependence of $A(\Delta\lambda)$ on $\Delta\lambda$ was well approximated by a linear function. We therefore fitted a straight line,

$$A(\Delta\lambda) \approx S_{J,E_0} \Delta\lambda, \quad (4.28)$$

to the numerically computed values of $A(\Delta\lambda)$ over a small range of positive and negative $\Delta\lambda$. The slope S_{J,E_0} links small spectral shifts to normalized donor intensity changes for a given baseline efficiency E_0 .

Within this linearized model, a general spectral perturbation $(\Delta\lambda_{\text{mut},V}, \alpha_{\text{mut},V})$ combines a shift $\Delta\lambda_{\text{mut},V}$ with an overall amplitude change $\alpha_{\text{mut},V}$. The amplitude change directly contributes $\alpha_{\text{mut},V}$ to the normalized donor response, while the shift contributes $S_{J,E_0} \Delta\lambda_{\text{mut},V}$. Together, these terms give the donor constraint

$$A_{\text{norm}}(E_0) = \alpha_{\text{mut},V} + S_{J,E_0} \Delta\lambda_{\text{mut},V}, \quad (4.29)$$

which defines a straight line in the $(\Delta\lambda_{\text{mut},V}, \alpha_{\text{mut},V})$ plane. Intersection points between this donor line and the 639 nm constraint band, corresponding to fractions f between 0.4 and 1.0 of B_{max} , were obtained analytically and plotted as shown in Fig. 4.5b. The same procedure was repeated for E_0 values between 0.10 and 0.20 to generate the trajectories in Fig. 4.5c. All simulations were implemented in Python using custom scripts based on `numpy`, `pandas`, and `matplotlib`.

BIBLIOGRAFIE

- [1] Michael Levin. “Molecular bioelectricity: How endogenous voltage potentials control cell behavior and instruct pattern regulation in vivo”. In: *Molecular Biology of the Cell* 25 (24 dec 2014), p. 3835–3850. ISSN: 19394586. DOI: [10.1091/mbc.E13-12-0708](https://doi.org/10.1091/mbc.E13-12-0708). PMID: [25425556](https://pubmed.ncbi.nlm.nih.gov/25425556/).
- [2] Laura Faith George en Emily Anne Bates. “Mechanisms Underlying Influence of Bioelectricity in Development”. In: *Frontiers in Cell and Developmental Biology* 10 (feb 2022). ISSN: 2296-634X. DOI: [10.3389/fcell.2022.772230](https://doi.org/10.3389/fcell.2022.772230).
- [3] Michael Levin. “Molecular bioelectricity in developmental biology: New tools and recent discoveries”. In: *BioEssays* 34 (3 mrt 2012), p. 205–217. ISSN: 02659247. DOI: [10.1002/bies.201100136](https://doi.org/10.1002/bies.201100136). PMID: [22237730](https://pubmed.ncbi.nlm.nih.gov/22237730/).
- [4] Daan Brinks, Aaron J. Klein en Adam E. Cohen. “Two-Photon Lifetime Imaging of Voltage Indicating Proteins as a Probe of Absolute Membrane Voltage”. In: *Biophysical Journal* 109 (5 sep 2015), p. 914–921. ISSN: 15420086. DOI: [10.1016/j.bpj.2015.07.038](https://doi.org/10.1016/j.bpj.2015.07.038). PMID: [26331249](https://pubmed.ncbi.nlm.nih.gov/26331249/).
- [5] Julia R. Lazzari-Dean, Anneliese M.M. Gest en Evan W. Miller. “Measuring Absolute Membrane Potential Across Space and Time”. In: *Annual Review of Biophysics* 50 (1 mei 2021), p. 447–468. ISSN: 1936-122X. DOI: [10.1146/annurev-biophys-062920-063555](https://doi.org/10.1146/annurev-biophys-062920-063555).
- [6] Jennifer Hou et al. “Simultaneous mapping of membrane voltage and calcium in zebrafish heart in vivo reveals chamber-specific developmental transitions in ionic currents”. In: *Frontiers in Physiology* 5 (2014). ISSN: 1664042X. DOI: [10.3389/fphys.2014.00344](https://doi.org/10.3389/fphys.2014.00344).
- [7] Dmitrii M. Nikolaev e.a. “Fluorescence Imaging of Cell Membrane Potential: From Relative Changes to Absolute Values”. In: *International Journal of Molecular Sciences* 24 (3 jan 2023), p. 2435. ISSN: 1422-0067. DOI: [10.3390/ijms24032435](https://doi.org/10.3390/ijms24032435).
- [8] Klaus Suhling e.a. “Fluorescence lifetime imaging (FLIM): Basic concepts and some recent developments”. In: *Medical Photonics* 27 (mei 2015), p. 3–40. ISSN: 2213-8846. DOI: [10.1016/J.MEDPHO.2014.12.001](https://doi.org/10.1016/J.MEDPHO.2014.12.001).
- [9] Helen H. Yang en François St-Pierre. “Genetically encoded voltage indicators: Opportunities and challenges”. In: *Journal of Neuroscience* 36 (39 sep 2016), p. 9977–9989. ISSN: 15292401. DOI: [10.1523/JNEUROSCI.1095-16.2016](https://doi.org/10.1523/JNEUROSCI.1095-16.2016). PMID: [27683896](https://pubmed.ncbi.nlm.nih.gov/27683896/).
- [10] Yongxian Xu, Peng Zou en Adam E. Cohen. “Voltage imaging with genetically encoded indicators”. In: *Current Opinion in Chemical Biology* 39 (aug 2017), p. 1–10. ISSN: 13675931. DOI: [10.1016/j.cbpa.2017.04.005](https://doi.org/10.1016/j.cbpa.2017.04.005).

- [11] Philipp Rühl e.a. “An Ultrasensitive Genetically Encoded Voltage Indicator Uncovers the Electrical Activity of Non-Excitable Cells”. In: *Advanced Science* 11 (20 mei 2024). ISSN: 2198-3844. DOI: [10.1002/adv.202307938](https://doi.org/10.1002/adv.202307938).
- [12] Yuansheng Sun e.a. “Förster resonance energy transfer microscopy and spectroscopy for localizing protein–protein interactions in living cells”. In: *Cytometry Part A* 83 (9 sep 2013), p. 780–793. ISSN: 1552-4922. DOI: [10.1002/cyto.a.22321](https://doi.org/10.1002/cyto.a.22321).
- [13] Yiyang Gong e.a. “Imaging neural spiking in brain tissue using FRET-opsin protein voltage sensors”. In: *Nature Communications* 5 (apr 2014). ISSN: 20411723. DOI: [10.1038/ncomms4674](https://doi.org/10.1038/ncomms4674). PMID: 24755708.
- [14] Peng Zou e.a. “Bright and fast multicoloured voltage reporters via electrochromic FRET”. In: *Nature Communications* 5 (aug 2014). ISSN: 20411723. DOI: [10.1038/ncomms5625](https://doi.org/10.1038/ncomms5625). PMID: 25118186.
- [15] Hidekazu Tsutsui e.a. “Improving membrane voltage measurements using FRET with new fluorescent proteins”. In: *Nature Methods* 5 (8 aug 2008), p. 683–685. ISSN: 1548-7091. DOI: [10.1038/nmeth.1235](https://doi.org/10.1038/nmeth.1235).
- [16] Y. Gong e.a. “High-speed recording of neural spikes in awake mice and flies with a fluorescent voltage sensor”. In: *Science* 350 (6266 dec 2015), p. 1361–1366. ISSN: 0036-8075. DOI: [10.1126/science.aab0810](https://doi.org/10.1126/science.aab0810).
- [17] Ahmed S Abdelfattah e.a. “Bright and photostable chemigenetic indicators for extended in vivo voltage imaging”. In: *Science* 16 (365(6454) 2019), p. 699–704. URL: <http://science.sciencemag.org/>.
- [18] Ahmed S. Abdelfattah e.a. “A general approach to engineer positive-going eFRET voltage indicators”. In: *Nature Communications* 11 (1 dec 2020). ISSN: 20411723. DOI: [10.1038/s41467-020-17322-1](https://doi.org/10.1038/s41467-020-17322-1). PMID: 32651384.
- [19] R Rippka, J Waterbury en G Cohen-Bazire. “A cyanobacterium which lacks thylakoids.” In: *Archives of Microbiology* 100 (1974), p. 419–436.
- [20] Ah Reum Choi e.a. “Cyanobacterial Light-Driven Proton Pump, Gloeobacter Rhodopsin: Complementarity between Rhodopsin-Based Energy Production and Photosynthesis”. In: *PLoS ONE* 9 (10 okt 2014), e110643. ISSN: 1932-6203. DOI: [10.1371/journal.pone.0110643](https://doi.org/10.1371/journal.pone.0110643).
- [21] Y. Nakamura. “Complete Genome Structure of Gloeobacter violaceus PCC 7421, a Cyanobacterium that Lacks Thylakoids”. In: *DNA Research* 10 (4 jan 2003), p. 137–145. ISSN: 1340-2838. DOI: [10.1093/dnares/10.4.137](https://doi.org/10.1093/dnares/10.4.137).
- [22] Xin M. “Novel microbial rhodopsins for optogenetics”. PhD thesis. Delft University of Technology, 2024.
- [23] Rajesh Babu Sekar en Ammasi Periasamy. “Fluorescence resonance energy transfer (FRET) microscopy imaging of live cell protein localizations”. In: *The Journal of Cell Biology* 160 (5 mrt 2003), p. 629–633. ISSN: 1540-8140. DOI: [10.1083/jcb.200210140](https://doi.org/10.1083/jcb.200210140).

- [24] Luís Loura. “Simple Estimation of Förster Resonance Energy Transfer (FRET) Orientation Factor Distribution in Membranes”. In: *International Journal of Molecular Sciences* 13 (11 nov 2012), p. 15252–15270. ISSN: 1422-0067. DOI: [10.3390/ijms131115252](https://doi.org/10.3390/ijms131115252).
- [25] Nathan C. Shaner e.a. “A bright monomeric green fluorescent protein derived from *Branchiostoma lanceolatum*”. In: *Nature Methods* 10 (5 mei 2013), p. 407–409. ISSN: 15487091. DOI: [10.1038/nmeth.2413](https://doi.org/10.1038/nmeth.2413). PMID: 23524392.
- [26] John Jumper e.a. “Highly accurate protein structure prediction with AlphaFold”. In: *Nature* 596 (7873 aug 2021), p. 583–589. ISSN: 0028-0836. DOI: [10.1038/s41586-021-03819-2](https://doi.org/10.1038/s41586-021-03819-2).
- [27] Xin Meng e.a. “A compact microscope for voltage imaging”. In: *Journal of Optics* 24 (5 mei 2022), p. 054004. ISSN: 2040-8978. DOI: [10.1088/2040-8986/ac5dd5](https://doi.org/10.1088/2040-8986/ac5dd5).
- [28] Maria Lobikin e.a. “Resting potential, oncogene-induced tumorigenesis, and metastasis: the bioelectric basis of cancer in vivo”. In: *Physical Biology* 9.6, 065002 (2012). DOI: [10.1088/1478-3975/9/6/065002](https://doi.org/10.1088/1478-3975/9/6/065002).
- [29] Junqi Yang e.a. *Solaris: a panel of bright and sensitive hybrid voltage indicators for imaging membrane potential in cultured neurons*. Feb 2024. DOI: [10.1101/2024.02.02.578569](https://doi.org/10.1101/2024.02.02.578569).
- [30] François St-Pierre e.a. “High-fidelity optical reporting of neuronal electrical activity with an ultrafast fluorescent voltage sensor”. In: *Nature Neuroscience* 17 (6 2014), p. 884–889. ISSN: 15461726. DOI: [10.1038/nn.3709](https://doi.org/10.1038/nn.3709). PMID: 24755780.
- [31] Srividya Ganapathy e.a. “Expanding the family of genetically encoded voltage indicators with a candidate Heliorhodopsin exhibiting near-infrared fluorescence”. In: *Journal of Biological Chemistry* 299 (6 jun 2023), p. 104771. ISSN: 00219258. DOI: [10.1016/j.jbc.2023.104771](https://doi.org/10.1016/j.jbc.2023.104771).

5

CONCLUSIONS, FUTURE OUTLOOK, AND SOCIETAL IMPACT

DEVELOPMENTAL bioelectric signals span rapid transients in excitable tissues and slower resting membrane potential (V_m) changes that evolve alongside morphogenesis.^{1,2} Embryogenesis relies on coordinated signals to guide pattern formation.³ Bioelectric dynamics are an important part of this coordination, but they remain hard to interpret without measurements that can be compared across cells, tissues, and time.^{2,4} A central barrier to mechanistic progress is that we still lack an *in vivo* method to quantify resting membrane potential on an absolute scale at cellular resolution over developmental time, so voltage patterns cannot be compared and directly related to defined developmental events.^{2,4} This thesis addresses this gap by establishing an integrated *in vivo* voltage imaging framework in zebrafish embryos that combines high-speed intensity imaging for fast electrical activity with an absolutely calibrated lifetime readout for resting potential comparisons. By moving from the relative contrast of standard voltage imaging to calibrated readouts of membrane potential estimates, this framework enables cross-sample comparison under photon-limited, optically heterogeneous embryonic conditions. To move closer to absolute interpretation *in vivo*, this thesis also explores indicator design strategies, using *Gloeobacter* rhodopsin (GR)-based electrochromic Förster resonance energy transfer (eFRET) constructs to identify key engineering constraints and design principles for lifetime-readable voltage indicators that are more sensitive than current sensors, with greater stability and reduced hysteresis. These advances can improve photon-limited precision and make calibration more robust.

The remainder of this chapter summarizes the key scientific contributions, clarifies the scope and limitations of the work, outlines future directions, and discusses the broader societal and scientific impact of quantitative bioelectric readouts in living embryos.

5.1. KEY SCIENTIFIC CONTRIBUTIONS

5.1.1. GENETIC AND EXPERIMENTAL ACCESS FOR *IN VIVO* VOLTAGE IMAGING DURING EMBRYOGENESIS (CHAPTER 2)

In this chapter, we build a zebrafish Ace2N-mNeon expression and promoter toolkit that supports diverse tissue- and cell-type-specific targeting, and we validate membrane-localized expression in early developmental stages, providing practical targeting options that can be selected based on biological context.⁵ Using this resource in live zebrafish embryos, we record early neuronal and cardiac electrical activity, demonstrating that physiologically meaningful voltage readouts can be obtained at early stages and establishing the necessary genetic resources and experimental setup for future quantitative work.⁵ We show, in a first proof-of-principle, the feasibility and importance of voltage measurements across developmental stages. These demonstrations include synchronous motor neuron activity during primary neurogenesis, which becomes reduced or absent at later stages, and detectable cardiac electrical activity prior to morphological chamber separation, with conduction features that mature over development. In this thesis, these observations are positioned as demonstrations of *in vivo* usability and as prompts for quantitative questions, rather than as mechanistic or causal explanations. Taken together, this contribution defines what can be measured in early embryos with the tools currently

available.

5.1.2. CELL-BASED FLIM FRAMEWORK FOR ABSOLUTELY CALIBRATED MEMBRANE POTENTIAL MAPPING IN DEVELOPING ZEBRAFISH (CHAPTER 3)

We then embark on creating improved tools. In [Chapter 3](#), we develop a framework for calibrated voltage imaging of resting membrane potential at cellular resolution in developing zebrafish using fluorescence lifetime imaging microscopy (FLIM). We calibrate lifetime to membrane voltage under controlled electrophysiological conditions as an external reference for interpreting *in vivo* embryonic data, and we establish a consistent acquisition and processing pipeline to ensure transfer of this calibration between samples, cell types, and developmental stages. To address the constraints that dominate embryonic FLIM datasets, including limited photon budgets, heterogeneous background, and membrane-localization requirements, we implement an analysis framework that converts Time-Tagged Time-Resolved (TTTR) data into a reproducible cell-level readout, turning qualitative voltage patterns into comparable quantitative measurements.

This framework integrates membrane-focused segmentation and pixel selection, photon-summing strategies, multi-component fitting, and explicit quality-check criteria, allowing the acquisition of stable per-cell fluorescence lifetimes even under optical inhomogeneity and low signal-to-noise conditions. We also developed tools for visualizing these data in 2D and 3D visualizations to better interpret the biological information.

Compared with pixel-level maps, cell-resolved views provide a more directly interpretable view of tissue organization and reduce ambiguity from mixed pixels, while signal-to-noise and statistical significance determinations are still based on underlying pixel- and photon-count data. Using this framework, we quantify resting membrane potential differences across multiple cell types and developmental stages and show the feasibility of longitudinal tracking of developmental trends. With calibration and a consistent acquisition, analysis, and visualization pipeline, cross-sample, cross-tissue, and cross-stage comparisons become possible.

5.1.3. ENGINEERING CONSTRAINTS AND DESIGN PRINCIPLES FOR NEXT-GENERATION LIFETIME-READABLE eFRET VOLTAGE INDICATORS (CHAPTER 4)

Motivated by the need for a more sensitive, calibrated voltage readout via FLIM, in [Chapter 4](#) we began designing a novel eFRET construct based on a GR voltage-sensing moiety. We systematically varied the linker length between the mNeonGreen donor and the GR acceptor, but found unexpectedly small, inverse-polarity responses. We developed a minimal model to explain these observations, based on realistic assumptions about how voltage perturbs the GR absorption spectrum, supported by control measurements. While both the measurements and some of the assumptions in the model (e.g., the value of E_0) require improved characterization, the model itself is internally consistent and will help with the interpretation of future GR-FRET data. The experimental data provide an exhaustive exploration of part of the parameter space (a range of linker lengths) that will feed into a larger-scale engineering effort, including donor choice, linker length, linker

flexibility, and linker attachment points, to achieve the required improved eFRET voltage sensor.

5.2. FUTURE OUTLOOK

5.2.1. TECHNICAL ADVANCES IN ABSOLUTE VOLTAGE IMAGING

ENHANCED ANALYSIS PIPELINES

The cell-based FLIM analysis and visualization framework established in [Chapter 3](#) provides a strong starting point, but larger *in vivo* datasets will require higher data retention and clearer interpretation. Future pipeline work will therefore focus on keeping more usable cells while making uncertainty and failure modes explicit.

First, we can replace hard exclusion with stratified quality classes. Instead of discarding all borderline cells, we can retain them as a separate tier and use them for sensitivity analyses.⁶ This reduces selection bias and improves robustness when comparing tissues or stages.⁶ Then, we can improve segmentation to reduce avoidable errors in lifetime estimation.⁷ We will use adaptive membrane segmentation that scales with cell size and local contrast, and we will also reduce background contamination by intensity-weighted photon summing, so low-confidence pixels contribute less to the pooled histogram.⁷ Machine learning can then flag unreliable segmentations and help identify recurring failure patterns.⁸ To reduce manual correction and improve consistency, we can extend CellPose training across developmental stages and cell types.⁹

Moreover, the remaining gap to absolute interpretation is to better match the sampling regime between calibration and *in vivo* imaging. As discussed in [Chapter 3](#), a practical route is frame-resolved lifetime analysis to align readout windows across datasets and reduce systematic offsets. Finally, 3D visualization is important because our samples are living 3D tissues. Building on our current workflow, we will continue to improve 3D visualization by adding registration and embryo-to-embryo alignment. This will allow 3D maps to capture tissue-scale gradients, pre-organ V_m changes, and statistical comparisons across embryos at matched stages. This should improve interpretability and comparability, both of which are critical to the broad acceptance of calibrated *in vivo* voltage imaging.

HARDWARE AND ACQUISITION STABILITY

Hardware and acquisition stability will be equally important for the broad adoption of *in vivo* quantitative lifetime imaging. Future work should increase photon efficiency and reduce drift by improving collection efficiency and detection stability, and by routinely tracking system lifetime standards across sessions. Light-sheet FLIM is a strong next step for *in vivo* organisms because it matches 3D development while reducing out-of-plane exposure and enabling faster volumetric acquisition at lower light doses.¹⁰ In embryos, motion and slow morphological changes can be handled by acquisition designs that minimize duty cycle and photodamage, and by registration strategies that make the resulting maps easier to compare across animals. Any such implementation should still

track Instrument Response Function (IRF) and lifetime standards across the field of view to keep calibration robust.

NEXT-GENERATION VOLTAGE INDICATOR FOR IN VIVO ABSOLUTE VOLTAGE IMAGING

In [Chapter 4](#), we identified design constraints that guide the next generation of GR-based eFRET GEVIs. A key finding was that spectral tuning can reduce donor–acceptor overlap sufficiently to lower FRET efficiency and even reverse the apparent response polarity, as observed with GR-D115N and mNeonGreen.

Future work will therefore focus on two practical steps. First, we will measure the spectra of GR-D115N under membrane-relevant conditions to ensure that donor–acceptor overlap is evaluated in the same regime as in vivo imaging. Then, we will rebuild spectral matching and coupling by pairing GR-D115N with redshifted donors and by testing more constrained linker geometries to stabilize donor–acceptor orientation.^{11,12} We will also add a staged workflow with early spectral and lifetime checkpoints, so patch-clamp screening is limited to candidates that meet these basic requirements. In addition, we will explicitly optimize usable dynamic range by prioritizing constructs that remain bright and monotonic across the calibrated voltage window, with minimal saturation and hysteresis, so lifetime-to-voltage conversion remains robust in vivo.

If successful, these efforts should yield indicators with larger lifetime changes per 100 mV than Ace2N–mNeon, thereby increasing practical sensitivity and reducing uncertainty in calibrated resting membrane potential measurements in developing embryos, and bringing in vivo measurements closer to truly absolute voltage imaging.^{2,4}

5.2.2. BIOLOGICAL APPLICATIONS

Many developmental bioelectricity studies link ion-channel perturbations to downstream phenotypes, but they rarely quantify how much resting membrane potential changes, or where and when those changes appear, because current in vivo readouts are not stably calibrated across cells and time.^{2,4,13} With the technical improvements outlined above, an improved calibrated FLIM framework can serve as a practical platform for biological studies that need a quantitative in vivo V_m readout.

A realistic first step is to use stage-matched resting membrane potential maps as a baseline and then quantify how specific perturbations shift that baseline in defined tissues. For example, the framework could be used to measure how increased Na^+/K^+ -ATPase activity shifts resting V_m , and whether the effect is uniform across a tissue or concentrated at specific regions such as boundaries.¹⁴ More generally, the same approach can be paired with genetic, pharmacological, or optogenetic perturbation models, so each manipulation is evaluated against a measured V_m change in the same preparation rather than inferred indirectly from downstream phenotypes.^{1,15,16} This creates a clearer link between perturbation strength and the bioelectric response, which can then be related to developmental outcomes in a controlled, comparable way.^{1,15,16}

5.2.3. CROSS-SPECIES TRANSLATION

Although this thesis focuses on zebrafish, the calibrated FLIM framework is transferable because it provides a cell-resolved voltage readout on a calibrated, comparable scale that can be compared across tissues and time. In future work, we will adapt the same pipeline to other model systems where bioelectric patterns are central. The main goal is to make voltage measurements comparable across labs and organisms by keeping analysis protocols and calibration practices aligned. For example, *Xenopus* embryos provide established assays for left-right patterning and regeneration.^{17,18} *Drosophila* enables genetic screens that link specific ion channels to voltage phenotypes,^{19,20} and mammalian organoids or human iPSC-derived tissues offer a controlled setting to test whether developmental voltage signatures generalize to mammalian contexts.²¹

5.2.4. INTEGRATION WITH OTHER IMAGING TECHNIQUES

In future work, our calibrated voltage imaging framework can be integrated with complementary modalities to link voltage patterns to mechanisms as well. For example, combining FLIM-based resting V_m mapping with high-speed intensity-based voltage imaging can separate fast electrical activity from slow resting-potential shifts in excitable tissues and test how these regimes interact.⁵ In addition, simultaneous calcium imaging can probe voltage–calcium coupling during key developmental transitions.²² Finally, linking voltage maps to single-cell RNA sequencing and computational modeling can connect measured voltage states to ion-channel programs and predict how changes in channel expression should reshape tissue-scale voltage patterns, which can then be tested experimentally.¹ At a broader level, multimodal datasets anchored by calibrated voltage readouts can help the field move from descriptive associations to mechanistic models that are easier to test and compare across studies.^{2,4,23}

5.3. SOCIETAL IMPACT

5.3.1. REDUCED ANIMAL EXPERIMENTS

Central to the work in this thesis is the ability to compare voltage measurements between embryos in time and space. We expect this to lead, in future years, to the adoption of absolute voltage imaging as a key tool in the neuroscience and developmental biology toolbox. Combined with our open-source workflows, this will result in reduced animal use, since direct comparisons between animals, experiments, and setups are directly incorporated into the concept of the work, facilitating reproducibility and reuse.²⁴

5.3.2. TOWARD PRECISION BIOELECTRIC PHENOTYPING

Preclinical research and precision medicine need functional biomarkers that are measurable, comparable and related to the mechanism, not only descriptive phenotypes.²⁵ By making voltage changes quantifiable on an absolute scale in live tissues, this thesis opens a practical route to treating the bioelectric signal as such a biomarker. Our framework

allows researchers to measure absolute resting V_m patterns and to measure how much a defined perturbation shifts V_m , rather than inferring electrical change indirectly from downstream phenotypes.^{2,4} This allows a comparison of the effects of the perturbation between tissues, stages, and laboratories using the same readout.

In patient-derived cells, organoids, and animal models, calibrated shifts in V_m can be used as an early functional readout.^{26,27} Researchers can classify perturbations or candidate interventions by effect size and direction, and then relate those measured changes to outcomes such as morphology, differentiation state, or excitability.^{2,4} Over time, this can support screening and stratification workflows where bioelectric readouts complement molecular markers, and where “what changed in voltage” becomes a concrete link between an intervention and its downstream phenotype.²⁶

5.3.3. DEVELOPMENTAL DISORDERS

Embryonic development remains one of the most poorly understood aspects of human biology.²⁸ This sad fact is exacerbated by the large impact developmental disorders have on the lives of all involved.²⁹ The work in this thesis is foundational, but in the cell-type and developmental-stage comparisons in zebrafish, a glimpse of the possibilities is already visible: to fundamentally add to our understanding of embryonic development. The work described here, if continued, will lead to the development of a new framework to understand tissue pattern formation, cellular specialization, tissue growth, and morphogenesis, including the role of bioelectrical signaling.^{2,30} This knowledge will lead to a renewed understanding of developmental disorders and the adoption of bioelectric biomarkers, for example, in the screening of drugs for these disorders.^{27,31}

5.3.4. SAMPLE-TO-SAMPLE COMPARISON OF NOISY LIFETIME READOUTS IN INDUSTRY

Fluorescence lifetime is a relatively robust readout of a fluorescence signal.³² In the context of biology, this thesis has shown that particular care needs to be taken to create a consistent analysis pipeline, and that there is room for improvement over standard visualization practices. These concepts can be translated beyond biology: for instance, in materials science, lifetime could be a valuable metrology readout, but industrial adoption would require consistency of approach across samples, experimental setups, and measurement sessions, and careful analysis, as outlined in this thesis. By standardizing this approach for metrology, we can add to the Dutch hardware industry.

5.4. CONCLUSION

In reviewing our research, we argue that our methodology addresses a key measurement gap in developmental bioelectricity by enabling quantitative, calibration-referenced voltage readouts *in vivo*, rather than relying only on qualitative patterns.^{2,16,33} In this thesis, we demonstrate the feasibility of cell-resolved, cross-tissue membrane voltage mapping during early embryonic development. By providing a calibrated *in vivo* readout

on a shared scale, we offer a practical framework that others can use to connect bioelectric dynamics to developmental processes and to test mechanistic hypotheses.

This thesis advances absolutely calibrated voltage imaging from several angles. First, we establish genetic expression platforms that target distinct tissues. Using existing tools, we add quantitative *in vivo* examples of fast electrical signals in early embryos, where such measurements remain relatively limited. Then, we describe a calibrated FLIM-based workflow that converts lifetime readouts into approximately absolute membrane voltage estimates. Next, we use these results to motivate engineering and selection strategies for voltage indicators that can improve sensitivity and practical accuracy in future recordings. Finally, we report bioelectrical trends at different scales during early development, providing a quantitative reference for studies that test how specific bioelectric changes relate to specific developmental events.

With continued improvements in indicators, analysis, and acquisition, this approach can support experiments that combine calibrated measurement with controlled perturbation. This makes perturbations easier to compare across tissues and stages because voltage changes are measured on the same calibrated axis. As a result, the field can move toward clearer causal and mechanistic explanations of how bioelectric signals shape development. At a societal level, broader access to reproducible *in vivo* voltage profiling can accelerate preclinical research by enabling more consistent functional phenotyping and safer, more testable bioelectric interventions in biomedicine.

BIBLIOGRAFIE

- [1] Michael Levin. “Molecular bioelectricity: How endogenous voltage potentials control cell behavior and instruct pattern regulation in vivo”. In: *Molecular Biology of the Cell* 25 (24 dec 2014), p. 3835–3850. ISSN: 19394586. DOI: [10.1091/mbc.E13-12-0708](https://doi.org/10.1091/mbc.E13-12-0708). PMID: [25425556](https://pubmed.ncbi.nlm.nih.gov/25425556/).
- [2] Michael Levin. “Molecular bioelectricity in developmental biology: New tools and recent discoveries”. In: *BioEssays* 34 (3 mrt 2012), p. 205–217. ISSN: 02659247. DOI: [10.1002/bies.201100136](https://doi.org/10.1002/bies.201100136). PMID: [22237730](https://pubmed.ncbi.nlm.nih.gov/22237730/).
- [3] Martin R. Silic en GuangJun Zhang. “Bioelectricity in Developmental Patterning and Size Control: Evidence and Genetically Encoded Tools in the Zebrafish Model”. In: *Cells* 12 (8 apr 2023), p. 1148. ISSN: 2073-4409. DOI: [10.3390/cells12081148](https://doi.org/10.3390/cells12081148).
- [4] Julia R. Lazzari-Dean, Anneliese M.M. Gest en Evan W. Miller. “Measuring Absolute Membrane Potential Across Space and Time”. In: *Annual Review of Biophysics* 50 (1 mei 2021), p. 447–468. ISSN: 1936-122X. DOI: [10.1146/annurev-biophys-062920-063555](https://doi.org/10.1146/annurev-biophys-062920-063555).
- [5] ZhenZhen Wu e.a. *Exploring Bioelectricity with Ace2N-mNeon during Zebrafish Embryogenesis*. Dec 2024. DOI: [10.1101/2024.12.12.628143](https://doi.org/10.1101/2024.12.12.628143).
- [6] Matthew Peverill e.a. “Balancing Data Quality and Bias: Investigating Functional Connectivity Exclusions in the Adolescent Brain Cognitive Development™ (ABCD Study) Across Quality Control Pathways”. In: *Human Brain Mapping* 46.1 (2025), e70094. DOI: [10.1002/hbm.70094](https://doi.org/10.1002/hbm.70094). PMID: [39788921](https://pubmed.ncbi.nlm.nih.gov/39788921/).
- [7] Sean C. Warren e.a. “Rapid Global Fitting of Large Fluorescence Lifetime Imaging Microscopy Datasets”. In: *PLOS ONE* 8.8 (2013), e70687. DOI: [10.1371/journal.pone.0070687](https://doi.org/10.1371/journal.pone.0070687). PMID: [23940626](https://pubmed.ncbi.nlm.nih.gov/23940626/).
- [8] Olaf Ronneberger, Philipp Fischer en Thomas Brox. “U-Net: Convolutional Networks for Biomedical Image Segmentation”. In: *arXiv:1505.04597 [cs.CV]* (2015).
- [9] Marius Pachitariu en Carsen Stringer. “Cellpose 2.0: how to train your own model”. In: *Nature Methods* 19 (12 dec 2022), p. 1634–1641. ISSN: 1548-7091. DOI: [10.1038/s41592-022-01663-4](https://doi.org/10.1038/s41592-022-01663-4).
- [10] Michael Weber, Michaela Mickoleit en Jan Huisken. “Multilayer Mounting for Long-term Light Sheet Microscopy of Zebrafish”. In: *Journal of Visualized Experiments* (84 feb 2014). ISSN: 1940-087X. DOI: [10.3791/51119](https://doi.org/10.3791/51119).
- [11] Connor Beck, Diming Zhang en Yiyang Gong. “Enhanced genetically encoded voltage indicators advance their applications in neuroscience”. In: *Current Opinion in Biomedical Engineering* 12 (dec 2019), p. 111–117. ISSN: 24684511. DOI: [10.1016/j.cobme.2019.10.010](https://doi.org/10.1016/j.cobme.2019.10.010).

- [12] Ágnes Szabó, János Szöllősi en Peter Nagy. “Principles of Resonance Energy Transfer”. In: *Current Protocols* 2 (12 dec 2022). ISSN: 2691-1299. DOI: [10.1002/cpz1.625](https://doi.org/10.1002/cpz1.625).
- [13] Daan Brinks, Aaron J. Klein en Adam E. Cohen. “Two-Photon Lifetime Imaging of Voltage Indicating Proteins as a Probe of Absolute Membrane Voltage”. In: *Biophysical Journal* 109 (5 sep 2015), p. 914–921. ISSN: 15420086. DOI: [10.1016/j.bpj.2015.07.038](https://doi.org/10.1016/j.bpj.2015.07.038). PMID: [26331249](https://pubmed.ncbi.nlm.nih.gov/26331249/).
- [14] M. B. Rook e.a. “Biology of cardiac sodium channel Nav1.5 expression”. In: *Cardiovascular Research* 93 (1 jan 2012), p. 12–23. ISSN: 0008-6363. DOI: [10.1093/cvr/cvr252](https://doi.org/10.1093/cvr/cvr252).
- [15] Kelly A. McLaughlin en Michael Levin. “Bioelectric signaling in regeneration: Mechanisms of ionic controls of growth and form”. In: *Developmental Biology* 433.2 (2018), p. 177–189. DOI: [10.1016/j.ydbio.2017.08.032](https://doi.org/10.1016/j.ydbio.2017.08.032). PMID: [29291972](https://pubmed.ncbi.nlm.nih.gov/29291972/).
- [16] Laura Faith George en Emily Anne Bates. “Mechanisms Underlying Influence of Bioelectricity in Development”. In: *Frontiers in Cell and Developmental Biology* 10 (feb 2022). ISSN: 2296-634X. DOI: [10.3389/fcell.2022.772230](https://doi.org/10.3389/fcell.2022.772230).
- [17] Brian Reid, Bing Song en Min Zhao. “Electric currents in *Xenopus* tadpole tail regeneration”. In: *Developmental Biology* 335 (1 nov 2009), p. 198–207. ISSN: 1095564X. DOI: [10.1016/j.ydbio.2009.08.028](https://doi.org/10.1016/j.ydbio.2009.08.028). PMID: [19733557](https://pubmed.ncbi.nlm.nih.gov/19733557/).
- [18] Vaibhav P. et al. “Transmembrane voltage potential controls embryonic eye patterning in *Xenopus laevis*”. In: *Development* 139 (2 jan 2012), p. 313–323. ISSN: 1477-9129. DOI: [10.1242/dev.073759](https://doi.org/10.1242/dev.073759).
- [19] Maya Emmons-Bell en Iswar K Hariharan. “Membrane potential regulates Hedgehog signalling in the *Drosophila* wing imaginal disc”. In: *EMBO reports* 22 (4 apr 2021). ISSN: 1469-221X. DOI: [10.15252/embr.202051861](https://doi.org/10.15252/embr.202051861).
- [20] Barry Ganetzky. “Genetic analysis of ion channel dysfunction in *Drosophila*”. In: *Kidney International* 57.3 (2000), p. 766–771. DOI: [10.1046/j.1523-1755.2000.00913.x](https://doi.org/10.1046/j.1523-1755.2000.00913.x). PMID: [10720927](https://pubmed.ncbi.nlm.nih.gov/10720927/).
- [21] K. A. Kruth e.a. “SCN2A channelopathies in the autism spectrum of neuropsychiatric disorders: a role for pluripotent stem cells?” In: *Molecular Autism* 11 (2020), p. 23. DOI: [10.1186/s13229-020-00330-9](https://doi.org/10.1186/s13229-020-00330-9). PMID: [32248815](https://pubmed.ncbi.nlm.nih.gov/32248815/).
- [22] Helen H H. Yang e.a. “Subcellular Imaging of Voltage and Calcium Signals Reveals Neural Processing In Vivo”. In: *Cell* 166 (1 jun 2016), p. 245–257. ISSN: 0092-8674. DOI: [10.1016/J.CELL.2016.05.031](https://doi.org/10.1016/J.CELL.2016.05.031). PMID: [27264607](https://pubmed.ncbi.nlm.nih.gov/27264607/).
- [23] Julia R Lazzari-Dean, Anneliese MM Gest en Evan W Miller. “Optical estimation of absolute membrane potential using fluorescence lifetime imaging”. In: *eLife* 8 (sep 2019). ISSN: 2050-084X. DOI: [10.7554/eLife.44522](https://doi.org/10.7554/eLife.44522).
- [24] Nathalie Percie du Sert e.a. “The ARRIVE guidelines 2.0: Updated guidelines for reporting animal research”. In: *PLOS Biology* 18.7 (2020), e3000410. DOI: [10.1371/journal.pbio.3000410](https://doi.org/10.1371/journal.pbio.3000410). PMID: [32663219](https://pubmed.ncbi.nlm.nih.gov/32663219/).

- [25] Stefan Schreiber e.a. “Rise of precision medicine: can it deliver on its promise in IBD?” In: *Gut* 75.1 (2025), p. 176–188. DOI: [10.1136/gutjnl-2023-330000](https://doi.org/10.1136/gutjnl-2023-330000). PMID: [41052915](https://pubmed.ncbi.nlm.nih.gov/41052915/).
- [26] J. H. Cha, K. Kim en I. J. Cho. “Beyond Structure: Next-Generation Electrophysiological Platforms for Functional Brain Organoids”. In: *International Journal of Stem Cells* 18.3 (30 aug 2025). Epub 2025-07-31, p. 215–236. DOI: [10.15283/ijsc25056](https://doi.org/10.15283/ijsc25056). PMID: [40739714](https://pubmed.ncbi.nlm.nih.gov/40739714/).
- [27] Qianmin Gao e.a. “Organoids: A new frontier in precision medicine and engineering”. In: *Precision Medicine and Engineering* 2.4 (dec 2025). Review article, p. 100049. DOI: [10.1016/j.preme.2025.100049](https://doi.org/10.1016/j.preme.2025.100049). URL: <https://doi.org/10.1016/j.preme.2025.100049>.
- [28] Peter J. Rugg-Gunn, Naomi Moris en Patrick P. L. Tam. “Technical challenges of studying early human development”. In: *Development* 150.11 (1 jun 2023). Epub 2023-06-01, dev201797. DOI: [10.1242/dev.201797](https://doi.org/10.1242/dev.201797). PMID: [37260362](https://pubmed.ncbi.nlm.nih.gov/37260362/).
- [29] Y. Xie e.a. “Global trends in developmental disabilities in children and adolescents 1990–2021: Sex- and sociodemographic Index-stratified analysis of Global Burden of Disease 2021”. In: *International Journal of Developmental Disabilities* (2025). Advance online publication, p. 1–16. DOI: [10.1080/20473869.2025.2581660](https://doi.org/10.1080/20473869.2025.2581660). URL: <https://doi.org/10.1080/20473869.2025.2581660>.
- [30] GuangJun Zhang en Michael Levin. “Bioelectricity is a universal multifaced signaling cue in living organisms”. In: *Molecular Biology of the Cell* 36.2 (2025), pe2. DOI: [10.1091/mbc.E23-08-0312](https://doi.org/10.1091/mbc.E23-08-0312). PMID: [39873662](https://pubmed.ncbi.nlm.nih.gov/39873662/).
- [31] C. Giorgi e.a. “Brain Organoids: A Game-Changer for Drug Testing”. In: *Pharmaceutics* 16.4 (22 mrt 2024), p. 443. DOI: [10.3390/pharmaceutics16040443](https://doi.org/10.3390/pharmaceutics16040443). PMID: [38675104](https://pubmed.ncbi.nlm.nih.gov/38675104/).
- [32] Mikhail Y. Berezin en Samuel Achilefu. “Fluorescence Lifetime Measurements and Biological Imaging”. In: *Chemical Reviews* 110 (5 mei 2010), p. 2641–2684. ISSN: 0009-2665. DOI: [10.1021/cr900343z](https://doi.org/10.1021/cr900343z).
- [33] GuangJun Zhang en Michael Levin. “Bioelectricity is a universal multifaced signaling cue in living organisms”. In: *Molecular Biology of the Cell* 36 (2 feb 2025). ISSN: 1059-1524. DOI: [10.1091/mbc.E23-08-0312](https://doi.org/10.1091/mbc.E23-08-0312).

A

USED THEORY AND CONVENTIONS

Appendix A summarizes the basic definitions, symbols, and equations used throughout this thesis, regarding membrane potential, Time-Correlated Single Photon Counting (TCSPC) (including Time-Tagged Time-Resolved (TTTR) data and Instrument Response Function (IRF)-corrected fitting), Förster Resonance Energy Transfer (FRET), and fluorescence lifetime. Implementation details, including acquisition settings, parameter choices, and computational workflows, are described in the Methods and Supplementary Information of Chapters 2-4, with the in vivo calibration and quantitative analysis framework developed in Chapter 3.

A.1. BIOELECTRIC ORIGIN OF RESTING MEMBRANE POTENTIAL: GOLDMAN-HODGKIN-KATZ FRAMEWORK AND ASSUMPTIONS

In many cells, the resting V_m can be related to the intra- and extracellular concentrations of major permeant ions together with their effective permeabilities under the constant field approximation.¹

A commonly used form for monovalent ions is the Goldman-Hodgkin-Katz (GHK) equation, which is an expansion of the Nernst equation:²

$$V_m = \frac{RT}{F} \ln \left(\frac{P_K [K^+]_{out} + P_{Na} [Na^+]_{out} + P_{Cl} [Cl^-]_{in}}{P_K [K^+]_{in} + P_{Na} [Na^+]_{in} + P_{Cl} [Cl^-]_{out}} \right) \quad (A.1)$$

Here V_m denotes the membrane potential, defined as $V_m = V_{in} - V_{out}$. R is the gas constant, T is the absolute temperature, and F is the Faraday constant. The variables P_K , P_{Na} , and P_{Cl} represent effective permeability weights for K^+ , Na^+ , and Cl^- , and $[ion]_{in/out}$ indicate their corresponding intra- and extracellular concentrations.² Under physiological conditions, this equilibrium emphasizes that the resting membrane potential is a function of both ionic gradients and relative permeabilities.³

At the core of the work in this thesis, is the fact that cellular developments change this equation. Notably, permeability weights are dynamic physiological variables that are continually modulated by changing ion channel expression, transporter activity, and gap junction coupling in embryonic development.^{4,5} As a result, changes in V_m are expected throughout development and serve as markers of developmental state and cell type.

Throughout this thesis, depolarization refers to an increase in V_m (a shift toward a less negative potential), whereas hyperpolarization signifies a decrease in V_m .

A.2. FLUORESCENCE PHOTOPHYSICS

Throughout this thesis, τ_{fl} presents the fluorescence lifetime of the donor emission, characterized as the time constant of excited-state depopulation under a rate-competition model. The radiative decay rate is denoted by k_f , and the lumped non-radiative decay rate is denoted by k_{nr} , which collects all non-radiative pathways that compete with fluorescence under the measurement conditions.⁶⁻⁸ The fluorescence quantum yield is written as QY .⁹

In the context of FRET, τ_D denotes the fluorescence lifetime of the donor fluorophore in the absence of an acceptor, τ_{DA} is the donor lifetime when an acceptor is present.¹⁰

Fluorescence is the radiative emission that accompanies relaxation from an excited electronic state, and its kinetics are summarized here through a minimal rate-competition model (Fig. A.1).^{7,8,11,12} A Jablonski diagram provides a schematic overview of excitation from ground singlet state (S_0) to an excited singlet state (S_1) and relaxation through radiative emission and competing non-radiative routes.¹³ The effective k_{nr} encapsulates all possible non-radiative decay pathways, which can include, for instance, internal

conversion, intersystem-crossing (as denoted in (Fig. A.1), and, crucial for the thesis, FRET.^{12,13}

Following excitation from S_0 to S_1 , the excited-state population remains in S_1 for a finite time before returning to S_0 . The fluorescence lifetime τ_{fl} describes the characteristic timescale of this excited-state deactivation and, under a single-exponential approximation, is given by the inverse of the total decay rate:⁶

$$\tau_{fl} = \frac{1}{k_f + k_{nr}} = \frac{1}{k_{tot}} \quad (\text{A.2})$$

Under a single-exponential approximation, the detected fluorescence decay can be written as:¹⁴

$$I(t) = I_0 e^{-t/\tau_{fl}} \quad (\text{A.3})$$

where τ_{fl} is the fluorescence lifetime.

The fluorescence quantum yield QY is defined as the fraction of excitations that relax through fluorescence, and can be expressed in the same rate framework as:⁶

$$QY = \frac{k_f}{k_f + k_{nr}} \quad (\text{A.4})$$

which implies:

$$QY = k_f \cdot \tau_{fl} \quad (\text{A.5})$$

These relations are included to link the lifetime to the ratio of radiative and non-radiative decay rates,⁶ although absolute QY is not measured *in vivo* in this thesis, or typically *in vivo* at all.¹⁵ For any required calculations, reference QY in solution will be used, assuming that an isolated fluorescent protein would have similar properties in a cellular environment as in solution.¹⁶ This will rarely be the case in this thesis since most measurements involve newly engineered FRET constructs, for which the QY is difficult to ascertain independently because they contain a water-soluble fluorescent protein (the donor) and a membrane-localized, voltage-sensitive quencher (the acceptor).¹⁷ When QY and τ_{fl} are independently available, they can be used to infer effective k_f and k_{nr} ,⁶ but in the present work, lifetime is primarily used as a robust readout that reflects voltage-mediated changes in FRET between donor and acceptor.¹⁷

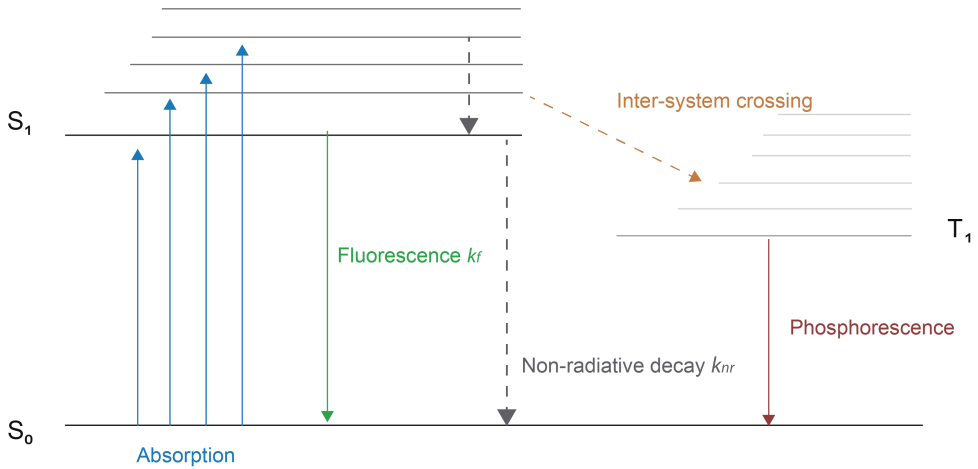


Figure A.1: Jablonski diagram of electronic manifolds and representative relaxation pathways. Shown are the excitation from S_0 to vibrational levels of S_1 , radiative relaxation via fluorescence, and competing non-radiative routes, including direct non-radiative decay and intersystem crossing to T_1 followed by phosphorescence. The diagram provides a visual reference for the competing pathways that underlie the lifetime observables used in Appendix A.2.

A.3. LIFETIME AS A FRET READOUT IN eFRET VOLTAGE INDICATORS

FRET describes non-radiative energy transfer from an excited donor to a nearby acceptor through dipole–dipole coupling.^{18,19} In the presence of an acceptor, FRET introduces an additional de-excitation pathway for the donor, which can be represented as an extra rate term:¹⁸

$$\tau_{DA} = \frac{1}{k_f + k_{nr} + k_{\text{FRET}}} \quad (\text{A.6})$$

where τ_{DA} is the donor lifetime in the presence of an acceptor and k_{FRET} denotes the effective FRET transfer rate.

In the Förster formalism, the transfer rate depends strongly on donor–acceptor separation:¹⁸

$$k_{\text{FRET}} = \frac{1}{\tau_D} \left(\frac{R_0}{r} \right)^6 \quad (\text{A.7})$$

where r is the donor–acceptor separation and R_0 is the Förster radius, which summarizes geometric and spectral determinants of FRET coupling. The Förster radius is typically on the order of a few nanometers and is dependent on the donor–acceptor pair and optical environment.

A standard expression is:^{6,18,20}

$$R_0^6 \propto \frac{\kappa^2 Q_D J(\lambda)}{n^4} \quad (\text{A.8})$$

in which κ^2 is the dipole–dipole orientation factor, Q_D is the donor quantum yield in the absence of acceptor, $J(\lambda)$ is the spectral overlap integral between donor emission and acceptor absorption, and n is the refractive index of the intervening medium. These dependencies imply that FRET efficiency can be tuned by changes in separation r , dipole orientation, and spectral overlap.

In electrochromic FRET (eFRET) voltage indicators, the acceptor is a voltage-sensitive chromophore whose absorption is modulated by membrane potential.^{21–23} Voltage-dependent changes in acceptor absorption alter the spectral overlap and thereby modulate k_{FRET} , producing corresponding shifts in donor lifetime that can be measured by FLIM as a proxy for membrane voltage.^{21,23–25} The sign and sensitivity of the lifetime-voltage relation are indicator-specific and depend on how voltage perturbs acceptor absorption within the donor emission band.²⁵

For the theoretical work in Chapter 4, FRET efficiency E_{FRET} can be expressed in terms of donor lifetimes measured in the absence and presence of the acceptor.^{6,18,19} Using the rate relations above, the efficiency is given by:^{6,18}

$$E_{\text{FRET}} = 1 - \frac{\tau_{DA}}{\tau_D} \quad (\text{A.9})$$

This relation highlights why donor lifetime is a direct readout of energy transfer; a shortening of donor lifetime corresponds to increased transfer efficiency, without requiring acceptor emission to be measured.^{6,18}

A.4. PRACTICAL LIFETIME ACQUISITION: TCSPC, TTTR AND IRF

In the TTTR acquisition, each detected photon is recorded as a timestamped event. For time-domain Fluorescence Lifetime Imaging Microscopy (FLIM), the microtime records the photon's arrival delay relative to the most recent excitation pulse and therefore populates the decay histogram used for lifetime estimation.^{14,26} The macrotime records the photon's arrival time on a coarse global clock across the full acquisition, enabling the reconstruction of temporal order across frames, lines, or experimental epochs.²⁶ In addition, marker events provide timestamped references for scanner or hardware synchronization (for example, line and frame boundaries or stimulus triggers), allowing photon events to be mapped to spatial and experimental context.²⁶ In raster-scanned imaging, streams must be combined with marker information to reconstruct spatial coordinates and measurement timeframes.²⁶ The specific restructuring of our measured TTTR streams into image and decay arrays for downstream analysis is described in [Methods](#) and [Supplementary Materials](#) of Chapter 3.

In general, photon events can be assigned to spatial sampling units (for example, pixels or regions of interest) using scanner coordinates reconstructed from marker timing.²⁶

For each unit, the microtime values are accumulated into a decay histogram over the excitation period, providing the time-domain signal used for lifetime estimation.²⁷ Estimated lifetime values can then be rendered as a pseudocolor map to visualize spatial heterogeneity across the field of view.²⁷

In time-domain FLIM, the measured decay is broadened by the finite timing response of the instrument, which includes contributions from the excitation pulse width, detector response, optics, and timing electronics.²⁷ This combined system response is described by the IRF. In an IRF-aware measurement model, the observed decay can be expressed as a convolution of the underlying fluorescence decay with the IRF, together with background contributions:²⁸

$$I_{\text{meas}}(t) = [I_{\text{true}}(t) \otimes \text{IRF}(t)] + B(t) \quad (\text{A.10})$$

where $I_{\text{true}}(t)$ denotes the underlying fluorescence decay, $\text{IRF}(t)$ is the instrument response function, \otimes denotes convolution, and $B(t)$ summarizes background contributions such as dark counts and voltage-insensitive photon sources.²⁸ To minimize pile-up distortion in TCSPC, the detected count rate should be kept well below the laser repetition rate, and acquisition settings should be chosen such that the microtime histogram is not biased toward early-arriving photons. The specific IRF handling and fitting procedures are described in the [Methods](#) and [Supplementary Materials](#) of [Chapter 3](#).

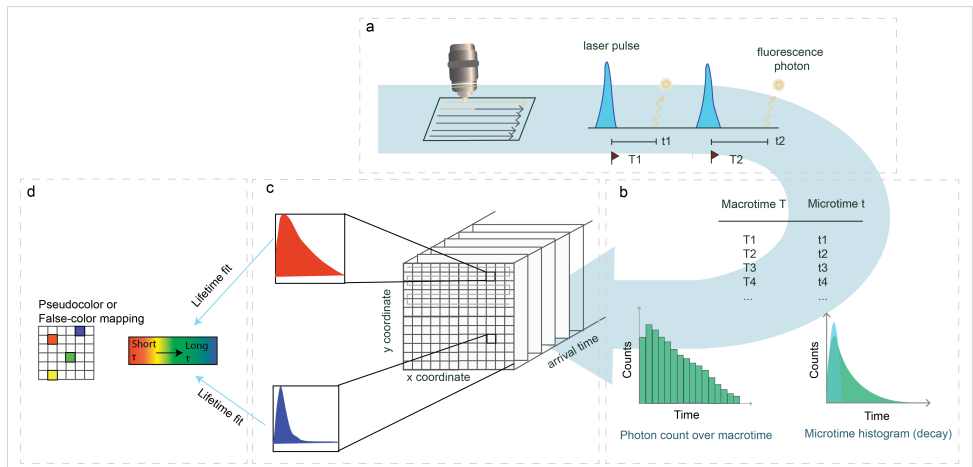


Figure A.2: Overview of TCSPC-based FLIM acquisition, TTR timing, and lifetime map formation. (a) In raster-scanned imaging with pulsed excitation, detected fluorescence photons are time-stamped relative to the excitation pulses. (b) In TTR acquisition, each photon event carries a coarse macrotime coordinate (ordering photons across the acquisition) and a fine microtime coordinate (delay within the current excitation period), enabling both temporal context and construction of the microtime decay histogram. (c) Photon events are assigned to spatial sampling units (for example, pixels), yielding a microtime decay histogram for each unit that can be used for lifetime estimation. (d) Estimated lifetimes are rendered as a pseudocolor map, providing an intuitive visualization of spatial lifetime heterogeneity across the field of view. Quantitative comparisons use the analysis framework described in [Chapter 3](#), and the thesis-wide lifetime feature is defined in [Appendix A.5](#).

A.5. LIFETIME DEFINITION IN THIS THESIS

TCSPC yields a fluorescence decay histogram rather than a single parameter. For quantitative comparison across cells, tissues, samples, and developmental stages, it is therefore necessary to compare these histograms. It is possible to do this in a two- or higher-dimensional vectorial way (polar plots are a relatively well-established method).²⁹ However, since the primary focus of the work in this thesis is to provide spatially resolved information in the context of development, we chose in this foundational work to try and summarize each decay with a reproducible scalar lifetime feature.^{26,27,30} We made this choice to facilitate intuitive 2D visualizations (x and y coordinates are spatial coordinates, color = lifetime = voltage).

Equation(A.3) denotes an ideal single-exponential decay, where the fluorescence lifetime would be the straightforward scalar representation of the decay histogram. However, measured decays often deviate from this strict single-exponential behavior.³¹ In biological measurements, observed decays often reflect mixtures of emitting contributions and background rather than a single ideal exponential.³⁰ Particularly, fluorescence decays measured in cells and tissues are often shaped by multiple emitting contributions within the detection volume. These contributions may reflect distinct microenvironments, multiple molecular states of the label, or additional photon sources that do not share the same decay kinetics. As a result, the recorded decay will not be single-exponential and the reported lifetime should be interpreted as an effective phenomenological readout for calibration, not as indication for a single underlying molecular state.^{8,32}

The detected decay can be represented as

$$I(t) = \sum_i A_i e^{-t/\tau_i}, \quad (\text{A.11})$$

where A_i and τ_i capture the relative contribution and characteristic timescale of each component. Again, these parameters can depend on background subtraction, IRF deconvolution, and fitting constraints, and should not be interpreted as direct fractions or as indicators of discrete physical states.

In live tissues, the reported lifetime can be influenced by factors beyond the fluorophore's intrinsic deactivation kinetics, including background photon contributions, heterogeneous indicator localization, and variation in the relative weights of decay components.^{8,33} In this thesis, changes in the reported lifetime can then arise from two conceptually distinct effects: a change in the intrinsic decay kinetics of a contributing population, or a change in the relative contribution of different populations to the detected signal.³¹ This distinction is important when comparing samples across tissues and developmental stages, because shifts in background contributions or in the fraction of properly localized indicator can modify baseline lifetimes and apparent dynamic range.³⁰

A reported single lifetime is then dependent on the above-mentioned analysis procedures, and the final choice in lifetime to report depends as much on the underlying physics as it does on its ability to separate experimental states in one sample (i.e., cell type, developmental states) and to facilitate comparison across samples and acquisitions.³⁴ Consequently, lifetime comparisons are most meaningful when acquisition settings and

analysis definitions are applied consistently across samples.³⁵ In the voltage imaging context, observed lifetime shifts should be attributed to membrane voltage only when they are consistent with the calibrated lifetime-voltage coupling and when plausible voltage-insensitive contributions are minimized or remain comparable across conditions.^{31,36} Practical analysis strategies for photon-limited in vivo decays, and criteria and validation used to support voltage attribution in vivo, are developed in [Chapter 3](#).^{31,37}

As a result of these considerations and the work in [Chapter 3](#), throughout this thesis, the reported lifetime is the amplitude-weighted mean lifetime after correction for dark counts, non-GEVI contributions, and IRF-deconvolution:³⁸

$$\langle \tau \rangle_A = \frac{\sum_{i=1}^n A_i \tau_i}{\sum_{i=1}^n A_i} \quad (\text{A.12})$$

The subscript A indicates that amplitudes A_i are used as the weights in the mean. Here, the amplitudes A_i are the fitted weights associated with the component lifetimes under the chosen decay model. The amplitude-weighted definition provides a single scalar summary of a multi-component decay while retaining sensitivity to components that dominate the fitted amplitude.^{38,39} In the special case where a single-exponential description is adequate, $\langle \tau \rangle_A$ reduces to the fitted mono-exponential lifetime parameter.

Several alternative scalar summaries are used in the FLIM literature, including intensity-weighted mean lifetimes and model-free moment-based measures.^{39,40} This section does not attempt to argue that $\langle \tau \rangle_A$ is universally optimal, but rather specifies the convention used throughout the thesis.

BIBLIOGRAFIE

- [1] Osvaldo Alvarez en Ramon Latorre. “The enduring legacy of the “constant-field equation” in membrane ion transport”. In: *Journal of General Physiology* 149 (10 okt 2017), p. 911–920. ISSN: 0022-1295. DOI: [10.1085/jgp.201711839](https://doi.org/10.1085/jgp.201711839).
- [2] A. L. Hodgkin en B. Katz. “The effect of sodium ions on the electrical activity of the giant axon of the squid”. In: *The Journal of Physiology* 108 (1 mrt 1949), p. 37–77. ISSN: 0022-3751. DOI: [10.1113/jphysiol.1949.sp004310](https://doi.org/10.1113/jphysiol.1949.sp004310).
- [3] Carolyn L. Powell en Angus M. Brown. “A classic experiment revisited: membrane permeability changes during the action potential”. In: *Advances in Physiology Education* 45 (1 mrt 2021), p. 178–181. ISSN: 1043-4046. DOI: [10.1152/advan.00188.2020](https://doi.org/10.1152/advan.00188.2020).
- [4] Michael Levin. “Molecular bioelectricity: How endogenous voltage potentials control cell behavior and instruct pattern regulation in vivo”. In: *Molecular Biology of the Cell* 25 (24 dec 2014), p. 3835–3850. ISSN: 19394586. DOI: [10.1091/mbc.E13-12-0708](https://doi.org/10.1091/mbc.E13-12-0708). PMID: 25425556.
- [5] Vaibhav P. et al. “Transmembrane voltage potential controls embryonic eye patterning in *Xenopus laevis*”. In: *Development* 139 (2 jan 2012), p. 313–323. ISSN: 1477-9129. DOI: [10.1242/dev.073759](https://doi.org/10.1242/dev.073759).
- [6] Joseph R. Lakowicz. *Principles of Fluorescence Spectroscopy*. Red. door Joseph R. Lakowicz. Boston, MA: Springer US, 2006. ISBN: 978-0-387-31278-1. DOI: [10.1007/978-0-387-46312-4](https://doi.org/10.1007/978-0-387-46312-4).
- [7] “Basic Principles of Fluorescence Spectroscopy”. In: Wiley, jan 2011, p. 1–30. DOI: [10.1002/9783527633500.ch1](https://doi.org/10.1002/9783527633500.ch1).
- [8] Mikhail Y. Berezin en Samuel Achilefu. “Fluorescence Lifetime Measurements and Biological Imaging”. In: *Chemical Reviews* 110 (5 mei 2010), p. 2641–2684. ISSN: 0009-2665. DOI: [10.1021/cr900343z](https://doi.org/10.1021/cr900343z).
- [9] Albert M. Brouwer. “Standards for photoluminescence quantum yield measurements in solution (IUPAC Technical Report)”. In: *Pure and Applied Chemistry* 83 (12 aug 2011), p. 2213–2228. ISSN: 1365-3075. DOI: [10.1351/PAC-REP-10-09-31](https://doi.org/10.1351/PAC-REP-10-09-31).
- [10] Th. Förster. “Zwischenmolekulare Energiewanderung und Fluoreszenz”. In: *Annalen der Physik* 437 (1-2 jan 1948), p. 55–75. ISSN: 0003-3804. DOI: [10.1002/andp.19484370105](https://doi.org/10.1002/andp.19484370105).
- [11] “IUPAC Gold Book: fluorescence”. In: Research Triangle Park, NC: International Union of Pure en Applied Chemistry (IUPAC), feb 2014. DOI: [10.1351/goldbook.F02453](https://doi.org/10.1351/goldbook.F02453).

- [12] Bernard Valeur en Mário Nuno Berberan-Santos. *Molecular Fluorescence: Principles and Applications*. 2de ed. Wiley-VCH, 2012.
- [13] A. Jablonski. "Efficiency of Anti-Stokes Fluorescence in Dyes". In: *Nature* 131 (3319 jun 1933), p. 839–840. ISSN: 0028-0836. DOI: [10.1038/131839b0](https://doi.org/10.1038/131839b0).
- [14] Wolfgang Becker. *Advanced Time-Correlated Single Photon Counting Techniques*. Red. door A. W. Castleman, J. P. Toennies en W. Zinth. Deel 81. Berlin: Springer Berlin, Heidelberg, 2005. ISBN: 978-3-540-26047-9. DOI: [10.1007/3-540-28876-0](https://doi.org/10.1007/3-540-28876-0).
- [15] D. Ruhlandt e.a. "Absolute quantum yield measurements of fluorescent proteins using a plasmonic nanocavity". In: *Communications Biology* 3.1 (30 okt 2020), p. 627. DOI: [10.1038/s42003-020-01316-2](https://doi.org/10.1038/s42003-020-01316-2). PMID: 33128009.
- [16] Klaus Suhling e.a. "Imaging the Environment of Green Fluorescent Protein". In: *Biophysical Journal* 83.6 (1 dec 2002), p. 3589–3595. DOI: [10.1016/S0006-3495\(02\)75359-9](https://doi.org/10.1016/S0006-3495(02)75359-9). PMID: 12496126.
- [17] Yongxian Xu, Peng Zou en Adam E Cohen. "Voltage imaging with genetically encoded indicators". In: *Current Opinion in Chemical Biology* 39 (aug 2017), p. 1–10. ISSN: 13675931. DOI: [10.1016/j.cbpa.2017.04.005](https://doi.org/10.1016/j.cbpa.2017.04.005).
- [18] Rahul Roy, Sungchul Hohng en Taekjip Ha. "A practical guide to single-molecule FRET". In: *Nature Methods* 5 (6 jun 2008), p. 507–516. ISSN: 1548-7091. DOI: [10.1038/nmeth.1208](https://doi.org/10.1038/nmeth.1208).
- [19] L Stryer en R P Haugland. "Energy transfer: a spectroscopic ruler." In: *Proceedings of the National Academy of Sciences* 58 (2 aug 1967), p. 719–726. ISSN: 0027-8424. DOI: [10.1073/pnas.58.2.719](https://doi.org/10.1073/pnas.58.2.719).
- [20] Ágnes Szabó, János Szöllősi en Peter Nagy. "Principles of Resonance Energy Transfer". In: *Current Protocols* 2 (12 dec 2022). ISSN: 2691-1299. DOI: [10.1002/cpz1.625](https://doi.org/10.1002/cpz1.625).
- [21] Peng Zou e.a. "Bright and fast multicoloured voltage reporters via electrochromic FRET". In: *Nature Communications* 5 (aug 2014). ISSN: 20411723. DOI: [10.1038/ncomms5625](https://doi.org/10.1038/ncomms5625). PMID: 25118186.
- [22] Y. Gong e.a. "High-speed recording of neural spikes in awake mice and flies with a fluorescent voltage sensor". In: *Science* 350 (6266 dec 2015), p. 1361–1366. ISSN: 0036-8075. DOI: [10.1126/science.aab0810](https://doi.org/10.1126/science.aab0810).
- [23] Madhuvanathi Kannan e.a. "Fast, in vivo voltage imaging using a red fluorescent indicator". In: *Nature Methods* 15 (12 dec 2018), p. 1108–1116. ISSN: 15487105. DOI: [10.1038/s41592-018-0188-7](https://doi.org/10.1038/s41592-018-0188-7). PMID: 30420685.
- [24] Yiyang Gong e.a. "Imaging neural spiking in brain tissue using FRET-opsin protein voltage sensors". In: *Nature Communications* 5 (apr 2014). ISSN: 20411723. DOI: [10.1038/ncomms4674](https://doi.org/10.1038/ncomms4674). PMID: 24755708.
- [25] Connor Beck, Diming Zhang en Yiyang Gong. "Enhanced genetically encoded voltage indicators advance their applications in neuroscience". In: *Current Opinion in Biomedical Engineering* 12 (dec 2019), p. 111–117. ISSN: 24684511. DOI: [10.1016/j.cobme.2019.10.010](https://doi.org/10.1016/j.cobme.2019.10.010).

- [26] Michael Wahl en Sandra Orthaus-Müller. *Time Tagged Time-Resolved Fluorescence Data Collection in Life Sciences*. Berlin, Germany, 2014.
- [27] Wolfgang Becker. *The bh TCSPC Handbook (8th ed.)* 8th. Berlin, Germany: Becker en Hickl GmbH, 2019.
- [28] Wolfgang Becker. *Recording the Instrument Response Function of a Multiphoton FLIM System*. 2008.
- [29] Jason P. Eichorst, Wen K. Teng en Robert M. Clegg. "Polar Plot Representation of Time-Resolved Fluorescence". In: *Fluorescence Spectroscopy and Microscopy*. Red. door Yves Engelborghs en Antonie Visser. Deel 1076. Methods in Molecular Biology. Totowa, NJ: Humana Press, 2014. DOI: [10.1007/978-1-62703-649-8_6](https://doi.org/10.1007/978-1-62703-649-8_6). URL: https://doi.org/10.1007/978-1-62703-649-8_6.
- [30] Rupsa Datta e.a. "Fluorescence lifetime imaging microscopy: fundamentals and advances in instrumentation, analysis, and applications". In: *Journal of Biomedical Optics* 25 (07 mei 2020), p. 1. ISSN: 1083-3668. DOI: [10.1117/1.JBO.25.7.071203](https://doi.org/10.1117/1.JBO.25.7.071203).
- [31] Julia R Lazzari-Dean, Anneliese MM Gest en Evan W Miller. "Optical estimation of absolute membrane potential using fluorescence lifetime imaging". In: *eLife* 8 (sep 2019). ISSN: 2050-084X. DOI: [10.7554/eLife.44522](https://doi.org/10.7554/eLife.44522).
- [32] Michelle A. Digman e.a. "The Phasor Approach to Fluorescence Lifetime Imaging Analysis". In: *Biophysical Journal* 94 (2 jan 2008), p. L14–L16. ISSN: 00063495. DOI: [10.1529/biophysj.107.120154](https://doi.org/10.1529/biophysj.107.120154).
- [33] Klaus Suhling e.a. "Fluorescence lifetime imaging (FLIM): Basic concepts and some recent developments". In: *Medical Photonics* 27 (mei 2015), p. 3–40. ISSN: 2213-8846. DOI: [10.1016/J.MEDPHO.2014.12.001](https://doi.org/10.1016/J.MEDPHO.2014.12.001).
- [34] Eva Fišerová en Martin Kubala. "Mean fluorescence lifetime and its error". In: *Journal of Luminescence* 132.8 (1 aug 2012), p. 2059–2064. DOI: [10.1016/j.jlumin.2012.03.038](https://doi.org/10.1016/j.jlumin.2012.03.038). URL: <https://doi.org/10.1016/j.jlumin.2012.03.038>.
- [35] N. Boens e.a. "Fluorescence lifetime standards for time and frequency domain fluorescence spectroscopy". In: *Analytical Chemistry* 79.5 (1 mrt 2007), p. 2137–2149. DOI: [10.1021/ac062160k](https://doi.org/10.1021/ac062160k). PMID: 17269654. URL: <https://doi.org/10.1021/ac062160k>.
- [36] Anagha Gopalakrishnan Nair e.a. "Absolute Membrane Potential Recording with ASAP-Type Genetically Encoded Voltage Indicators Using Fluorescence Lifetime Imaging". In: *ACS Chemical Neuroscience* 16.24 (17 dec 2025). Epub 2025-11-22, p. 4636–4646. DOI: [10.1021/acscchemneuro.5c00670](https://doi.org/10.1021/acscchemneuro.5c00670). PMID: 41273308. URL: <https://doi.org/10.1021/acscchemneuro.5c00670>.
- [37] Daan Brinks, Aaron J. Klein en Adam E. Cohen. "Two-Photon Lifetime Imaging of Voltage Indicating Proteins as a Probe of Absolute Membrane Voltage". In: *Biophysical Journal* 109 (5 sep 2015), p. 914–921. ISSN: 15420086. DOI: [10.1016/j.bpj.2015.07.038](https://doi.org/10.1016/j.bpj.2015.07.038). PMID: 26331249.
- [38] Daniel J. Liput e.a. "A Guide to Fluorescence Lifetime Microscopy and Förster's Resonance Energy Transfer in Neuroscience". In: *Current Protocols in Neuroscience* 94 (1 dec 2020). ISSN: 1934-8584. DOI: [10.1002/cpns.108](https://doi.org/10.1002/cpns.108).

- [39] Yahui Li e.a. “Investigations on Average Fluorescence Lifetimes for Visualizing Multi-Exponential Decays”. In: *Frontiers in Physics* 8 (okt 2020). ISSN: 2296-424X. DOI: [10.3389/fphy.2020.576862](https://doi.org/10.3389/fphy.2020.576862).
- [40] Suman Ranjit e.a. “Fit-free analysis of fluorescence lifetime imaging data using the phasor approach”. In: *Nature Protocols* 13 (9 sep 2018), p. 1979–2004. ISSN: 1754-2189. DOI: [10.1038/s41596-018-0026-5](https://doi.org/10.1038/s41596-018-0026-5).

ACKNOWLEDGEMENTS

More than five years of PhD life have passed, almost in the blink of an eye. Looking back on these years, with all their challenges, uncertainty, discovery, and growth, I feel deeply grateful to the many people who have supported me along the way. This PhD has been a period of scientific training, but it has also been a time in which I grew, slowly and profoundly, through the kindness, encouragement, and love of the people around me.

First, I would like to express my gratitude to my promotor and daily supervisor, **Daan Brinks**. Thank you for giving me the opportunity to come to Delft for my PhD. I still clearly remember my first visit to Delft for the interview at the end of 2019, and the anticipation I felt at the thought of starting a new chapter here. I also remember the joy I felt when I received the offer while waiting at the airport on my way back. Thank you for your guidance, trust, and support over the past years. You have always followed my project with care and attention, and whenever I needed it, I could count on your timely and thoughtful feedback. Our discussions helped me move my experiments forward, but they also often gave me new ways of thinking about my work. I am especially grateful for the freedom you gave me to explore my project at my own pace, develop my own ideas, and learn through trial, adjustment, and sometimes failure. You encouraged me to step outside my comfort zone, try unfamiliar directions, and build confidence in fields that were new to me. You often reminded me that a PhD is not only about completing a project, but also about learning how to conduct independent research. Through this training, I gradually learned how to ask questions, think through problems, make decisions, and find my own way forward.

I would also like to express my sincere gratitude to my promotor, **Jacob Hoogenboom**. Thank you, together with the Imaging Physics Department, for hosting and supporting my PhD research. Thank you for your advice, encouragement, and support throughout my PhD. Your guidance helped me see my development as a PhD candidate from a broader perspective and helped me regain a sense of direction at moments when I felt uncertain. I would also like to thank **Elizabeth Carroll** for your guidance and support during the early stages of my PhD. I am grateful to **Kees Hagen** and the other PIs in the MINT group for their questions, suggestions, and discussions during group meetings and many other conversations.

I would like to give special thanks to my paranymphs, **Xin Meng** and **Marco Locarno**. Having you as both colleagues and close friends has been one of the greatest gifts of my PhD. Thank you for your friendship, warmth, and steady support throughout these years. After you graduated, I often missed the days when we worked together, and I am very happy that we have continued to see each other often. We went through the pandemic together, witnessed each other's growth and changes, and shared many moments of joy and sadness. Because you were there, the difficult days became easier to bear. **Xin**, thank you for picking me up at Delft station when I first came here for my interview, and for all

the help, patience, and encouragement you have given me in both my project and my life. In this unfamiliar country, the warmth and sense of connection you gave me have always been extremely precious to me. **Marco**, thank you for bringing risotto to my apartment late at night on the first day I arrived in the Netherlands. I have kept that warm memory in my heart ever since. Thank you also for inviting us to your hometown, introducing me to your family, and, above all, for caring about my growth, making space for my emotions, and supporting me with such sincerity and care over the years. Thank you both also for all the effort you have put into today's celebration and for making this important day truly special.

I would also like to thank many friends and colleagues who helped me at different stages of my PhD. **Srividya Ganapathy**, thank you for helping me get started at the beginning of my PhD and for giving me so much care and kindness, like an elder sister. I have always treasured the thoughtful wishes you wrote for me on special occasions, and I will always remember the beautiful time we shared. **Laura Maddalena**, thank you for your guidance on the zebrafish experiments, and also for the many warm and joyful memories you brought. **Nicolò Ceffa**, thank you for your kindness and warmth when I first arrived in the Netherlands, and for letting me taste truly authentic Italian pizza. These seemingly ordinary moments later became some of the brightest memories of my PhD.

Monika Molnar, thank you for filling the last year of my PhD with warmth and unexpected joy. Thank you for being there for me with so much comfort, support, and encouragement. I truly enjoyed our deep conversations about work and life, and I treasure this sincere friendship very much. **Arent Kievits**, thank you for choosing me as your paranymph. We started our PhDs around the same time, and I have truly enjoyed sharing this journey with you and growing alongside each other over the years. **Mike Simons**, thank you for the encouragement and comfort you gave me through so many of our conversations. Your kindness and understanding often helped me feel more grounded. **Martijn Adriaans**, thank you for always bringing smiles and energy to the people around you. Talking with you has always been one of the great joys outside work. **Rui Silva**, thank you for your help and support with my project, and thank you, together with **Catarina**, for the wonderful time we spent together and for the Portuguese food that always made me happy. **Tibbe Höppener**, thank you for your help with the coding part of my project, and for the coffee chats and Limburg rice cake that I will always remember.

I would also like to thank my officemates, **Marco Post**, **Alejandro Castañeda Garcia**, and **Laurens Engwegen**. **Marco**, thank you for your help with my project and for your support and encouragement during difficult moments. I miss the days when you taught me Dutch in the office, and I have always appreciated your warmth, sincerity, and infectious enthusiasm. **Alejandro** and **Laurens**, thank you for the many conversations, laughter, and relaxed moments we shared in the office. I truly enjoyed the time we spent together.

Thanks to **Johan van der Cingel** and **Han van der Linden** for all the technical support you provided throughout my project. Whenever I ran into problems with equipment, I always knew I could turn to you for advice and support. **Johan**, I would also like to thank you especially for the incredibly sweet figs you bring every year. I have always enjoyed our conversations, full of humor, kindness, and warmth. I also thank **Huma Safdar**, **Apilina**, **Mariska**, and **Aleksandra** for all your help in the lab, for the friendly conversations, and for all the delicious food that made our days in the lab even better.

I would like to thank my students, **Adriana João Falcão Neves**, **Fabiola Marques Trujillo**, **Jordan Gotti**, **Lijing Hu**, **Robin Liu**, **Ruya Houssein**, **Thomas van Aarle**, **Titouan Luciani**, and **Zehra Kaynak**. Thank you for your contributions to this thesis, and for allowing me to learn so much through supervision and collaboration. The time we spent discussing, experimenting, and working together was a very meaningful part of my PhD.

I would also like to thank all my colleagues in MINT. You made this group a warm, open, and friendly place. I am deeply grateful to have spent these years here, and I will always cherish my time in MINT.

I would also like to thank the friends who shared these years with me in the Netherlands. Because of you, life in a foreign country felt warmer, fuller, and much more like home. **Nol Duindam** and **Isa de Boer**, thank you for your kindness, care, and warmth. The times we made Chinese noodles and baozi together, went camping, celebrated birthdays, and, especially, the fact that you traveled all the way to China for my wedding are memories I will always treasure. **Dennis Aschmann**, thank you for organizing our Christmas market trips every year, for inviting us to your hometown, Düsseldorf, and for all the BBQ evenings filled with good food and laughter. Your kindness and cheerful spirit made those gatherings very special to me. **Ferhat Oz**, thank you for the many happy moments we shared. With you, there were always endless things to talk about, and even our complaints somehow became a source of joy. **Jillian Zwemmer**, thank you for the warmth and energy you brought into my life. Every time I visited your home, whether for hotpot or BBQ, I felt relaxed and at ease. Thank you all for making my life here not only about work and study, but also about friendship, everyday life, and a feeling of home.

I would also like to thank all my Chinese friends who shared these years with me in Delft: **Bo Li**, **Chi Jin**, **Dantong Qin**, **Desong Du**, **Di Yan**, **Jiao Zhao**, **Jing Yu**, **Jingyi Liu**, **Kai Wu**, **Qingru Li**, **Sen Yuan**, **Tianlong Jia**, **Tingting Wang**, **Wenxiu Wang**, **Wenyi Lu**, **Xiaoyu Liu**, **Xueqing Miao**, **Xun Zhang**, **Yifei Li**, **Yigu Liu**, **Yueer Li**, **Yun Li**, and **Zichao Li**. Thank you for the dinners, board games, festivals, weekends, holidays, and all the small moments we shared. Especially during the uncertain and difficult period of the pandemic, the time we spent together brought so much warmth and comfort to my life in Delft.

Thank you to my wonderful travel buddies, **Yigu**, **Desong**, and **Sen**. I will always remember our trips to Paris, Mallorca, and Norway, and especially the legendary trip where all our luggage was stolen, but somehow not our mood. Together with **Xiaoyu**, **Jiao**, and **Wenyi**, thank you for being part of so many weekends in Delft and for celebrating almost every Chinese New Year I spent in the Netherlands with me. These ordinary but precious moments have become some of my warmest memories here. **Di**, **Tingting**, and **Xueqing**, you were among the first friends I made after coming to the Netherlands. I still remember the first Christmas and the first Chinese New Year we spent together, when everything here still felt new and unfamiliar. Thank you for being there from the very beginning and for making those early days feel much more like home. **Di**, I would also like to thank you especially for staying close to me through different stages of this journey, for accepting me even when I was not at my best, and for being genuinely happy for my achievements. Also **Xueqing**, for walking through these years with me and for sharing so many important moments of life along the way. **Dantong** and **Xun**, thank you for being such wonderful neighbors and friends, for always sharing delicious food with us, and for bringing the taste of home into my life in the Netherlands. Your kindness and cheerful

energy brought me so much joy.

Because of all of you, my years in Delft were filled not only with research, but also with friendship, laughter, and many memories that I will always carry with me.

I would also like to thank my dear friends in China, **Bailu Zhao**, **Guangyu Guo**, **Jing-jing Ye**, **Mengyang Xu**, **Qing Zhang**, and **Xin Zheng**. Thank you for being there for me throughout these PhD years, for listening to me when things were difficult, for encouraging me, and for always believing in me. Even though we were not always in the same city, or even the same country, your friendship has always made me feel supported and understood.

I would like to thank my family for the love and support that have carried me through this journey. I am deeply grateful to my grandparents, **Jinfang Wu** and **Xiutai Wang**, to my parents, **Zengxing Wu** and **Yanqin Wang**, and to my uncle, **Tiqiang Wu**. Thank you for your unconditional love and support, for trusting me even when my choices were not always easy to understand, and for being proud of me at every step. I am also deeply grateful to my parents-in-law, **Biyuan Wu** and **Yuxia Zhu**. Thank you for respecting and supporting the life we have chosen, and for giving us so much care, understanding, and encouragement over the years. I also thank all my other family members who have cared for me and supported me along the way. No matter the distance, your love has always reached me. It has shaped who I am today and given me the courage to keep moving forward.

I would like to thank my husband, **Dinghao Wu**, for sharing this journey with me with so much love, patience, and understanding. Through successes and failures, through joyful moments and difficult days, you have always been by my side. Thank you for supporting the choices I made, for celebrating my achievements, and for carrying the difficult moments with me when I felt lost or overwhelmed. During the hardest period of this PhD, you stayed with me as I slowly found my way forward again. Thank you for giving me courage, comfort, and love, and for making me feel that, no matter how difficult the journey became, I was never facing it alone. You witnessed every part of this journey, including all the ways I changed and grew along the way. This PhD has never been only my story, but also part of the life we have built together. The road ahead is still long. Let us keep walking it, together.

Finally, I would like to thank myself. Thank you for not giving up, especially in the hardest moments. Thank you for continuing to move forward when the path was unclear, and for finding the courage to try again after every disappointment. I am grateful to the person I was at the beginning of this journey, to the person who made it through the most difficult days, and to the person I have become today.

Zhenzhen Wu
04 May 2026

CURRICULUM VITÆ

Zhenzhen WU

05-06-1993 Born in Hebei, China.

EDUCATION

2012–2016 Bachelor of Science in Biotechnology
Ningxia University, Yinchuan, China

2013–2016 Minor in Management
Shanghai Jiao Tong University, Shanghai, China

2016–2019 Master of Science in Neurobiology
Zhejiang University, Hangzhou, China

2020–2025 PhD Candidate in Imaging Physics
Delft University of Technology, Delft, The Netherlands

Thesis: Investigating membrane voltage in embryonic develop-
ment

Promotor: Prof. dr. ir. J.P. Hoogenboom and Dr. ir. D. Brinks

AWARDS

2024 Best Poster Award (1st Place), NWO Biophysics Conference, The Netherlands

LIST OF PUBLICATIONS

5. *Engineering FRET-based GEVIs for quantitative absolute voltage imaging*, In preparation. (Chapter 4 of this dissertation)
4. **Z. Wu**, A. João Falcão Neves, M. Post, T. Höppener, R. Liu, T. Luciani, D. Brinks, *Absolutely calibrated lifetime-imaging voltage sensing in developing zebrafish embryos*, In preparation. (Chapter 3 of this dissertation)
3. **Z. Wu**, R. Oliveira Silva, R. Houssein, F. Marques Trujillo, J. Gotti, S. Ganapathy, Z. Gao, D. Brinks, *Zebrafish Ace2N-mNeon expression toolkit for in vivo voltage imaging of neuronal synchrony and cardiac maturation*, [Neurophotonics 13\(S2\), S23205 \(2026\)](#). (Chapter 2 of this dissertation)
2. C. Wang, H. Liu, K. Li, **Z. Wu**, C. Wu, J.Y. Yu, et al., *Tactile modulation of memory and anxiety requires dentate granule cells along the dorsoventral axis*, [Nature Communications 11, 6045 \(2020\)](#). (Not related to this dissertation)
1. **Z. Wu**, X.-D. Wang, *Progress on the role of synaptic cell adhesion molecules in stress*, [Acta Physiol Sin 72\(2\), 220–226 \(2020\)](#). (Not related to this dissertation)

